

https://dspace.org/

Geochemical and geochronological analysis of post-impact hydrothermal alteration in the Morokweng impact structure, South Africa

Malelu, Liseloane Lucia

2025-03

University of the Witwatersrand, Johannesburg

https://hdl.handle.net/10539/47689

Malelu, Liseloane Lucia. (2025). Geochemical and geochronological analysis of post-impact hydrothermal alteration in the Morokweng impact structure, South Africa. [Master's dissertation, University of the Witwatersrand, Johannesburg]. WIReDSpace. https://hdl.handle.net/10539/47689

Downloaded from a DSpace repository. https://dspace.org/

GEOCHEMICAL AND GEOCHRONOLOGICAL ANALYSIS OF POST-IMPACT HYDROTHERMAL ALTERATION IN THE MOROKWENG IMPACT STRUCTURE, SOUTH AFRICA

Liseloane L. Malelu

Student number: 746283



UNIVERSITY OF THE
WITWATERSRAND,
JOHANNESBURG

Supervisors:

Prof. Robert Bolhar

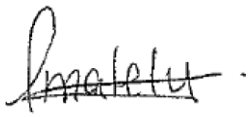
Prof. Roger L. Gibson

March 4th , 2025

Johannesburg, South Africa

CANDIDATE'S DECLARATION

I declare that this dissertation is my own unaided work. This work is submitted for the Master of Science Degree at the University of the Witwatersrand, Johannesburg, South Africa. This work has not been submitted before for any degree or examination at any other University.



Liseloane Lucia Malelu

4th day of March at the University of the Witwatersrand

ABSTRACT

This study investigates evidence of post-impact hydrothermal activity in the 369 m long M4 drillcore, located 18 km NNW of the centre of the 80 km-wide, 146 Ma, Morokweng Impact Structure (MIS), South Africa. The core intersects fractured, faulted, brecciated and cataclased Archaean granitoid gneisses and minor dolerites that are intruded by mm- to m-wide pseudotachylite and suevite dykes, for which a peak ring setting has been proposed. Petrographic evidence indicates that impact-related shock features and breccias are overprinted by a dominantly zeolite-smectite paragenesis that contains some evidence of high-temperature (>350 °C) minerals such as actinolite, clinopyroxene, andradite and titanite, as well as minor amounts of calcite and anhydrite. Biotite shows varying degrees of alteration to chlorite. Pyrite occurs as part of the post-impact assemblage locally, but the dominant Fe-bearing phases are magnetite, haematite and iron hydroxides such as goethite. The impact-related structures and the post-impact hydrothermal veins are cut by younger, mostly subhorizontal, mm- to cm-wide, calcite veins in the upper parts of the core that contain minor amounts of zeolite. The calcite vein textures vary from blocky coarse-grained to fibrous/stretched to elongate-blocky and blocky/fine-grained and cross-cutting relationships indicate multiple veining events.

Smectite-illite K-Ar ages range from 105.80 ± 4.43 Ma (214.40 m) to 68.88 ± 48.87 Ma (121.8 m), 59.45 ± 7.74 Ma (216 m) and 57.41 ± 7.14 (119 m). The correlation of age with grain size suggests that these ages might reflect resetting of the original impact hydrothermal assemblages formed at 146 Ma, although new mineral growth during discrete post-impact hydrothermal events cannot be completely ruled out. Four calcite veins analyzed via LA-ICP-MS yielded U-Pb ages of 66.46 ± 0.74, 16 ± 47, 28.1 ± 1.1, and 13.95 ± 4.32 Ma. The broad agreement between the oldest U-Pb calcite age and three of the smectite-illite ages suggests a significant hydrothermal event close to the Cretaceous-Palaeogene boundary.

Stable isotope analysis indicates that the older calcite veins record heavier $\delta^{18}O$ and varying $\delta^{13}C$ values ranging from 21.45 to 27.39 ‰ and -21.80 to -9.24 ‰, respectively, whereas the younger veins record lighter $\delta^{18}O$ and varying $\delta^{13}C$ values of 19.00 to 22.04 ‰ and -19.79 to -3.99 ‰, respectively. Negative $\delta^{13}C_{PDB}$ values are consistent with a meteoric groundwater influence

enriched in dissolved organic carbon; however, the combined $\delta^{13}C_{PDB}$–$\delta^{18}O_{SMOW}$ values suggest connate waters that interacted with a marine carbonate source. The $\delta^{13}C_{PDB}$–$\delta^{18}O_{SMOW}$ values and age values vary between samples. The temperature of crystallization of the vein carbonate is estimated between 8.5 to 140.7 and > 200°C, using the stable isotope thermometer.

Rare earth element (REE) patterns in the calcite veins are also sample-specific and show little to no correlation with the REE patterns of the host rocks, suggesting derivation from an external source and little to no interaction between the fluids and the wallrocks. One sample exhibits a pattern enriched in light rare earth elements relative to middle and heavy rare earth elements, with a negative Ce, slightly positive Gd, and positive Y anomalies, suggestive of precipitation under oxidizing conditions. However, two samples show flat REE patterns with strong positive Eu and Y anomalies, indicative of oxygen-poor hydrothermal fluids, while the fourth sample shows a flat REE pattern with a positive Y anomaly. These patterns indicate different fluid sources and may imply temporal variation in fluid composition related to different veining events. In conclusion, the calcite veins in the upper parts of the M4 drillcore appear to represent polyphase fluid infiltration events unrelated to the Morokweng impact event, and most likely are associated with discrete events relating to the poorly understood Late Cretaceous to Cenozoic tectonic and exhumation/burial history of the region.

ACKNOWLEDGEMENTS

This journey has been an opportunity to partake in cutting-edge research, collaborating with another MSc student, Tshepang Masiu, filling in the gaps in a relatively advanced field of planetary geology.

I would like first to thank my supervisor (50%), Prof. Roger Gibson, for his unwavering commitment to advising this project and keeping me on my toes to ensure that, as a team, we are all on the same wavelength. His encouragement throughout goes unnoticed. I would also like to express my gratitude to my other supervisor (50%), Prof. Robert Bolhar, for his guidance throughout the research process, for upskilling my analytical data integration, and for conducting U-Pb and trace element data. Their demeanour has allowed me to develop a robust research acumen, and their mentorship has been instrumental in shaping this dissertation.

To my team member and friend, Tshepang Masiu, you have made this journey bearable. First, thank you for being my sister in Christ. You have been my pillar of strength, and walking this journey with you has given me a broader view of this project. The team is incomplete without Dr. Nonkuselo Madlakana, Tshepang's Co-supervisor, who is also the head of the TIMA automated scanning electron microscope. Thank you, Nonku, for your help and instrument training in preparing samples and conducting TIMA analysis. To Dr. Tonguc Uysal, thank you for collaborating on the clay K-Ar dating and for providing feedback for this dissertation's clay and C-O isotopic sections.

Thank you to Caiphas Majola, Louis Mudalahothe, and Sam Tshabalala for preparing samples for geochemistry and geochronology, to the MMU labs team for instrument training for the scanning electron microscope and to Sarah Glynn and the GFZ Potsdam, Germany, team who facilitated the SIMS analysis. Dr Zubair Jinnah provided me with alternative software for the XRD analysis and Terracore provided hyperspectral data. Pan African Mineral Development Company (Pty) Ltd. donated the drillcore to the School of Geosciences, Wits. To my friends and colleagues, Thoriso Lekoetje, Mmasetena Molekwa, Motseoa Lephatsi, Peace Zowa, Tariye Onyeogu and Obehi Atita. For your encouragement and unwavering support.

The tuition was paid by the National Manpower Development Secretariat (NMDS) bursary, the Research Office Carnegie Bursary, and the Geoscience Provision Account. The analytical work was supported by the Barringer Family Fund for the Meteorite Impact Research Grant and research grants to Prof. Roger Lawrence Gibson from DSI-NRF.

This work is dedicated to the Malelu clan and my pillars of strength, my brother, George Malelu; my mother, Mamolefi Malelu; my father, Thabo Azael Malelu; my aunt, Mphokololi Rakuoane and to the Rakuoane family. Thank you for your love and belief in me, which have sustained me through the ups and downs of completing this dissertation. To God be the glory.

TABLE OF CONTENTS

Candidate's Declaration ii

Abstract iii

Acknowledgements v

List of Figures xi

List of tables xvii

1. Introduction 1

1.1. Impact-induced hydrothermal system 4

1.1.1. Sources of heat 4

1.1.2. Permeability 5

1.1.3. Availability of fluids 6

1.1.4. Shock deformation features 7

1.1.4.1. Planar fractures 7

1.1.4.2. Planar deformation features 8

1.1.4.3. Feather features 8

1.1.4.4. Kink bands 8

1.2. Post-impact hydrothermal mineralization 9

1.3. Calcite Geochemistry 12

1.3.1. Stable isotopes 12

1.3.2. Trace elements 12

1.4. Geochronology of post-impact veins and clays 13

2. Geological Setting 15

2.1. Introduction 15

2.2. Late Cretaceous to late Miocene history of the Morokweng region 17

2.3. Kalahari group stratigraphy 18

2.4. The M4 drillcore 20

2.4.1. Granitic and granodioritic gneisses 21

2.4.2. Trondhjemitic gneiss 21

2.4.3. Monzonitic gneiss 21

2.4.4. Metadolerite and dolerite 22

2.4.5. Pseudotachylite 24

2.4.6. Suevites 24

2.4.7. Veins 25
3. Hypothesis and Methodology 28
3.1. Hypothesis, Aims and Objectives 28
3.1.1. Hypothesis and Questions 28
3.1.2. Aims and Objectives 28
3.2. Methodology 29
3.2.1. Macroscopic analysis 29
3.2.2. Optical Microscopy 29
3.2.3. Scanning Electron Microscopy 30
3.2.4. X-Ray Powder Diffraction 31
3.2.5. Secondary Ion Mass Spectrometry 31
3.2.6. Laser Ablation Inductively Coupled Plasma Mass Spectrometry 32
3.2.7. Mass spectrometer 32
4. Post-impact hydrothermal alteration 34
4.1. Introduction 34
4.2. Post-impact hydrothermal alteration in shock microdeformation features 36
4.2.1. Quartz 36
4.2.2. Feldspars 39
4.2.3. Biotite 43
4.2.4. Epidote 46
4.3. Post-impact hydrothermal alteration in brittle structures 47
4.3.1. Impact-generated breccias 51
4.4. Post-impact hydrothermal veins 55
4.4.1. Macroscopic observations 55
4.4.2. Microscopic observations 58
4.4.2.1. Cross-cutting relations 58
4.4.2.2. Anhydrite veins 61
4.4.2.3. Zeolite veins 62
4.4.2.4. Calcite veins 70
4.5. Geochemistry of calcite veins 75
4.5.1. Oxygen and carbon stable isotopic compositions 76
4.5.2. Trace element geochemistry 79
4.5.2.1. Elemental compositions 79

4.5.2.2. Rare earth elements 79
4.6. Geochronology 85
4.6.1. U-Pb dating 85
4.6.2. K-Ar dating 91
5. Discussion 93
5.1. Petrography and Mineralogy 93
5.1.1. Controls on Alteration 93
5.1.2. Mineral assemblages in the M4 drillcore 94
5.1.2.1. Mineralization trend in fractures and alteration temperatures 94
5.1.2.2. Lower temperature post-impact veins 95
5.2. Potential sources of fluids 97
5.3. Chronology of calcite vein and clay formation 97
5.4. Trace element compositions of vein calcite 99
5.4.1. Genetic relationships between calcites 99
5.4.2. Influence of hydrothermal fluids 100
5.4.3. Influence of connate waters from marine carbonates 102
5.4.4. Temperature of calcite veins 104
5.4.4.1. Oxygen reservoir ranges and isotope temperature 105
5.5. Comparison with other impact structures 107
5.5.1. Chicxulub impact structure 107
5.5.2. Puchezh-Katunki structure 108
5.6. Implications for regional tectonic setting 108
5.7. Recommendations and future work 111
6. Conclusions 112
7. References 113
8. Appendices 131
Appendix 1: Petrography 131
Appendix 1.1 Post-impact hydrothermal alteration around biotite 131
Appendix 1.2A Elemental map distribution of sample M4 R12 135
Appendix 1.2B Elemental map distribution of sample M4 R12 136
Appendix 1.3A Aired-dried XRD illite-smectite clays 137
Appendix 1.3B Glycolated 141
Appendix 1.4 Zeolite veins with titanite-apatite grains 148

Appendix 2: Geochemistry 149
Appendix 2.1 Stable isotope data 149
Appendix 2.2: Trace element geochemical data for calcite veins 152
Appendix 2.3 Rare earth elements and yttrium for calcite veins 158
Appendix 3: Geochronology 164
Appendix 3.1. U-Pb ages of calcite veins. 164

LIST OF FIGURES

Figure 1.1. Illustration of a complex impact crater (adapted from Chen and Sun, 2017). A) Schematic cross-section showing arrows visually depicting differential crater floor movement in response to the impact and subsequent crater modification under gravitational forces. This process forms the ring of uplifted material known as the peak-ring. B) Photomicrograph of a lunar crater, showing the 3D key features of the cross-section in A, including central uplift, peaking ring and crater rim. 2

Figure 1.2. Thermal model of the Chicxulub Structure with contours illustrating temperature distribution and the circulation of hydrothermal fluids into and through the peak ring (modified from Kring et al., 2020; and half-space of Figure 1.1). The position of the M0077A drillcore, which is used for comparison with the M4 Morokweng drillcore in this study, is shown. 3

Figure 1.3. Illustration of regressive hydrothermal circulation of fluids within a complex crater showing three successive stages. Stage I (initial/early stage) displays variability in temperature from top downward, with hydrothermal activity occurring in the periphery of central uplift. Stage II (main stage) displays lateral variations in temperature with circulation of fluids within both the central uplift and its periphery. Stage III (final stage) is characterised by temperatures < 100 ℃ and fluid circulation occurs only near the surface. Pink colour = Brecciated crystalline basement; Brown-black = lithic breccias; Green colour = impact melt rock responsible for local circulation systems in the annular depression; white color = crater basin deposits; the dotted lines = isotherms; blue arrows = direction of circulation. (Modified from Naumov, 2005). 10

Figure 1.4. Proposed sequence of the cooling of post-impact mineral growth. Gr: garnet; Ep: epidote; Ab: albite; Kfs = alkali feldspar; Chl = chlorite; Sm = smectite; I-S = mixed-layer illite–smectite; Anh = anhydrite. (Adapted from Kirsmae and Osinski, 2013). 11

Figure 2.1. A) Simplified geological map of the Morokweng Impact Structure displaying concentric rings identified by Andreoli et al. (2007) from geophysical data. Also shown are locations of boreholes, and B) stratigraphic columns of boreholes M4, M3, WF5, WF4 and WF3 borehole. The locations of the KBF03A seismic profile and KHK-1 drillcore discussed, respectively, in Westgate et al. (2021) and Reimold et al. (2002) are also shown. Inset shows the locality of the MIS in South Africa. (From Gibson et al. 2024a). 16

Figure 2.2. A generalized Kalahari Group stratigraphy (Adapted from Patridge et al., 2006) 19

Figure 2.3. Microphotographs of quartz grains showing multiple sets of decorated PDFs (images from Wela, 2017). A) Cross polarised light image showing two sets of decorated PDFs from Sample M4 GG 4 (109.20 m). B) Enlargement of A, showing fluid inclusion trails. C) Cross polarised light image showing microfractures and PDFs in shocked quartz grain from sample M4 FZ-2 (219.30 m). D) Enlargement of C, showing three sets of decorated PDFs and microfractures containing zeolite fill. PDFs = planar deformation features. 23

Figure 2.4 Drillcore trays from 110 – 119 m (Box 2; upper part), 194.46 – 202.6 m (Box 12; middle part) and 297.08 – 305.35 m (Box 25; deeper part), showing host rocks and vein types within the M4 drillcore. The veins show different abundances and orientations: Subhorizontal veins occur in the upper part, inclined

to vertical orientations occur in the middle part, and the deeper part shows little to no veins. Box 12 shows thick pre-impact quartz veins. Drillcore width is 4.5 cm. *26*

Figure 4.1. Quartz grains hosting post-impact hydrothermal minerals in shock and other impact-related deformation features. A) BSE image of sample M4 GG10 (166 m) showing quartz grain displaying three sets of PDFs filled with zeolite and clay. Quartz grain boundary also exhibits interstitial K-feldspar. B) BSE microphotograph of zeolite and sulphide (pyrite) cementing fragments within the jigsaw brecciated quartz grain from sample M4 AM 1 (342 m). For transmitted light images of this texture see Figure 4.4A-B. C) BSE microphotograph of sample M4 R8 (348.4 m) showing micron-sized cavities (interpreted as fluid inclusions) along PDFs, with cross-cutting fractures partially filled with pyrite. D) BSE image of sample M4 SB 2 (~355 m) showing evidence of irregular anastomosing calcite-filled fracture network cutting and locally replacing PDFs in quartz. BSE = backscattered electron; PDFs = planar deformation features; Zeo = zeolite; Kfs = alkali feldspar; Sm = smectite; Ab = albite; Qtz = quartz; Bt = biotite; Mgt/Hmt = magnetite/haematite; Cal = calcite *38*

Figure 4.2. Optical microscope images (A - PPL; B - XPL) of sample M4 GG8 (152 m) showing closely spaced decorated PDFs showing fluid inclusion trails cut by a polymineralic vein. PPL = plane polarised light; XPL = crossed polarised light; Pyr = pyrite; Mgt/Hmt = magnetite/haematite; Qtz = quartz; PDFs = planar deformation features. *39*

Figure 4.3. Microphotographs and phase map of sample M4 INJ2 (158.06 m) showing a subvertical pseudotachylite vein and alkali feldspar veins cutting through albite and quartz (box). A) Plane-polarized light image showing alkali feldspar cutting through albite and quartz and terminating at the pseudotachylite dyke boundary. Zeolite veins cut through both the pseudotachylite and granodioritic gneiss wallrock. B) cross-polarised light of A. C) TIMA phase map of A, B. D) Close-up PPL image of white box in A-C, showing alkali feldspar vein cut by zeolite vein. E) Cross-polarised light of D. PPL = plane polarised light; XPL = crossed polarised light; Kfs = alkali feldspar; Zeo = zeolite; Ab = albite; Qtz = quartz. *41*

Figure 4.4. Photomicrographs of altered feldspar. A, B) Sample M4 GG15 (324 m) showing microcline with tartan twins and fine-grained alteration; above the grain is quartz grain showing PFs, PDFs, and jigsaw brecciation filled with opaques, and cataclasites in PPL and XPL. C, D) Sample M4 GG8 (152 m) showing microcline with distinct chevron pattern and plagioclase with inclusions of biotite in PPL and XPL. The microcline shows oblique planar features that show differing degrees of alteration. PPL = plane polarised light; XPL = crossed polarised light; Pyr = pyrite; Ccl = cataclasites; Kfs = alkali feldspar; Qtz = quartz; Bt = biotite; Pl = plagioclase. *42*

Figure 4.5. Plane-polarized light and BSE photomicrographs of partially oxidized biotite from the upper section of the M4 drillcore. A, B) Thin section of a monzonite sample M4 GG1.1 (129 m) showing colour variation in biotite and variable amounts of replacement by ilmenite along kink bands and around the grain edge. C) BSE image of sample M4 V1 (~114.5 m) showing neoblastic ilmenite aggregates around the edges and along the biotite cleavage. D) Metadolerite sample (M4 Sill-1) from mid-drillcore (262 m), showing oxides around the edges and along the cleavage of biotite. PPL = plane polarised light; BSE = backscattered electron; Bt = biotite; Qtz = quartz; Ilm = ilmenite; Ab = albite; Ccl = cataclasite. *44*

Figure 4.6. Kinked biotite replaced by secondary minerals in sample M4 R8 (348.4 m). A-B) Strongly pleochroic biotite rimmed by zeolite and Ti-oxides (white rim with black neoblasts in (A)) in monzonitic gneiss; PPL- XPL. C-D) BSE images of A-B showing titanite, prehnite and ilmenite replacing the biotite, which locally shows conjugate kink bands. The zeolite rim contains neoblastic titanite and a single zircon

grain. The black box in C extrapolates to image D. Light grey laths in C are igneous biotite inclusions in plagioclase (Gibson et al., 2022). PPL = plane polarised light; XPL = crossed polarised light; BSE = backscattered electron; Bt = biotite; Ttn = titanite; Prehn = prehnite; Ilm = ilmenite; Zeo = zeolite; Chl = chlorite; Zr = zircon. *45*

Figure 4.7. Primary epidote grains from sample M4 R8 (348.4 m). A) PPL image of Brecciated and fractured epidote string along the cataclasite displaying magnetite and smectite along the rims. B) XPL image of A. C) BSE image of smectite and magnetite alteration of epidote and biotite within the host rock and cataclasite. D) Close-up of C shows magnetite texture and smectite between brecciated grains. PPL = plane polarised light; XPL = crossed polarised light; BSE = backscattered electron; Pst = pseudotachylite; Ep = epidote; Bt = biotite; Zeo = zeolite; Ccl = cataclasite; Sm = smectite; Mgt = magnetite; Qtz = quartz. *46*

Figure 4.8. Hand specimens showing shear faults within target rocks of the M4 drillcore. A) Shear fault network showing reverse slip and monoclinic-sigmoidal internal fabric of cataclasites (131.0 m; Gibson et al., 2024a) in a granitoid gneiss. B) Shear fault network defined by white zeolite and clay cutting and displacing a vertical magnetite ± haematite fracture in a granitic gneiss (272.73 m). C) Cataclasites and zeolite-smectite-filled fractures in granodioritic gneiss (347,4 – 354,38 m), hosting a thin suevitic dyke containing mineral and dark melt clasts. Drillcore width is 4.5 cm. *48*

Figure 4.9. Microphotograph showing shear fault / cataclasite network in granitic gneiss (299.76 m; partial crossed-polars). The cataclasites extend within the quartz and feldspar grains. The sample is dominated by feldspar and quartz and contains interstitial biotite and titanomagnetite. The quartz grains are highly fractured and form an approximately in situ breccia (centre), whereas feldspar is typically altered to microcrystalline clay aggregates, both in situ and in cataclasite (left). Fe-oxides are typically smeared along the faults. Bt = biotite; Zeo = zeolite; Ccl = cataclasite; Sm = smectite; Ti. Mgt = titanomagnetite; Qtz = quartz; Fs = feldspar; f = fault. *49*

Figure 4.10. Photomicrograph of granitic gneiss sample M4 R12 (264 m). (A) Overview in plane polarised light (B) Closeup of box in A in plane polarised light, showing ~1 mm wide, steeply oriented shear fault defined by thin magnetite-dominated fractures and vugs characterised by neoblastic andradite and zeolite. The magnetite-pseudotachylite fractures are cut by a shallowly dipping shear fault with normal displacement, and by zeolite veins. C) TIMA phase map of B. For elemental distribution maps of this texture in Appendix 1.2A-B. PPL = plane polarised light; Ab = albite; Kfs = alkali feldspar; Adr = andradite; Mgt = magnetite; Zeo = zeolite; Ap = apatite; Cpx = clinopyroxene; Pst = pseudotachylite. *50*

Figure 4.11. BSE scans showing post-impact hydrothermal alteration in impactite rocks. A) Sample M4 GG15 (324 m) showing zeolite cement in suevite matrix. B) Close-up of A showing the matrix-supported nature of the suevite. C) Sample M4 IM9 (299 m) showing a lithological contact between suevite and cataclasite. D) Close-up of the suevite matrix in C, showing alteration in biotite and magnetite. BSE = backscattered electron; Zeo = zeolite; Qtz = quartz; Ccl = cataclasite; Ab = albite; Bt = biotite; Mgt = magnetite; Prehn = prehnite. *52*

Figure 4.12. BSE microphotographs showing smectite minerals within the M4 drillcore. A) Sample M4 SB3 (353 m) showing smectite, zeolite and magnetite in brecciated suevite. B) Sample M4 R8 (348.4 m) showing smectite in brecciated quartz in cataclasite. C) Sample M4 RG2 (262 m) shows flaky smectite morphology within suevite matrix. D) Sample M4 RG3 (301 m) shows fibrous smectite within a pseudotachylite matrix.

The matrix is a mix of zeolites and smectites (Wela, 2017). BSE = backscattered electron; Zeo = zeolite; Sm = smectite; Qtz = quartz; Bt = biotite; Mgt = magnetite; Ab = albite. *54*

Figure 4.13. Drillcore images show changes in frequency and orientation of veins within the M4 drillcore. The top drillcore box shows monzonitic gneiss (110.08 – 119.39 m depth) displaying subhorizontal calcite veins. The bottom drillcore box shows metadolerite (194.46 – 202.6 m depth) and suevite displaying subvertical veins of zeolite veins (annotated with arrows) and pre-impact quartz veins. The drillcore width is 4.5 cm. *56*

Figure 4.14. Macroscopic evidence of post-impact vein in the M4 drillcore. A) Suevite within the upper fault zone at a depth of 146.05 m. The calcite vein exhibits both vertical and sub-horizontal orientations and crosscuts mafic melt clasts and lithic fragments. B) Metadolerite containing cataclasite and pseudotachylite cut by zeolite veins within the lower fault zone at depth of 292 m. C) Contact between granitic gneiss and grey suevite, showing zeolite and calcite veins in the suevite matrix at a depth of 302.74 m. The drillcore width is 4.5 cm. Zeo = zeolite; Cal = calcite; x-cut = crosscut; Ccl = cataclasites. *57*

Figure 4.15. Macroscopic evidence of monomineralic veins in the M4 drillcore. A) Metadolerite sample M4 ML (195.30 m) showing white anhydrite vein. B) Granodioritic gneiss from Box 2 (110.08 – 119.39 m) showing irregular to anastomosing subhorizontal calcite veins. Anh = anhydrite; Cal = calcite. *58*

Figure 4.16. Photomicrographs showing crosscutting relationships of calcite veins with other minerals. A) calcite veins crosscutting zeolite veins from M4 V3 (142.95 m). Cross polarised light. B) Calcite-smectite--zeolite vugs in M4 RG1 (146 m), crosscutting zeolite veins, in plane polarised light. C) Cross polarised light image of B. D) Stretched to syntaxial elongate blocky calcite vein in sample M4 GG1.1 (129 m), crosscutting altered biotite, in plane polarised light. E) Sample M4 GG1.1 shows Stretched to syntaxial elongate blocky calcite cutting through biotite, titanite, and quartz. F) BSE scan of sample M4 V1 (114 m) showing calcite vein cutting through partially altered biotite. G) Sample M4 V1 shows a sharp contact between calcite veins and granodioritic gneiss containing partially altered biotite. No obvious enhanced alteration occurs along the vein edge. PPL = plane polarised light; XPL = crossed polarised light; BSE = backscattered electron; Zeo = zeolite; Cal = calcite; Bt = biotite; Ttn = titanite; Ilm = ilmenite; Qtz = quartz; f = fault; Pst = pseudotachylite. *60*

Figure 4.17. Photomicrographs of sample M4 ML (195.30 m) showing anhydrite vein cutting across pseudotachylite. A) Plane polarised light image showing subidioblastic granoblastic grains. B) Cross-polarised light of A. C) Calcium elemental map showing Ca enrichment localized within anhydrite vein. D) Phase map showing anhydrite vein with minor dolomite inclusions. PPL = plane polarised light; XPL = crossed polarised light. Pst = pseudotachylite; Anh = anhydrite; Qtz = quartz. *61*

Figure 4.18. Photomicrographs of sample M4 R22 (139 m) showing relatively high-T assemblage of zeolite, clinopyroxene, smectite, calcite and Fe-(hydr)oxide in a vein matrix. A) Plane-polarized image showing the oxides are magnetite and ilmenite. The zeolite vein contains inclusions of calcite, actinolite, smectite, and biotite showing alteration to ilmenite. B) Crossed-polarized image of A. C) Reflected light of A-B. D) A close-up plane-polarized light image of inclusions within the zeolite veins. PPL = plane polarised light; XPL = crossed polarised light; REF = reflected light; Zeo = zeolite; Cal = calcite; Bt = biotite; Ilm = ilmenite; Ab = albite; Mgt = magnetite; Pst = pseudotachylite; Heul = heulandite; Sm = smectite; Act = actinolite. *64*

Figure 4.19. BSE images showing morphology and textures of zeolite veins across the M4 drillcore. A) Monomineralic zeolite vein in pseudotachylite from sample M4 IM9 (299 m). B) Close-up of A. C) Zeolite vein from M4 RG2 (262 m) through pseudotachylite matrix and merging in the suevite. D) Close-up of C showing titanite neoblasts along vein edge. E) Sample M4 Sill1 (261 m) showing zeolite veins with haematite rims. F) Close-up of E. G) Sample M4 GG10 (166 m) showing smectite and haematite/goethite pseudomorphs (possibly after clinopyroxene, see Figure 4.21) in zeolite veins. H-I) Close-up of G. BSE = backscattered electron; Zeo = zeolite; Pst = pseudotachylite; Ttn = titanite; Hmt = haematite; Ccl = cataclasites; Gth = goethite. *66*

Figure 4.20. Microphotographs, and BSE image of sample M4 GG10 (166 m) showing highly irregular zeolite veins/vugs enclosing neoblastic clinopyroxene that is rimmed by smectite and skeletal haematite/ goethite also rimmed by smectite. A) Overview in plane-polarized light image showing monzonite sample. B) Close up image showing white cloudy heulandite with light brown inclusions at the margins. C) BSE image showing K-feldspar metasomatic replacement of primary plagioclase in the wallrock and corroded quartz grains with zeolite replacing PDF lamellae (See also Fig. 4.2). PPL = plane polarised light; BSE = backscattered electron; Zeo = zeolite; Ab = albite; Kfs = alkali feldspar; Qtz= quartz; Cpx = clinopyroxene; Sm = smectite; Gth = goethite. *67*

Figure 4.21. A) Close up BSE scans showing zeolite vein/vug in M4 GG10 (166 m) with clinopyroxene and smectite on the rims and alkali feldspar alteration. B) Close up BSE scan of zeolite vug showing titanite, calcite, clinopyroxene and smectite. BSE = backscattered electron; Zeo = zeolite; Cpx = clinopyroxene; Sm = smectite; Kfs = alkali feldspar; Ttn = titanite; Cal = calcite. *68*

Figure 4.22. TIMA elemental maps and phase map of sample M4 GG10 (116 m) showing a steeply-inclined irregular zeolite vein network linked to a vertical fracture (left) that shows smectite + goethite > zeolite. A) Ca distribution abundant in apatite, titanite, and clinopyroxene crystals on the zeolite margins. B) Mg distribution abundant along the fractures and zeolite vugs. C) Na distribution depleted in the zeolite vugs and enriched in the matrix. D) Phase map showing albite and quartz cut by fractures and vugs filled with heulandite. For further details, see Figures 4.19 and 4.20. Elemental scale increases from dark purple (0%; left) to white (100%; right). Zeo = zeolite; Ab = albite, Qtz = quartz, Kfs = alkali feldspar; Ttn = titanite; Cal = calcite; Gth = goethite; Ap = apatite; Cpx = clinopyroxene; Ilm = ilmenite. *69*

Figure 4.23. BSE image showing a polymineralic vein sample M4 ML (195.30 m). The zeolite vein cuts through the pseudotachylite and contains inclusions of anhydrite, clay and pseudotachylite clasts. BSE = backscattered electron; Zeo = zeolite; Pst = pseudotachylite; Ttn = titanite; Hmt = haematite; Ccl = cataclasites; Gth = goethite. *70*

Figure 4.24. Photographs of hand specimens, plane and crossed polarised light, and phase maps of three calcite veins in the upper part of the M4 drillcore. A) Sample M4 V1 (114 m) shows white composite calcite veins with spacing < 5 cm cutting through a granodioritic gneiss. The vein, in plane polarised light (B), shows elongated calcite veins pointing towards fine-grained calcite. The phase map (C) identifies the entire vein as filled with calcite. D) Sample M4 V3 (142.95 m) shows vitreous grey zeolite enclosing a white calcite vein; the calcite grains are up to 15 mm wide. G) Coarse-grained calcite-zeolite vein cutting suevite from 143.02 m. Calcite grains occur along vein walls and around clasts, with zeolite forming the core of the vein. *71*

Figure 4.25. Photomicrograph showing morphology and textures of calcite across the M4 drillcore. A) Blocky calcite vein in PPL and XPL of sample M4 S1 (2) (144.09 m). B) Sample M4 S12 (148 m) showing

fine-grained calcite around zeolite vugs. C) Sample M4 S3 (160 m) in XPL showing fine-grained calcite cement. D) Combined PPL and XPL image showing a polymineralic, calcite-dominated vug in granitoid gneiss. Apart from calcite, the vug contains quartz, zeolite, haematite/magnetite, and neoblasts of actinolite in sample M4 R22 (139 m). E) Phase map of D. Colors in phase maps labelled in the legend provided. XPL = crossed polarized light; PPL = plane polarized light. *74*

Figure 4.26. $\delta^{18}O_{V\text{-}SMOW}$ - $\delta^{13}C_{V\text{-}PDB}$ *diagram showing compositions of vein calcites from the M4 drillcore. The oxygen and carbon isotope reservoirs and diagenetic trends are adapted from literature sources (Liu et al., 2007; Duuring et al., 2008; Broom-Fendley et al., 2016; Guo et al., 2018; Tan et al., 2015; Quandt et al., 2019).* *78*

Figure 4.27. Crosscutting relationships between two calcite veins in sample M4 V2, show variation in $\delta^{13}C$ *and* $\delta^{18}O$ *values from three points. Two points are from the older vein and one from the younger vein.* .. *78*

Figure 4.28. Laser spot locations in sample M4 V1a-b and within the five layers of calcite in M4 V1c. .. *80*

Figure 4.29. MUQ-normalized REE + Y patterns of calcite veins sampled from the upper section of the M4 drillcore (114 – 145 m). A) Sample M4 V1a blocky calcite vein (114 m) cutting through granodioritic gneiss. B) M4 V1b blocky calcite vein with fine-grained core (114 m). C) M4 V1c layers of blocky and fine-grained calcite vein (114 m). D) M4 S1(2) blocky calcite veins (144.09 m) cutting through a suevite. E) Sample M4 GG2 blocky calcite veins (131.9 m) cutting through leucocratic granitic gneiss. F) Sample M4 V2 blocky calcite in composite zeolite-calcite vein (143.02 m), cutting suevite. *83*

Figure 4.30. MUQ-normalized REE + Y patterns of calcite veins and host rocks (Wela, 2017; granodioritic gneiss, leucocratic granitic gneiss, and suevite). *84*

Figure 4.31. A laser spot location map generated using the camera embedded in LA-ICPMS shows sample depths. *86*

Figure 4.32. Terra-Wasserburg diagrams for four calcite vein samples from the M4 drillcore: (a) M4 V1, (b) M4 S1(2), (c) M4 V2, and (d) M4 GG2. The graphic presentation and age calculation are obtained using IsoplotR (Vermeesch, 2019). The age determination is obtained from the lower intercept with Concordia. The second value represents the "studentized 100(1-α)% confidence interval for t using the appropriate number of degrees of freedom," and the third value represents the "approximate 100(1-α)% confidence interval for t with overdispersion, calculated as z = y√MSWD." "n" represents the number of spot analyses. MSDW = mean squared weighted deviations, p(χ2) = chi- squared p-value for the isochron fit. The data ellipses are color-coded according to their 238U/206Pb value, displayed in the individual color scales at the right margin of the diagrams. *89*

Figure 4.33. Relationship between U-Pb ages versus A) depth and B) calcite grain spot size analysis for the calcite veins from sample M4 V1, M4 GG2, M4 V2, and M4 S1(2). The plots include error estimates for each age. *90*

Figure 4.34. Plots showing the relationship between smectite-illite clay K-Ar ages grain size and depth for samples in the M4 drillcore. The plots include error estimates for K-Ar ages. *92*

Figure 5.1. Y/Ho versus MUQ-normalised Eu anomalies (Eu/Eu) of calcite veins in the M4 drillcore. Hydrothermal and marine Y/Ho ratios refer to Bau and Dulski (1996) and Bau et al. (1996), respectively. 101*

Figure 5.2. MUQ-normalised (mud sediments from Queensland) REE patterns of calcite veins in samples M4 S1(2) shown in A and M4 GG2 shown in B, matched with hydrothermal fluids (Bau and Dulski, 1999). 102

Figure 5.3. Elemental maps of calcite veins within a granodioritic gneiss from 114m showing Ca and Mg distribution. 103

Figure 5.4. MUQ-normalised (mud sediments from Queensland) REE patterns of calcite veins in samples M4 V1C from calcite line 1 to line 5, matched with calcite veins from Uysal et al. (2011). S1-3 represents stage 1 of formation to stage 3. 104

Figure 5.5. Schematic proposed exhumation-related events around the Morokweng impact structure region. 110

LIST OF TABLES

Table 4.1. Description of 31 samples for petrographic, geochemical and geochronological analysis 34

Table 4.2. A summary of the type of veins in the M4 drillcore and the analytical techniques applied. 75

Table 4.3. EMPA major elements (Wt.%) results from spot analysis of calcite grains forming at the grain margins of zeolite and along the vein edges from 143.02 m. 79

Table 4.4. MUQ-normalized REE ratios and Y in ppm of vein calcites from the M4 drillcore. 81

1. INTRODUCTION

Impact cratering is the excavation of a planetary body when an asteroid or cometary projectile strikes its surface at hypervelocity. The size, angle and speed of the impactor and the subjected target rocks, as well as the gravitational field of the planetary body, create a variety of crater morphologies from small, simple craters to larger, complex, and multi-ring types (French, 1998). A complex impact crater forms with an internal central uplift or a peak ring that involves material that is both strongly shocked and exhumed from deeper levels of the crust that would have been pre-heated by the regional geothermal gradient (Figure 1.1; Abramov and Kring, 2007; Kenkmann et al., 2013).

Approximately 200 impact structures are preserved on Earth (Kenkmann and Artemieva, 2021); of these, at least one-third show evidence of post-impact hydrothermal alteration (Naumov, 2005; Kirsimae and Osinski, 2013; Schmieder and Kring, 2020). The extent of hydrothermal alteration in these impact structures is driven mainly by impact-induced permeability, availability of fluids and heat (Naumov, 2005). In smaller craters, alteration mostly occurs in the porous and permeable crater-fill lithic and suevitic impact breccias (Zürcher and Kring, 2004; Simpson et al., 2020). In larger impact structures with a peak ring, like Chicxulub, the heat to drive hydrothermal activity may come from multiple sources, including: (1) exhumation of rocks from deeper levels in the central uplift, (2) shock heat in the central crater basement, (3) impact melt-bearing breccia crater fill, and (4) intrusive dykes of friction melt, impact melt and impact breccia in the crater basement (Naumov, 2005; Abramov and Kring, 2007; Kirsimae and Osinski, 2013). Consequently, the hydrothermal system extends below the crater fill breccias into the central crater basement where extensive impact-induced fracturing enhances permeability, and additional shock heating and geothermal gradient associated heat are present (Kirsimae and Osinski, 2013; Simpson et al., 2020). Although disintegration of volatile-rich minerals in the target rocks associated with shock heating and contact metamorphism of wallrocks and/or clasts in the impact breccias could be a potential fluid source (Osinski et al., 2001), the principal source of fluid for post-impact alteration is likely to be from near-surface groundwater/meteoric water in the case of terrestrial impacts, and seawater for marine impacts, with marine craters likely to receive a significantly larger fluid influx relative to their subaerial counterparts (Kirsimae and Osinski, 2013).

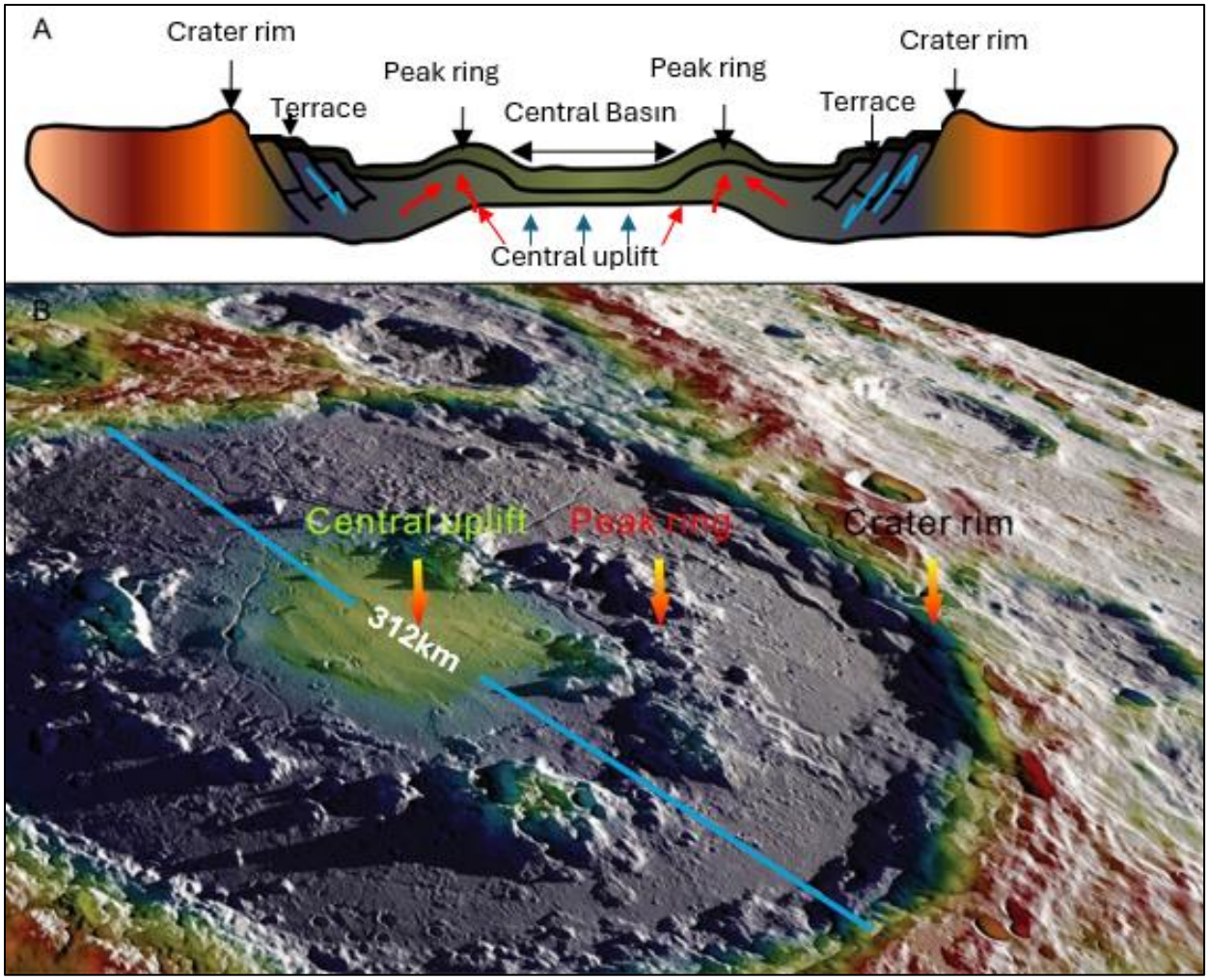


Figure 1.1. Illustration of a complex impact crater (adapted from Chen and Sun, 2017). A) Schematic cross-section showing arrows visually depicting differential crater floor movement in response to the impact and subsequent crater modification under gravitational forces. This process forms the ring of uplifted material known as the peak-ring. B) Photomicrograph of a lunar crater, showing the 3D key features of the cross-section in A, including central uplift, peaking ring and crater rim.

Typical temperatures of equilibration of hydrothermal alteration assemblages in impact structures range from < 100 to ~ 350 ℃ (Zurcher and Kring, 2004; Abramov and Kring, 2007; Simpson et al., 2020), mainly because at > 350 - 400 ℃, T is high enough to inhibit fracturing and, thus, fluid movement is restricted. Clays and zeolites are the most common alteration minerals reported from impact hydrothermal systems; they indicate relatively low T conditions (Naumov, 2005; Zurcher and Kring, 2004). However, higher-T assemblages involving feldspar, actinolite, andradite garnet, epidote, and/or chlorite have been found in craters such as Manson, Boltysh, Chicxulub and Puchezh-Katunki (Naumov, 2005; Gallegos et al., 2015; Kring et al., 2020). The longevity of a

hydrothermal system depends on the amount of available heat (which is a function of crater size and volume of melt retained within the crater), the availability of fluid, and host rock permeability (Abramov and Kring, 2007; Kirsimae and Osinski, 2013). Kring et al. (2020) quantified the post-impact T distribution and cooling history of the crater basement in different parts of the 180 km diameter marine Chicxulub structure (Figure 1.2). The authors observed that rocks between cooler outer parts and hotter inner parts of the crater experienced initially highly focussed fluid flow at T > 300 ℃ and that hydrothermal activity leading to cooling to T < 100 ℃ lasted up to 1 Myr (Kring et al., 2020). Figure 1.2 also shows that hydrothermal activity is particularly strongly focussed in the shocked and fractured peak ring volume.

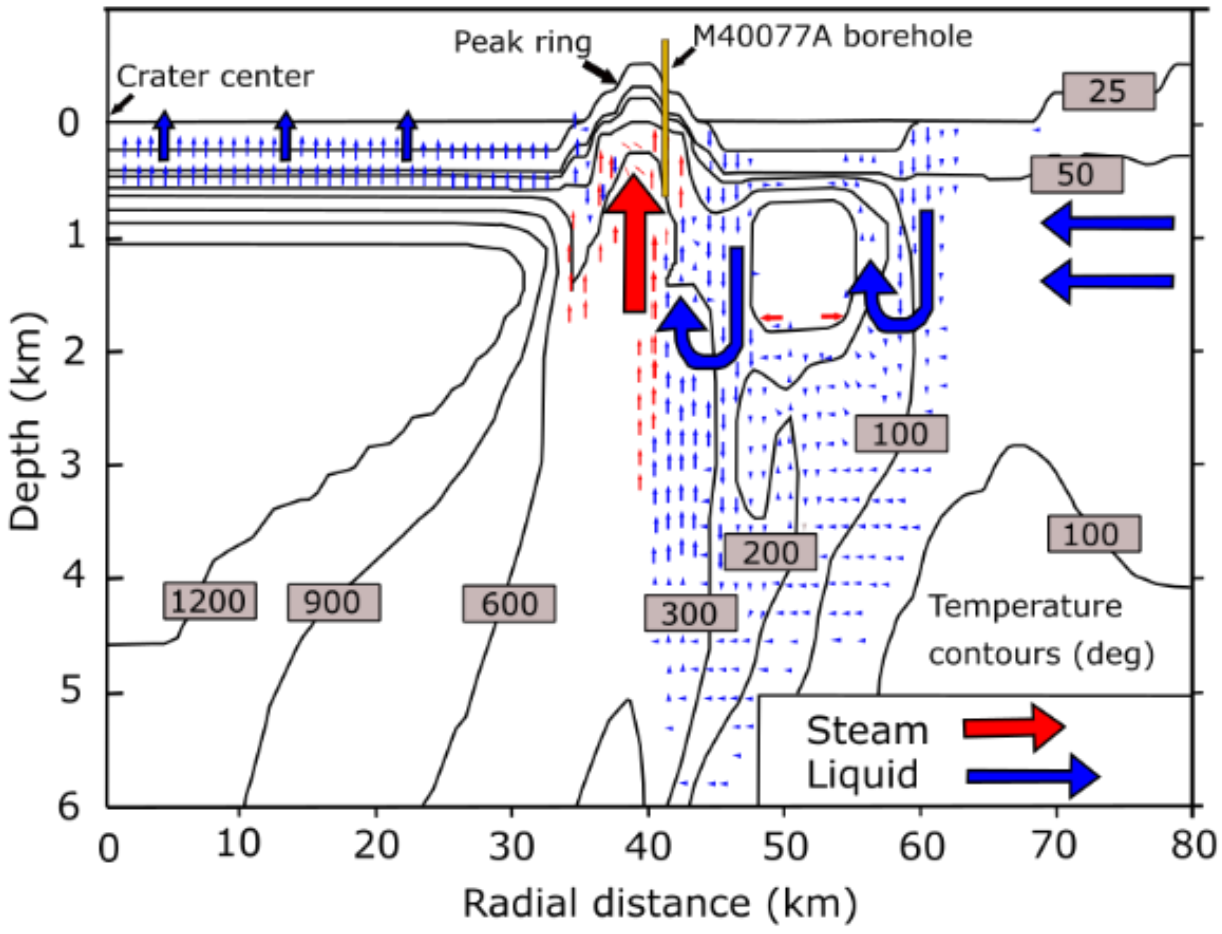


Figure 1.2. Thermal model of the Chicxulub Structure with contours illustrating temperature distribution and the circulation of hydrothermal fluids into and through the peak ring (modified from Kring et al., 2020; and half-space of Figure 1.1). The position of the M0077A drillcore, which is used for comparison with the M4 Morokweng drillcore in this study, is shown.

This MSc study investigates hydrothermal effects in rocks intersected in the M4 drillcore from near the centre of the ~80 km wide (Gibson et al., 2024) Morokweng impact structure (MIS) in South Africa. The drillcore has been interpreted as intersecting the peak ring of the crater (Wela, 2017; Gibson et al., 2019; Gibson et al., 2024), thus inviting comparison with the M0077A borehole core of the Chicxulub Structure (Simpson, 2020). The study by Wela (2017) focused on the lithological, petrographic, and geochemical characteristics of lithologies in the M4 drillcore to understand the pre-impact history, shock deformation, melting and other impact-induced structural processes. Post-impact hydrothermal alteration assemblages involving mostly zeolite and clay minerals were noted; however, textural, mineralogical, and compositional characteristics were not fully described and interpreted. This study addresses these gaps in conjunction with the MSc of Ms. T. Masiu (Masiu, 2025, unpublished dissertation), which focuses primarily on the post-impact alterations and mineral associations in the M4 drillcore through the lenses of hyperspectral imaging, petrographic and mineral chemical aspects of the alteration assemblages to characterize the spatial distribution of hydrothermal minerals as a function of depth and host rock type.

The present study conducts the petrographic analysis of post-impact hydrothermal alteration features affecting quartz, feldspars and biotite within granitoid wallrocks and clasts in the impact-related breccias, as well as the mineral assemblages found in vugs and fracture-hosted veins cutting the wallrocks. This analysis aims to establish the relative chronology of the hydrothermal mineral assemblages and veins. It also provides the context for the major and trace element geochemistry and stable and radiogenic isotope characteristics of post-impact hydrothermal calcite veins and clays to establish the physicochemical conditions of hydrothermal alteration within the M4 drillcore, including the source(s) of fluids and age(s) of clay alteration and calcite veining.

1.1. IMPACT-INDUCED HYDROTHERMAL SYSTEM

1.1.1. Sources of heat

Large hypervelocity impacts generate a shock wave that results in transient elevated pressure conditions usually >1 GPa in the underlying target rock volume and the meteorite, and which drives the target rocks away from the impact point during a period of tens - and sometimes even

up to hundreds - of seconds (Melosh 1989). The shock wave loses energy as it expands downwards and outwards into the target rock, causing pressures to drop from > 40-60 GPa to below 1 – 2 GPa (French, 1998; French and Koeberl, 2010; Hargitai et al., 2015). This generates broadly subspherical zones of shock metamorphism with intensity decreasing radially outwards in the crater basement, ultimately giving way to fracturing and brecciation at low- and sub-shock pressures. Apart from the distinctive shock metamorphic features that are produced in mineral grains (see Section 1.1.4), another consequence of these high pressures is that decompression back to ambient lithostatic confining pressures releases excess heat energy in proportion to the magnitude of the shock pressure that is reached (Stöffler and Langenhorst, 1994).

According to French (1998), at the point of impact, the generated shock heating of > 1500 ℃ produces whole-rock melting at > 60 GPa. At shock pressures between 35 and 45 GPa, the amount of shock heat varies from 300 to 900 ℃, allowing partial melting of rocks or formation of diaplectic mineral glasses, whereas between 10 and 30 GPa, the amount of shock heat is between 100 and 275 ℃ (French, 1998). Dissipation of the shock heat could occur by conduction, but at shallow levels is more likely to involve convecting fluids, which will migrate from hotter to cooler regions of the crater basement (Figure 1.2). Because in large craters the central crater basement undergoes strong uplift and later collapse of the central peak, and the shock-heated rock volume extends to deep crustal levels that were already heated by different amounts according to the crustal geotherm, the initial isotherm pattern after the impact may be quite complex (Figure 1.2 and Figure 1.3).

1.1.2. Permeability

Drillcores from impact sites typically reveal extensive fracturing and in situ brecciation within the crater basement, in addition to the evidence of allochthonous clasts in the various crater fill breccias (Reimold et al., 1994; Osinski et al., 2001; Naumov, 2002; 2005; Gibson et al., 2019; Simpson et al. 2020). Care must be taken to confirm that the brittle structures were induced by the impact, but pre-impact fractures could also contribute to permeability for an impact-induced hydrothermal system, and care must be taken to check for any post-impact fractures with hydrothermal alteration unrelated to the impact. Polymict impact breccias, termed suevites, and fault rocks (breccias, cataclasites) are likely to be the most permeable rocks. Suevites often contain

hydrothermal alteration minerals, contributing up to 10 to 25 % by volume (Naumov, 2005), whereas cataclasites, also referred to as crushed microbreccia, contain angular mineral fragments with or without a cement of hydrothermal minerals (Aldahan, 1990). Pseudotachylite in granitoids rocks is thought to reflect an interplay between brittle and ductile deformation processes (Kovaleva et al., 2018). In contrast, Gibson et al. (2024) suggest pseudotachylite originates from friction melting caused by high-strain-rate faulting of the crater basement, a process that can self-seal fault zones and thereby reduce permeability (Kirsimae and Osinski, 2013); however, its matrix is typically glassy, which makes it highly reactive to fluids, which could lead to an increase in permeability through wallrock interactions. Impact melt rock has low permeability because it remains hot long enough to prevent the formation of fractures that would allow fluid infiltration. In the target rocks, permeability decreases downwards and outwards from the centre of the crater (Abramov and Kring, 2007).

An unpublished honours project by Fakudze (2021) studied the density and P-wave velocity characteristics of the rocks in the M4 drillcore and states the suevite has a low seismic velocity of < 4000 m/s indicating a low density of 2 – 2.50 g/cm^3. This is attributed to the high proportion of zeolite cementing the breccia, which confirms a high original porosity. In contrast, the target rock dolerites and granites have a higher seismic velocity of > 4000 m/s, indicating a higher density of 2.8 – 2.9 and 2.56 g/cm^3, respectively, that would have led to a lower porosity and limited presence of fluids (Fakudze, 2021). Generally, after they have cooled down completely, terrestrial impact structures are thought to have low permeability due to the formation of hydrothermal minerals that effectively seal the rocks and limit fluid flow (Turtle et al., 2003).

1.1.3. Availability of fluids

Post-impact fluids are typically hydrous and begin as hot fluids that evolve over time towards cooler temperatures (Osinski et al., 2005; Kring et al., 2020). Initially, these fluids circulate within the annular trough, situated between the central uplift and the crater rim and infiltrate through faults in the collapsed transient crater rim (Osinski et al., 2001; Abramov and Kring, 2004; Kirsimae and Osinski, 2013) and further channel through cataclasite zones, fractures, and veins (Kring et al., 2020). The fluids may be derived from various reservoirs, including meteoric water,

seawater, groundwater, magmatic fluids from the impact melt sheet and metamorphic fluids (Naumov, 2005; Kirsimae and Osinski, 2013). Flow rates are estimated at 10^{-4} to 10^{-3} m s^{-1} (Naumov, 2005). Fluid characteristics include salinity (low or high), pH (ranging from weakly alkaline to near neutral, pH = 6-8), and chemical compositions, which are derived from target and parental source (Naumov, 2005; Kirsimae and Osinski, 2013).

1.1.4. Shock deformation features

The nature of hydrothermal activity is favoured by a long-term thermal anomaly, extensive fault zones and micro-scale shock damage of mineral grains (Naumov, 2005). Although shock micro deformation features do not appear to generate significant volumes of fluid, their presence is a useful time marker to confirm that a hydrothermal alteration feature or mineral postdates the impact event (French, 1998; Kring et al., 2020). Common minerals used as petrographic indicators of shock deformation features include quartz, feldspars, olivine, pyroxene, garnet, titanite, apatite zircon and to a lesser extent biotite in impactites and target rocks (Stöffler and Langenhorst 1994; Grieve et al. 1996; Ferrière and Osinski, 2012; Walton et al., 2017).

A range of shock micro deformation features reported in impact structures occur at pressures between ~ 5 and 60 GPa and include planar deformation features (PDFs), planar fractures (PFs), diaplectic glass, mosaicism, jigsaw brecciation, toasting, to name the most studied (Dressler, 1990; Stöffler and Langenhorst 1994; Poelchau and Kenkmann, 2011; Ferrière and Osinski, 2012; Walton et al., 2017; Cox et al., 2020; Gibson et al., 2024a). For more descriptions on the shock features in the M4 drillcore, the reader is referred to Wela (2017) and Gibson et al. (2024a). This chapter only highlights the obvious shock-diagnostic internal deformation features to identify the post-impact hydrothermal mineral assemblages that can be seen replacing and/or cutting through the shock deformation features.

1.1.4.1. Planar fractures

Planar fractures formed due to impact cratering are usually > 3 µm wide and closely spaced (about 15 – 20 µm apart) parallel micro-fissures formed by low shock pressure of ~ 5 – 8 GPa (Poelchau

and Kenkmann, 2011; Ferrière and Osinski, 2012; Osinski et al., 2022). The fractures are mostly controlled by crystallographic cleavage and occur as a set of 2 or 3 planes within a mineral grain such as quartz, feldspars, garnet, titanite, zircon and apatite (Sarinya, 2008; Simpson, 2015; Osinski et al., 2022).

1.1.4.2. Planar deformation features

Planar deformation features, termed PDFs, are created at ~ 8 – 30 GPa and occur as sets of narrow parallel planes of glass less than 2 µm thick, and more closely spaced than planar fractures (2 – 10 µm) (Stöffler and Langenhorst, 1994; French and Koeberl, 2010; Ferrière and Osinski 2012; Osinski et al., 2022). Their abundance and spacing increase with increasing shock pressure (Pickersgill et al., 2021; Gibson et al., 2024a). PDFs within the mineral grain such as quartz, feldspars, and zircon follow preferred crystallographic orientations (Osinski et al., 2022). PDFs can be decorated or non-decorated (Ferrière and Osinski, 2012). Decorated PDFs are observed through planar fluid inclusion trails that are < 2 µm in diameter (Ferrière and Osinski, 2012). They are considered to form by post-shock annealing and hydrothermal alteration effects (Ferrière and Osinski, 2012).

1.1.4.3. Feather features

Feather features refer to a plumose-like pattern of short, narrow, closely-spaced, parallel to subparallel lamellae branching out from planar fractures or planar deformation features (Poelchau and Kenkmann, 2011). This shock deformation feature is produced at pressures of ~ 7 – 10 GPa in quartz (Osinski et al., 2022). They develop due to shearing along planar fractures under shock conditions (Poelchau and Kenkmann, 2011; Ferrière and Osinski, 2012).

1.1.4.4. Kink bands

Kink bands are commonly observed in micas, but are not a definitive indicator of shock metamorphism as they can also occur in response to tectonic events (French and Koeberl, 2010; Ferrière and Osinski, 2012). Kink bands experienced at Steen River impact structure (Walton et al., 2017) occur ~ 100 - 200 µm from shocked veins. The intensity of band geometries in biotite and kinks fineness is proposed to support the shock origin (Gibson et al., 2024a).

1.2. POST-IMPACT HYDROTHERMAL MINERALIZATION

Hydrothermal alteration involves interaction of fluids and rock at low T during cooling after metamorphic or magmatic events. It invariably follows a declining T trend, such that lower-T mineral assemblages overprint higher-T assemblages, and can extend as low as near-surface temperatures (< 50 ℃), although lack of available fluid and/or kinetic barriers may prevent lower-T assemblages from forming (Kirsimae and Osinski, 2013). As mentioned previously, the fluid source is most commonly likely to be seawater or meteoric water that can interact with the shallow subsurface crust down to several kilometres depth; however, fluids may also come from overlying sedimentary rocks (connate water) (Osinski et al., 2001).

Figure 1.3 shows a regressive hydrothermal process model (Osinski et al. 2001; Naumov, 2005) applicable to complex impact craters with diameters ranging from ~5 to 100 km (Osinski et al., 2005). The model suggests that, in the early stage, referred to as the high-temperature stage, rocks in the central uplift setting initially experience highly focused fluid flow at T > 300 ℃ (Versh et al., 2003; Kirsimae and Osinski, 2013; Simpson et al., 2020), concentrated along concentric listric normal faults that serve as pathways for fluids penetrating inwards from the outer crater region created during the modification stage (Osinski et al., 2001). Initially, temperatures in the central uplift would decrease downwards and outwards (Figure 1.3; Naumov, 2005). This early stage is the start of a regressive paragenetic mineralization trend (Figure 1.4), and is dominated by alkali metasomatism and albitization. It also involves the formation of high-T hydrothermal minerals such as garnet, epidote and actinolite (Osinski et al., 2001; Naumov, 2005; Kirsimae and Osinski, 2013), although these appear to occur only locally. The main stage, denoted stage II, is characterized by progressive cooling of the central uplift, with fluids circulating within the central uplift and in the fractures around it (Figure 1.3; Naumov, 2005). The temperatures range from ~300 to 100 ℃ and lower-T hydrothermal minerals (zeolites, smectites and chlorites; Figure 1.4) crystallize abundantly (Versh et al., 2003; Kirsimae and Osinski, 2013). The final stage, denoted stage III, is characterised by pervasive crystallization of mainly; carbonate – zeolite cements in a low-temperature environment at T < 100 ℃ (Figure 1.3 and Figure 1.4; Osinski et al., 2001; Versh et al., 2003; Naumov, 2005; Kirsmae and Osinski, 2013). The convecting fluids cool the rocks and the hydrothermal system decreases in volume with time. The crater form should lead to the

development of a crater lake. Heat may also be lost and conduction may occur towards the surface and towards cooler underlying rocks (Osinski et al., 2001; Naumov, 2005).

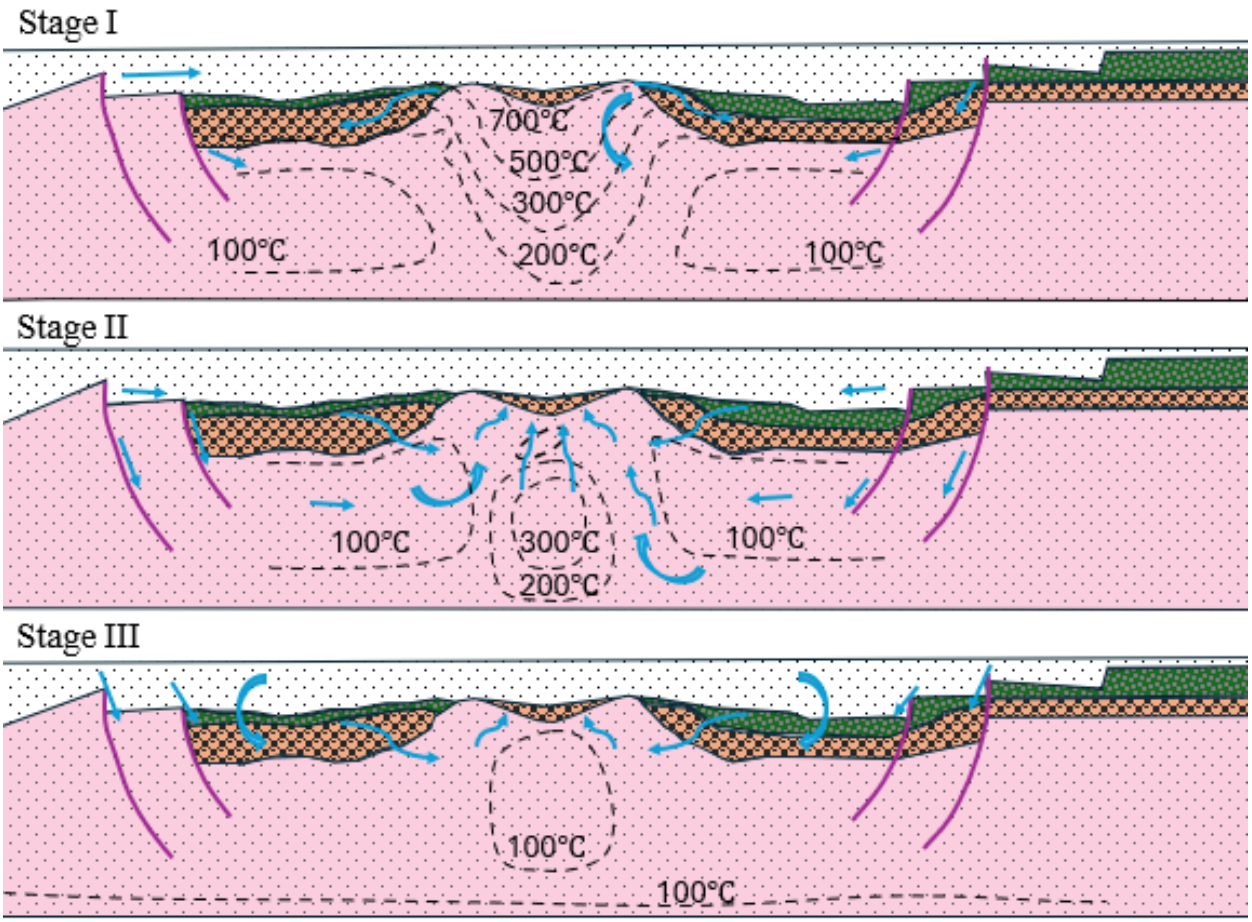


Figure 1.3. Illustration of regressive hydrothermal circulation of fluids within a complex crater showing three successive stages. Stage I (initial/early stage) displays variability in temperature from top downward, with hydrothermal activity occurring in the periphery of central uplift. Stage II (main stage) displays lateral variations in temperature with circulation of fluids within both the central uplift and its periphery. Stage III (final stage) is characterised by temperatures < 100 ℃ and fluid circulation occurs only near the surface. Pink colour = Brecciated crystalline basement; Brown-black = lithic breccias; Green colour = impact melt rock responsible for local circulation systems in the annular depression; white color = crater basin deposits; the dotted lines = isotherms; blue arrows = direction of circulation. (Modified from Naumov, 2005).

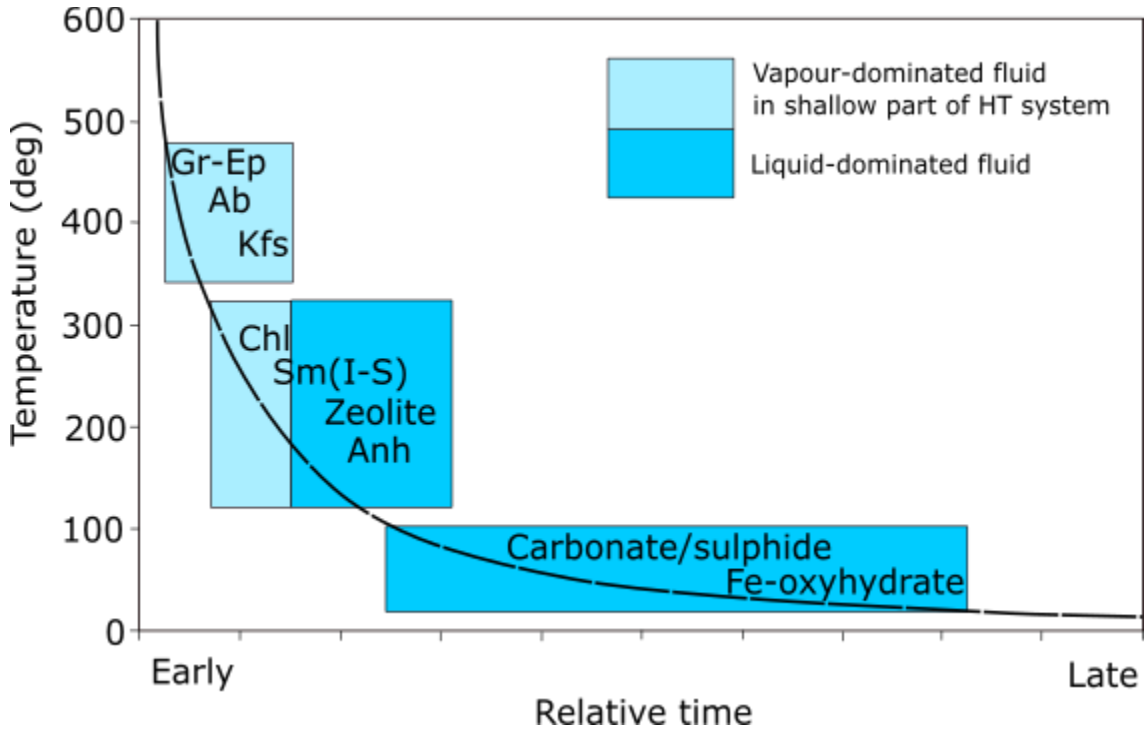


Figure 1.4. Proposed sequence of the cooling of post-impact mineral growth. Gr: garnet; Ep: epidote; Ab: albite; Kfs = alkali feldspar; Chl = chlorite; Sm = smectite; I-S = mixed-layer illite–smectite; Anh = anhydrite. (Adapted from Kirsmae and Osinski, 2013).

Vertical zonation of hydrothermal mineral assemblages in central uplifts has been noted in impact structures such as Puzhezh-Katunki, Ries and Haughton, with smectites and zeolite dominating at higher levels (Naumov, 2005; Kirsimae and Osinski, 2013). The upper parts observed through drillcores from these impact structures, represented by impact breccia and shocked target rocks is dominated by Na zeolite–calcite. This assemblage is progressively replaced by Na-Ca-zeolite–calcite as depth increases, followed by Ca-zeolite in the deepest parts. Smectite composition changes from high alumina varieties to Mg-Fe varieties with increasing depth (Naumov, 2005; Kirsimae and Osinski, 2013). At even greater depths (> 200 m), brecciated and shocked basement rocks contain hydrothermal chlorite and anhydrite, which replace, respectively, smectites and calcite. In this zone, pyrite and Ca-Fe silicate minerals like andradite, epidote, prehnite and actinolite may also occur (Naumov, 2005; Kirsimae and Osinski, 2013). Kirsmae and Osinski (2013) proposed that the alteration evolves from (Na)-K series in stage I and II to Ca-Mg series in stage II and III, allowing carbonate precipitation. Simpson et al. (2020) noted a similar trend in the peak ring of the Chicxulub Impact Structure, where early K metasomatism was followed by zeolite and clay minerals, then later by carbonate mineralization.

1.3. CALCITE GEOCHEMISTRY

1.3.1. Stable isotopes

Among the hydrothermal minerals identified in the MIS, oxygen and carbon isotope dynamics in calcite can be used to determine potential fluid sources and reconstruct the thermal history during the final stage of post-impact hydrothermal alteration. Examining stable isotopes requires an understanding of isotopic exchange between minerals and co-existing fluids, which is influenced by temperature, fluid source composition and pressure (Farver, 1994).

Oxygen in nature occurs as three stable isotopes: ^{16}O (99.757 %), ^{17}O (0.038 %) and ^{18}O (0.205 %) (Hoefs, 2009). The isotope ratio $^{18}O/^{16}O$ is commonly used to determine $\delta^{18}O$ values. The fractionation processes throughout the hydrologic cycle influence the changes in the oxygen isotopic composition of meteoric water, such as lakes and groundwater (Gat, 1996). As rain falls, part of it is lost by evaporation and on vegetation cover as well as other surface reservoirs i.e., lakes, which become enriched in heavy ^{18}O (Gat, 1996) because the heavier isotope (^{18}O) tends to condense and precipitate out first and water moving towards colder regions is depleted in heavy O values and enriched in ^{16}O (Simpson, 2015). Thus, water infiltrated through the soil cover and percolated downward (i.e., groundwaters) and stored in aquifers with up to 60 – 80 °C becomes depleted in $\delta^{18}O$ by about < 1 ‰ (Gat, 1996). Carbon is found in two stable isotopes: ^{12}C (98.93 %) and ^{13}C (1.07 %) (Hoefs, 2009). The isotope ratio $^{13}C/^{12}C$ is used to determine $\delta^{13}C$ values in fluids containing CO_2. The C in CO_2-rich fluids is derived from atmospheric CO_2 dissolved in water and carbonate minerals. Therefore, the isotopic composition of $\delta^{13}C$ is regulated by the equilibrium reactions between CO_2-rich water and calcite, and temperature in equations such as $T_{°C} = 15.7 - 4.36(\delta^{18}O_{cl} - \delta^{18}O_w) + 0.12(\delta^{18}O_{cl} - \delta^{18}O_w)$. (Hays and Grossman, 1991). Therefore, carbon and oxygen isotope ratios can be used as tracers for different (marine, sedimentary, metamorphic, magmatic, basinal, or meteoric) reservoirs (Roberts and Gee, 1985).

1.3.2. Trace elements

Wela (2017) examined the whole-rock geochemical characteristics, encompassing trace elements (TE) in both the target rocks and the impactites. The addition of TE analysis of post-impact calcite

veins can serve as a proxy for recording fluid-wallrock interactions and the physio-chemical conditions that govern the formation of calcite veins.

The TE elements are classified as lithophile elements due to their affinity for silicate minerals. Lithophile elements are further subdivided into two groups: 1) Large Ion Lithophile Elements (LILE), which encompass K, Rb, Sr, Cs, and Ba. LILEs generally carry a charge of one or two positive ions, facilitating their integration into the silicate minerals forming the continental crust (Rudnick and Gao, 2014); 2) High Field Strength Elements (HFSE), characterized by a small atomic radius and high ionic charges of trivalent or higher. Because of their small radius-to-charge ratio, they possess high field strength and are often immobile, hence, they are infrequently incorporated into the mineral lattice of silicate minerals. This group includes Zr, Hf, Nb, Y, Ta, Th, and U (Lee et al., 2012). The REE (La to Lu) compatibility in mineral structures depends on atomic number, i.e. the degree to which a REE can be incorporated into a mineral structure increases with decreasing size. Thus, large ion lithophile elements with atomic radii 2^+ and REE^{3+} elements can substitute easily with Ca^{2+} in the calcite lattice (Zhong and Mucci, 1989).

The REEs can display geochemical signatures such as Ce and Eu anomalies, which can provide details on the mode of minerogenesis (Bau and Möller, 1992). Yttrium is often included alongside REEs because it behaves chemically in a similar way to holmium (Ho) (Shannon, 1976). The incorporation of REEs into mineral structures or retention in fluids during fluid-rock interaction along fluid pathways is termed partitioning of REEs (Bau and Möller, 1992). The incorporation of REEs into carbonates during fluid transport depends on trace element availability, calcite growth rate, pH, Eh, pCO_2, Ca^{2+}, CO_3^{2-} ratio, and U complexation (Roberts et al., 2020).

1.4. GEOCHRONOLOGY OF POST-IMPACT VEINS AND CLAYS

Constraining the formation ages for post-impact hydrothermal alterations is essential for characterizing fluid flux dynamics and their role in the geological evolution following impact cratering events. The presence of post-impact hydrothermal alteration includes hematite, zeolite, carbonates, gypsum, epidote, chlorite and pyrite (Reimold et al., 1999; Koeberl and Reimold, 2003; Wela 2017). Secondary minerals with an affinity for Uranium (U) include zircon, apatite and titanite (McGregor et al., 2020), and calcite can also accommodate U in its crystal lattice

(Sturchio et al., 1998). The absence of sufficiently large epidote, zircon, and apatite grains in the hydrothermal assemblage for geochronological analysis led to the U-Pb analysis of calcite veins. ^{238}U decays to ^{206}Pb and ^{235}U decays to ^{207}Pb. These isotopes are preserved in calcite from the time of formation to the present day (Dickin, 1997). For calcite to be a useful U-Pb chronometer, the amount of U in calcite must be sufficiently high (i.e., high μ ($^{238}U/^{204}Pb$)) (Rasbury and Cole, 2009; Roberts et al., 2017).

Besides radiometric age determination using the U-Pb method, the study combines K-Ar analysis of clay minerals to further investigate the timing of hydrothermal alteration in the M4 drillcore. The K-Ar dating will provide insight into whether there was resetting of the original impact hydrothermal assemblages, as indicated by the loss of daughter isotopes (^{40}K to ^{40}Ar), or whether new clay-forming events occurred.

2. GEOLOGICAL SETTING

2.1. INTRODUCTION

The 146.06 ± 0.16 Ma (U-Pb zircon, impact melt rock: Kenny et al., 2021) Morokweng Impact Structure (MIS) in the Northwest Province of South Africa (Figure 2.1) is completely buried under the Upper Cretaceous to Cenozoic Kalahari Group sediments (see Section 2.3). Regional geological maps, interpretation of geophysical data, and drillcore intersections beneath the Kalahari Group sediments indicate that it is situated in Archaean to Palaeoproterozoic rocks of the Kaapvaal craton that may have had a thin covering of Phanerozoic Karoo Supergroup (350-180 Ma; Reimold et al., 2002) rocks at the time. In some areas the basement of the MIS comprises primarily Neoarchaean granitoid gneisses dated at 2.91-2.92 Ga (U-Pb zircon, Cornell et al., 2018; Gibson et al., 2022) that are overlain by the Neoarchean Ventersdorp Supergroup and Palaeoproterozoic rocks of the Griqualand West Supergroup (1.8-2.78 Ga; Andreoli et al., 1999; Reimold et al., 2002; Khumalo et al., 2024), all of which display evidence of pre-impact mafic dyke intrusions. Phanerozoic Dwyka Group rocks are also known from the area (Westgate et al., 2021). Corner et al. (1997) suggested the NNW – SSE Linopen anomaly corresponds to a greenstone belt, which underlies the western part of the MIS. Hart et al. (2002) noted "pyroxene gneisses" (amphibolite) as a major constituent of the basement section in the M3 drillcore (Figure 2.1B).

The exact size of the Morokweng crater remains uncertain. Although gravity, airborne magnetic geophysics and satellite imagery were initially interpreted to suggest a large central uplift with a diameter of ~65-70 km and an outer crater rim of ~240 km (Andreoli et al., 2008), more recent investigations suggest a 70-80 km apparent crater rim diameter (Corner et al., 1997; Henkel et al., 2002; Gibson et al., 2024a), which would correspond to Ring III in Figure 2.1A. The boreholes M3, WF4, WF5, and WF3 within Ring I intersect several hundred metres of impact melt (Figure 2.1B; Hart et al., 1997; 2002; Andreoli et al., 1999), with the M3 drillcore intersecting 800 m of impact melt rock and a further 300 m of crater basement. The lack of an upper chill margin in all 4 drillcores indicates that the top of the melt sheet was removed by erosion prior to Kalahari Group deposition (Figure 2.1B; Hart et al., 1997; Koeberl et al., 1997; Kenny et al., 2021). The impact

melt rocks within the 4 drillcores show petrographic and geochemical evidence of differentiation (Hart et al., 1997; Andreoli et al., 1999; Reimold et al., 2002; Koeberl and Reimold, 2002; Kenny et al., 2021) and contain inclusions of meteorite fragments (Maier et al., 2006) as well as granitic, ultramafic, mafic and quartzitic lithic clasts (Hart et al., 1997, 2002; Koeberl et al., 1997; Koeberl and Reimold, 2003).

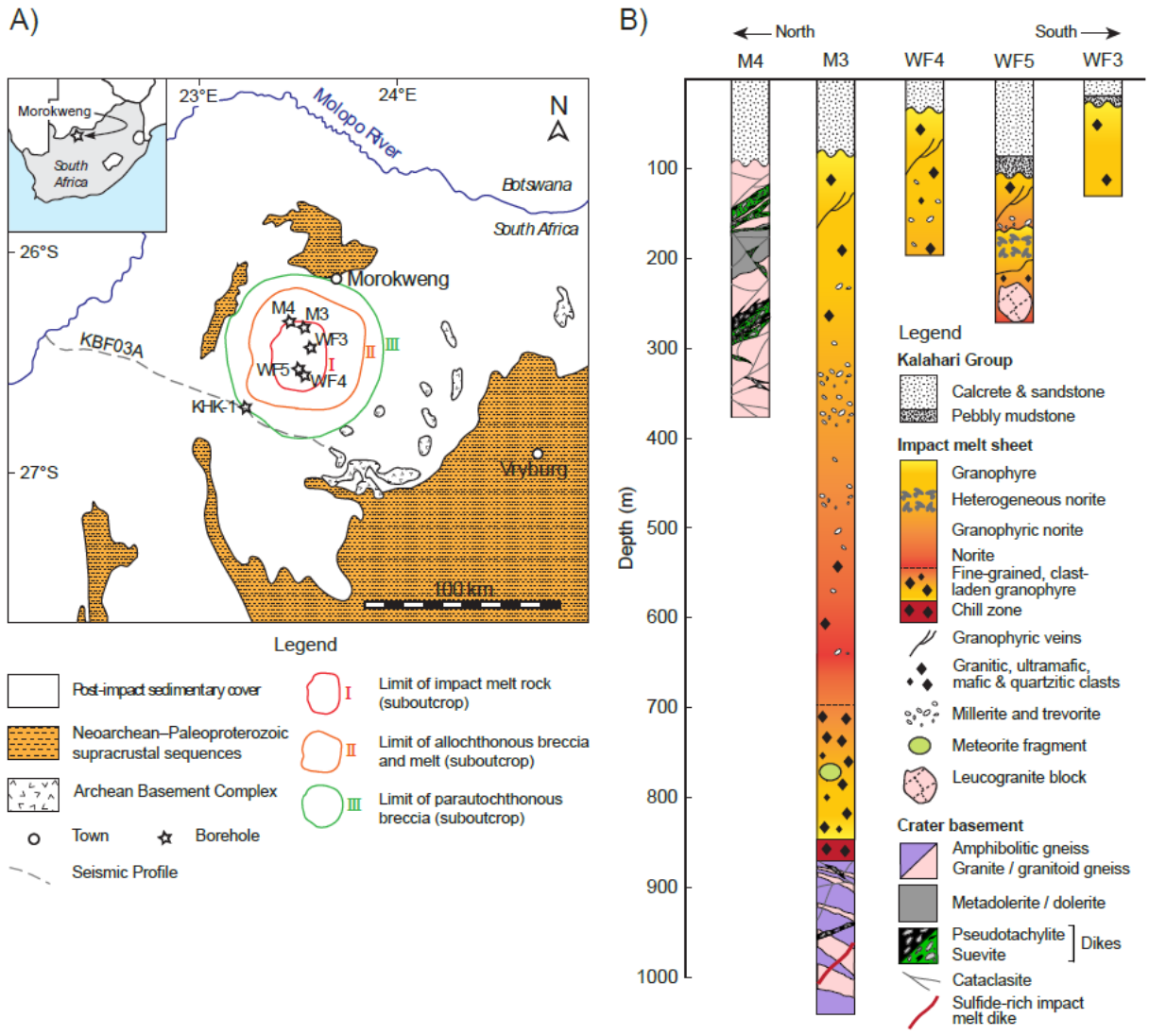


Figure 2.1. A) Simplified geological map of the Morokweng Impact Structure displaying concentric rings identified by Andreoli et al. (2007) from geophysical data. Also shown are locations of boreholes, and B) stratigraphic columns of boreholes M4, M3, WF5, WF4 and WF3. The locations of the KBF03A seismic profile and KHK-1 drillcore discussed, respectively, in Westgate et al. (2021) and Reimold et al. (2002) are also shown. Inset shows the locality of the MIS in South Africa. (From Gibson et al. 2024a).

2.2. Late Cretaceous to late Miocene history of the Morokweng region

The break-up of Gondwana in the mid-Mesozoic (< 170 Ma) led to significant tectonic events, one being the regional extension between Africa and South America (Encarnacion et al., 1996). The rifting resulted in the opening of the South Atlantic Ocean at ~135 – 115 Ma, with these tectonic stresses impacting the terrestrial evolution of the neighbouring regions (Jelsma et al., 2009; Westgate et al., 2021). At <135 Ma, the rifting caused volcanism, exposed as an erosional remnant, in Etendeka (Namibia) (Renne et al., 1992; Beccaluva et al., 2020). The lava might have covered the crater before the erosional exhumation (1-2 km) of the MIS during the Late Cretaceous to Cenozoic periods (Hanson et al., 2009). The Group I and Group II kimberlites were emplaced between 140 and 114 Ma, and ~100 and 75 Ma, respectively (Hanson et al., 2009).

The progressive arching, thinning, and rifting of the continental crust of southern Africa accompanied volcanism (Beccaluva et al., 2020). Further rifting and reactivation of faults along the western margin of the Kaapvaal Craton resulted in the formation of the Kalahari Basin (Haddon and McCarthy, 2005; Tinker et al., 2007; Westgate et al., 2021), which may have commenced between 86-93 Ma due to the disruption of regional drainage systems caused by faulting and folding of the local basins (Wessel Formation; Partridge et al., 2006). Westgate et al. (2021) suggested that the region experienced both compressional and extensional tectonics that produced small-scale faults of varying orientations, and km-scale wavelength gentle folds. The faults correspond to the ±80 – 65 Ma Campanian-Maastrichtian rifting events (Westgate et al., 2021). The faulting events in the Kalahari Group reactivated faults in the underlying basement lithologies (Westgate et al., 2021). However, the KBF03A seismic profile (Figure 2.1) suggests that a single regional dyke identified from magnetic data, called the Machavie Dyke (Westgate et al., 2021), cuts the faults and the MIS crater but not the Kalahari Group sediments, thus the dyke may have contributed to hydrothermal events. In addition, prior to the deposition of the Kalahari Group sediments, the Morokweng impact structure appears to have been differentially eroded by the proto-Morokweng River (Haddon and McCarthy, 2005).

The reactivation of tectonic faulting and folding continued into the Cenozoic (66 Ma) (Partridge et al., 2006; Westgate et al., 2021). The regional extension ceased at 30 Ma and the paleoenvironmental reconstructions of the region indicate that the south Kalahari Basin bulged upwards leading to erosion (Partridge et al., 2006; Westgate et al., 2021). During the Miocene (~23 to 5.3 Ma), erosion and uplift of sedimentary cover and underlying country rocks continued, leading to the regional exposure of the craton's basement rocks. Periods of accelerated uplift at ~20 Ma and ~5 Ma indicate tectonic readjustments and changes in the geological landscape (Partridge et al., 2006). Haddon and McCarthy (2005) suggest that the 12 – 15 Ma ages for pedogenic manganese crust obtained by Van Niekerk et al. (1999) imply post-African I surface erosion. The elevated surfaces that were eroded include the uplift along the Etosha-Griqualand-Transvaal axis (Partridge and Maud, 2000; Haddon and McCarthy; 2005).

2.3. KALAHARI GROUP STRATIGRAPHY

The MIS is partially eroded but is also buried under ~ 130 – 210 m thick Kalahari Group sediments (Andreoli et al., 1999; Partridge et al., 2006; Westgate et al., 2021). The sediments cover an extensive area of ~ 2.7 million km^2 of southern Africa, reaching as far as the Congo River in the DRC from the Orange River in South Africa (Linol et al., 2015). The Kalahari Group consists of eight formations (Figure 2.2; Smit, 1977; Thomas and Shaw, 1991; Haddon, 2005; Partridge et al., 2006): the sequence begins with the Wessel Formation, a basal gravel unit, which is succeeded by the Budin Formation, which consists of calcareous clay. The overlying Eden Formation consists of sandstones, thin gravel and clay layers. Above it lies the Mokalanen Formation, characterized by calcrete. Continuing upward, the Obobogorop Formation is marked by gravel units, followed by the Gordonia Formation, characterized by widespread unconsolidated sands. References to the Goeboe Goeboe and Lonely Formations, characterized by loosely consolidated limestone, are noted but their stratigraphic positions remain unclear (Haddon, 2005; Partridge et al., 2006). Generally, the Kalahari Group Sediments were deposited by rivers from the Late Cretaceous to the Quaternary period.

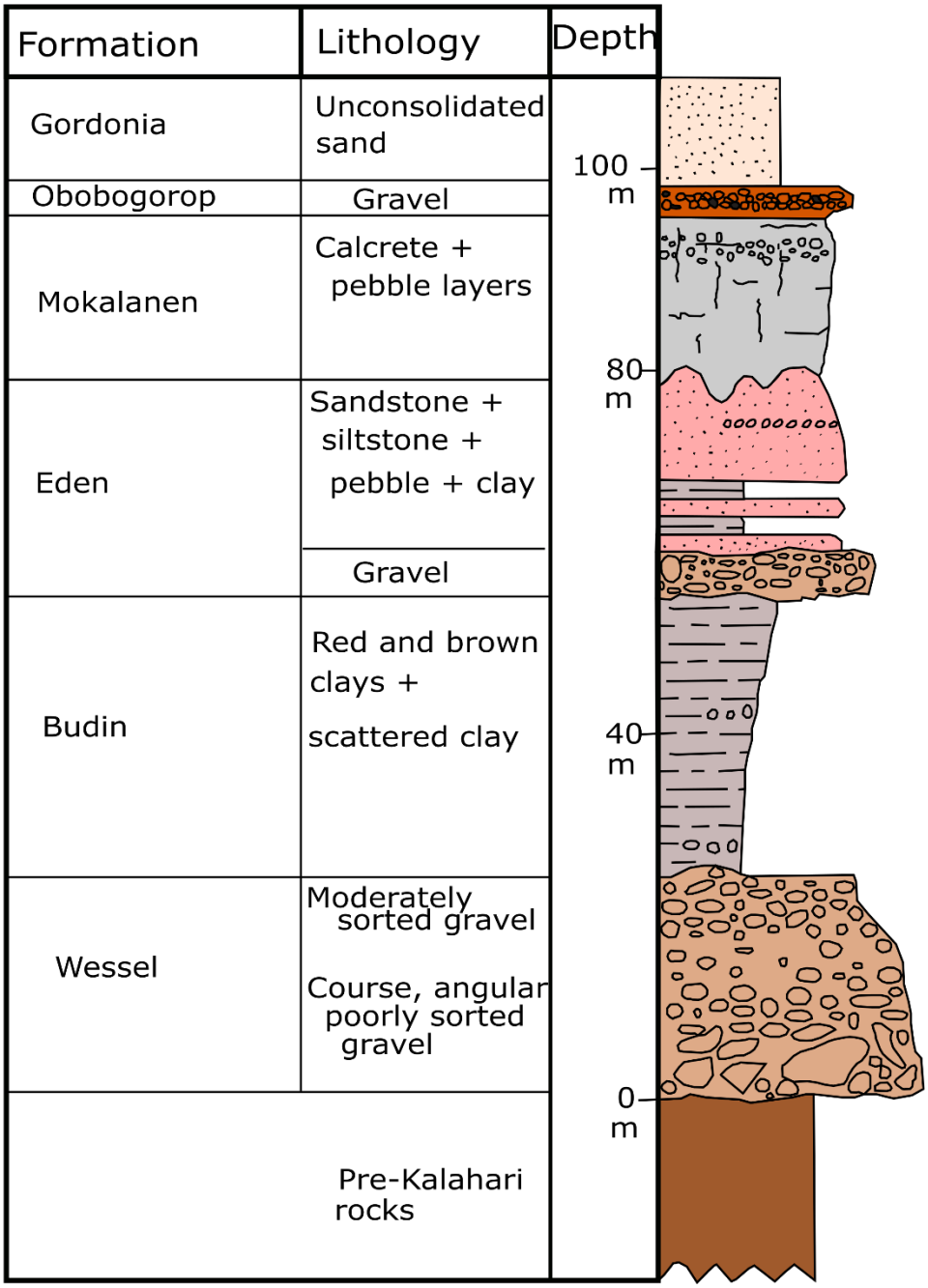


Figure 2.2. A generalized Kalahari Group stratigraphy (Adapted from Patridge et al., 2006)

For reasons that will become apparent in the results section (Section 4), it is necessary to consider potential meteoric and groundwater reservoirs in the Morokweng region. It is suggested that the Kalahari lithologies and the underlying rocks of the Griqualand and Transvaal Supergroup around

the MIS serve as the primary modern-day aquifers in the region (Haddon, 2005; Jonker and Abiye, 2017). However, these formations do not outcrop everywhere (Partridge et al., 2006), but the sub-Kalahari topographical surface and isopach map of the Kalahari Group display valleys flanking the crater (Haddon, 2005). The basal unit, the Wessel Formation, suboutcrops over a large geographical area and is best preserved in the deeper palaeovalleys (Partridge et al., 2006); the Budin Formation is also found within the limits of these palaeovalleys (Botha et al., 1986). Both formations are characterized by brackish to saline water (de Beer and Blume, 1985; Haddon, 2005). The Budin Formation is defined by lacustrine reworked deposits in the southern part to the northeasterly direction of the Kalahari Basin, covering about 400 km long (Haddon, 2005). The middle Kalahari aquifer, the Eden Formation, outcrops along dry river valleys (e.g., Moshwaneng River and Kalahari Gemsbok Park calcrete deposits reworked by rivers) (Haddon, 2005). Their exposure is restricted to newly formed lakes along the floor of the Kalahari Basin (Haddon, 2005).

2.4. THE M4 DRILLCORE

The M4 borehole, which is 369 m deep, was drilled ~18 km NNW of the estimated centre of the MIS geophysical anomaly, which Wela (2017) interpreted as the peak ring of the crater (Figure 2.1). She identified a suite of granitic, granodioritic, trondhjemitic, and dioritic (monzonitic – Gibson et al., 2022) gneisses with the contact relationships between the granitoid rock types generally appearing gradational and cm to dm scale interlayering being common (banded gneiss). The mafic rocks were classified by Wela (2017) as metadolerites and dolerites based on petrographic differences. The drillcore is highly faulted and disrupted by two dm-scale reverse-slip faults occurring at ~140 – 160 m and ~260 – 300 m that contain polymictic clastic and melt breccias (Gibson et al., 2024b). These rocks host cataclasites and pseudotachylite and suevite dykes ranging from mm to m width (Wela, 2017; Gibson et al., 2024a). The rocks display evidence of shock, particularly in quartz, some feldspars and zircon (Wela, 2017; Gibson et al., 2024b). Based on the elevated position of the basement rocks in the M4 drillcore relative to the other 4 drillcores, quartz PDF shock barometry indicating moderately high shock levels (~16 GPa), and the intense structural effects, Gibson et al. (2024b) concluded that the drillcore represents part of a deeply eroded (1.5-2 km) section through the peak ring of the impact structure.

2.4.1. Granitic and granodioritic gneisses

The granitic and granodioritic gneisses are found mainly between 94 and 117 m and 290 and 337 m depths, but are also intercalated with monzonite at 150 to 160 m and with trondhjemitic gneiss at 214 to 260 m depths (Gibson et al., 2022). They range from light pink to pale grey-white, and their grain size ranges from medium to coarse (1 – 2 mm). These rocks consist of modal abundances of alkali feldspar of 30 – 45%, plagioclase of 20 – 40%, quartz of 20 – 30%, biotite of 1 – 5% and titanomagnetite of < 1% (Gibson et al., 2022). More leucocratic granitic gneiss was intersected between 130 and 140 m and has an overall coarser grained to pegmatitic texture (up to 4 mm) and a weaker foliation (Gibson et al., 2022).

2.4.2. Trondhjemitic gneiss

Trondhjemitic gneiss is grey-white, with a grain-size range from 2.5 mm – 5 mm, and has a stronger foliation than the leucocratic granitic gneiss (Gibson et al., 2022). It is interbanded with metadolerite at 212 – 260 m depth, within what Wela (2017) interpreted as a pre-impact brittle-ductile fault zone at 205.85 – 234.33 m. The fault zone in this region is characterized by abundant white quartz veining that occurs as a network cementing hydraulic breccia. Petrographically, quartz in the trondhjemitic gneiss shows evidence of crystal plastic and brittle strain (Wela, 2017; Gibson et al., 2024a). In terms of modal mineralogy, the trondhjemitic gneiss consists of plagioclase 50%, quartz 40%, biotite 4%, epidote 5% and titanomagnetite and sulfides < 1% (Gibson et al., 2022).

2.4.3. Monzonitic gneiss

Monzonitic gneiss in the drillcore is intercalated with granitic and granodioritic gneisses at 119 to 166 m depth, and with magnetite-bearing granodioritic gneiss below 331 m depth (Gibson et al., 2022). It is dark grey and is medium- to coarse-grained (0.5 – 5 mm) and slightly magnetic; its main minerals are plagioclase 58%, alkali feldspar 10%, quartz 10%, biotite 15%, and accessory minerals are epidote 3%, titanite 2%, apatite 1% and titano-magnetite 1%.

2.4.4. Metadolerite and dolerite

The metadolerite occurs at 166.10 – 236.60 m and contains pre-impact quartz veining at 173.30 – 179.75 m and 196.63 – 236.60 m (Wela, 2017). The metadolerite is brownish-red and uniformly fine-grained (<0.5 mm). The metadolerite contains a greenschist facies metamorphic assemblage of amphibole ~40% (actinolite-actinohornblende; Wela, 2017), albite-andesine 40%, quartz 10%, and titanite 2%, epidote 2%, zoisite 2%, ilmenite 2%, with retrograde chlorite and a few relict clinopyroxene cores making up the remaining 2% (Wela, 2017). Wela (2017) noted a “siliceous metadolerite" consisting of highly oxidized amphibole-pyroxene 50%, quartz 40%, plagioclase 3%, titanite 2%, epidote 2%, rutile 1%, ilmenite 1%, magnetite 1%, that produced a highly elevated SiO_2 content, owing to very finely quartz veins (Wela, 2017). The quartz in the veins and host rock matrices shows PDFs and, thus, is pre-impact. The grains are granoblastic and contain multiple sets of PDFs (Figure 2.3; Wela, 2017). On average the quartz grains exhibit 2 sets of PDFs (Wela, 2017).

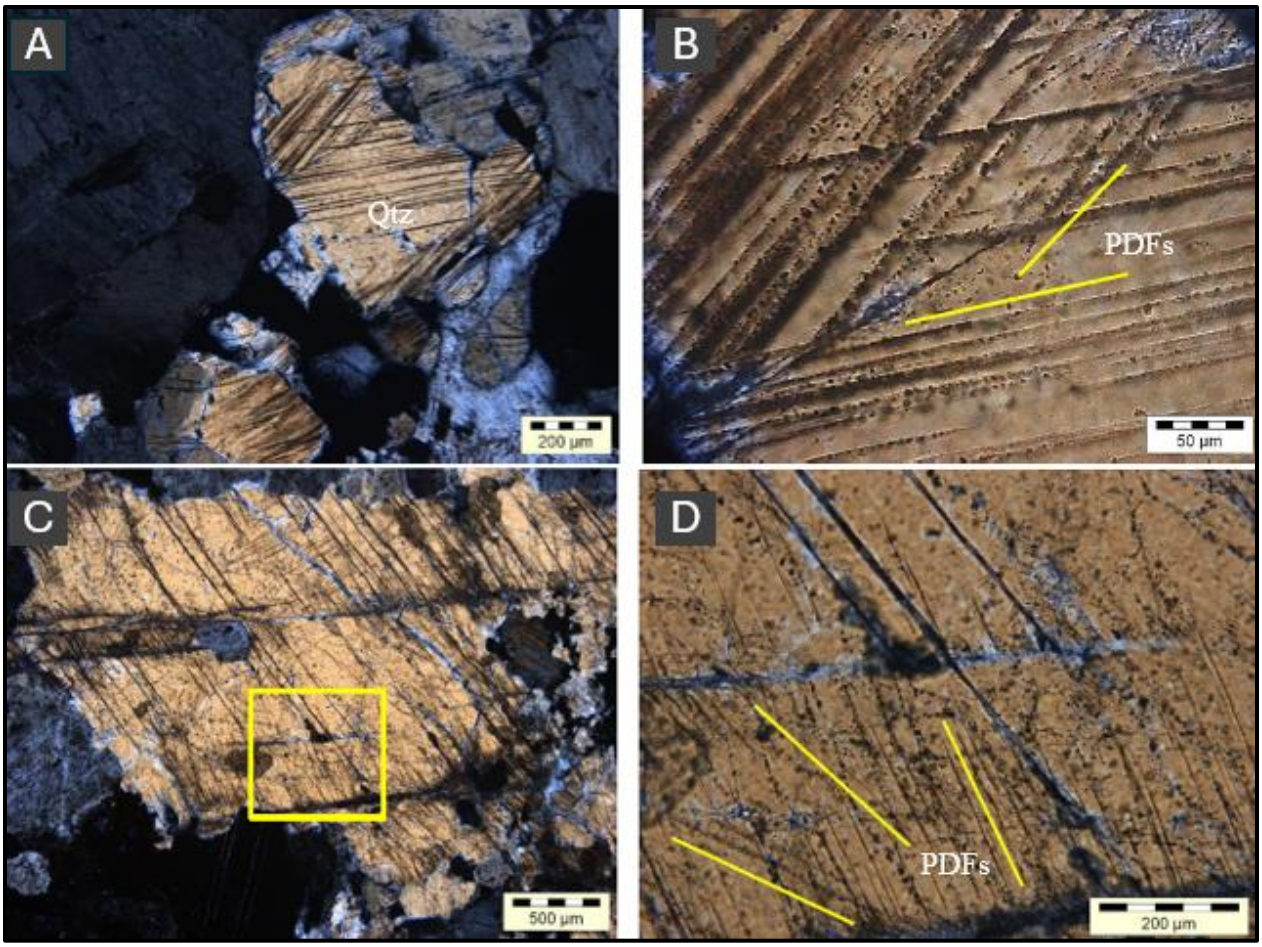


Figure 2.3. Microphotographs of quartz grains showing multiple sets of decorated PDFs (images from Wela, 2017). A) Cross polarised light image showing two sets of decorated PDFs from Sample M4 GG 4 (109.20 m). B) Enlargement of A, showing fluid inclusion trails. C) Cross polarised light image showing microfractures and PDFs in shocked quartz grain from sample M4 FZ-2 (219.30 m). D) Enlargement of C, showing three sets of decorated PDFs and microfractures containing zeolite fill. PDFs = planar deformation features.

The dolerite occurs at 264 – 290.71 m depth in a zone characterised by cataclasite, pseudotachylite and suevite dykes that Gibson et al. (2024a) interpret as a fault zone. The dolerite intersections may, thus, represent clasts in the fault zone breccias. The dolerite is dark brown and fine- to medium-grained (0.5 – 1 mm) and has a mineralogy consisting of plagioclase 60%, clinopyroxene 35%, and accessory minerals quartz, biotite, titanite and ilmenite 5%. The dolerite was not included in the present study because textural analysis was difficult due to the highly oxidised matrix. It displays slightly magnetic, shiny black, oval spots with diameters of ~1 cm that are also found in the adjacent suevite and pseudotachylite, which indicate Fe-metasomatism. Wela (2017)

was not able to distinguish these spots from the rock matrix in thin sections but interpreted them as hydrothermal.

2.4.5. Pseudotachylite

The pseudotachylite dykes are aphanitic and display a homogeneous to flow-banded matrix containing lithic and mineral clasts (Wela, 2017). The dyke morphology is suggested to result from a low-viscosity melt that preserves fluidal internal textures (Gibson et al., 2024b). The dykes range from orange to orange-red in the granitoid rocks and grey to red-brown in the mafic rocks, and locally show margins that are intimately infolded with cataclasites or suevites (Wela, 2017; Gibson et al., 2024b). The maximum dyke width is ~ 2 m (Wela, 2017), which comprises both mafic and felsic melts. Thin dykes and discontinuous lenses and stringers (a few mm in length and < 1 mm – 10 cm wide) occur along small faults (Gibson et al., 2024b). The largest dykes occur in the two main fault zones, suggesting a link between the volume of the dykes and the size of the faults (Gibson et al., 2024b). Microscopically, the flow is laminar, complexly folded and variegated melts (Wela, 2017; Gibson et al., 2024b). The variegated melt represents different bands of felsic and mafic melts (Wela, 2017). The melt contains lithic clasts and mineral clasts of the granitoid gneisses and dolerites. The mineral clasts such as quartz, feldspar (up to several mm) show evidence of PDFs in quartz and non-shock-diagnostic features like kinking and undulose and patchy extinction in feldspars (Gibson et al., 2024a).

2.4.6. Suevites

Polymictic suevite dykes range between < 1 mm and 3 m wide (Wela, 2017). The colour of suevites ranges from red (above ~200 m depth), grey (207-310 m), and green (below ~310 m) (Figure 2.4). Wela (2017) attributed the colour change to increased chlorite content from below 300 m. They contain clastic mixtures of angular rock fragments, melt fragments and mineral clasts exhibiting a brecciated texture and PDFs in quartz (Wela, 2017; Gibson et al., 2024a). The mineral clasts are more abundant than in the pseudotachylites and are up to several mm in size (Gibson et al., 2024a). Lithic clasts range from cm to dm size and melt clasts up to 1-2 cm in size (Wela, 2017). The

suevite matrix is dominated by zeolite minerals, with secondary amounts of smectites, but zeolite and calcite veins also cut across the dykes.

2.4.7. Veins

All lithological units are cut by mm- to cm-wide veins, including all impact-related faults and dykes (Wela, 2017; Gibson et al., 2019). The pre-impact stockwork quartz veins (mm- to cm-thick; Figure 2.4) occurring in the metadolerite section are cut by impact faults and pseudotachylite and occur as clasts in the suevite; the quartz also shows shock PDFs (Wela, 2017; see Section 2.4.4). These are not discussed further. The veins that crosscut the pseudotachylite and suevite dykes are attributed to post-impact hydrothermal alteration (Wela, 2017).

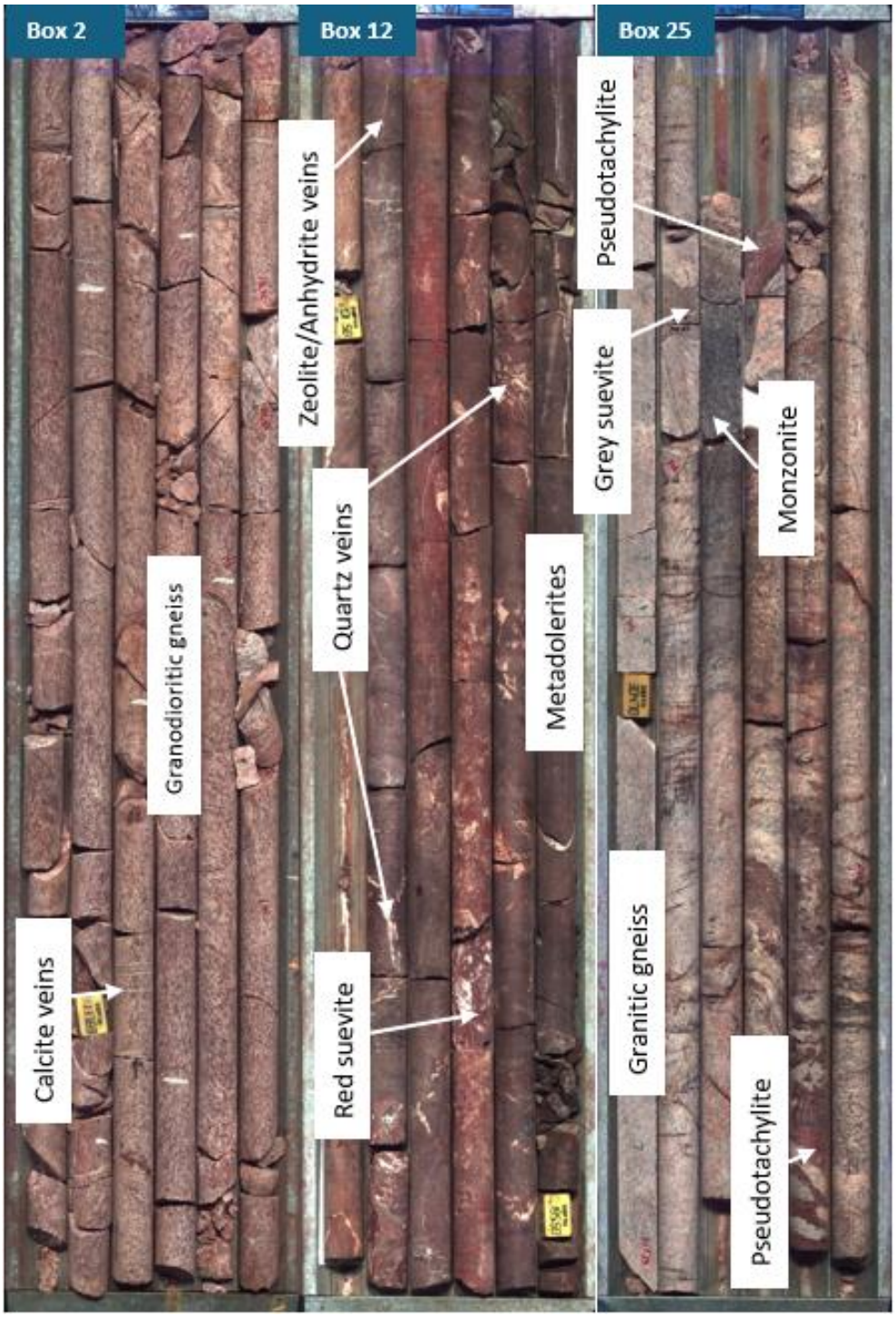


Figure 2.4 Drillcore trays from 110 – 119 m (Box 2; upper part), 194.46 – 202.6 m (Box 12; middle part) and 297.08 – 305.35 m (Box 25; deeper part), showing host rocks and vein types within the M4 drillcore. The veins show different abundances and orientations: Subhorizontal veins occur in the upper part, inclined to vertical orientations occur in the middle part, and the deeper part shows little to no veins. Box 12 shows thick pre-impact quartz veins. Drillcore width is 4.5 cm.

The veins exhibit erratic patterns, composed of a variety of cements such as carbonates, zeolite or gypsum (Wela, 2017). Carbonates are more abundant in the upper parts of the drillcore and decrease with depth, while the deeper parts below 300 m show zeolites, clays. Fe-oxides and small amounts of calcite in fractures (Wela, 2017).

3. HYPOTHESIS AND METHODOLOGY

3.1. HYPOTHESIS, AIMS AND OBJECTIVES

3.1.1. Hypothesis and Questions

This study is part of a broader investigation of the hydrothermal alteration features in the M4 drillcore, in conjunction with the MSc dissertation of Ms T. Masiu. The hypothesis proposed is that the structurally uplifted, highly deformed crater basement rocks and associated breccias in the peak ring of the Morokweng impact crater, represented by the lithological association intersected in the M4 drillcore, were heated by the impact and were cooled by circulation of hydrous fluids of meteoric origin at 146 Ma, with possible further low-T alteration related to meteoric or groundwater influx either during erosional exhumation prior to the deposition of the Kalahari Group or during Kalahari Group deposition. The following questions are addressed in this study:

- What was the nature, extent, and duration of fluid-rock interaction in the peak ring of the MIS following the impact?
- Can the composition and prevalent physico-chemical characteristics of the post-impact hydrothermal fluid(s) be determined?
- Is there evidence for more than one fluid-related alteration event following the impact?

3.1.2. Aims and Objectives

The main aim of this study is to investigate whether the hydrothermal veining in the M4 drillcore can be unequivocally linked to the impact. This is done by linking microtextural observations with geochemical data to constrain the physico-chemical conditions of fluid flow within the M4 drillcore responsible for the veining, and with radiometric age dating of hydrothermal minerals in the post-impact alteration sequence. The objectives are:

- Use hand specimen, transmitted, and reflected light thin section and scanning electron microscope (SEM) petrography and cathodoluminescence (CL) imaging to characterise the vein mineralogy and morphology.

- Use trace element data to trace fluid signatures within calcite veins in order to provide insights into the fluid origin and chemical conditions under which the calcite crystallized.
- Use stable isotopic ratios to investigate possible sources of fluids and temperatures of equilibration.
- Apply radiometric dating to constrain the absolute timing of hydrothermal mineral formation within calcite veins (U-Pb) and clay minerals (K-Ar).

The overall study will enable comparison with the fluid sources proposed by Simpson (2020) for Chicxulub and with those of similar-sized impact structures, such as the Puchezh-Katunki structure. These findings will contribute to the understanding of hydrothermal activity and post-impact cooling within the Morokweng impact structure.

3.2. METHODOLOGY

3.2.1. Macroscopic analysis

The M4 drillcore was examined at the petrology lab, University of Witwatersrand. The drillcore analysis was done using basic geological drillcore observation techniques. The following tools were used: Measuring tape, camera, handlens, magnetic pen, and water (to wet the rock). Assessment of macroscopic features of veins involved identification based on their spatial distribution, spacing between the veins, orientation, thickness, morphology, mineralogy (including whether the veins are polymineralic or monomineralic), evidence of wallrock interactions and cross-cutting relationships between various type of veins, and between veins and impact related features.

3.2.2. Optical Microscopy

A total of ~ 120 thin sections, involving 110 studied by Wela (2017) and 10 newly-prepared as part of this study, were examined using optical microscopy in the School of Geosciences at the University of Witwatersrand. An optical microscope was employed in both cross-polarized light (XPL) and plane-polarized light (PPL) modes. In conjunction with microphotographs, vein-related

samples were analysed under a Leica DM-LSP microscope to capture mineralogy and variation in the internal texture and morphology of cross-cutting veins and any evidence of fluid-wallrock interaction. Considering the aims of the project, the focus was on examining highly altered samples containing clay, zeolite, and other hydrothermal minerals within the impact shock and structural features to establish the textural and spatial relationships and to provide the framework for other petrographic methods, i.e., Backscatter scanning electron microscopy (BSEM), Tescan integrated mineral analyzer (TIMA) and cathodoluminescence (CL-BSE) which, in turn, allowed selection of targets for advanced geochemical and stable isotopic analysis, as discussed below.

3.2.3. Scanning Electron Microscopy

Ten carbon-coated samples were analysed using the built-in TESCAN TIMA 2.4.0 software installed on a scanning electron microscope at the WAMLAB, University of Witwatersrand. The operating conditions during quantitative analysis were 25 kV accelerating voltage, 43 $\boldsymbol{\mu}$A emission current, with a working distance of 15.00 mm, a specimen beam current of 17.68 nA and the spot size of 590.00 nm. The scanning electron microscope spectrometer is equipped with energy dispersive X-ray analysis (EDXA) Element 30 and set with a calibration point of 370 keps, and data processing was done using TIMA to search for mineral and vein elemental zoning and identify fine-grained alteration minerals in phase and elemental mapping, as well as to understand paragenetic sequences within hydrothermal mineralization. Additionally, twelve carbon-coated samples were analysed in BSE mode using Tescan Vega 3 scanning electron microscope at MMU labs, University of Witwatersrand, Johannesburg. The operating conditions in this lab were 30 kV accelerating voltage, operating pressure of $7.5e^{-2}$ Pa with a working distance of 10 – 15.00 mm. The SEM is equipped with cathodoluminescence (CL) and back scattered electron (BSE) detectors for obtaining high-resolution imaging. The BSE signal was used to determine the grain boundaries based on the mineral contrast in brightness and resolve fine-grained textures not possible under transmitted light (TL). CL was used to search for mineral growth zoning in individual crystals.

3.2.4. X-Ray Powder Diffraction

Following Wela's (2017) bulk powder XRD analysis of pseudotachylite and suevite matrices, which indicated a mixed clay population and non-clay phases that were only partly resolved via EMPA owing to the fine grain size, eight powdered clay-rich aliquots were analysed at İstanbul Üniversitesi – Cerrahpaşa, following the methodology outlined in Uysal et al. (2006), and using an X-ray diffractometer (XRD) equipped with parallel beam geometry and CuKα radiation to determine differences in clay type. Clay mineral analysis required separation of clay into fractions of <2 micron. The fractions were obtained by centrifugation and were then suspended and sedimented on glass slides and dried. Since the samples contained significant amounts of smectite-type clay, they were treated with placed ethylene-glycol at 30 – 40℃ overnight before additional XRD analysis. The XRD patterns display peak positions and intensities that allow clay mineral identification. Although it was not possible to obtain clay separates specifically from the veins, this procedure was necessary to provide the background to the clay mineral geochronology (Section 4.6). The XRD machine was operated at 40 kV and 40 mA using a scanning rate of 1°2θ/min.

3.2.5. Secondary Ion Mass Spectrometry

Three samples were analysed for carbon and oxygen isotopes in 25 mm round polished mounts using the "virtual SIMS facility" at the University of the Witwatersrand and operated at the Helmholtz Zentrum Potsdam using a Cameca 1280-HR instrument. For better visuals, a motorised Nikon Eclipse LVDIA-N microscope was used to navigate and select points along calcite veins. Sputtering was achieved using a ^{133}Cs+ primary beam with -10 kV secondary energy and a primary beam current of 2 nA and 1.6 nA, respectively. A normal incidence electron gun was used for charge compensation. Each analysis was preceded by a 70-second pre-sputtering with a 20 µm raster, which removed the gold coating and established stable sputtering conditions. The instrument was operated in multi-collection mode with the L´2 and the H´2 Faraday cups (FC) analysing δ^{16}O and δ^{18}O, respectively. For carbon, ^{12}C was detected using L´2 trolley, and mono-collection central-position Faraday cup FC2 was used to detect ^{13}C. The instrument was operated at a mass resolving power of 2400 M/ΔM (for oxygen) and 4500 M/ΔM (for carbon). The average

pressure in the sample for oxygen analysis was 4.2 x 10^{-6} pascals, and for carbon analysis 8.1 x 10^{-6} pascals. The reference material used for oxygen is UWC-3 calcite and IAEA-603 (Kozdon et al., 2009; IAEA, 2016), and the reference material used for carbon is UWC-3 (Kozdon et al., 2009). The C and O isotope analytical results were normalised to the Vienna Pee Dee Belemnite (VPDB) and Standard Mean Ocean Water (SMOW) certified reference materials (CRM), respectively, with a precision of 0.26 ‰ and 0.19 ‰ for UWC-3 and 0.20 ‰ for IAEA-603.

3.2.6. Laser Ablation Inductively Coupled Plasma Mass Spectrometry

Five samples of the widest calcite veins (mainly from the upper parts of the drillcore) were prepared as polished thick sections for trace element analysis by LA-ICP-MS. The trace element concentrations were additionally used as a guide for U-Pb isotopic analysis. The analysis was conducted in the Advanced Mass Spectrometry facility within the Earth Observatory at the University of Witwatersrand using a Thermo Fisher Scientific Element XR single collector ICPMS coupled with an Applied Spectra/Australian Scientific Resolution SE-155 excimer laser. U-Pb analysis followed the protocol outlined in Ring and Bolhar (2020). The data were acquired by single spot analysis (100 µm), using a laser repetition rate of 10 Hz, a fluence of 2.5 Jcm^{-2} and 10 seconds of gas blank. The iolite software was used for data reduction and map creation (Paton et al., 2011). The calibration standard is carbonate WC-1 (254.3 ± 1.3 Ma; Roberts et al., 2017), and secondary standards were Rio calcite (ca. 55 Ma, C. Lana, per Comms.), Duff Brown limestone (64.0 ± 0.67, 60.5 ± 4.6 and 66.3 ± 3.9 Ma; Hill et al., 2016) and Richard's Spur speleothem (RS; 289 ± 0.68 Ma; Woodhead et al., 2010). For tuning, NIST 612 glass was analysed for maximum sensitivity for ^{238}U and ^{206}Pb. Oxide levels (ThO^+/Th) were maintained at < 0.2% and the Th/U ratio > 0.9. Overview images were taken on the samples to document laser spot locations. Ages were calculated using the software ISOPLOT-R (Vermeesch, 2019).

3.2.7. Mass spectrometer

Four of the eight powdered clay-rich aliquots (see Section 3.24) were analysed for K-Ar dating at the CSIRO Argon facility in Perth, Australia, following the methodology outlined in Uysal et al. (2020). The standards used are detailed by Dalrymple and Lanphere (1969). Argon was extracted

from retained clay-rich aliquot fractions by fusing the sample in a vacuum line equipped with an online ^{38}Ar spike pipette and the isotopic composition of the spiked Ar was measured using a highly sensitive VG3600 mass spectrometer operated online set with a calibration of ^{38}Ar that was performed against the standard biotite GA1550 (Uysal et al., 2020). Potassium content was determined using atomic absorption. The K error incurred for the standards is better than 1.2% (1 σ), and the K blank measurement was 0.50 ppm (Uysal et al., 2020). The K–Ar age was computed using ^{40}K abundance and decay constants recommended by Steiger and Jäger (1977) (Uysal et al., 2020). K-Ar dating technique is used to constrain the timing of the clay formation within the MIS.

4. POST-IMPACT HYDROTHERMAL ALTERATION

4.1. INTRODUCTION

Initially, 120 samples from the M4 drillcore were examined in thin section to select a subset of 31 samples for further investigation (Table 4.1). The results first detail the relationship between hydrothermal minerals and the impact-induced shock and non-shock-diagnostic structural (fault rocks and breccias) features to confirm the post-impact nature of the hydrothermal alteration. For instance, the presence of PDFs in hydrothermal quartz veins (see Section 4.2; Figure 2.3) indicates that quartz crystallized before the impact, whereas hydrothermal minerals replacing these shocked quartz crystallized after the impact. The results secondly show evidence of post-impact hydrothermal minerals cutting or replacing pseudotachylite dykes, or infilling the matrices of cataclasite and suevite that contain shocked mineral clasts (see Section 4.3). The results in Section 4.2-4.3 set a foundation to present in Section 4.4 similar macroscopic mm- to cm-wide, white-grey veins seen throughout the drillcore. These veins cross-cut the impact-related suevite and pseudotachylite dykes and the anastomosing to conjugate network of faults with a cm- to dm-scale spacing and mm- to cm-scale displacements that Wela (2017) and Gibson et al. (2019, 2024a,b) describe as shear faults (Section 4.3). The veins contain calcite and clay-zeolite fill, and calcite and clay are further analyzed to provide the context for the geochemical and geochronological results presented in Sections 4.5 and 4.6, respectively.

Table 4.1. Description of 31 samples for petrographic, geochemical and geochronological analysis

Depth (m)	Sample No.	Microscopic/macroscopic features	Hydrothermal minerals	Type of analysis
114	M4 V1	Veins	calcite, biotite, ilmenite	Optical microscopy, TIMA, BSE, SIMS, LA-ICPMS
121	M4 R20	decorated PDFs, FFs, fractures, microcracks, poikiblastic albite + biotite grains, sericite, veins	pyrite, phyllosilicate, magnetite	Optical microscopy
129	M4 GG1 x2	Kinks, microcracks, fractures, veins	calcite, zeolite, hematite, biotite	Optical microscopy
131.90	M4 GG2	PDFs, PFs, microcracks, veins	calcite	Optical microscopy, LA-ICPMS
139	M4 R22	Microcracks, fractures, vugs, veins	zeolite, clay, calcite, amphibole, albite	Optical microscopy, TIMA

142.95	M4 V3	Crosscutting veins, network veins	calcite, zeolite	Optical microscopy, TIMA, BSE, SIMS
144.09	M4 S1(2)	Conjugate network fractures, veins,	calcite, zeolite	Optical microscopy, LA-ICPMS
144.35	M4 RG1 M4 V4	Crosscutting veins, vugs	calcite, zeolite	Optical microscopy, XRD Optical microscopy, TIMA, BSE, SIMS
145.3	M4 V2	Crosscutting veins, network veins	calcite, zeolite	Optical microscopy, TIMA, BSE, SIMS, LA-ICPMS
148	M4 S12	Veins, vugs	calcite, zeolite, sericite	Optical microscopy
152	M4 GG8	PDFs, kinks, chevron pattern, microcracks, veins	albite, zeolite, phyllosilicates, hematite	Optical microscopy
158	M4 INJ2	Veins	calcite, zeolite, K-feldspar	Optical microscopy, TIMA
160	M4 S3	Veins	calcite	Optical microscopy
166	M4 GG10	Quartz jigsaw brecciation, fractures, veins, vugs	zeolite, clinopyroxene, smectite, alkali feldspar, hematite/goethite, calcite	Optical microscopy, TIMA, BSE
197	M4 ML	Veins	anhydrite, zeolite, smectite	Optical microscopy, TIMA
261	M4 SILL 1	Fractures	amphibole, zeolite, epidote, smectite	Optical microscopy, BSE
262	M4 RG2	Fractures, veins	smectite, zeolite, apatite, hematite/magnetite, pyrophyllite	Optical microscopy, BSE
264	M4 R12	PFs, fracture	epidote, garnet, titanite, sulphide, prehnite, hematite	Optical microscopy, TIMA
299	M4 IM9	Veins, matrix	clay, sulphide, ilmenite, smectite, magnetite, rutile	Optical microscopy, BSE-EDS, XRD
301	M4 RG3	Fractures, kinks	smectite, calcite	Optical microscopy, BSE-EDS, XRD
324	M4 GG15	PFs, PDFs, fractures, Jigsaw brecciation in quartz, brecciated feldspar, tartan twins	smectite, zeolite, sulphide, magnetite,	Optical microscopy, BSE
333	M4 MG1	Jigsaw breccia, fracture	titanomagnetite, ilmenite, sulphide, zeolite	Optical microscopy
342	M4 AM1	Jigsaw breccia, fracture	zeolite, sulphide, magnetite, chlorite, oxidised epidote,	Optical microscopy, TIMA, BSE
346	M4 R9	PDFs, kinks, jigsaw brecciation quartz, fractures	rutile, apatite, sericite, garnet, zeolite, ilmenite, sulphide, magnetite, titanite	Optical microscopy, BSE-EDS
347	M4 MG3	Sericite, PFs, FFs, microcracks,	calcite, zeolite, smectite	Optical microscopy, TIMA

348.4	M4 R8	Jigsaw breccia, kinks, PDFs, fractures	sulphide, apatite, prehnite, epidote, clay, titanite, zeolite	Optical microscopy, BSE-EDS
353	M4 SB3	Kinks, microcracks,	zeolite, smectite, pyrophyllite, prehnite, hematite/magnetite	Optical microscopy, BSE
354.84	M4 SB2	PDFs, PFs, FFs, microcracks, fractures	calcite, zeolite,	Optical microscopy, BSE-EDS
363	M4 AM5C	PDFs, Jigsaw brecciation, fractures	garnet, hematite, zeolite, phyllosilicate, epidote	Optical microscopy, BSE

4.2. POST-IMPACT HYDROTHERMAL ALTERATION IN SHOCK MICRODEFORMATION FEATURES

The granitoid gneisses in the drillcore contain minerals that display a variety of shock deformation features such as planar fractures, decorated planar deformation fractures, feather features, and others that are most likely linked to the impact but cannot be regarded as shock-diagnostic, such as kink bands (Wela, 2017; Gibson et al., 2024a). In this section, quartz, feldspar, biotite and epidote are presented to show evidence of post-impact hydrothermal alteration. Titanite, apatite and zircon have been presented by Gibson et al. (2024a). In contrast to the granitoid gneisses, the doleritic rocks show little to no evidence of shock features (Wela, 2017) and are strongly oxidised, so these are not considered further here.

4.2.1. Quartz

Quartz throughout the drillcore displays various shock and brittle petrographic features that can be linked to the impact, such as planar fractures (PFs) and planar deformation features (PDFs), feather features (FFs), toasting, and a jigsaw brecciation pattern (Wela, 2017; Gibson et al., 2019; Gibson et al., 2024a). As a result of subsequent hydrothermal activity, quartz grains host different hydrothermal minerals, such as zeolites, clay, calcite, sulphides, and Fe-oxides (Figure 4.1). Quartz is highly susceptible to strain when compared to other mineral grains. A single grain can exhibit both shock features and brittle features, and evidence of internal lattice strain. The PDFs are recrystallized and are now only defined by trails of micron-sized fluid inclusions (decorated PDFs; Figure 2.3 and Figure 4.2).

Quartz in the granitoid gneisses in the M4 drillcore commonly displays up to three decorated PDF sets (Figure 4.1A,C) as well as PFs and jigsaw brecciation pattern that are ≤ 40 µm wide (Figure 4.1A-B). PDFs commonly show partial replacement by zeolite, which occurs from the edge of the quartz grain inwards, while other hydrothermal minerals (smectite, calcite, magnetite and pyrite) either occur with the zeolite or as individual mineral phases (e.g., calcite). The widening of the zeolite-fill towards the edge of the quartz grain, scalloped margins infilled with zeolite, and merging with zeolite in the matrix shows replacement of the planar features (Figure 4.1A).

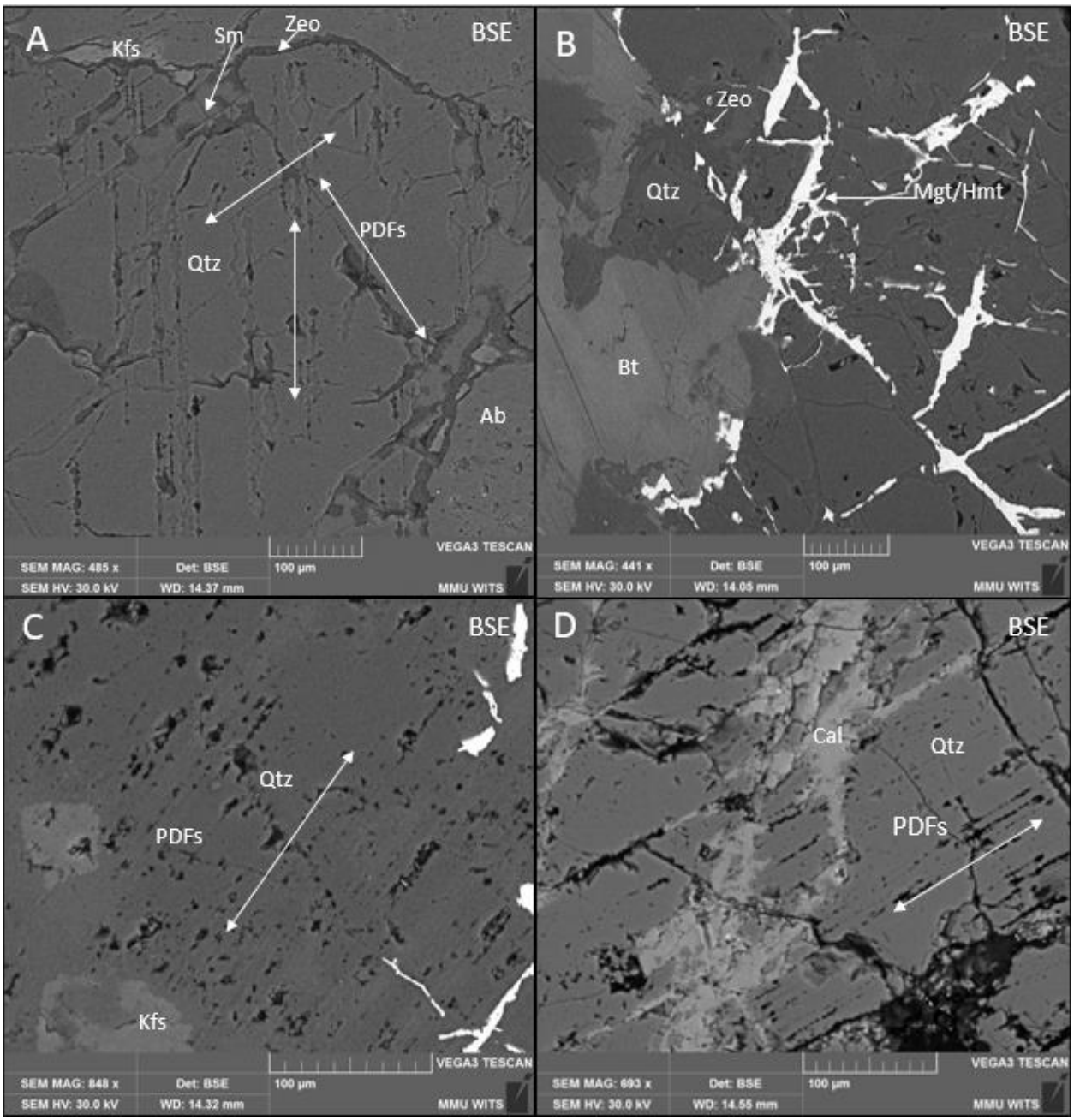


Figure 4.1. Quartz grains hosting post-impact hydrothermal minerals in shock and other impact-related deformation features. A) BSE image of sample M4 GG10 (166 m) showing quartz grain displaying three sets of PDFs filled with zeolite and clay. Quartz grain boundary also exhibits interstitial K-feldspar. B) BSE microphotograph of zeolite and sulphide (pyrite) cementing fragments within the jigsaw brecciated quartz grain from sample M4 AM 1 (342 m). For transmitted light images of this texture see Figure 4.4A-B. C) BSE microphotograph of sample M4 R8 (348.4 m) showing micron-sized cavities (interpreted as fluid inclusions) along PDFs, with cross-cutting fractures partially filled with pyrite. D) BSE image of sample M4 SB 2 (~355 m) showing evidence of irregular anastomosing calcite-filled fracture network cutting and locally replacing PDFs in quartz. BSE = backscattered electron; PDFs = planar deformation features; Zeo = zeolite; Kfs = alkali feldspar; Sm = smectite; Ab = albite; Qtz = quartz; Bt = biotite; Mgt/Hmt = magnetite/haematite; Cal = calcite.

Calcite, pyrite and magnetite occur as minor phases in the zeolite-dominated veins (Section 4.4). After zeolite, magnetite or pyrite are the most common phases in fractures that are ≤20 µm wide in jigsaw brecciated quartz grains; their distribution is restricted to quartz and does not extend to neighbouring minerals (e.g., biotite and feldspars: Figure 4.1B). The magnetite/pyrite mineralization transgresses PDFs (Figure 4.1C). These minerals locally infill PDFs, but only close to planar or irregular fractures. Calcite occurs locally in quartz as irregular micro-veins ≤ 50 µm wide, from which thin offshoots replace PFs and PDFs (Figure 4.1D). Like the pyrite, the calcite is localised in the quartz and at its margin with the adjacent matrix, but is not apparent in fractures cutting other minerals in the vicinity. Fractures < 100 µm wide and hosting polymineralic vein fill are also found cutting quartz containing PDFs (Figure 4.2). The fractures contain variable amounts of phyllosilicates, zeolite, magnetite/haematite and/or pyrite. In PPL, the fractures may appear completely or partially opaque owing to oxidation to haematite and the very fine-grained texture (< 0.5 microns) of their fill.

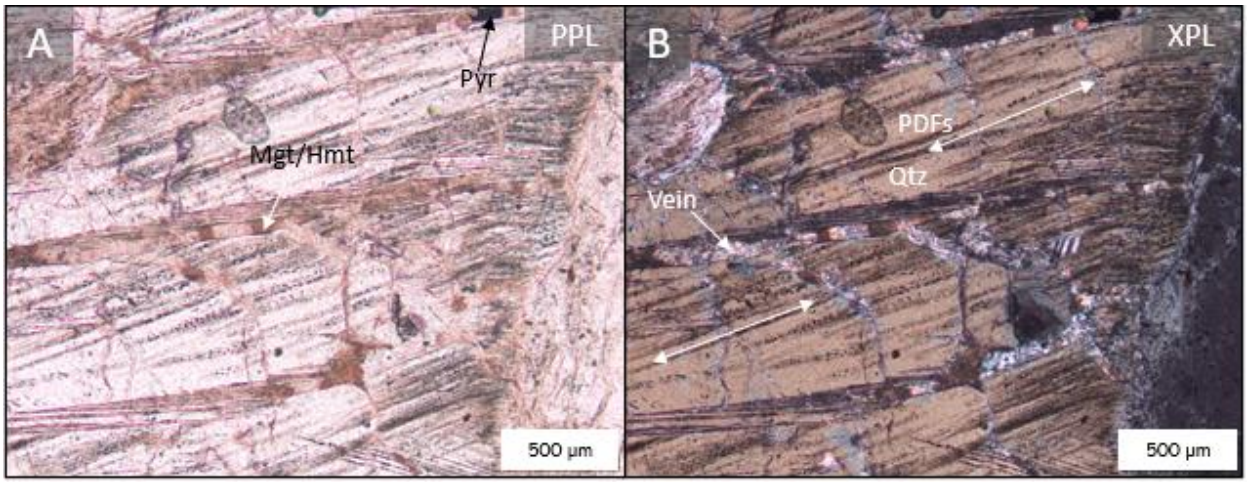


Figure 4.2. Optical microscope images (A - PPL; B - XPL) of sample M4 GG8 (152 m) showing closely spaced decorated PDFs showing fluid inclusion trails cut by a polymineralic vein. PPL = plane polarised light; XPL = crossed polarised light; Pyr = pyrite; Mgt/Hmt = magnetite/haematite; Qtz = quartz; PDFs = planar deformation features.

4.2.2. Feldspars

Sodic plagioclase (albite-oligoclase) and K-feldspar (microcline, orthoclase) are major constituents in the granitoid target rocks, although K-feldspar is only found in significant amounts

in the granitic gneiss (Wela, 2017; Gibson et al., 2022). In the mafic rocks, igneous-textured Ca-plagioclase (labradorite and andesine) occurs in dolerite and metamorphic oligoclase in the metadolerite (Wela, 2017).

One or two samples show microcline with thin (< 150 µm wide) K-feldspar veins in transgranular fractures (Figure 4.3). Although some K-feldspar has been identified adjacent to impact-related zeolite-filled fractures and is interpreted as part of the high-T K-metasomatic stage of hydrothermal alteration (Masiu, 2025, unpublished dissertation), it is not clear if these monomineralic veins are also related to the impact or predate the impact. Alteration assemblages, however, are noted within and around margins of microcline clasts in cataclasite and suevite are mostly healed and show a fine-grained texture, possibly consisting of zeolite, K-feldspar and smectite-illite clays (Figure 4.4A-B). Plagioclase displays poikiloblastic texture, containing oxidised neoblastic biotite grains (Figure 4.4C-D). The neoblastic biotite in the plagioclase crystals locally shows kinking. Although this is not shock-diagnostic, Gibson et al. (2024) suggested that the fact that the kinking occurs in inclusions in the largely undeformed plagioclase host may indicate a shock origin. Both the biotite and epidote inclusions show variable amounts of oxidation, leading to microcrystalline aggregates of opaque minerals. Where feldspars are cut by transgranular fractures the inclusions are absent.

Figure 4.4C-D also shows unusual spindle-shaped twin lamellae in alkali feldspar that produce a chevron pattern oblique to microcline tartan twins, as well as reduced birefringence and discoloration resembling toasting that are unknown from other granitoid gneiss samples from the region (Wela, 2017). Although these cannot be unequivocally linked to shock, they suggested that they are attributed to the impact event. BSE images of the darkened/toasted cores of plagioclase and microcline grains (detailed in unpublished data of Masiu, 2025) show that the feldspar is partially dissolved, leaving elongated cavities that are lined with clays, and which appear to be aligned with the crystal structure of the host grain.

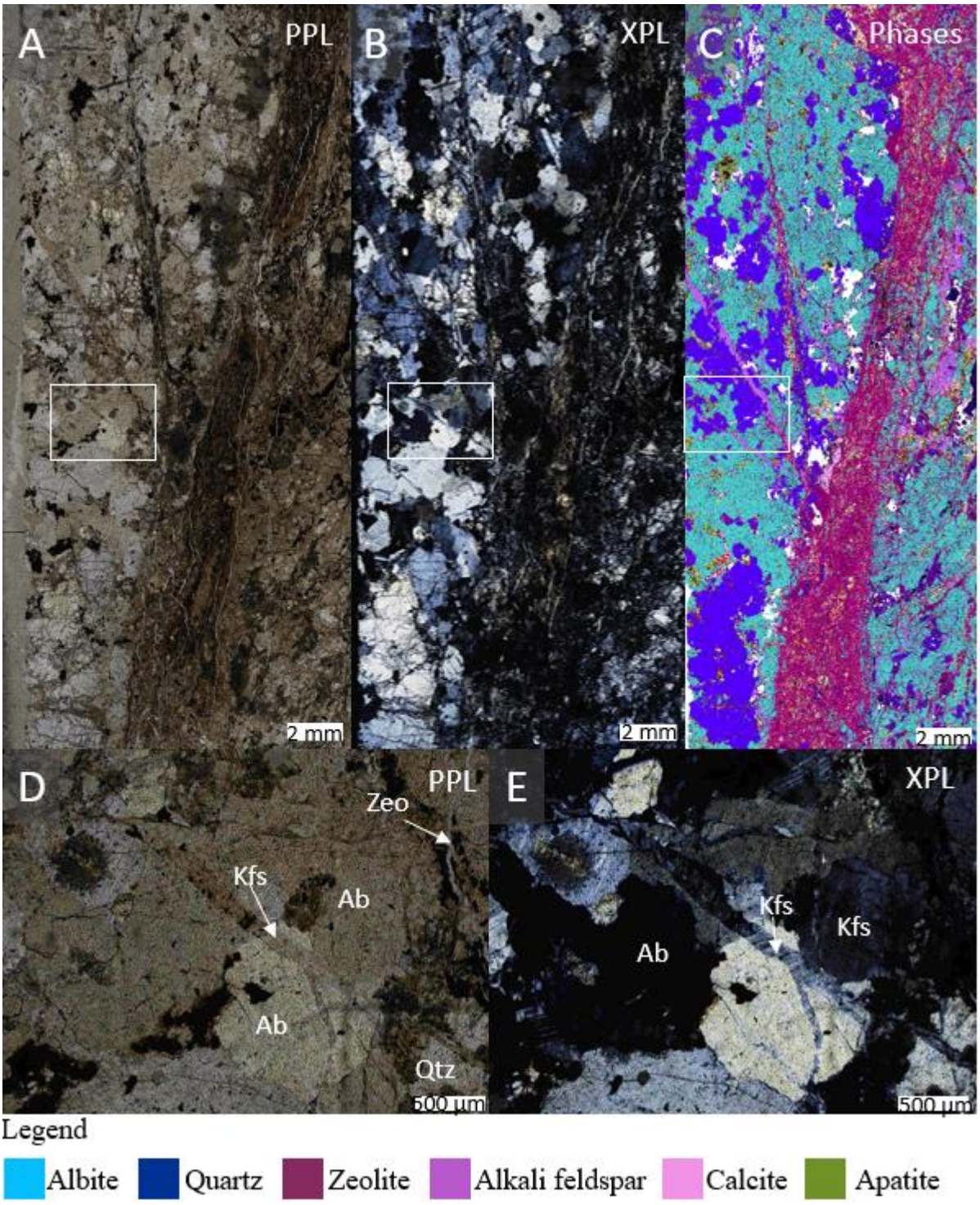


Figure 4.3. Microphotographs and phase map of sample M4 INJ2 (158.06 m) showing a subvertical pseudotachylite vein and alkali feldspar veins cutting through albite and quartz (box). A) Plane-polarized light image showing alkali feldspar cutting through albite and quartz and terminating at the pseudotachylite dyke boundary. Zeolite veins cut through both the pseudotachylite and granodioritic gneiss wallrock. B) cross-polarised light of A. C) TIMA phase map of A, B. D) Close-up PPL image of white box in A-C,

showing alkali feldspar vein cut by zeolite vein. E) Cross-polarised light of D. PPL = plane polarised light; XPL = crossed polarised light; Kfs = alkali feldspar; Zeo = zeolite; Ab = albite; Qtz = quartz.

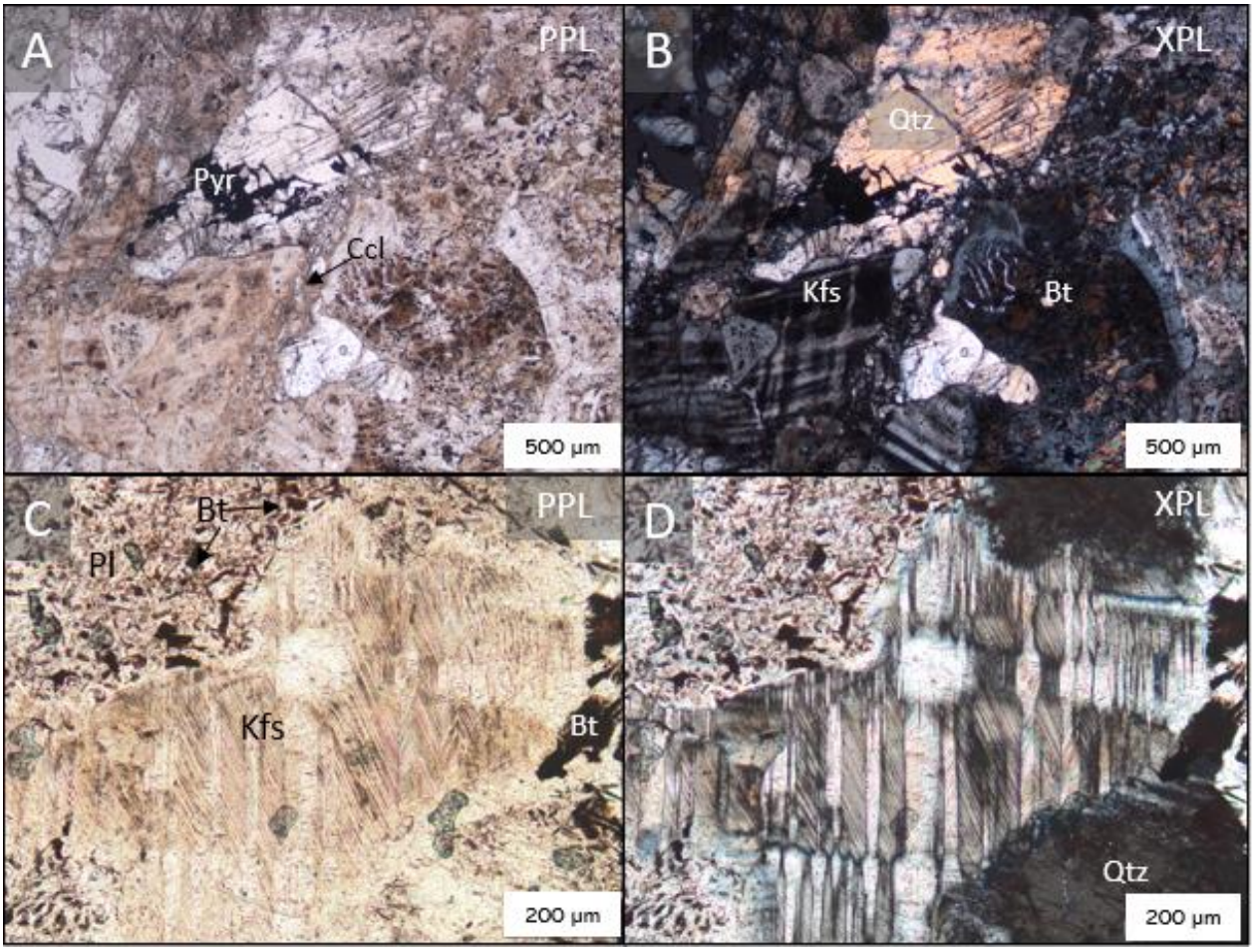


Figure 4.4. Photomicrographs of altered feldspar. A, B) Sample M4 GG15 (324 m) showing microcline with tartan twins and fine-grained alteration; above the grain is quartz grain showing PFs, PDFs, and jigsaw brecciation filled with opaques, and cataclasites in PPL and XPL. C, D) Sample M4 GG8 (152 m) showing microcline with distinct chevron pattern and plagioclase with inclusions of biotite in PPL and XPL. The microcline shows oblique planar features that show differing degrees of alteration. PPL = plane polarised light; XPL = crossed polarised light; Pyr = pyrite; Ccl = cataclasites; Kfs = alkali feldspar; Qtz = quartz; Bt = biotite; Pl = plagioclase.

Samples close to fault zones show intense fracturing, filled with minerals, like zeolite, calcite and smectite. Hence, feldspar in the cataclasite and suevite show more alteration and are dustier in appearance than grains in the host gneisses.

4.2.3. Biotite

Besides distinguishing features like rock colour, minerals including biotite assisted with spatially outlining the distribution of iron oxidation within the M4 drillcore; biotite margins are variably replaced by iron oxides (ilmenite) in the upper parts of the drillcore, and biotite typically shows a yellow to brown pleochroism (Figure 4.5). In the lower parts of the drillcore biotite is variably replaced by chlorite (Wela, 2017). The pleochroism of biotite in the lower parts of the drillcore ranges from reddish brown to pale green to light brown (Figure 4.6). TIMA analysis has confirmed that the variable colour in biotite indicates variable Fe - Ti concentrations related to the chloritization process that also involves growth of neoblastic prehnite, titanite and ilmenite (see Section 4.3). The degree of oxidation varies in the upper part of the drillcore, for example, within the same sample (Figure 4.5A-B) biotite grains are yellow-brown and are marked by ilmenite rims and local ilmenite along kinks, whereas other grains appear completely opaque; however, rather than being opaque pseudomorphs after biotite, BSE shows that the texture involves only slightly more extensive replacement of the biotite by ilmenite (Figure 4.5C-D).

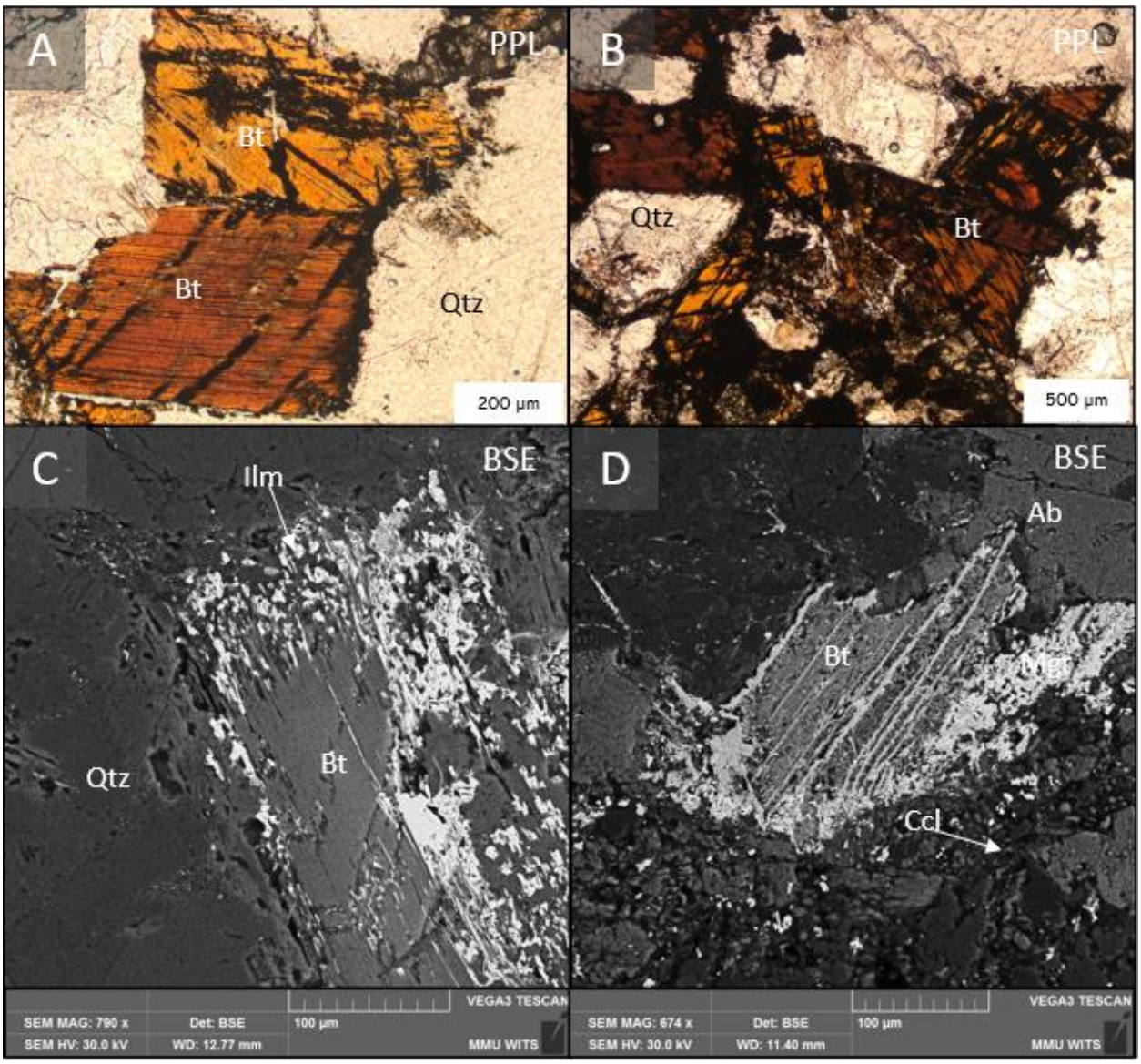


Figure 4.5. Plane-polarized light and BSE photomicrographs of partially oxidized biotite from the upper section of the M4 drillcore. A, B) Thin section of a monzonite sample M4 GG1.1 (129 m) showing colour variation in biotite and variable amounts of replacement by ilmenite along kink bands and around the grain edge. C) BSE image of sample M4 V1 (~114.5 m) showing neoblastic ilmenite aggregates around the edges and along the biotite cleavage. D) Metadolerite sample (M4 Sill-1) from mid-drillcore (262 m), showing oxides around the edges and along the cleavage of biotite. PPL = plane polarised light; BSE = backscattered electron; Bt = biotite; Qtz = quartz; Ilm = ilmenite; Ab = albite; Ccl = cataclasite.

In relation to shock metamorphism, biotite is less studied, and kinks in biotite have been noted as an indicator of shock metamorphism (see discussion in Wela, 2017; Gibson et al., 2024b). Preferential location of ilmenite and titanite along the kinks could indicate that the kinks formed during the impact and that the alteration must also be impact-related (Figure 4.6; EDS data in

Appendix 1.1). The apparent increase in Ca-bearing minerals (prehnite, titanite) in the biotite alteration assemblages with increasing depth, supports an increase in Ca-metasomatism in the deeper levels of the drillcore. This is discussed more fully by Masiu (2025, unpublished dissertation)

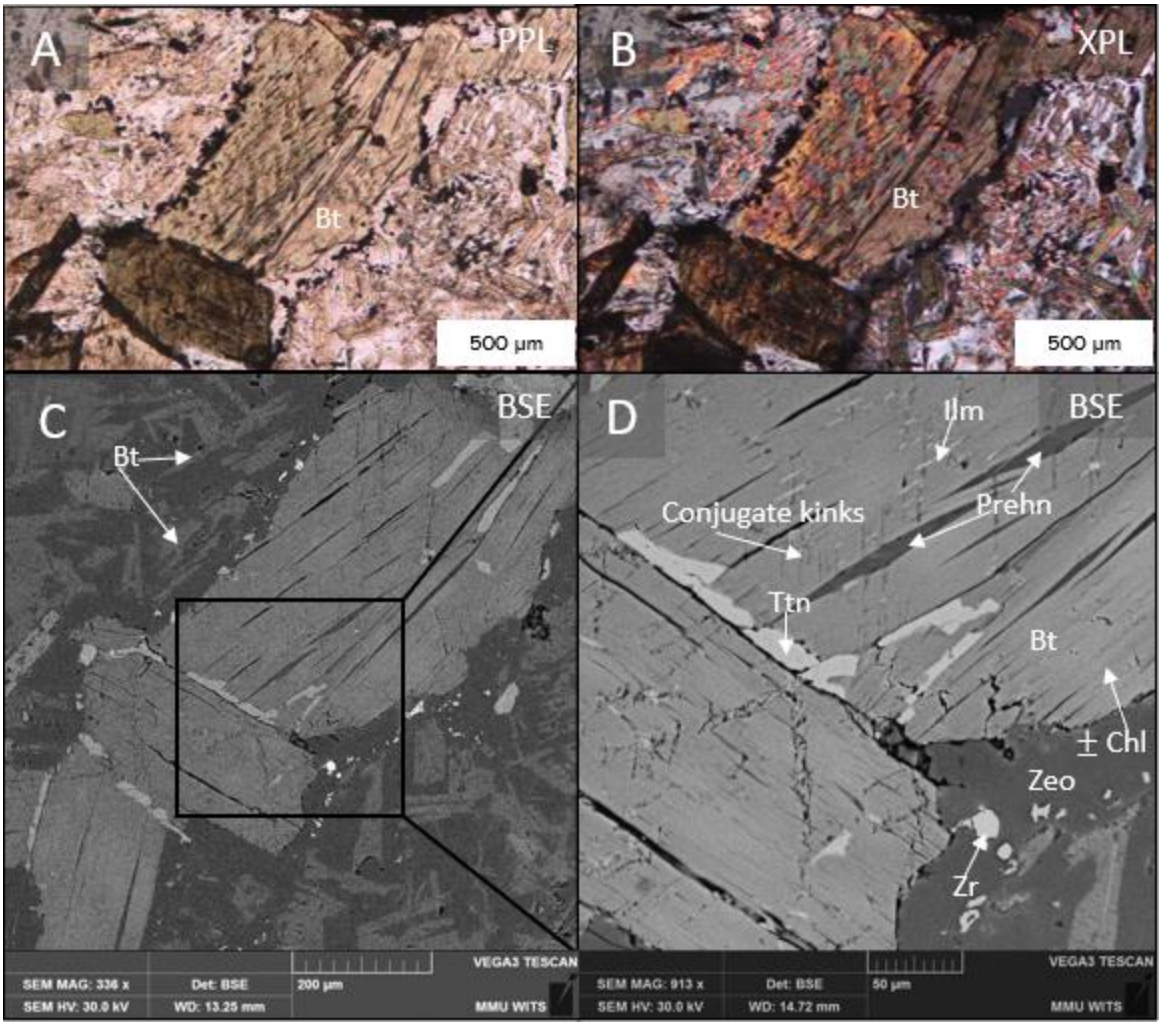


Figure 4.6. Kinked biotite replaced by secondary minerals in sample M4 R8 (348.4 m). A-B) Strongly pleochroic biotite rimmed by zeolite and Ti-oxides (white rim with black neoblasts in (A)) in monzonitic gneiss; PPL- XPL. C-D) BSE images of A-B showing titanite, prehnite and ilmenite replacing the biotite, which locally shows conjugate kink bands. The zeolite rim contains neoblastic titanite and a single zircon grain. The black box in C extrapolates to image D. Light grey laths in C are igneous biotite inclusions in plagioclase (Gibson et al., 2022). PPL = plane polarised light; XPL = crossed polarised light; BSE = backscattered electron; Bt = biotite; Ttn = titanite; Prehn = prehnite; Ilm = ilmenite; Zeo = zeolite; Chl = chlorite; Zr = zircon.

4.2.4. Epidote

Epidote in the granitoid gneisses is typically strongly fractured, and is strung out as brecciated masses in the cataclasite (Figure 4.7A-B); however, no definitive shock deformation features have yet been reported from this mineral in the M4 drillcore. Figure 4.7C-D display in situ fractured and brecciated epidote. The fractured and brecciated grains typically show enhanced alteration to smectite and magnetite that surrounds fragments and occurs along microcracks (Figure 4.7).

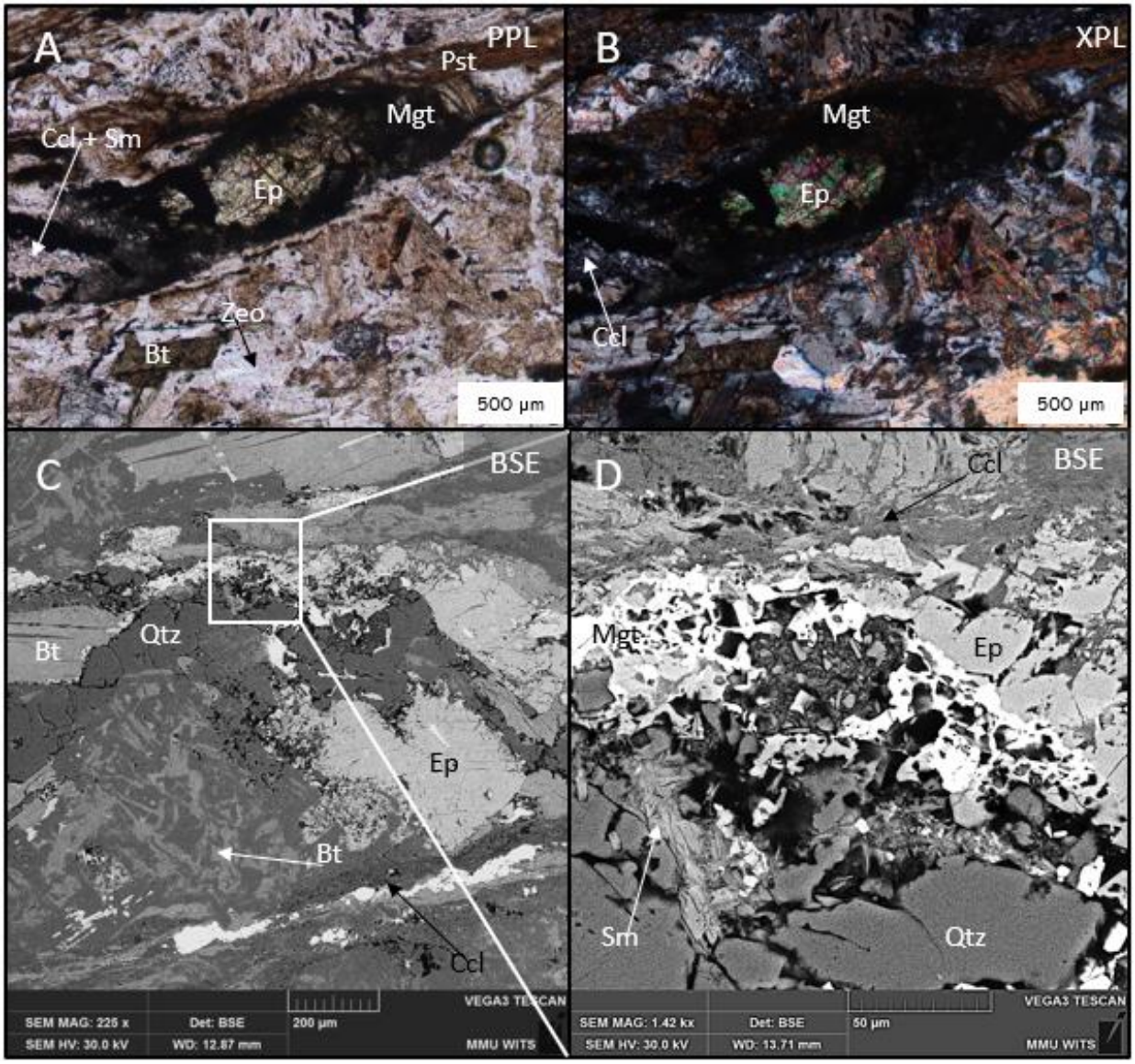


Figure 4.7. Primary epidote grains from sample M4 R8 (348.4 m). A) PPL image of Brecciated and fractured epidote string along the cataclasite displaying magnetite and smectite along the rims. B) XPL

image of A. C) BSE image of smectite and magnetite alteration of epidote and biotite within the host rock and cataclasite. D) Close-up of C shows magnetite texture and smectite between brecciated grains. PPL = plane polarised light; XPL = crossed polarised light; BSE = backscattered electron; Pst = pseudotachylite; Ep = epidote; Bt = biotite; Zeo = zeolite; Ccl = cataclasite; Sm = smectite; Mgt = magnetite; Qtz = quartz.

4.3. POST-IMPACT HYDROTHERMAL ALTERATION IN BRITTLE STRUCTURES

Drillcore samples show a complex set of anastomosing to conjugate shear faults displaying cm- to dm-scale spacing (Gibson et al., 2019, 2024a) that range from discrete planes < 1 mm wide, to mm- to cm-wide cataclasite zones (Figure 4.8). The cataclasite-bearing faults are reverse-slip, and show a moderate to steep dip angle (Figure 4.8A-B; 30 – 60℃ dip, Gibson et al., 2019). On a small scale, the displacements form a network of microfractures locally distributed within the rock units and filled by alteration products from neighbouring minerals, commonly smectite, zeolite and haematite (Figure 4.8).

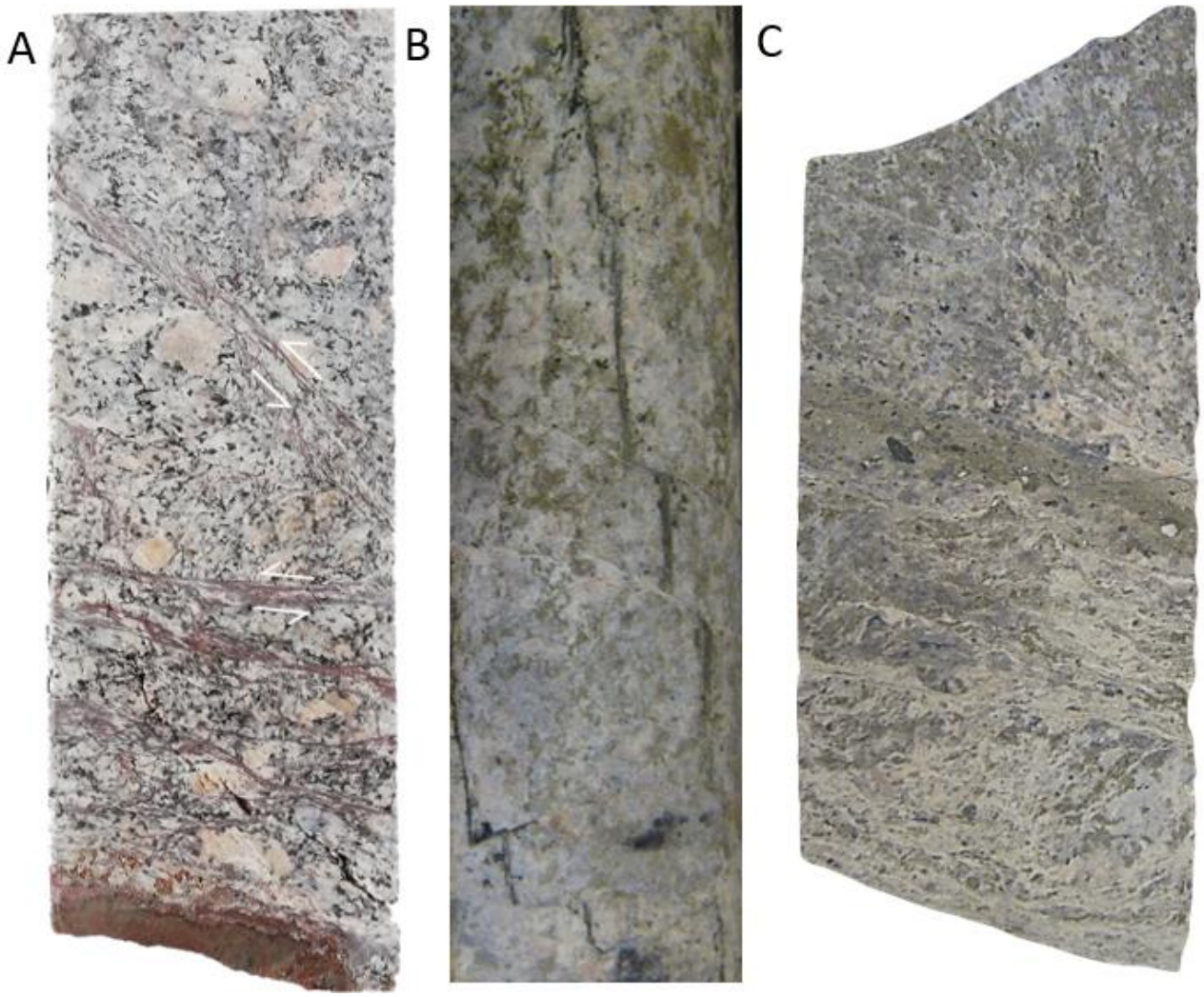


Figure 4.8. Hand specimens showing shear faults within target rocks of the M4 drillcore. A) Shear fault network showing reverse slip and monoclinic-sigmoidal internal fabric of cataclasites *(131.0 m; Gibson et al., 2024a) in a granitoid gneiss. B) Shear fault network defined by white zeolite and clay cutting and displacing a vertical magnetite ± haematite fracture in a granitic gneiss (272.73 m). C) Cataclasites and zeolite-smectite-filled fractures in granodioritic gneiss (347,4 – 354,38 m), hosting a thin suevitic dyke containing mineral and dark melt clasts. Drillcore width is 4.5 cm.*

The shear faults merge into cataclasites. The cataclasites are usually most intensely developed near suevitic breccias and show a gradational relationship with them (Figure 4.8C). The faults cut and displace quartz grains with PDFs, and the cataclasites contain shocked mineral fragments (Figure 4.9), indicating the shear faults postdated the shock event; however, they are regarded as impact-related because (a) Wela (2017) and Gibson et al. (2024a) showed from macroscopic and petrographic observations that the pseudotachylite and suevite dykes are genetically linked to the

cataclasite faults, and (b) the post-impact hydrothermal assemblages have clearly exploited and overprinted them (Section 4.3.1).

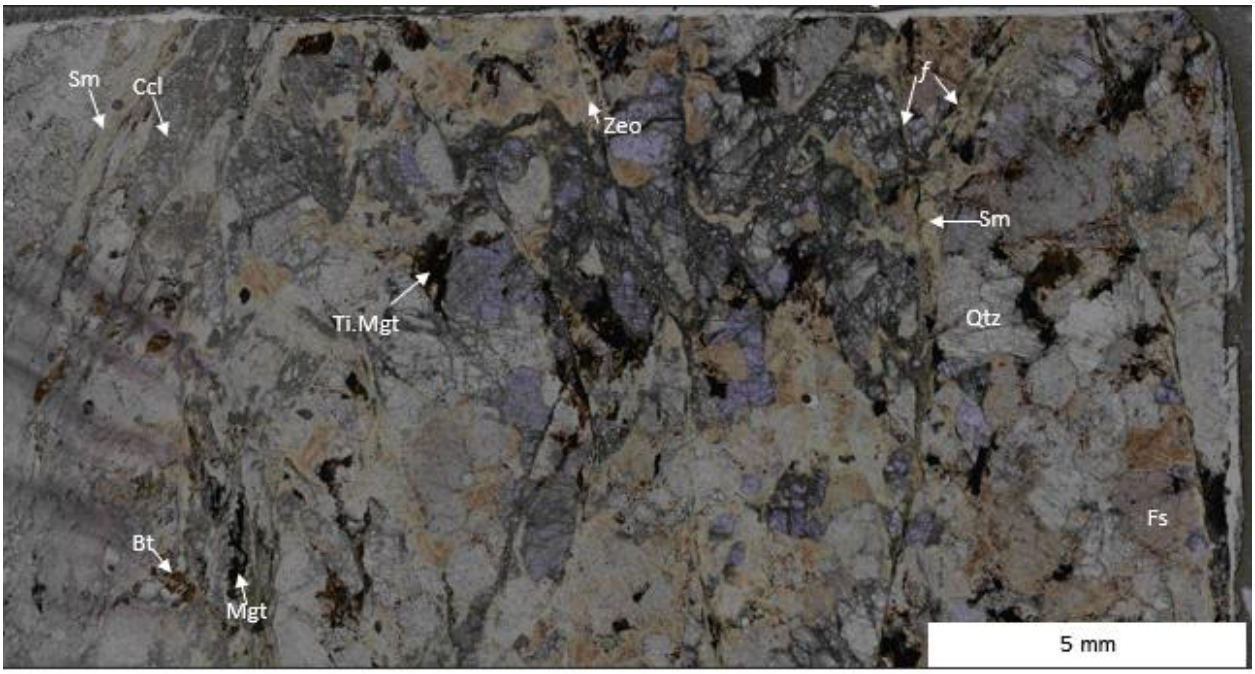


Figure 4.9. Microphotograph showing shear fault / cataclasite network in granitic gneiss (299.76 m; partial crossed-polars). The cataclasites extend within the quartz and feldspar grains. The sample is dominated by feldspar and quartz and contains interstitial biotite and titanomagnetite. The quartz grains are highly fractured and form an approximately in situ breccia (centre), whereas feldspar is typically altered to microcrystalline clay aggregates, both in situ and in cataclasite (left). Fe-oxides are typically smeared along the faults. Bt = biotite; Zeo = zeolite; Ccl = cataclasite; Sm = smectite; Ti. Mgt = titanomagnetite; Qtz = quartz; Fs = feldspar; f = fault.

Microscopically, complex structural relationships are found between the shear faults and pseudotachylite dykes and lenses. Figure 4.10 shows a thin dyke cut by a fault with a small normal slip displacement. The faults are locally associated with vugs that contain neoblastic high-temperature hydrothermal minerals such as andradite and diopsidic clinopyroxene cemented by zeolite (Figure 4.10C; Masiu, 2025, unpublished dissertation).

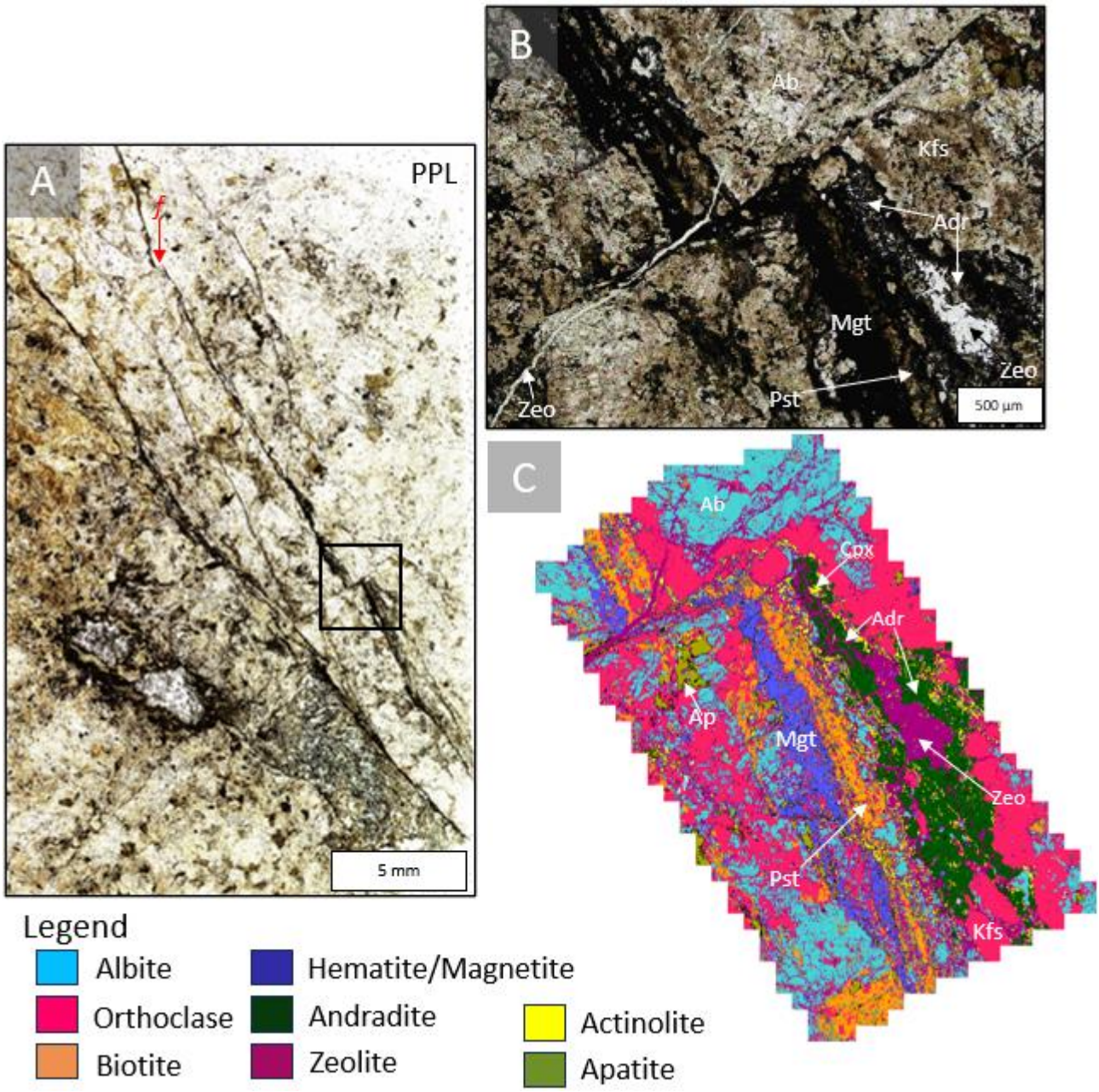


Figure 4.10. Photomicrograph of granitic gneiss sample M4 R12 (264 m). (A) Overview in plane polarised light (B) Closeup of box in A in plane polarised light, showing ~1 mm wide, steeply oriented shear fault defined by thin magnetite-dominated fractures and vugs characterised by neoblastic andradite and zeolite. The magnetite-pseudotachylite fractures are cut by a shallowly dipping shear fault with normal displacement, and by zeolite veins. C) TIMA phase map of B. For elemental distribution maps of this texture in Appendix 1.2A-B. PPL = plane polarised light; Ab = albite; Kfs = alkali feldspar; Adr = andradite; Mgt = magnetite; Zeo = zeolite; Ap = apatite; Cpx = clinopyroxene; Pst = pseudotachylite.

4.3.1. Impact-generated breccias

Petrographically, the suevite is made up of angular lithic and felsic fragments set in a matrix of medium- to coarse-grained low-temperature hydrothermal zeolite with finer-grained smectite, and aggregates and individual grains of neoblastic magnetite. Suevite and cataclasite contain up to 40 – 60% zeolite + smectite, indicating high initial porosity (Figure 4.11A-B). However, cataclasite is more fine-grained than suevites (Figure 4.11C). Evidence of resorption of clasts (rounding, scalloped margins) indicates porosity may have been partially enhanced by the reaction between the hydrothermal fluid and the clasts (Figure 4.11). In contrast to magnetite clasts that show ilmenite exsolution textures, magnetite displays a porous internal structure (Figure 4.11D). The magnetite neoblasts are restricted within the suevite matrix and absent in cataclasites.

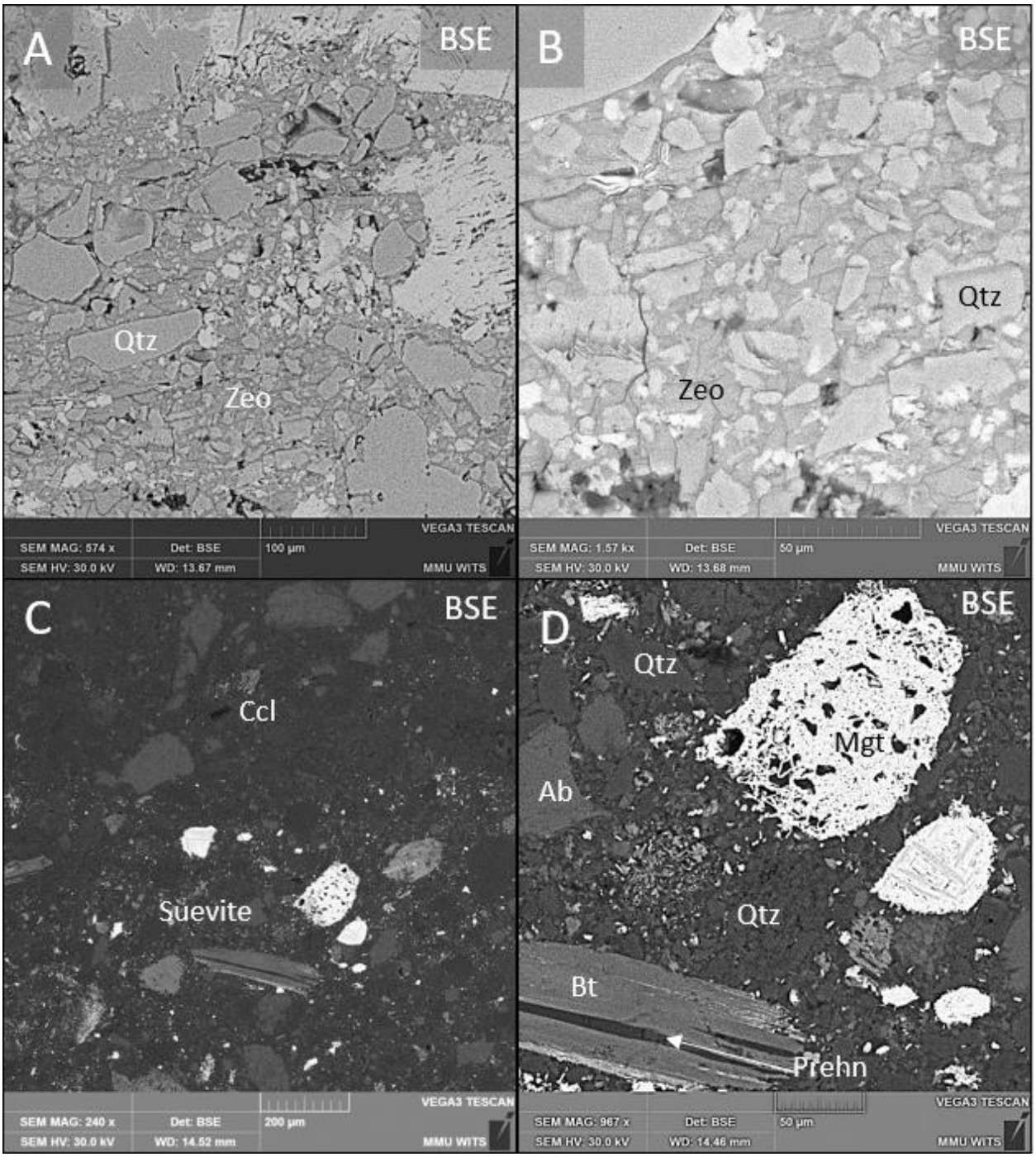


Figure 4.11. BSE scans showing post-impact hydrothermal alteration in impactite rocks. A) Sample M4 GG15 (324 m) showing zeolite cement in suevite matrix. B) Close-up of A showing the matrix-supported nature of the suevite. C) Sample M4 IM9 (299 m) showing a lithological contact between suevite and cataclasite. D) Close-up of the suevite matrix in C, showing alteration in biotite and magnetite. BSE = backscattered electron; Zeo = zeolite; Qtz = quartz; Ccl = cataclasite; Ab = albite; Bt = biotite; Mgt = magnetite; Prehn = prehnite.

Pseudotachylite and glass fragments in the suevites are comprehensively replaced by smectite with limited amounts of zeolite ± calcite (Section 4.4.2; Masiu, 2025, unpublished dissertation). Smectite is also found around clasts and lining pore spaces in cataclasites and suevites, as well as in veins and vugs (Figure 4.12). Four samples from deeper parts (> 262 m) of the drillcore were analysed by XRD (two shown in Figure 4.12C-D), with the assumption that deeper parts are likely to have experienced less overprinting by fluids in the near-surface environment during subsequent exhumation and burial beneath the Kalahari Group. X-ray diffraction and SEM-EDS analyses indicate that the dominant clay mineral type in the M4 drillcore samples is a mixed-layer smectite with minor illite (Figure 4.12; Appendix 1.3A; see also Wela, 2017). Wela (2017) and Masiu (2025; unpublished dissertation) obtained mixed results owing to bulk-powder XRD analysis (Wela, 2017) and defocussed EPMA (both) that were unable to fully discriminate individual crystals. Following clay mineral separation in this study, the XRD 001 peak position indicates the presence of mixed-layer illite-smectite (I-S) due to the expansion of peaks after ethylene glycol treatment of the samples (Appendix 1.3B).

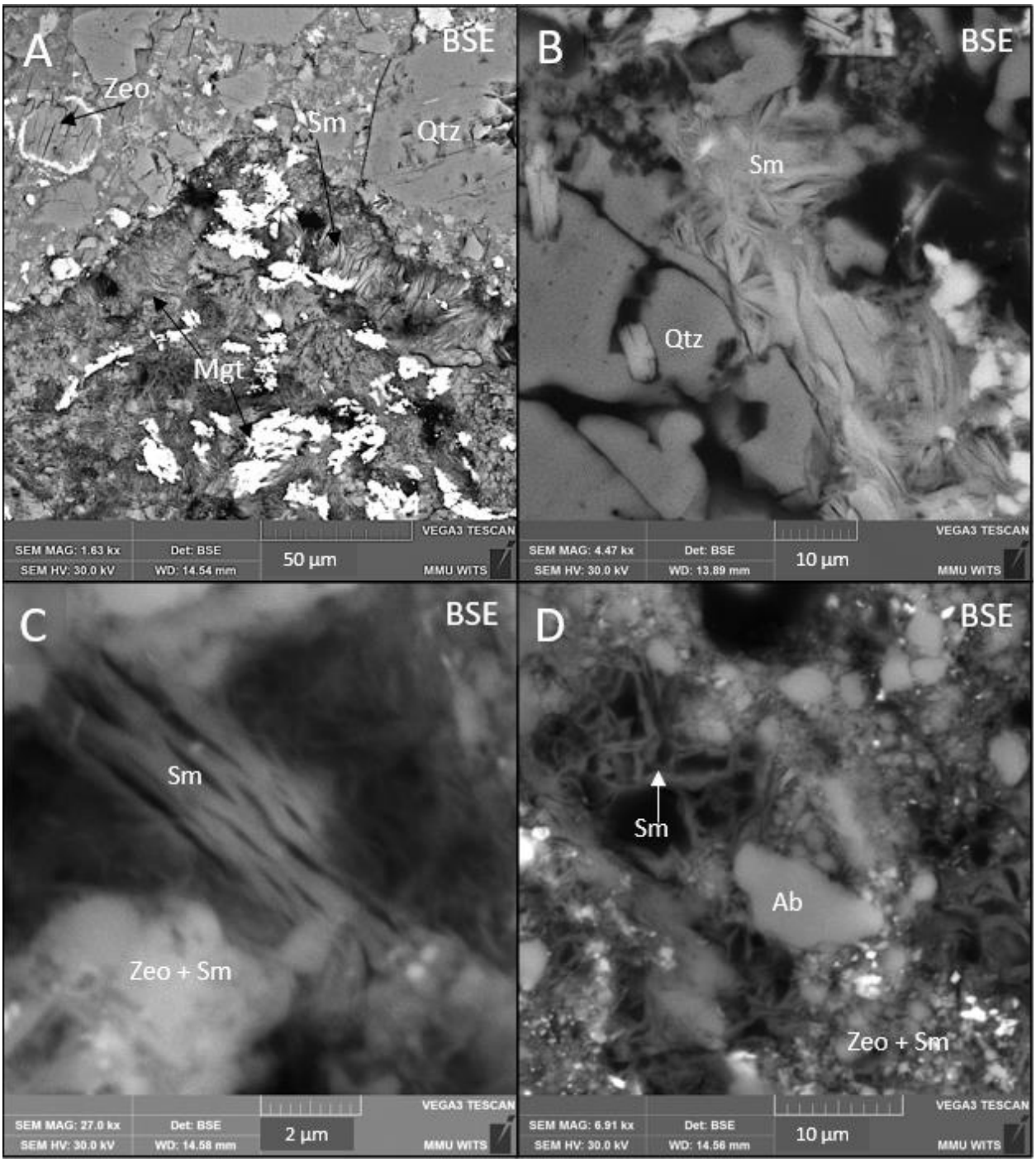


Figure 4.12. BSE microphotographs showing smectite minerals within the M4 drillcore. A) Sample M4 SB3 (353 m) showing smectite, zeolite and magnetite in brecciated suevite. *B) Sample M4 R8 (348.4 m) showing smectite in brecciated quartz in cataclasite. C) Sample M4 RG2 (262 m) shows flaky smectite morphology within suevite matrix. D)* Sample M4 RG3 (301 m) shows f*ibrous smectite within a pseudotachylite matrix.* The *matrix is a mix of zeolites and smectites (Wela, 2017). BSE = backscattered electron; Zeo = zeolite; Sm = smectite; Qtz = quartz; Bt = biotite; Mgt = magnetite; Ab = albite.*

The samples show a minimal shift following ethylene glycolation, suggesting very little illite content of < 5 %; 1) sample M4 RG1 shows minimal shifts in the 001 peak from 14.74 – 14.95 Å to 16.72 – 16.92 Å, 2) sample M4 RG2 shows shifts of peaks in the 001 peak from 15.01 – 15.06 Å to 16.79 – 17.38 Å, and 3) sample M4 IM9 show shifts in the 001 peak from 14.82 – 15.01 Å to 16.66 Å. Sample M4 RG3 shows the same 16.66 peak following ethylene glycolation, indicating pure smectite. The powder XRD patterns also revealed the presence of other smectites, such as pyrophyllite, which has peaks around ~9.15 Å and 4.06 Å, and possibly altered biotite or Fe-rich illite at ~10 Å and non-clay minerals, such as oligoclase (inherited from the host rock) in all samples and calcite in sample M4 RG1 (Appendix 1.3A).

4.4. POST-IMPACT HYDROTHERMAL VEINS

The M4 drillcore contains a variety of post-impact veins dominated by zeolite, calcite or anhydrite that show cross-cutting relationships with the impact-related cataclasites, suevites and pseudotachylite breccias. This section focuses on these post-impact hydrothermal veins.

4.4.1. Macroscopic observations

The post-impact veins within the M4 drillcore are identified by their crosscutting relationships with the impactites and melt clasts within the suevites (Wela, 2017; Figure 4.12 and Figure 4.13). The absence of shock deformation within mineral structure confirms post-impact timing (Wela, 2017). There are sub-horizontal and inclined-to-vertical hydrothermal veins. Overall frequency and width of the veins decrease with depth, and the wider veins are predominantly sub-horizontal (Figure 4.13; the pre-impact quartz veins in the bottom drillcore should not be misinterpreted as part of the hydrothermal assemblage) and more abundant in the upper parts of the drillcore. The deeper levels are pervaded by inclined-to-vertical veins, usually zeolite-filled networks (Figure 4.13). Veins cut the fault zones identified at depth intervals of 140 – 160 m and 260 – 300 m (Gibson et al., 2019), and shear faults close to the fault zones contain fine-grained zeolite and smectite.



Figure 4.13. Drillcore images show changes in frequency and orientation of veins within the M4 drillcore. The top drillcore box shows monzonitic gneiss (110.08 – 119.39 m depth) displaying subhorizontal calcite veins. The bottom drillcore box shows metadolerite (194.46 – 202.6 m depth) and suevite displaying subvertical veins of zeolite veins (annotated with arrows) and pre-impact quartz veins. The drillcore width is 4.5 cm.

Most of the post-impact hydrothermal veins appear monomineralic in hand specimen and are dominated by either zeolite, anhydrite or calcite (Figure 4.14). These veins range from ≪ 1 mm to 15 mm in width; they form networks (zeolite) to discrete veins (Figure 4.14B). Anastomosing networks of shear faults (Gibson et al., 2024a) that are locally associated with mm-scale vugs are dominated by creamy white zeolite fill. This fracture-fill network is dispersed throughout the drillcore, cutting across all lithologies and structural features. These veins are subvertical to steeply dipping, with sharp, well-defined contacts against wallrock granitoid gneisses, dolerites, and pseudotachylites. However, thin section petrography shows that zeolite veins locally also contain calcite, anhydrite, clinopyroxene, smectite, titanite and various iron oxides and hydrates (magnetite, haematite, goethite; see Section 4.4.2 and Masiu, 2025, unpublished dissertation).

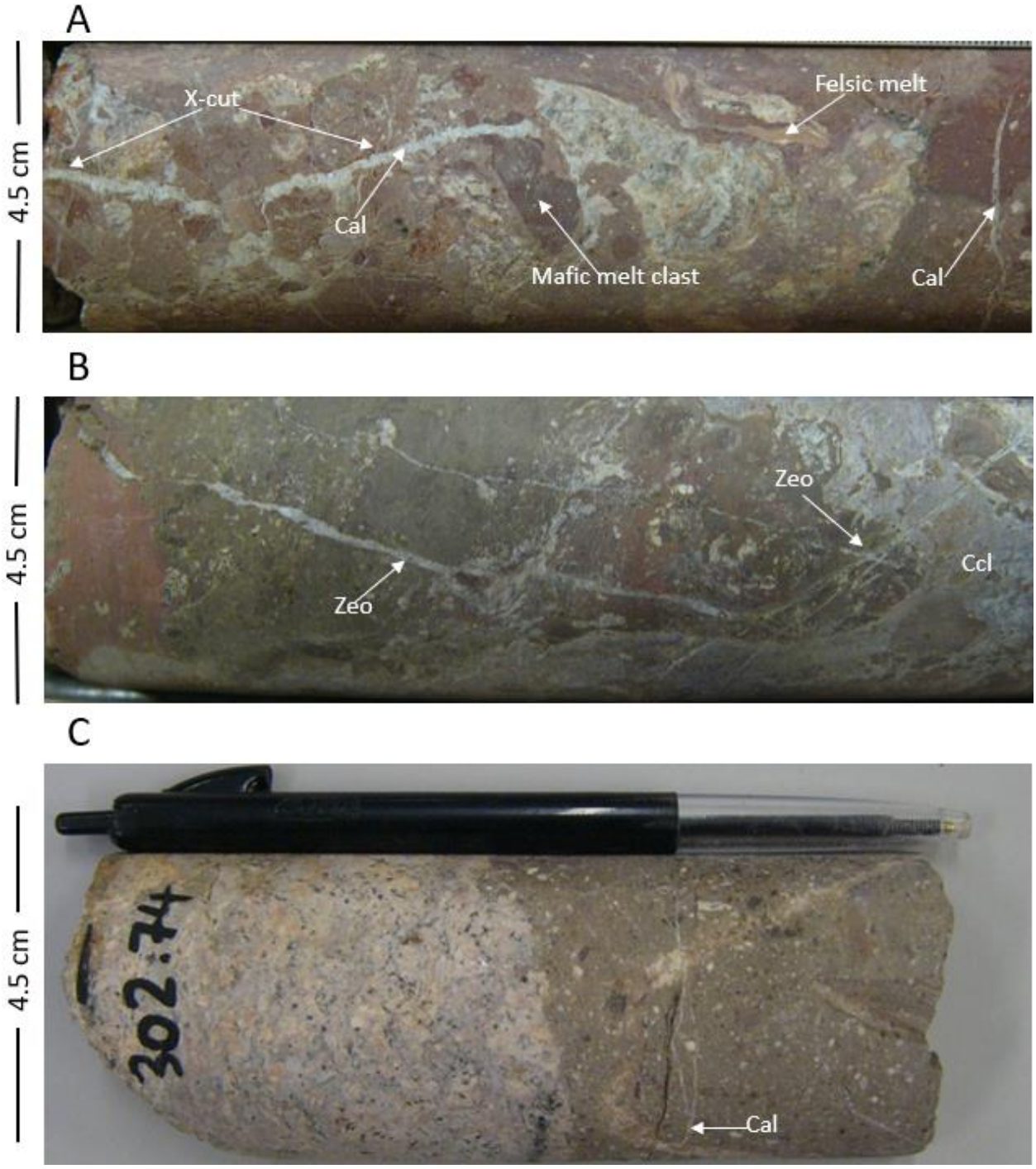


Figure 4.14. Macroscopic evidence of post-impact vein in the M4 drillcore. A) Suevite within the upper fault zone at a depth of 146.05 m. The calcite vein exhibits both vertical and sub-horizontal orientations and crosscuts mafic melt clasts and lithic fragments. B) Metadolerite containing cataclasite and pseudotachylite cut by zeolite veins within the lower fault zone at depth of 292 m. C) Contact between granitic gneiss and grey suevite, showing zeolite and calcite veins in the suevite matrix at a depth of 302.74 m. The drillcore width is 4.5 cm. Zeo = zeolite; Cal = calcite; x-cut = crosscut; Ccl = cataclasites.

Anhydrite veins are observed at 180 m depth to the bottom of the drillcore. They are white, moderately steeply to vertically dipping and range from < 0.1 to 2 mm in width (Figure 4.15A). They can be distinguished from the zeolite and calcite veins by their greater hardness. The calcite veins in the upper part of the drillcore are shallowly-dipping to sub-horizontal (103.00 – 136.25 m), with a few that steeply dip at 143 m depth. The spacing of the veins in drillcore boxes 1 to 4 (103 to 136 m) ranges from 1 to 10 mm (Figure 4.15B). The thickness of calcite veins ranges from 0.6 to 7 mm. Their morphology ranges from planar to undulating-anastomosing and locally they consist of linked en echelon segments that isolate lenses and fragments of the wallrock.

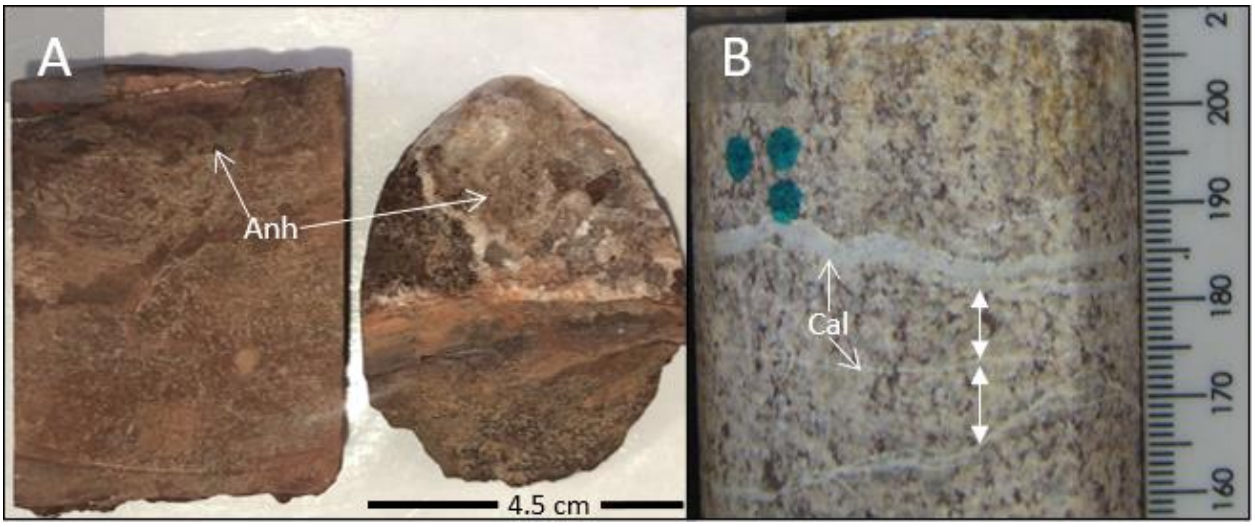


Figure 4.15. Macroscopic evidence of monomineralic veins in the M4 drillcore. A) Metadolerite sample M4 ML (195.30 m) showing white anhydrite vein. B) Granodioritic gneiss from Box 2 (110.08 – 119.39 m) showing irregular to anastomosing subhorizontal calcite veins. Anh = anhydrite; Cal = calcite.

4.4.2. Microscopic observations

4.4.2.1. Cross-cutting relations

The zeolite veins are crosscut by fine-grained calcite veins (Figure 4.16A) and possibly cut by vugs filled with calcite, clay, and zeolite (Figure 4.16B-C). Local evidence of metasomatic alteration of feldspar along zeolite vein margins and changes in minor mineralogy along single zeolite veins intersect different compositions of wallrock (e.g., granitoid gneiss vs pseudotachylite; see Section 4.4.2.3). In contrast, calcite-dominated veins have sharp contacts and cut through minerals like biotite, quartz, titanite, feldspars and magnetite with no evidence of wall rock

interaction (Figure 4.16D-G). Zeolite rims around biotite that are associated with Ca-metasomatic alteration of the biotite (prehnite, titanite) that occurs with chlorite + ilmenite replacement contrast with the calcite veins that postdate chlorite and ilmenite alteration within biotite (Figure 4.16D-F). Anhydrite shows no macroscopic evidence of crosscutting relations within the drillcore. However, angular anhydrite clasts in a zeolite vein (Figure 4.23) in sample M4 ML suggest that they predate at least some of the zeolite veining. Based on crosscutting relationships, the veins thus appear to have formed at different times during post-impact hydrothermal activity. Several relationships prove that calcite veins within stratigraphically uppermost sections are the last phase to crystallize within the M4 drillcore, and that anhydrite veins preceded some or all of the zeolite veining.

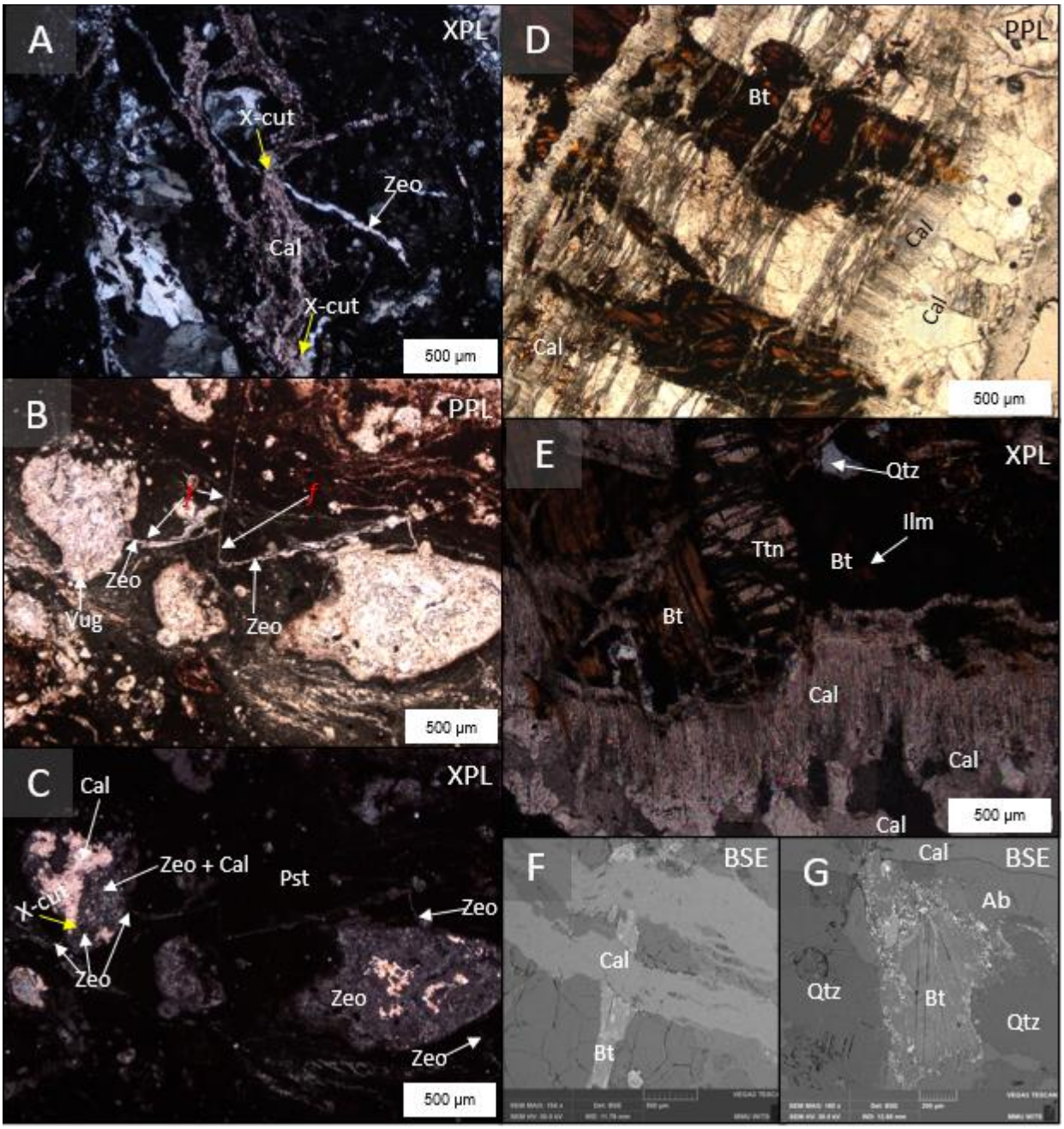


Figure 4.16. Photomicrographs showing crosscutting relationships of calcite veins with other minerals. A) calcite veins crosscutting zeolite veins from M4 V3 (142.95 m). Cross polarised light. B) Calcite-smectite--zeolite vugs in M4 RG1 (146 m), crosscutting zeolite veins, in plane polarised light. C) Cross polarised light image of B. D) Stretched to syntaxial elongate blocky calcite vein in sample M4 GG1.1 (129 m), crosscutting altered biotite, in plane polarised light. E) Sample M4 GG1.1 shows Stretched to syntaxial elongate blocky calcite cutting through biotite, titanite, and quartz. F) BSE scan of sample M4 V1 (114 m) showing calcite vein cutting through partially altered biotite. G) Sample M4 V1 shows a sharp contact between calcite veins and granodioritic gneiss containing partially altered biotite. No obvious enhanced alteration occurs along the vein edge. PPL = plane polarised light; XPL = crossed polarised light; BSE = backscattered electron; Zeo = zeolite; Cal = calcite; Bt = biotite; Ttn = titanite; Ilm = ilmenite; Qtz = quartz; f = fault; Pst = pseudotachylite.

4.4.2.2. Anhydrite veins

Anhydrite veins occur mostly in the pseudotachylite and metadolerite rocks. Microscopically, they exhibit a subidioblastic granular texture, with a lack of well-defined cleavage (Figure 4.17). The anhydrite vein contains minor inclusions that are less Ca-rich than the vein (Figure 4.17C-D).

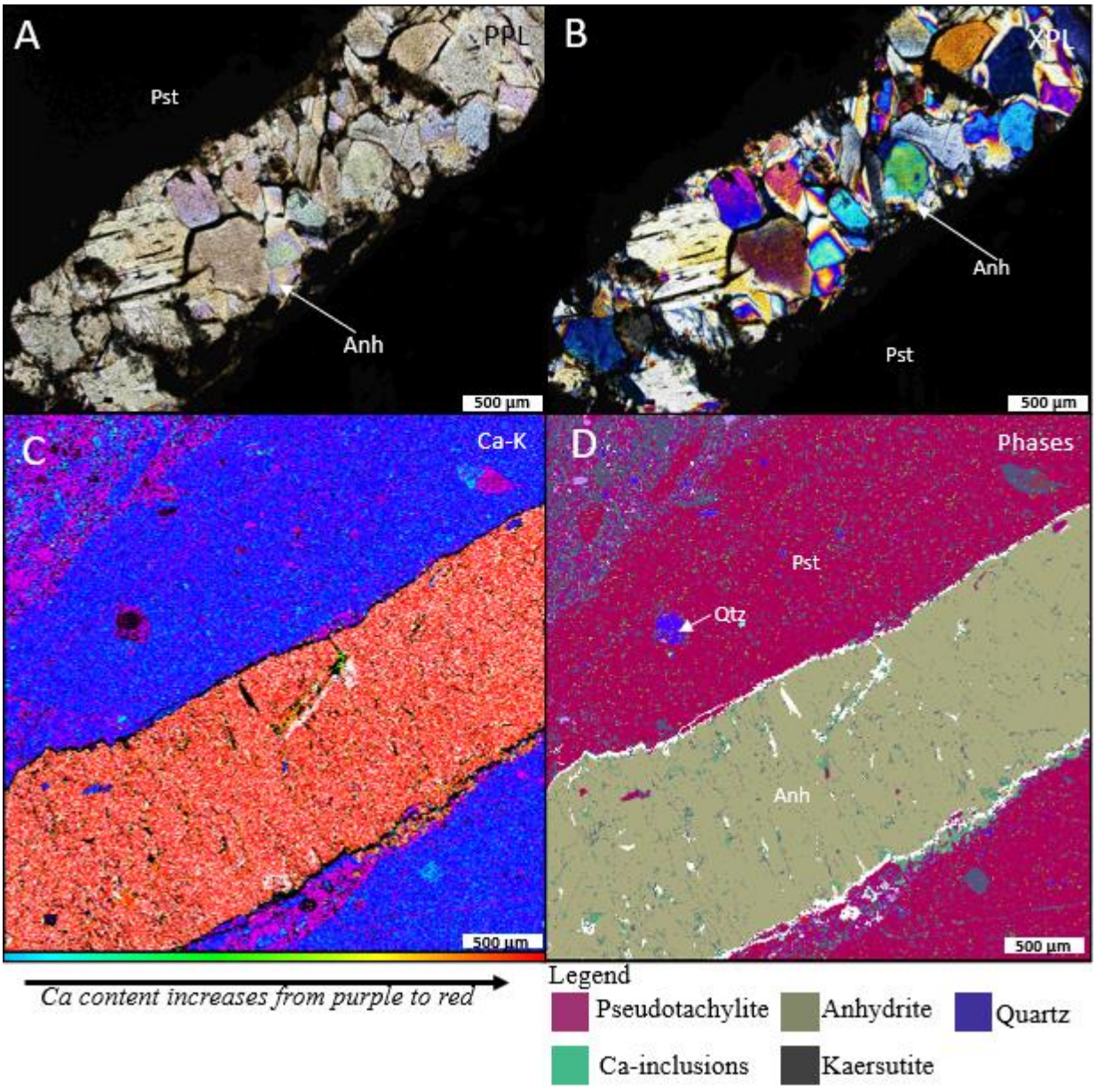


Figure 4.17. Photomicrographs of sample M4 ML (195.30 m) showing anhydrite vein cutting across pseudotachylite. A) Plane polarised light image showing subidioblastic granoblastic grains. B) Cross-polarised light of A. C) Calcium elemental map showing Ca enrichment localized within anhydrite vein. D)

Phase map showing anhydrite vein with minor dolomite inclusions. PPL = plane polarised light; XPL = crossed polarised light. Pst = pseudotachylite; Anh = anhydrite; Qtz = quartz.

4.4.2.3. Zeolite veins

Zeolite veins cut through all lithologies with relatively sharp but locally irregular contacts; however, contacts are less distinct in suevites and cataclasites that contain zeolite cement. Mineralogically, thin zeolite veins << 1 mm wide can display monomineralic segments (only zeolite) that grade into polymineralic segments. Wider veins tend to be polymineralic, incorporating neoblastic phases, but are dominated by zeolite. Backscattered electron images reveal that the zeolite crystals are relatively coarse, even in thin veins, and show a single planar cleavage and sub-planar partings (Figure 4.19A-D). As a result of this complexity, the zeolite veins are subdivided into 5 types:

1. Zeolite + calcite: Exclusively zeolite + calcite veins occur in two main forms. In the first form, calcite is found locally throughout the drillcore as dendritic crystals replacing shock PDFs and PFs in quartz in a texture that is identical to the zeolite texture replacing these features (see Figure 4.1). In the second form, distinctive coarse zeolite-calcite veins occur in the upper part of the drillcore cutting suevite (see Section 4.4.2.4 under calcite veins). The vein is inclined and zoned, with relatively coarse calcite crystals at the edges of the vein and zeolite in the core. The crystal shape of calcite shows a subidioblastic/rounded edge facing towards the zeolite-fill (calcite Section 4.4.2.4). Calcite is also found in polymineralic zeolite veins involving Fe-Mg phases.

2. Zeolite + clinopyroxene + smectite + calcite + Fe-(hydr)oxide: This vein assemblage occurs in the upper parts of the drillcore in monzonitic gneisses between 139 m and 166 m, which corresponds to the upper fault zone identified by Gibson et al. (2024a). In samples such as GG-10 from 166 m depth, the veins form a highly irregular network that seemingly isolates wallrock fragments based on a 2D thin section view (Figure 4.1). Electron microprobe results point to zeolite within these samples having a complex chemistry varying between heulandite, chabazite and laumontite (Masic, 2025; unpublished MSc data). Ca-Heulandite is more abundant throughout, and laumontite occurs together in some vugs and veins with heulandite, but the chemistry changes to more Na-rich zeolite (Na-

Chabazite) down the drillcore. Neoblasts at vein edges are ~10 µm long (Figure 4.18D and Figure 4.21A) and are rimmed by radiating smectite aggregates (Figure 4.18D; Figure 4.20C; Figure 4.21A). The neoblasts show mineral chemistry of actinolite in Figure 4.18 and clinopyroxene in Figure 4.20 (Masiu, 2025, unpublished dissertation). The smectite surrounding the actinolite/clinopyroxene neoblasts and lining the vein walls appears dark brown-yellow in crossed polarized light and light brown in plane polarized light (Figure 4.18 and Figure 4.20). Skeletal iron oxides/iron hydrates (magnetite, haematite, goethite) display a complex morphology which could represent either a pseudomorph or possibly a residual texture from replacement of shock features in quartz (Figure 4.20B-C and Figure 4.22). Other secondary minerals within the zeolite vugs are calcite. Calcite within this assemblage is interstitial and forms idioblastic grains (Figure 4.18A-C, Figure 4.20C and Figure 4.21B). Patchy alkali metasomatism of albite adjacent to the zeolite vein and corroded shocked quartz clasts (Figure 4.20) supports these being relatively high-T hydrothermal veins. Apart from the limited K-metasomatism, Na, Mg and Ca elemental map (Figure 4.22) shows that the veins involved an ingress of Ca-Mg-rich fluid.

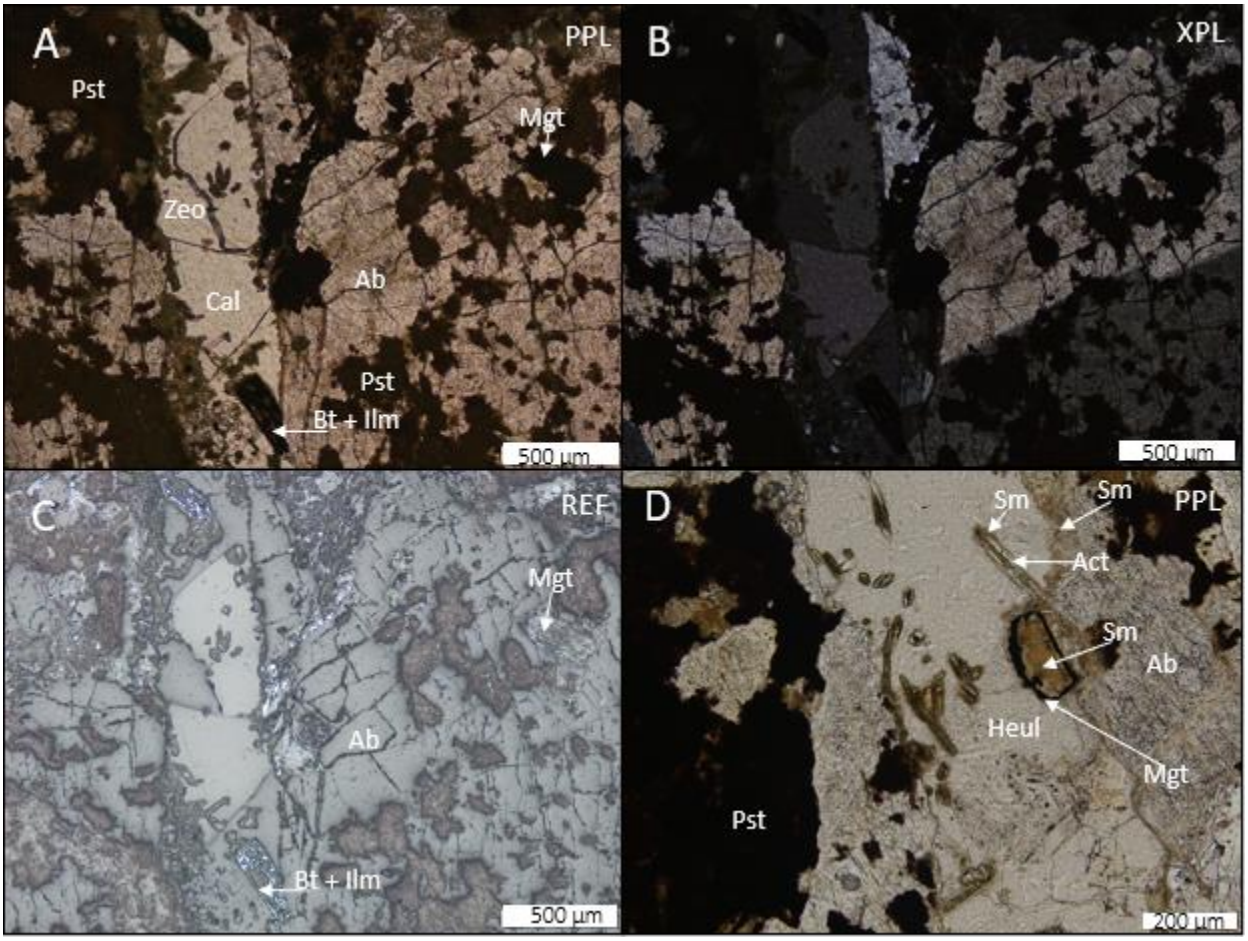


Figure 4.18. Photomicrographs of sample M4 R22 (139 m) showing relatively high-T assemblage of zeolite, clinopyroxene, smectite, calcite and Fe-(hydr)oxide in a vein matrix. A) Plane-polarized image showing the oxides are magnetite and ilmenite. The zeolite vein contains inclusions of calcite, actinolite, smectite, and biotite showing alteration to ilmenite. B) Crossed-polarized image of A. C) Reflected light of A-B. D) A close-up plane-polarized light image of inclusions within the zeolite veins. PPL = plane polarised light; XPL = crossed polarised light; REF = reflected light; Zeo = zeolite; Cal = calcite; Bt = biotite; Ilm = ilmenite; Ab = albite; Mgt = magnetite; Pst = pseudotachylite; Heul = heulandite; Sm = smectite; Act = actinolite.

3. Zeolite + haematite / Fe-hydroxides: Haematite and/or Fe-hydroxides such as goethite are found along fracture walls, vein walls, and vugs throughout the drillcore in both felsic and mafic rocks (Figure 4.19E-I). It is possible that the discrete fine-grained haematite "crystals" along vein walls represent oxidation of neoblastic clinopyroxene or amphibole rather than direct crystallization product from the fluid; however, BSE was unable to resolve this question.

4. Zeolite + titanite: In the suevite-pseudotachylite sample M4 RG2 (262 m depth), zeolite veins show inclusions of neoblastic, subidioblastic, titanite-apatite along the vein margins (Figure 4.19C-D; see EDS data in Appendix 1.4). These grains are also present replacing chloritized biotite within the matrix (Figure 4.6)

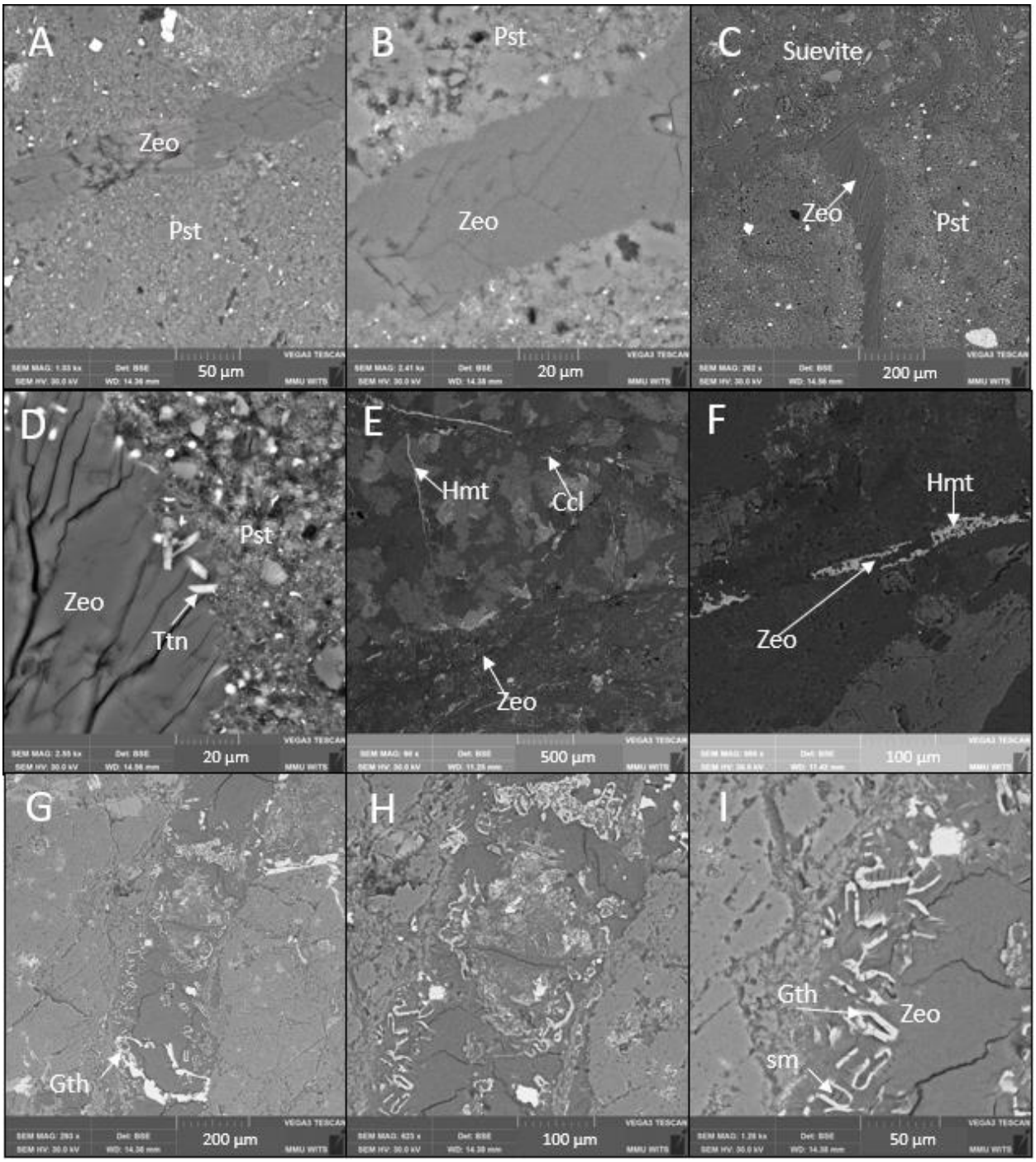


Figure 4.19. BSE images showing morphology and textures of zeolite veins across the M4 drillcore. A) Monomineralic zeolite vein in pseudotachylite from sample M4 IM9 (299 m). B) Close-up of A. C) Zeolite vein from M4 RG2 (262 m) through pseudotachylite matrix and merging in the suevite. D) Close-up of C showing titanite neoblasts along vein edge. E) Sample M4 Sill1 (261 m) showing zeolite veins with haematite rims. F) Close-up of E. G) Sample M4 GG10 (166 m) showing smectite and haematite/goethite pseudomorphs (possibly after clinopyroxene, see Figure 4.21) in zeolite veins. H-I) Close-up of G. BSE = backscattered electron; Zeo = zeolite; Pst = pseudotachylite; Ttn = titanite; Hmt = haematite; Ccl = cataclasites; Gth = goethite.

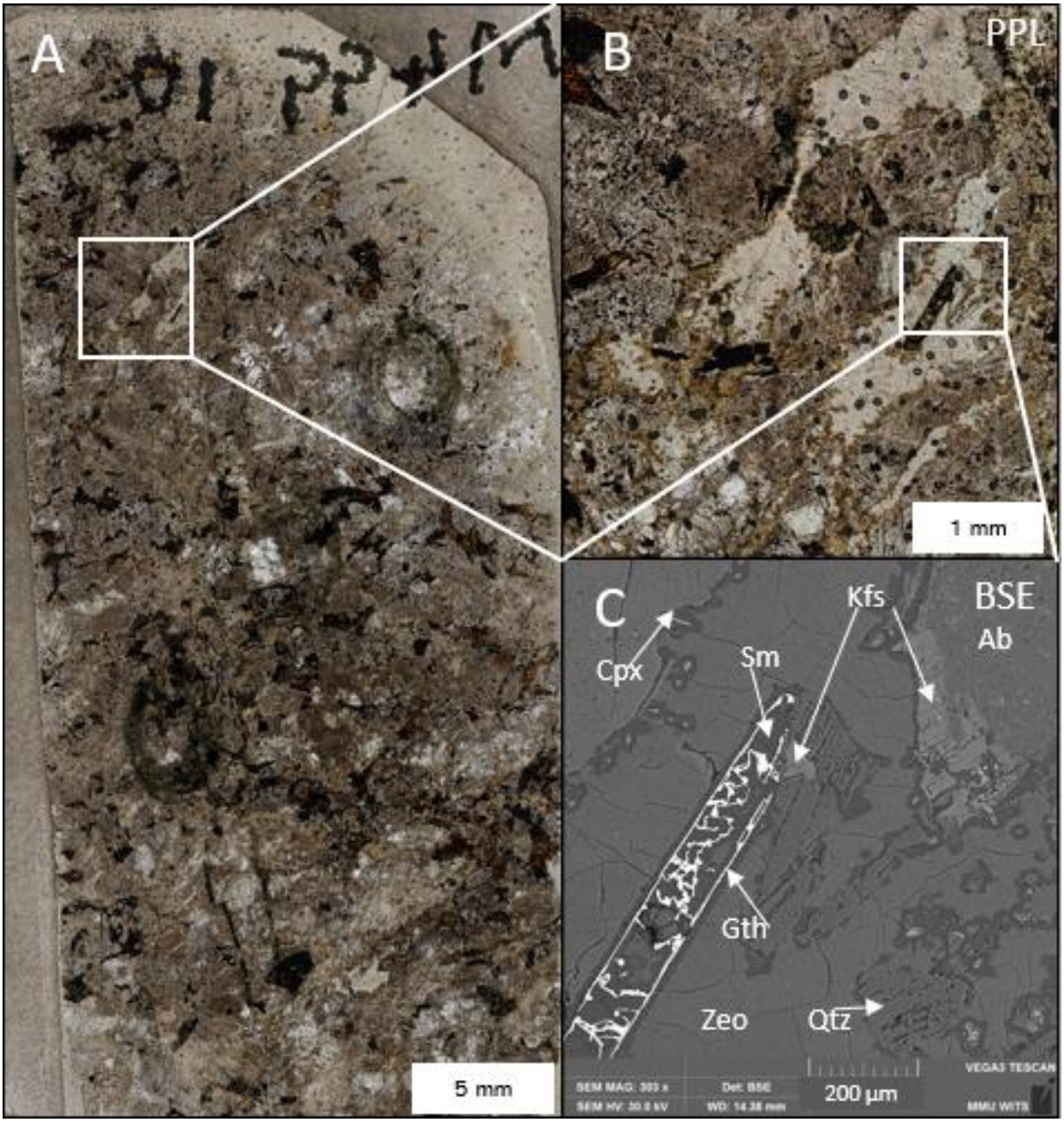


Figure 4.20. Microphotographs, and BSE image of sample M4 GG10 (166 m) showing highly irregular zeolite veins/vugs enclosing neoblastic clinopyroxene that is rimmed by smectite and skeletal haematite/ goethite also rimmed by smectite. A) Overview in plane-polarized light image showing monzonite sample. B) Close up image showing white cloudy heulandite with light brown inclusions at the margins. C) BSE image showing *K-feldspar metasomatic replacement of primary plagioclase in the wallrock and corroded quartz grains with zeolite replacing PDF lamellae* (*See also Fig. 4.2). PPL = plane polarised light; BSE = backscattered electron; Zeo = zeolite; Ab = albite; Kfs = alkali feldspar; Qtz= quartz; Cpx = clinopyroxene; Sm = smectite; Gth = goethite.*

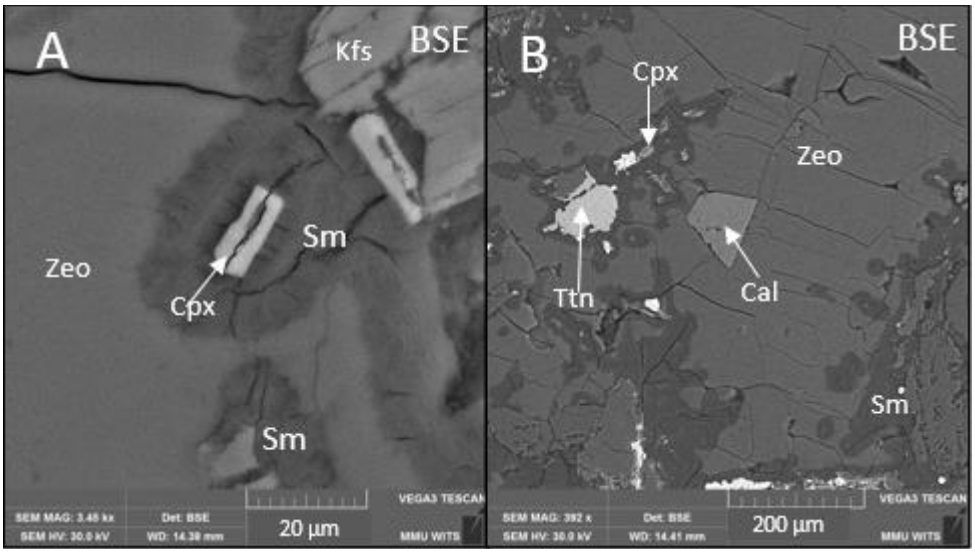


Figure 4.21. A) Close up BSE scans showing zeolite vein/vug in M4 GG10 (166 m) with clinopyroxene and smectite on the rims and alkali feldspar alteration. B) Close up BSE scan of zeolite vug showing titanite, calcite, clinopyroxene and smectite. BSE = backscattered electron; Zeo = zeolite; Cpx = clinopyroxene; Sm = smectite; Kfs = alkali feldspar; Ttn = titanite; Cal = calcite.

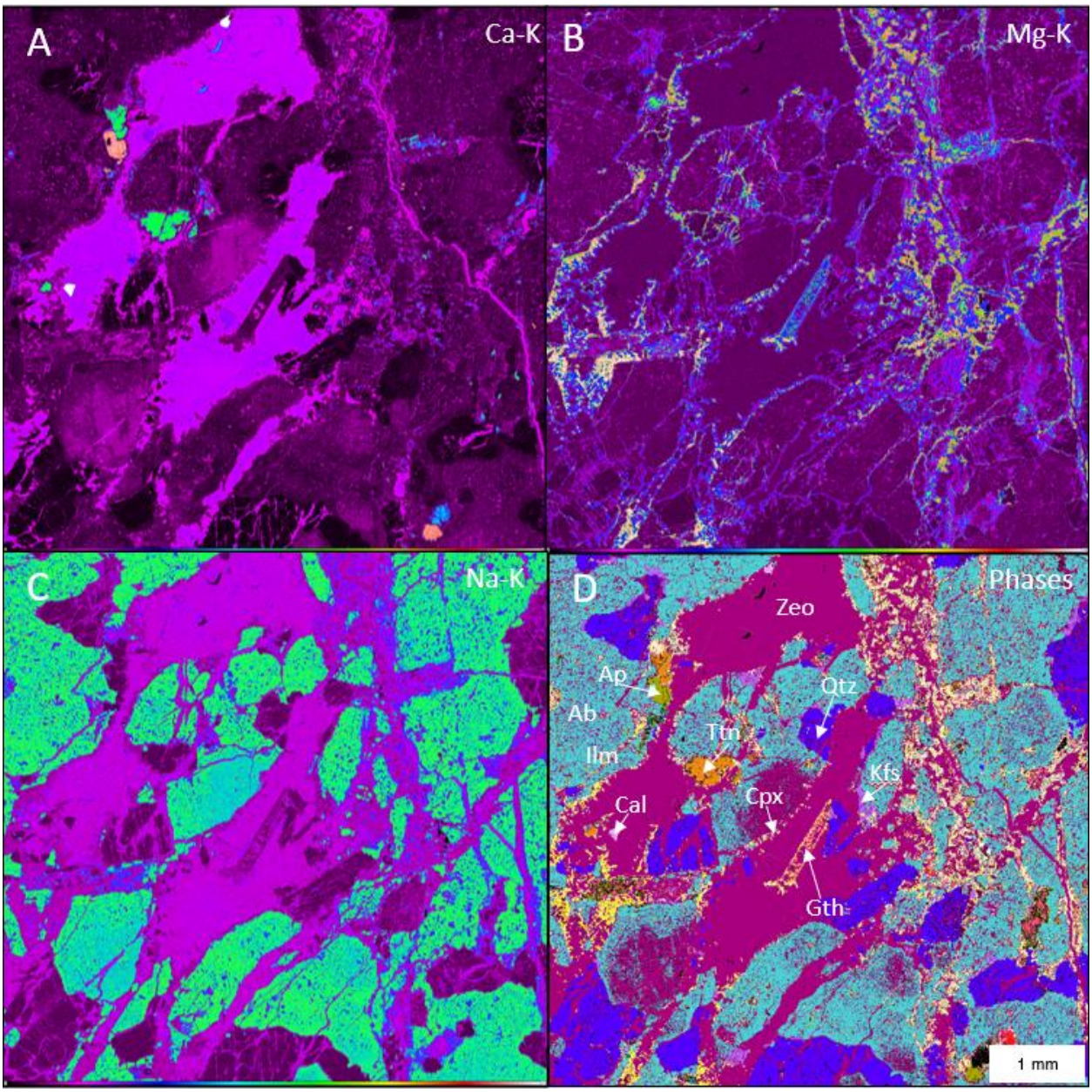


Figure 4.22. TIMA elemental maps and phase map of sample M4 GG10 (116 m) showing a steeply-inclined irregular zeolite vein network linked to a vertical fracture (left) that shows smectite + goethite > zeolite. A) Ca distribution abundant in apatite, titanite, and clinopyroxene crystals on the zeolite margins. B) Mg distribution abundant along the fractures and zeolite vugs. C) Na distribution depleted in the zeolite vugs and enriched in the matrix. D) Phase map showing albite and quartz cut by fractures and vugs filled with heulandite. For further details, see Figures 4.19 and 4.20. Elemental scale increases from dark purple (0%; left) to white (100%; right). Zeo = zeolite; Ab = albite, Qtz = quartz, Kfs = alkali feldspar; Ttn = titanite; Cal = calcite; Gth = goethite; Ap = apatite; Cpx = clinopyroxene; Ilm = ilmenite.

5. Zeolite + anhydrite: Figure 4.23 shows angular anhydrite crystals (grain size; < 200 µm) and clasts of pseudotachylite hosted in zeolite vein breccia. The vein cuts through a pseudotachylite matrix.

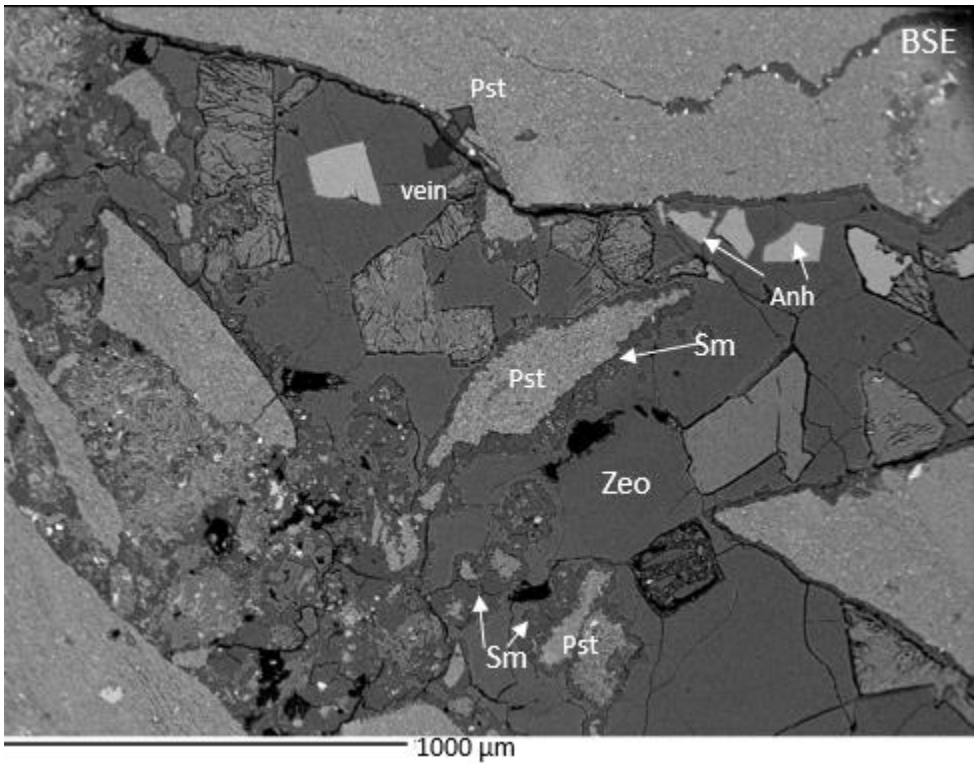


Figure 4.23. BSE image showing a polymineralic vein sample M4 ML (195.30 m). The zeolite vein cuts through the pseudotachylite and contains inclusions of anhydrite, clay and pseudotachylite clasts. BSE = backscattered electron; Zeo = zeolite; Pst = pseudotachylite; Ttn = titanite; Hmt = haematite; Ccl = cataclasites; Gth = goethite.

4.4.2.4. Calcite veins

The focus of the microbeam geochemical and geochronological studies is the calcite veins, which are thus discussed in more detail. Monomineralic calcite veins are common and are dominated by blocky calcite, but composite veins with fine-grained calcite fill between more coarse-grained blocky calcite rims are found (Figure 4.24A-C). However, calcite associated with zeolite, as previously mentioned, is present and the veins are often moderately dipping. Figure 4.24D-F shows composite veins with atypical elongate-prismatic zeolite crystals along the margins

separated by a coarse granoblastic calcite core, while Figure 4.24G-I shows subidioblastic to blocky calcites along the vein walls and surrounding clasts enclosing a coarse zeolite core.

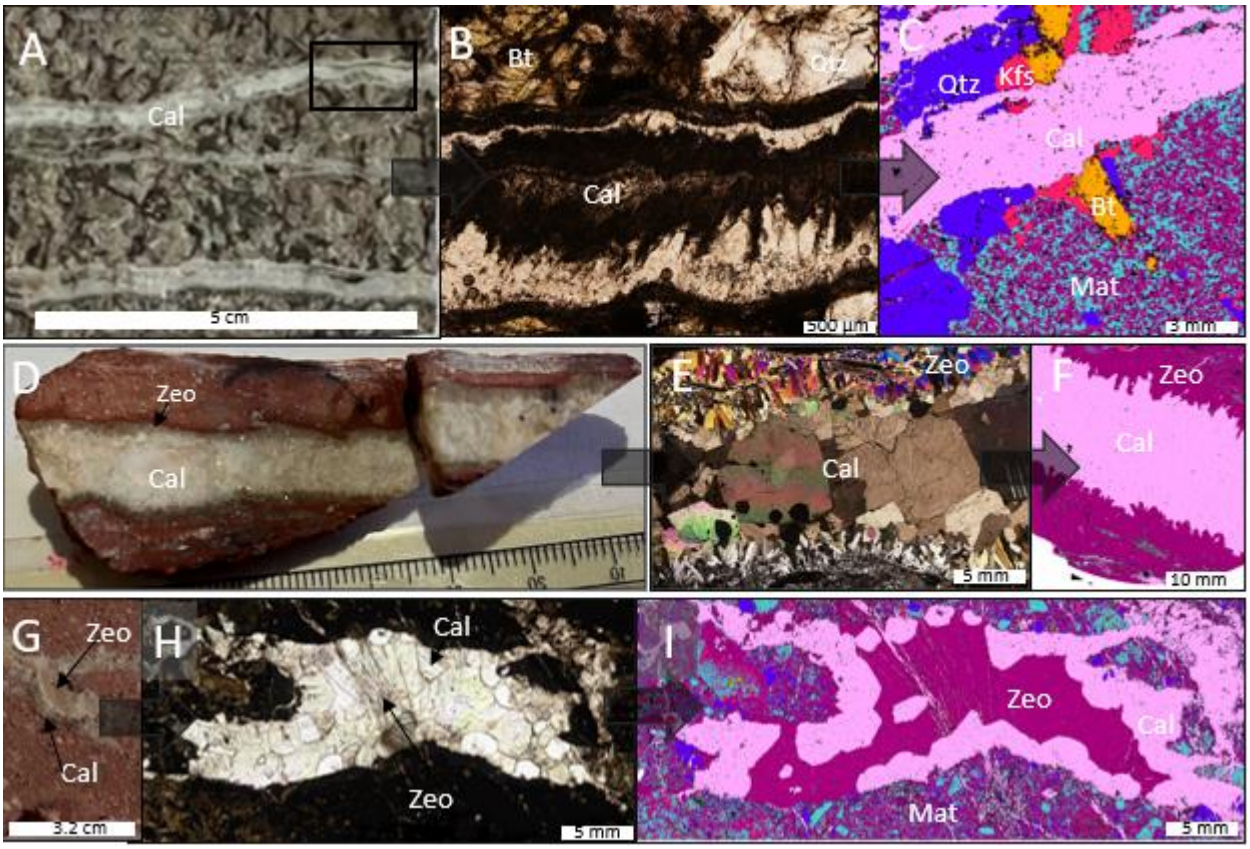


Figure 4.24. Photographs of hand specimens, plane and crossed polarised light, and phase maps of three calcite veins in the upper part of the M4 drillcore. A) Sample M4 V1 (114 m) shows white composite calcite veins with spacing < 5 cm cutting through a granodioritic gneiss. The vein, in plane polarised light (B), shows elongated calcite veins pointing towards fine-grained calcite. The phase map (C) identifies the entire vein as filled with calcite. D) Sample M4 V3 (142.95 m) shows vitreous grey zeolite enclosing a white calcite vein; the calcite grains are up to 15 mm wide. G) Coarse-grained calcite-zeolite vein cutting suevite from 143.02 m. Calcite grains occur along vein walls and around clasts, with zeolite forming the core of the vein.

Although calcite is found replacing cleavages, PDFs/PFs, and microfractures of quartz and as an accessory phase in the zeolite veins and as a variable but significant phase in the vugs (Figure 4.25) in various parts of the drillcore, veins comprising calcite as the sole or major phase are only found in the upper parts of the drillcore. This has implications for the calcite geochronology results (see Section 4.6). Calcite veins display four different textural types: 1) Stretched to syntaxial

elongate blocky calcite veins, 2) Blocky calcite veins, 3) fine-grained calcite veins, and 4) within or rimming around vugs/amygdales.

Stretched to syntaxial elongate blocky calcite veins

Wall-perpendicular stretched calcite veins are found in the target rocks. The stretched cements fill the entire vein width and are < 500 µm wide (Figure 4.16D). In some places in the same sample (M4 GG1.1), the vein is filled by sequential growth from stretched cement to syntaxial elongate blocky calcite cement (Figure 4.16E). These veins reach up to a thickness of ~15 mm wide. It is clear the crystals grew at the vein wall interface; closer to the wall rock in the stretched calcite zone, the calcite is darker and possibly filled with inclusions, whereas the elongate blocky crystals away from the wall rock are free from inclusions and exhibit homogenous and idiomorphic texture (Figure 4.16E; see also Figure 4.24B). The syntaxial elongate blocky veins can be divided into completely sealed syntaxial veins with almost the same size crystals interlocking away from the wall-rock towards the center of the vein (Figure 4.16D) and into incompletely sealed syntaxial calcite veins composed of stretched to elongated-blocky (Figure 4.16; Figure 4.24B) filled with fine-grained to blocky calcite cement identified by SEM-EDS (Figure 4.24B-C). The elongate blocky crystals in Figure 4.24B exhibit growth zonation as seen in optical microscopy. But these veins are non-luminescent in CL and, thus, may contain Mn-poor low-luminescent fluid inclusions.

Blocky calcite veins

Blocky calcite veins contain equant to subangular-sized calcite grains and are 0.5 to 15 mm thick. They are the dominant calcite vein type in the drillcore, with the majority found in suevite dykes. Some veins contain fluid inclusions of < 2 µm in size (Figure 4.25A). The veins form sharp and dilational veins within the host rocks. Figure 4.24H contains a network of veins ranging from 2 mm to 1 cm thick; the thinner calcite veins are crosscut by a blocky calcite-zeolite vein (See overview image in Figure 4.27 also showing the veins yield different oxygen and carbon isotopes values; Section 4.5.1). Both generations of calcite veins show minor concentrations of MnO (see EMPA table in Section 4.5.2) and are non-luminescent in CL.

Fine-grained calcite veins

The occurrence of very fine-grained calcite is seen throughout the drillcore, even in deeper parts of the drillcore, as deep as 354 m. The grains are too small to be seen with the unaided eye or are presented by aphanitic texture, whereby crystals did not have time to grow into large crystals (see Figure 4.25C).

Calcite within vugs

Although this study focuses on veins and smectite-illite minerals, vugs occur locally in the target rocks and impactites that are also filled by post-impact hydrothermal minerals (Figure 4.25B; D-E) and that typically are connected to vein-filled fractures. In some cases, vugs show fine-grained calcite replacements along zeolite grain margins (Figure 4.25B). In other cases, calcite forms the groundmass of the vugs, which also contain other hydrothermal minerals, such as smectite, zeolite and haematite alongside higher temperature minerals, such as actinolite (Figure 4.25D-E). This assemblage is reminiscent of the zeolite veins.

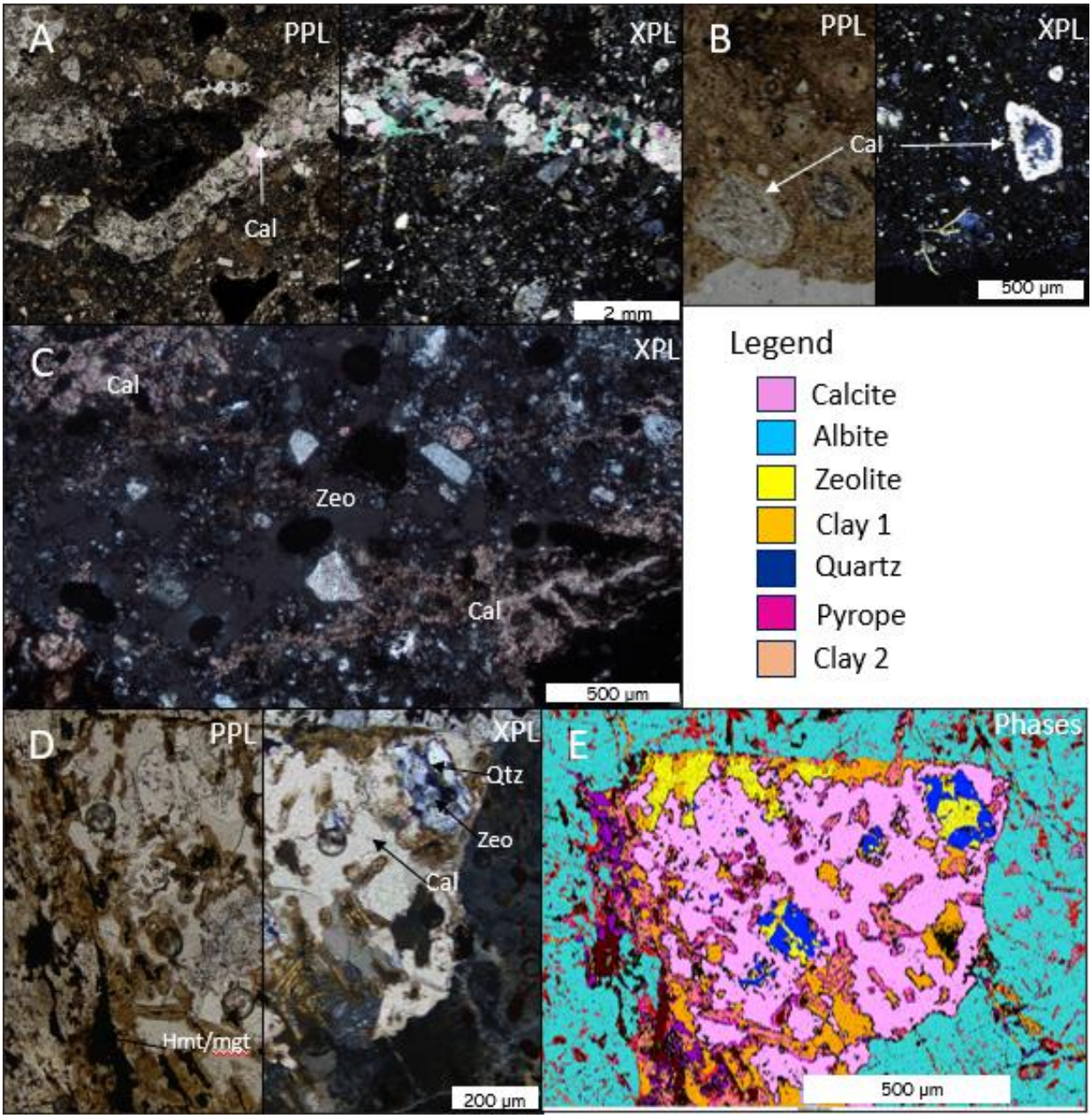


Figure 4.25. Photomicrograph showing morphology and textures of calcite across the M4 drillcore. A) Blocky calcite vein in PPL and XPL of sample M4 S1 (2) (144.09 m). B) Sample M4 S12 (148 m) showing fine-grained calcite around zeolite vugs. C) Sample M4 S3 (160 m) in XPL showing fine-grained calcite cement. D) Combined PPL and XPL image showing a polymineralic, calcite-dominated vug in granitoid gneiss. Apart from calcite, the vug contains quartz, zeolite, haematite/magnetite, and neoblasts of actinolite in sample M4 R22 (139 m). E) Phase map of D. Colors in phase maps labelled in the legend provided. XPL = crossed polarized light; PPL = plane polarized light.

4.5. GEOCHEMISTRY OF CALCITE VEINS

This section describes microbeam analysis of calcite veins using Laser Ablation Inductively Coupled Plasma Mass Spectrometry (LA-ICP-MS) and Secondary Ion Mass Spectrometry (SIMS). The challenge is that geochemically investigating these calcite veins can thus only unravel the fluid history and the temperature of hydrothermal mineral formation of the final stages of alteration. Combining oxygen ($\delta^{18}O$) and carbon ($\delta^{13}C$) isotopic, rare earth elemental (REE + Y) geochemical compositions and microtextural information, the extent of fluid-rock interaction and the origin and chemical compositions of fluids can be investigated.

Geochemical and geochronological data for calcite veins (Section 4.6) were used from six vein samples (Table 4.2). The veins were sampled in the uppermost part of the drillcore, with four sampled from suevite host rocks and two from granitoid rocks. All veins show different growth morphologies, different mineral associations, and slightly different REE patterns, and all record different ages.

Table 4.2. A summary of the type of veins in the M4 drillcore and the analytical techniques applied.

Sample #	Depth	Rock type	Vein type	Mineralogy	Cathodoluminescence (CL)	Figure and type of analysis
M4 V1	114 m	granodioritic gneiss			non-luminescent	
: A			blocky	blocky and fine-grained calcite		Figure 4.24A-C; TE, U-Pb, C-O for blocky calcite vein
: B			syntaxial	elongate-blocky and fine-grained calcite		Figure 4.24A-C; TE, U-Pb, C-O for elongate-blocky dolomite grains
: C			blocky			Figure 4.24A-C; TE

				blocky and fine-grained calcite		and U-Pb for 5 layers of calcite veins (Figure 4.28)
M4 GG2	131.90 m	Leucocratic Granitic Gneiss	Blocky	Blocky calcite with impurities	Not analysed	TE and U-Pb dating
M4 V3	142.95 m	Suevite	Blocky	Blocky calcite; syntaxial zeolite	Weak luminescent bands	Figure 4.24D-F; C-O isotope
M4 S1 (2)	144.09 m	Suevite	Blocky	Blocky calcite	Not analysed	Figure 4.25A; TE and U-Pb
M4 V4	143.02 m	Suevite	Blocky	Blocky calcite; zeolite	Not analysed	Figure 4.24G; C-O isotope
M4 V2	145.3 m	Suevite	Blocky	Blocky calcite; zeolite	Not analysed	Figure 4.24H-I; TE, U-Pb dating, C-O analysis of middle calcite vein

4.5.1. Oxygen and carbon stable isotopic compositions

Analyzed samples and stable isotope compositions are tabulated in Appendix 2.1. The results for carbon isotopes are reported as ‰ relative to VPDB and oxygen isotopes are reported as ‰ relative to VSMOW. The $\delta^{18}O$ and $\delta^{13}C$ values of the calcite veins range from 19.00 to 27.39 ‰ and -21.03 to -3.99 ‰, respectively (Figure 4.26).

The M4 V1 calcite veins occur in the uppermost part of the drillcore. The sample was cut and prepared into 3 different mounts: M4 V1a, M4 V1b and M4 V1c because the veins on each sub-sample represent different growth morphologies. The blocky calcites vein from sample M4 V1a shows a small variation from rim to the core, with values of up to 23.50 ‰ for $\delta^{18}O$ and up to -9.40 ‰ for $\delta^{13}C$ in the core, and up to 25.97 ‰ for $\delta^{18}O$ and -8.61‰ for $\delta^{13}C$ in the rims, indicating that heavier oxygen and carbon isotope compositions are found in the rims when compared to the core. The M4 V1b syntaxial-blocky elongate calcite crystals with low-Mg content, positioned closer to the centre of the vein, display lighter $\delta^{18}O$ (up to 24.88 ‰) and $\delta^{13}C$ (up to -8.13 ‰) values when compared to the fine-grained calcite veins at the margins, which displays values up to 27.39 ‰ for $\delta^{18}O$ and -7.16 ‰ for $\delta^{13}C$.

Samples M4 V2, M4 V3 and M4 V4 were obtained from deeper levels than the M4 V1 calcites. The samples all cut suevite dykes and contain at least two generations of calcite veins within each sample. All three show a similar trend whereby the older generation of calcite veins is marked by thin (a few µm wide) monomineralic veins and younger calcite veins are blocky and commonly associated with zeolite. However, the isotopic composition within each sample varies and shows no relationship when plotted in $\delta^{13}C_{PDB}$–$\delta^{18}O_{SMOW}$ diagram:

1. M4 V2 older calcite veins record $\delta^{18}O$ and $\delta^{13}C$ values ranging from 25.39 to 26.65 ‰ and -14.33 to -10.60, respectively. The younger calcite veins record $\delta^{18}O$ and $\delta^{13}C$ values ranging from 20.62 to 21.81 ‰ and -5.19 to -3.99 ‰, respectively. This relative chronology is depicted in Figure 4.27, where two spot analyses from an older vein (Points 6 and 8) straddle the Point 7 of the younger vein, and the two spots record heavier oxygen isotope compositions and lighter carbon isotope compositions and vice versa for younger calcite veins (Point 7).

2. M4 V4 exhibit a similar trend whereby older veins record heavier $\delta^{18}O$ values ranging from 21.80 to 24.71 ‰ and lighter $\delta^{13}C$ values ranging from -21.03 to -15.02 ‰. Whereas younger veins record lighter oxygen isotope compositions and heavier carbon isotope compositions ranging from 19.90 to 22.04 ‰ and -7.03 to -4.69 ‰.

3. M4 V3 also shows older veins record heavier oxygen isotope compositions and lighter carbon isotope compositions ranging from 21.45 to 23.31 ‰ and -18.96 to -16.16, respectively. Unlike samples M4 V2 and M4 V4, M4 V3 younger calcite veins record lighter $\delta^{18}O$ and lighter $\delta^{13}C$ values ranging from 19.00 to 20.03 ‰ and -19.79 to -19.41, respectively.

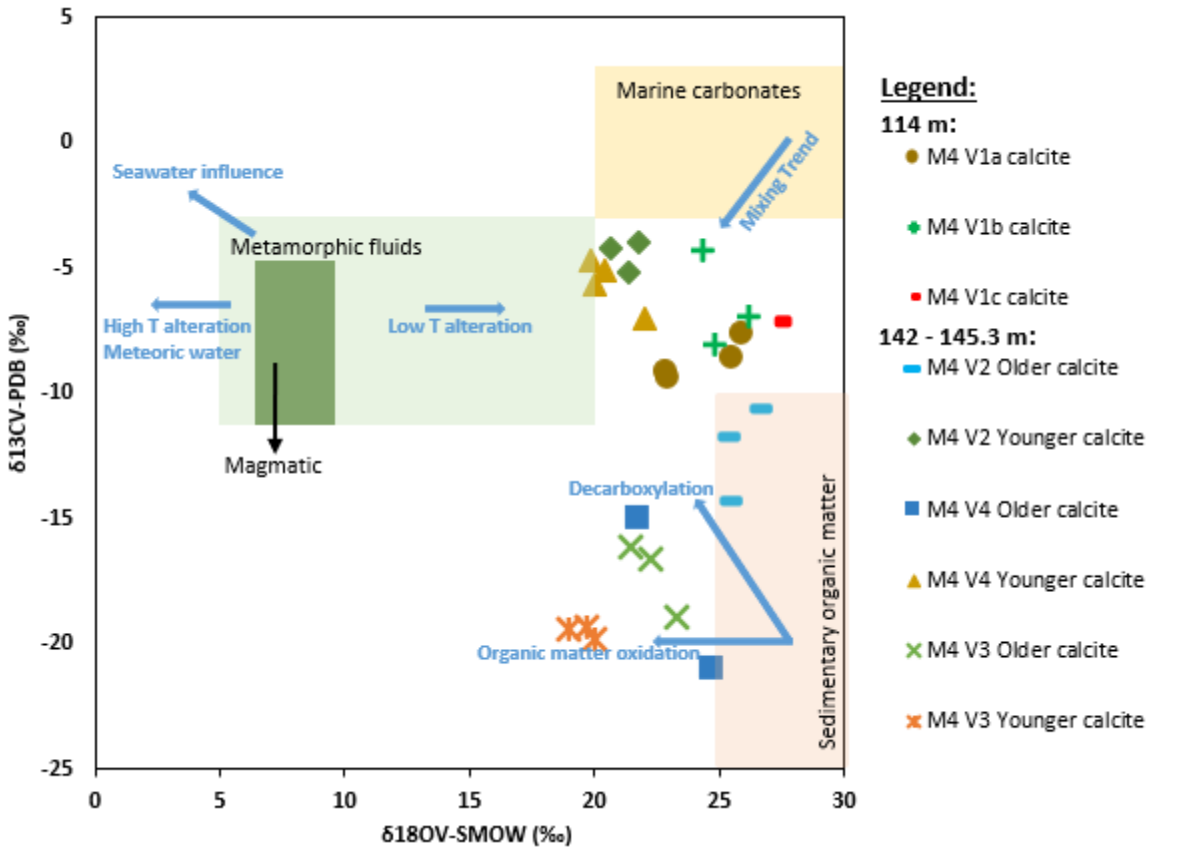


Figure 4.26. $\delta^{18}O_{V\text{-}SMOW}$ - $\delta^{13}C_{V\text{-}PDB}$ diagram showing compositions of vein calcites from the M4 drillcore. The oxygen and carbon isotope reservoirs and diagenetic trends are adapted from literature sources (Liu et al., 2007; Duuring et al., 2008; Broom-Fendley et al., 2016; Guo et al., 2018; Tan et al., 2015; Quandt et al., 2019).

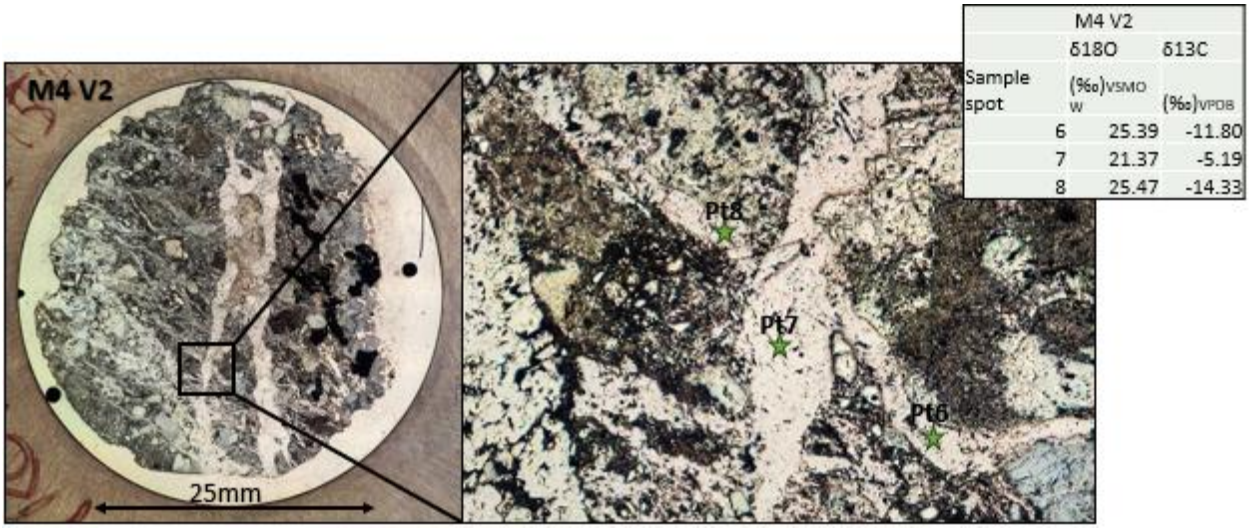


Figure 4.27. Crosscutting relationships between two calcite veins in sample M4 V2, show variation in $\delta^{13}C$ and $\delta^{18}O$ values from three points. Two points are from the older vein and one from the younger vein.

4.5.2. Trace element geochemistry

4.5.2.1. Elemental compositions

Trace element data are reported in Appendix 2.2. Sr concentrations (290 ± 11.80 ppm) are relatively uniform, while Ba concentrations vary significantly from 7.91 ± 1.67 ppm to 1632 ± 134 ppm. Only one sample was analysed for major element compositions to check the Mn and Mg contents (Table 4.3). The M4 V2 calcite is Mg-poor (< 0.03 wt.%) and Mn-rich (< 0.62 wt.%). As calcite CL is favoured by the abundance of Mn^{2+}, M4 V2 shows no visible luminescence in CL. This is attributed to the presence of Fe^{2+}, which is known to suppress the luminescence of carbonates (Kempe and Götze, 2002). The M4 V2 sample shows an average Fe content of 844 ± 249 ppm. M4 V1, M4 V3 and M4 V4 also show no luminescence in CL, therefore, it can be assumed they also contain low-Mg, high Fe and Mn.

Table 4.3. EMPA major elements (Wt.%) results from spot analysis of calcite grains forming at the grain margins of zeolite and along the vein edges from 143.02 m.

Spot analysis	Al2O3	MgO	Cl	CaO	FeO	MnO	TiO2	Total
58 / 1 .	0.02	0.01	0	56.31	0	0.62	0.01	57.02
59 / 1 .	0	0.02	0	57.36	0	0.1	0.01	57.51
64 / 1 .	0	0.02	0.01	56.95	0.05	0.25	0.01	57.32
65 / 1 .	0	0.03	0.01	57.17	0	0.37	0.04	57.67

4.5.2.2. Rare earth elements

In this study, the four samples (M4 V1, GG2, S1(2) and M4 V2) are analyzed for REEs. The intra-sample (M4 V1a to M4 V1c; M4 V1c is further divided into 5 layers of calcite vein growth (see micrograph in Figure 4.28). Elemental ratios are listed in Appendix 2.3.

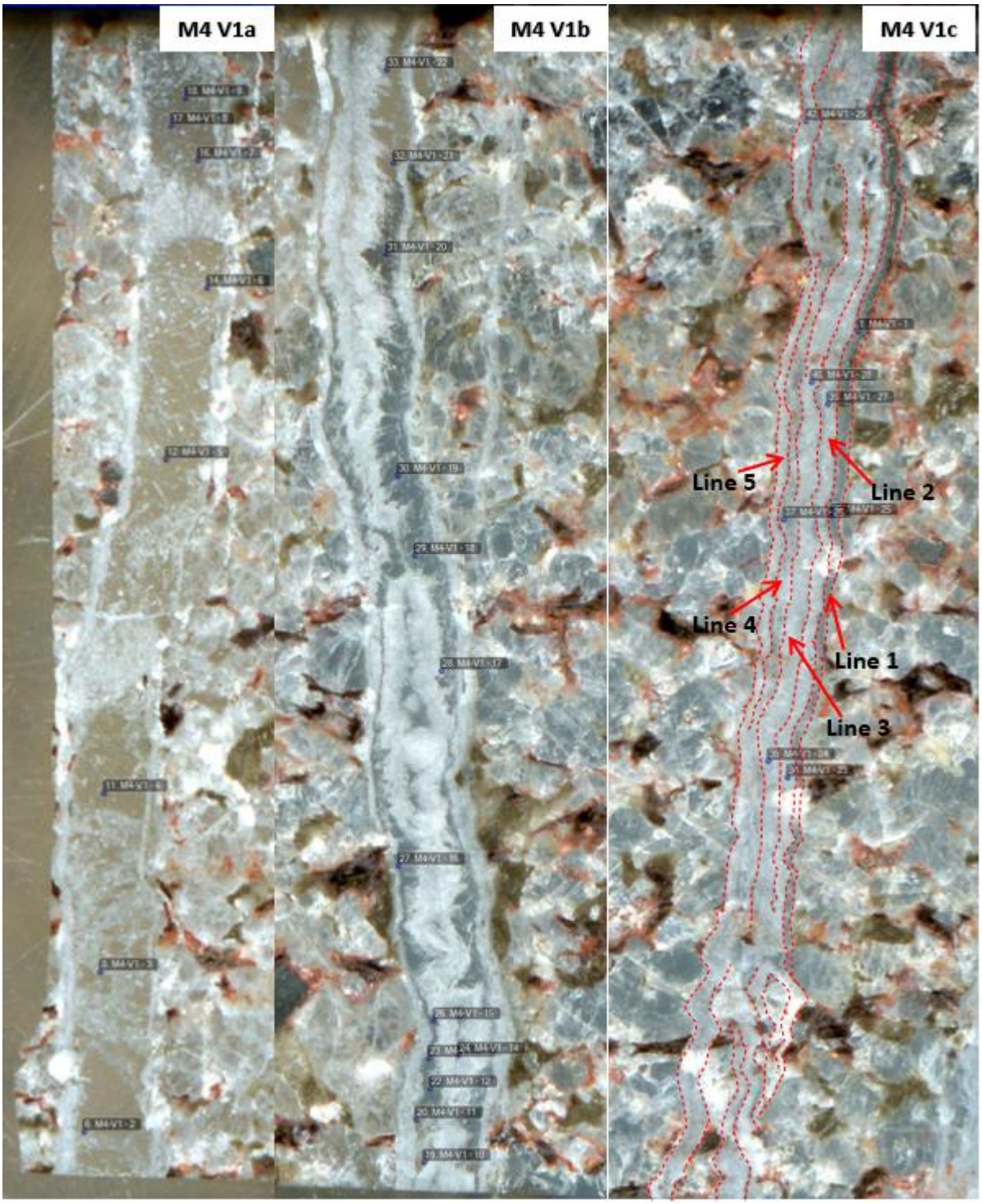


Figure 4.28. Laser spot locations in sample M4 V1a-b and within the five layers of calcite in M4 V1c.

REEs are normalized to "MUQ" ("Mud of Queensland"), which serves as an alternative to upper continental crust (UCC) proxies. The MUQ composition represents an upper crustal average, incorporating mixed felsic and mafic sources (Kamber et al., 2005). The MUQ-normalized REE

patterns are depicted in Figure 4.29. The REEs comprise light REE (LREE; La – Sm), middle REE (MREE; Nd – Tb), and heavy REE (HREE; Gd – Lu). Ratios such as LREE/MREE, LREE/HREE, MREE/HREE, Ce/Ce* (Ce/Ce* = $Ce_{MN}/[Pr_{MN}\text{^}2)/Nd_{MN}]$; Lawrence et al., 2006; Tostevin et al., 2016; Barrat et al., 2023), Eu/Eu* (Eu/Eu* = $2 \times Eu_{MN}/[Sm_{MN} + Gd_{MN}]$ Tostevin et al., 2016), La/La* ($La_{MN}/(Pr_{MN}*(Pr_{MN}/Nd_{MN})\text{^}2$) and Gd/Gd* values ($Gd/Gd* = Gd_{MN}/((2*Tb_{MN}) - Dy_{MN})$ are reported in Table 4.4.

Table 4.4. MUQ-normalized REE ratios and Y in ppm of vein calcites from the M4 drillcore.

Sample # / mineral	Spot location	LREE/ HREE (La/Yb)	LREE/ MREE (La/Sm)	MREE/ HREE (Dy/Yb)	Ce/Ce*	Eu/Eu*	Y/Ho	La/La*	Gd/Gd*	∑REE
M4 V1a blocky calcite	core	270	6.58	3.86	0.01	0.58	40.5	1.35	1.73	26.3
M4 V1b blocky elongate calcite and fine-grained calcite	blocky grains	27.7	3.36	1.78	0.01	0.66	50.9	1.44	1.58	1.41
M4 V1c blocky and fine-grained calcite	5 layers (from line 1 to 5)	1.85 to 20.4	1.29 to 3.55	1.26 to 1.62	0.12 to 0.05	0.96 to 0.72	41.6	1.77 to 1.43	1.16 to 1.35	34.7 to 13.1
M4 V1 Blocky grains to fine-grained	Overall	64	3.37	1.89	0.05	0.76	44.9	1.54	1.42	18.7
M4 GG2 blocky calcite	massive - entire section	3.75	3.70	0.96	0.47	11.18	30.3	1.65	1.13	5.48
M4 S1(2) blocky calcite	massive - entire section	1.09	1.45	0.75	0.02	1.18	29.4	1.39	1.14	6.08
M4 V2 blocky calcite	euhedral shapes close the zeolite veins far from fracture walls	2.09	1.00	2.05	0.95	1.14	40.5	1.25	1.28	4.14

The four analysed samples (M4 V1, GG2, S1(2) and M4 V2) show different REE patterns. The intra-sample (M4 V1a to M4 V1c; M4 V1c is further divided into 5 layers of calcite vein growth, see micrograph in Figure 4.28) in M4 V1 also shows variation in REE distribution. The M4 V1a-

b is characterized by enrichments of light relative to heavy REE (Table 4.4; Figure 4.29A-C). Sample M4 V1 shows strong negative Ce anomalies, slight enrichments of La and Y, and slight enrichment of Gd in M4 V1b-c. The Eu anomaly is slightly negative in M4 V1a-b and Line 4 -5 calcite layers in M4 V1c (lines 4-5 lie next to V1b; See Figure 4.28). M4 GG2 REE patterns are flat, with a pronounced positive Eu anomaly, slight enrichment in La and Y and a slight depletion in Ce (Figure 4.29D). Sample M4 S 1(2) shows a concave-up REE patterns and has a pronounced positive Eu anomaly and slight enrichment in Y (Figure 4.29E). The M4 V2 REE patterns are flat and show a slight positive Y anomaly, and no Ce anomaly was detected (Figure 4.29F).

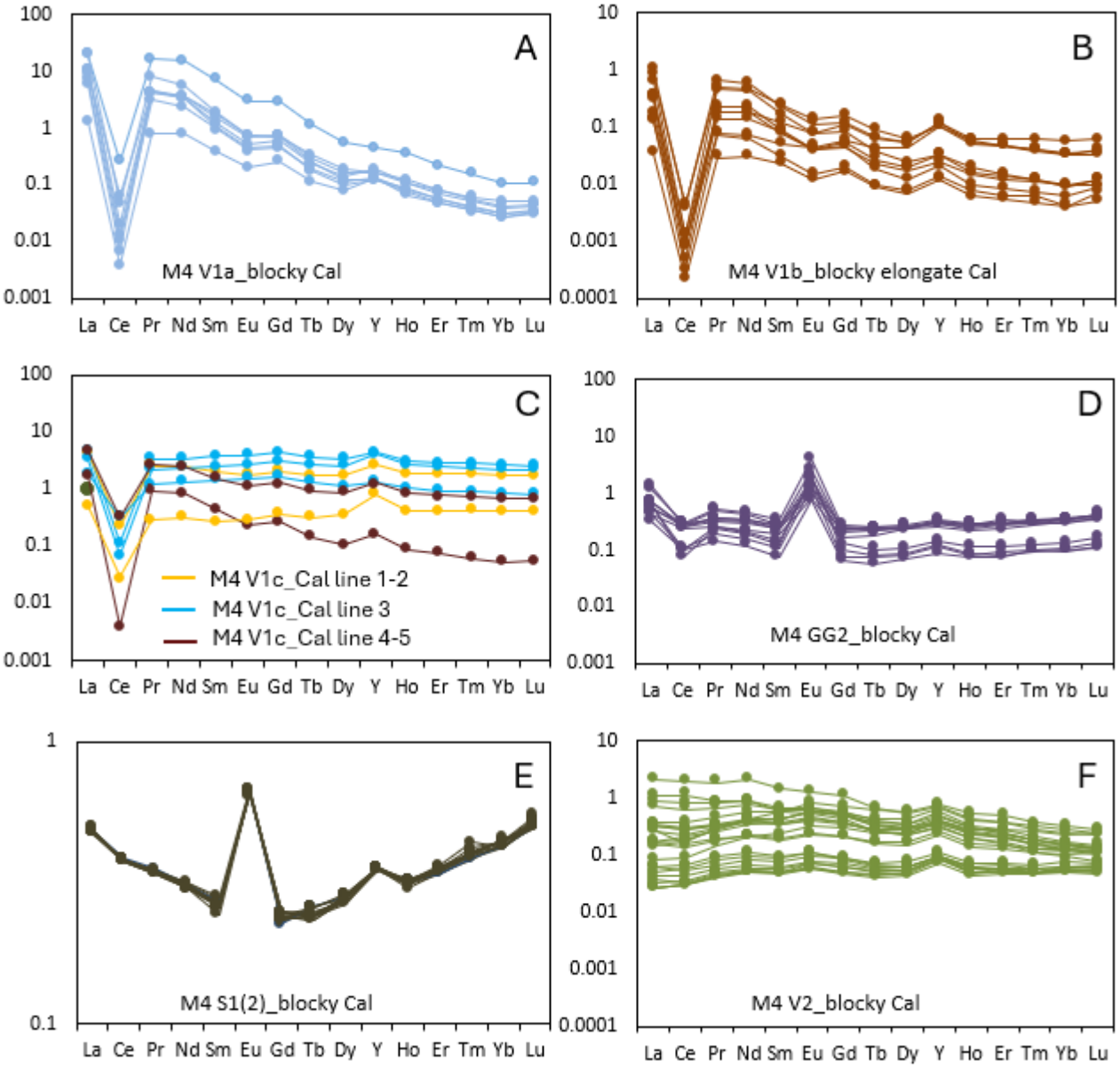


Figure 4.29. MUQ-normalized REE + Y patterns of calcite veins sampled from the upper section of the M4 drillcore (114 – 145 m). A) Sample M4 V1a blocky calcite vein (114 m) cutting through granodioritic gneiss. B) M4 V1b blocky calcite vein with fine-grained core (114 m). C) M4 V1c layers of blocky and fine-grained calcite vein (114 m). D) M4 S1(2) blocky calcite veins (144.09 m) cutting through a suevite. E) Sample M4 GG2 blocky calcite veins (131.9 m) cutting through leucocratic granitic gneiss. F) Sample M4 V2 blocky calcite in composite zeolite-calcite vein (143.02 m), cutting suevite.

Comparison with the matrix

The MUQ-normalized REEYs of blocky and fine-grained calcite veins and host rocks exhibit similar patterns in Figure 4.30B-D but not in Figure 4.30A. The REE profiles of granodioritic gneiss, granitic gneiss, and suevites indicate an enrichment of LREE relative to HREE, a

characteristic shared by the calcite veins that intersect the matrices. The target rocks, granitic-granodioritic gneisses, are distinguished by a positive Eu anomaly, a slight negative Ce anomaly, and no anomaly detected for Y (Figure 4.30A-B). The suevites show a flat REE pattern, also a characteristic shared by vein calcites in M4 S(1) and M4 V2 hosted in suevites (Figure 4.30C-D).

The normalized REE concentrations in the host rocks are 1 (in granitoids) and 2 (in suevites) orders of magnitude higher than those in the calcite veins (Figure 4.30). Although similar patterns are seen in some of the figures, the geochemical anomalies seen in calcite veins show differences with host rocks, which indicates that the fluids that entered the fractures during precipitation have less to no interaction with the host rocks.

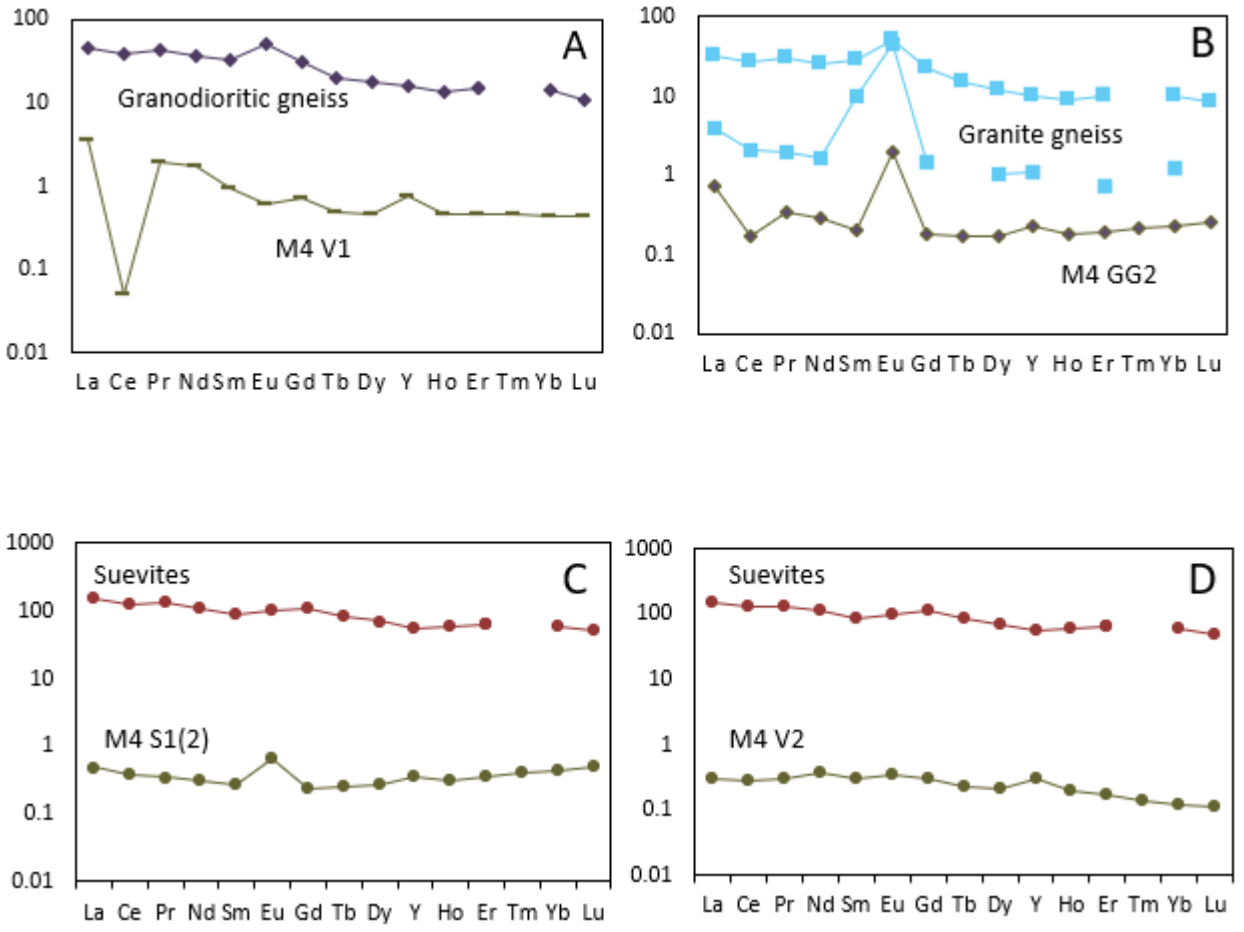


Figure 4.30. MUQ-normalized REE + Y patterns of calcite veins and host rocks (Wela, 2017; granodioritic gneiss, leucocratic granitic gneiss, and suevite).

4.6. GEOCHRONOLOGY

The age of the Morokweng impact structure has been confirmed in 3 studies using zircons from the impact melt sheet. Recrystallized zircon in the impact melt sheet from borehole WF4 drillcore yielded a $^{206}Pb/^{238}U$ age of 146.2 ± 1.5 Ma and a $^{208}Pb/^{238}Th$ age of 144.7 ± 1.9 Ma (Koeberl et al., 1997). Hart et al. (1997) estimated a $^{206}Pb/^{238}U$ single zircon age of 145.2 ± 0.8 Ma from WF05 drillcore. Kenny et al. (2021) established a more precise age of 146.06 ± 0.16 Ma and showed from zircon thermochronology that the impact melt sheet cooled from the top downwards, indicating that the samples highest in stratigraphy have the possibility to be closest to the impact age. Petrographic observations indicate calcite is part of the hydrothermal assemblages as it occurs along the PDFs (Figure 4.1) and is associated with evidence of K-metasomatism and high-temperature hydrothermal minerals such as clinopyroxene, actinolite and titanite within zeolite veins and vugs (Figure 4.18, Figure 4.21D and Figure 4.25D). Unfortunately, calcite in these veins could not be dated and the current study is limited to the youngest veins that cross-cut earlier generations, opening the possibility that they may be unrelated to the impact event.

4.6.1. U-Pb dating

The laser spot locations for TE (Figure 4.31) guided the setting of the laser spots analyses on each sample. Like CL imaging, the growth zonation was not visible under the LA-ICPMS camera due to low contents of TE and Mn (Roberts et al., 2020). An effort was made to avoid fine-grained calcite as the grains are likely to be prone to contamination and oxidation (Figure 4.24B); thus, for better representation of the calcite veins, only blocky calcites were targeted, as they were easier to analyse and free of, or contained minimal amounts of, inclusions.

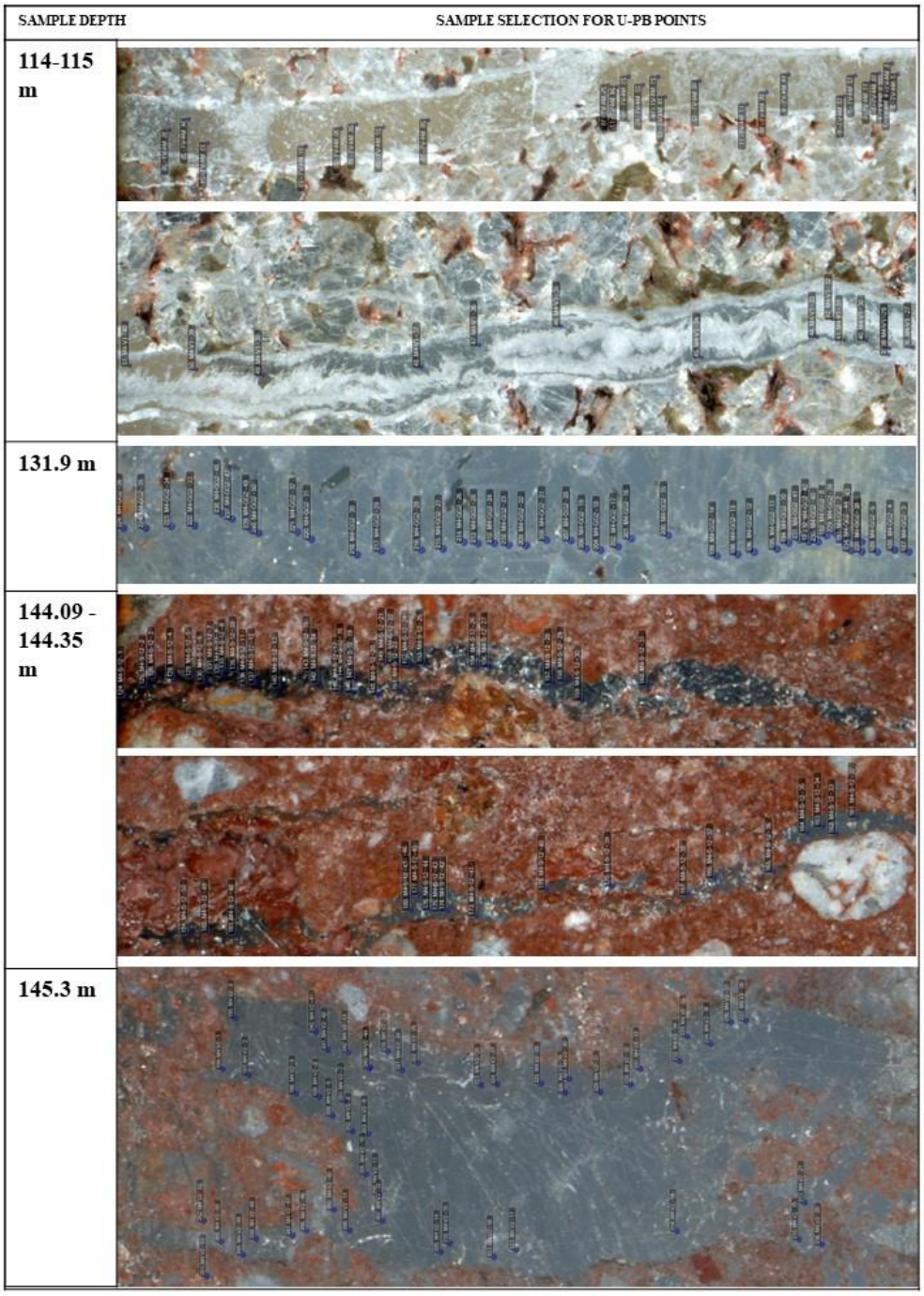


Figure 4.31. A laser spot location map generated using the camera embedded in LA-ICPMS shows sample depths.

The U-Pb data are presented in Tera-Wasserburg Concordia diagrams, which plot $^{207}Pb/^{206}Pb$ versus $^{238}U/^{206}Pb$ (Figure 4.32; Tera and Wasserburg, 1972) and display the resulting lower intercept age. The plots show spot analyses along a linear array, where the upper intercept ("y-

axis") represents the common Pb composition, and the lower intercept along the Concordia represents the crystallization age. All vein samples (M4 V1, M4 S1(2), M4 V2 and M4 GG2) were selected from the upper parts of the drillcore (114 m – 145.3 m; tabulated in Appendix 3.1 and resulted in ages ranging from 12 to 74 Ma, i.e., considerably younger than the impact event seen in sample M4 V1, M4 S1(2), M4 V2 and M4 GG2 (Figure 4.32).

M4 V1

A total of 48 analyses obtained from the blocky calcite vein record a precise age and resemble a well-behaved closed system because the results contain high U counts with small uncertainties (Roberts et al., 2020). A lower intercept age of 67.09 ± 0.72 Ma with an upper intercept ($^{207}Pb/^{206}Pb$) of 0.914 ± 0.027 (MSWD = 6.6) can be regressed. After the removal of 10 outliers with low U and Pb abundances, the Tera-Wasserburg plot corresponds to a lower intercept age of 66.46 ± 0.74 (MSWD = 1.7) and regressed upper intercept composition ($^{207}Pb/^{206}Pb$) of 0.911 ± 0.028.

M4 S1(2)

The blocky calcite vein is characterized by less radiogenic isotope compositions. The data show large uncertainties due to low count rates (Roberts et al., 2020). The overall data give a lower intercept age of 21.11 ± 0.48 Ma (n = 64, MSWD = 32), and regressed upper intercept ($^{207}Pb/^{206}Pb$) of 0.8070 ± 0.0041. After reducing the scatter in the regression array by removing ellipses that do not fall on the regression line, the Tera-Wasserburg lower-intercept age for M4 S1(2) is 28.1 ± 1.1 Ma (n = 34, MSWD = 1.6) with a $^{207}Pb/^{206}Pb$ composition intercept of 0.8131 ± 0.0055.

M4 V2

The dataset related to M4 V2 lacks radiogenic isotopic compositions; however, the tight clustering of data points allows for a realistic age to be determined (Roberts et al., 2020). The Tera-Wasserburg regression, based on all data points, records a lower intercept age of 11.9 ± 7.3 Ma (n = 37, MSWD = 7.2) with a $^{207}Pb/^{206}Pb$ intercept of 0.8268 ± 0.0042. When low U/Pb ratio analyses (n = 13) are excluded, the Tera-Wasserburg plot yields an age of 13.95 ± 4.32 Ma (MSWD = 1.6) with a $^{207}Pb/^{206}Pb$ composition intercept of 0.835 ± 0.016.

M4 GG2

This sample yields the most imprecise age because of large individual uncertainties due to low U-Pb concentrations. Therefore, the data make it difficult to differentiate if M4 GG2 is caused by open-system behaviour due to external influences that may have altered the isotopic ratios, or it is the actual age of the sample at the time of deposition (Roberts et al., 2020). The crystallization age is 16 ± 47 Ma (n = 25, MSWD = 2.1) with a $^{207}Pb/^{206}Pb$ intercept of 0.921 ± 0.014. The overall data give an intercept age of 57 ± 25 Ma (n = 51, MSWD = 15), and regressed upper intercept composition ($^{207}Pb/^{206}Pb$) of 0.9374 ± 0.0062.

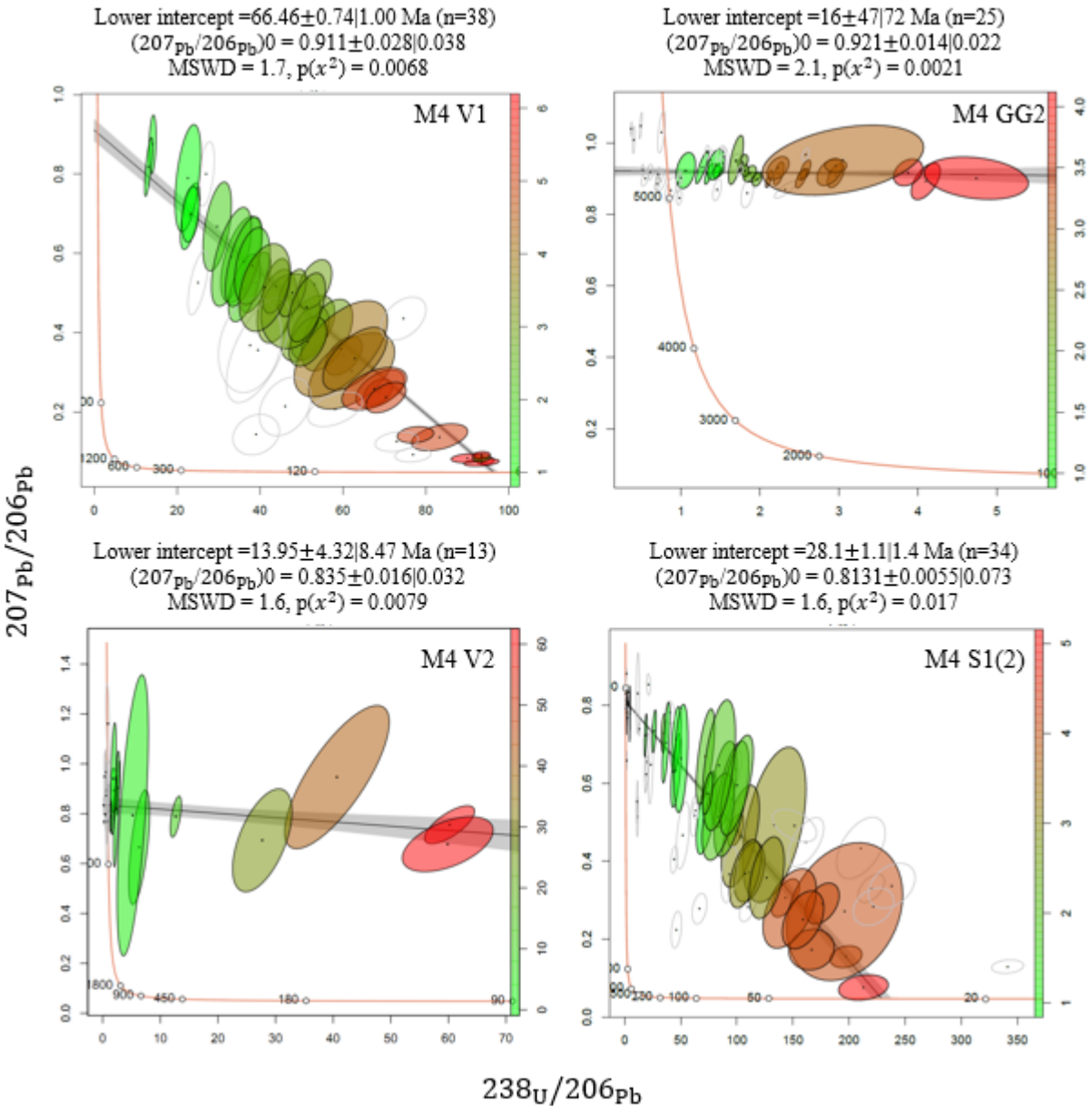


Figure 4.32. Terra-Wasserburg diagrams for four calcite vein samples from the M4 drillcore: (a) M4 V1, (b) M4 S1(2), (c) M4 V2, and (d) M4 GG2. The graphic presentation and age calculation are obtained using IsoplotR (Vermeesch, 2019). The age determination is obtained from the lower intercept with Concordia. The second value represents the "studentized 100(1-α)% confidence interval for t using the appropriate number of degrees of freedom," and the third value represents the "approximate 100(1-α)% confidence interval for t with overdispersion, calculated as z = y√MSWD." "n" represents the number of spot analyses. MSDW = mean squared weighted deviations, p(χ2) = chi- squared p-value for the isochron fit. The data ellipses are color-coded according to their 238U/206Pb value, displayed in the individual color scales at the right margin of the diagrams.

The age results obtained for the four calcite veins are considerably younger than ~146 Ma impact age and appear to be related to multiple events ranging from 66.46 ± 0.74 to 13.95 ± 4.32 Ma

(Figure 4.32; Figure 4.33). These results indicate a polyphase post-impact hydrothermal history for the rocks that may be interpreted in terms of the Late Cretaceous to Cenozoic tectonic history of the region. However, none of the ages are consistent with the calcite having crystallized as part of the impact hydrothermal system, even though calcite is found in a high-temperature hydrothermal assemblage that is most reasonably explained by the impact-induced hydrothermal system (Masiu, 2025, unpublished dissertation).

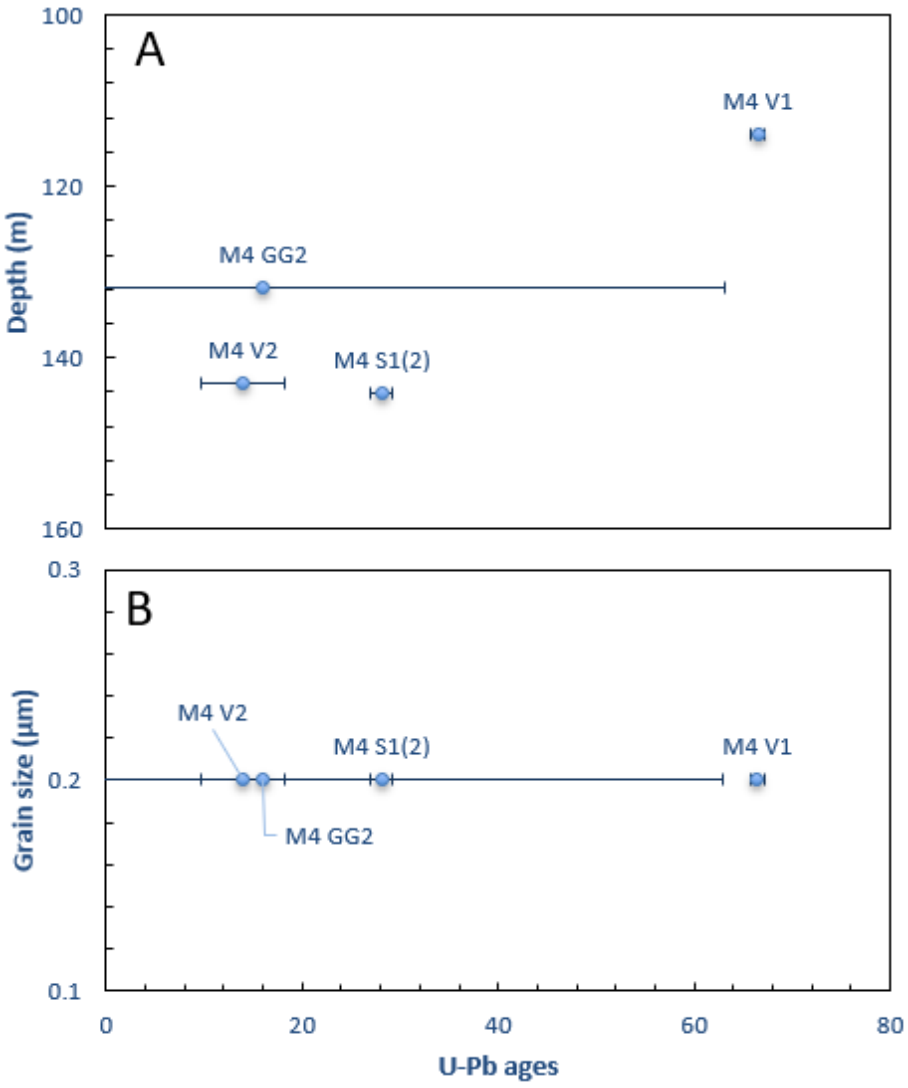


Figure 4.33. Relationship between U-Pb ages versus A) depth and B) calcite grain spot size analysis for the calcite veins from sample M4 V1, M4 GG2, M4 V2, and M4 S1(2). The plots include error estimates for each age.

4.6.2. K-Ar dating

In order to understand whether the calcite U-Pb dating reflects incomplete but variable resetting of structural features related to a 146 Ma impact hydrothermal system or discrete post-impact hydrothermal events, a set of bulk clay separates was obtained from faulted and hydrothermally altered samples from various depths in the M4 drillcore for K-Ar dating. The selection of samples for dating the clays was done in two sets; the initial set was based on macroscopic evidence for abundant clay along fractures in granitoids, and no XRD was performed. Two samples were taken at the upper part of the drillcore (M-2 and M-6) and two from deeper parts (M-10 and M4-11) to investigate any depth dependence. A second set was sampled from deeper levels (> 262 m), targeting the most K-rich rocks (K-feldspar bearing granite and biotite-rich monzonitic gneiss) by hand specimen inspection and with the aid of micro-XRF and phase map analysis by SEM. Unfortunately, XRD of the separated clay fractions again showed insignificant K-bearing clays (see Section 4.3.1 and Appendix 1.3A-B), and further dating was not attempted. Also, the precise petrographic context of the clays within the hydrothermal assemblage could not be determined via this method, therefore a direct link to veins could not be established.

Using the initial set of whole-rock smectite-illitic clays from <216 m, the following K-Ar dates could be obtained: 57.4 ± 7.14 Ma (< 0.2 µm fraction) from 119 m, 59.45 ± 7.74 Ma (< 0.2 µm; at 216 m), 105.8 ± 4.4 Ma (< 1.0 µm; 214.5 m), and 68.9 ± 48.9 Ma (< 0.5 µm; at 121.8 m) (Figure 4.34). All but one of the absolute ages are < 100 Ma, and all are considerably younger than the impact. Younger K-Ar ages were obtained from finer grain size fractions, and the two samples showing identical grain fractions yield identical ages within the analytical uncertainties (Figure 4.34).

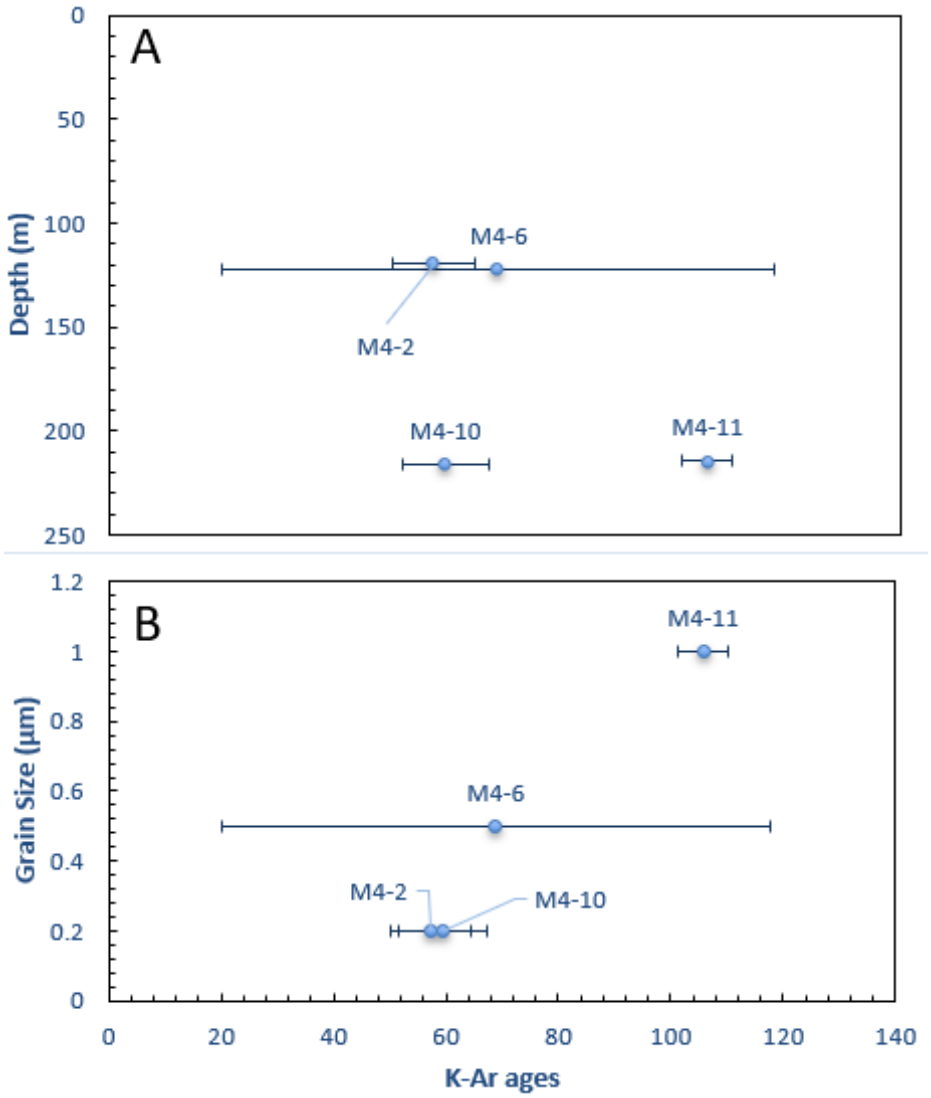


Figure 4.34. Plots showing the relationship between smectite-illite clay K-Ar ages *grain size and depth for samples in the M4 drillcore. The plots include error estimates for K-Ar ages.*

Geochronological data and crosscutting relations show that the calcite veins appear younger than 146 Ma.

5. DISCUSSION

5.1. PETROGRAPHY AND MINERALOGY

5.1.1. Controls on Alteration

The crosscutting relations observed between hydrothermal minerals and shock deformation features and the filling or overprinting of induced fracture zones by secondary minerals indicate post-impact hydrothermal activity within the M4 drillcore. Petrographic, electron microprobe and X-ray diffraction results combined with data from a related MSc study (Masiu, 2025, unpublished dissertation) confirm the presence of post-impact hydrothermal alteration, dominated by zeolite, diopside, actinolite, alkali feldspar, anhydrite, andradite, titanite, chlorite, smectite-illite, calcite, haematite/magnetite, pyrophyllite, and pyrite.

The degree of post-impact hydrothermal alteration within the rocks is variable and appears to be linked directly to permeability, among other factors (Newhouse, 1969; Naumov, 1999). Suevites and cataclasites show textural evidence of having been high-permeability zones with porosities ranging from 30 to 60% (Figure 4.11), and are primarily cemented by hydrothermal zeolite and some clay minerals. While pseudotachylite dykes appear to have been highly reactive owing to an unstable glassy matrix, which is now primarily made up of clay minerals with some zeolite and Fe-oxides. Melt clasts in the suevites also show a dominantly clay-rich replacement assemblage, and concentric zoning that indicates extensive reaction with an external fluid (Masiu, 2025, unpublished dissertation). However, it is not possible to establish if residual heat from the pseudotachylite and melt clasts enhanced hydrothermal reactions in these rocks. These impactites only constitute 12 vol% of the drillcore (Gibson et al., 2019), indicating the MIS was water-starved as the target rocks show less alteration of minerals (i.e., biotite is not highly altered more so in the deeper parts of the drillcore) and show lower porosity than the impactites. Post-impact alteration within target rocks mostly occurs along fractures related to the impact-induced shear faults, and later fractures, as well as along intragranular fractures and PDFs in quartz. This indicates that rock-

and grain-scale fracture-induced permeability and reactivity of shock glasses appear to be the major controls on alteration in the wallrocks.

5.1.2. Mineral assemblages in the M4 drillcore

The post-impact alteration occurred in a variety of forms: 1) Alteration of minerals and glasses like PDFs is observed in host rocks. The dendritic replacement of shock glass lamellae (PDFs) is interpreted as related to the impact hydrothermal system (Figure 4.1) rather than the younger phase of calcite veining (Figure 4.24), and must involve fluid infiltration into the quartz grains from transgranular fractures. 2) Fluids infiltrated, particularly porous or highly permeable areas within fractures and breccias. The latter is seen macroscopically as $\leq$ 3 µm – 400 µm conjugate networks of fractures (Figure 4.8) and veins crosscutting all lithological units in a 369 m drillcore (Figure 2.4).

5.1.2.1. Mineralization trend in fractures and alteration temperatures

The zeolite, clinopyroxene, smectite, alkali feldspar, haematite and calcite assemblage within a fracture fill in sample GG10 shows a sequence of crystallization and mineral effects that are consistent with a cooling hydrothermal system:

1. The presence of alkali feldspar partially replacing at the albite wall rock against the fracture fill in sample GG10 shows evidence of fracture-related marginal K-metasomatism (Figure 4.20 and Figure 4.21), at temperatures allowing local dissolution and diffusion of K^+ and Na^+ within the fracture-wall rock interface.
2. Early-stage clinopyroxene crystallized as tiny prisms that grew along the edges, indicating that the fracture fluid started at higher temperatures (Zurcher and Kring, 2004), of 400 $\pm$ 50 ℃ (Pan and Fleet, 1989). In other samples, clinopyroxene is replaced by amphibole, andradite or titanite (Figure 4.10 and Figure 4.18). Andradite garnet forms at > 350℃ (Kirsmae and Osinski, 2013). The occurrence of these high-T minerals from sample to sample must have been a result of fluid/rock interaction.

3. Smectite then surrounds the actinolite/clinopyroxene neoblasts and lines the vein walls; this alteration can occur at intermediate temperatures of 300 – 150/100 ℃ (Kirsmae and Osinski, 2013).
4. The fracture then proceeded to form Na-Ca-heulandite. The temperature range for heulandite is below 190 ℃, as heulandite is stable at pressures of > 600 bar and temperatures between the stability fields of stilbite and laumontite between 150 – 190 ℃ (Cho et al., 1987).
5. The fracture later experienced oxidation, now present as haematite/magnetite + goethite (Figure 4.22). Fe-hydroxides can form at very low T in the near-surface environment and so may be alteration of vein-related Fe-Mg silicate or Fe-oxide minerals. Oxidation of haematite/magnetite appears more dominant in the upper parts of the drillcore; BSE scans show it is more widespread throughout the drillcore around the rims (Figure 4.19), within cleavages (Figure 4.5) and microcracks of minerals grains (Figure 4.4). The occurrence of haematite ± magnetite with pyrite in the quartz jigsaw pattern in the deeper parts of the drillcore suggests a redox change from Fe^{2+} to Fe^{3+} with time. This pattern of increasing oxidation is expected as oxidised near-surface meteoric water penetrates deeper into the rocks and the temperature of the system cools (Koeberl and Reimold, 2004).
6. Sometimes, subidiomorphic calcite crystals (about one or two grains) are found in these zeolite veins (Figure 4.21). Calcite-zeolite are lower temperature minerals overprinting higher temperature minerals (Figure 4.18; Figure 4.21). This alteration is noted to form at temperatures < 100℃ (Kirsimae and Osinski, 2013).

5.1.2.2. Lower temperature post-impact veins

The vein evidence indicates that shear faults and extensional fractures acted as fluid channels that may be locally linked to vugs within the target rocks and impactites. The veins show similar features of the vertical zonation of hydrothermal mineralization known to occur in other craters, like Chicxulub, Manson, Puchezh-Katunki, Ries, Boltysh, and Siljan Ring (McCarville and Crossey, 1996; Koeberl and Reimold, 2004; Zurcher and Kring, 2004; Naumov, 2005). Zeolite is a dominant mineral phase in these veins and usually occurs with other hydrothermal minerals. The dominant zeolite is Ca-heulandite. Detailed mineral chemistry of zeolite, clay and amphiboles is documented in a related MSc study (Masiu, 2025, unpublished data), including other zeolites:

Chabazite and laumontite within the vugs. Zeolite veins may appear monomineralic macroscopically in thin sections, but many veins show microscopic evidence of minor amounts of other phases that suggest crystallization under relatively high-T hydrothermal conditions as mentioned in the above section.

Calcite and anhydrite are also common minerals observed in vein morphologies. In some cases, calcite veins are associated with Ca-heulandite veins (Figure 4.24), but their abundance decreases down the drillcore. Below 180 m depth, anhydrite + zeolite is more common (Figure 4.23). This spatial distribution could be a result of vertical zonation seen in the central uplift impact-induced hydrothermal systems (Naumov, 2005; Kirsmae and Osinski, 2013). However, calcite and anhydrite, in other cases, occur as monomineralic veins that crystallized post-impact. Whether their formation is linked to the impact remains a question for investigation. However, morphological observations indicate that the fluid-precipitated material exhibits a sharp contact with the host rock, and wallrock interaction, as visible in BSE images, appears to be limited (Figure 4.16). The monomineralic anhydrite veins intersect metadolerites and pseudotachylite; their orientation is oblique to the drillcore axis, starting at 180 m depth and continuing to the bottom of the drillcore, cutting through impact-related features. The inclined channel observed at 180 meters may suggest that sulphate-rich fluids were potentially derived locally by groundwater fluids.

The calcite veins in the uppermost part of the drillcore comprise blocky calcites. These veins have been the last to form, as evidenced by their distinct cutting through the haematite/magnetite rimming around the biotite grains (Figure 4.16F and Figure 4.24C). These monomineralic blocky and fine-grained calcite veins are crosscut by blocky calcite veins associated with zeolite, suggesting more than one generation. The morphological change of veins transitions from fibrous/stretched to elongated blocky to blocky to fine-grained calcite (Figure 4.16D-E and Figure 4.24A-B). This sequential growth (Figure 4.16D) may indicate that the fibrous/stretched calcite veins at the wall rock formed first, followed by elongate-blocky calcite filling the open cavity (Bons, 2000). The cavity infill was cemented by overgrowth of the first elongate-blocky calcites and the infill was complete by blocky calcites (Figure 4.16E). In some cases, the infill was completed by fine-grained blocky calcites (Figure 4.24B).

The fibrous/stretched veins may have formed by diffusion through the host rock (Quandt et al., 2018). This was proposed by Mügge (1928), stating the absence of growth competition in fibrous aggregates indicates stable growth with no evidence of open fracture. This theory was supported by Means and Li (2001), who experimentally produced synthetic fibrous veins without fracturing. But for the combination of fibrous/stretched and elongate blocky to blocky veins to form, there must be an open fracture or cavity for blocky crystals to form (Bons et al., 2012). Therefore, a fractured opening may occur after the cementation of fibrous/stretched veins. The elongate blocky calcites are thought to have formed when the opening rate of the fracture was slower than the maximum but faster than the minimum potential growth rate (Mügge, 1928; Bons, 2000). Blocky calcites, on the other hand, formed when the opening rate of the fracture was faster than the maximum potential growth rate (Mügge, 1928; Bons, 2000).

5.2. POTENTIAL SOURCES OF FLUIDS

At 146 Ma during the formation of the MIS, its location was > 1000 km away from any coastline within the southern part of the Gondwana supercontinent, and therefore, this may have limited the availability of hydrothermal fluid originating from a meteoric source (Gibson et al., 2024c). The MIS was likely water-starved at the time of formation. Additional fluids could have originated from the shock-induced decomposition of hydrous minerals and the crystallization of impact melts into anhydrous minerals (Wela, 2017), but the predominantly granitic target with generally very low mica contents would have been an added constraint. Based on calcite age data, the MIS experienced one or more episodes of fluid influxes younger than 100 Ma, which precipitated calcite veins. One may have been the proto-Morokweng River flooding the MIS between 86 and 65 Ma (Partridge, 1998; Haddon, 2005). Fluids advecting through fractures and precipitating veins are likely to have travelled over considerable distances, thus having an external source and being often blocky (Bons et al., 2012).

5.3. CHRONOLOGY OF CALCITE VEIN AND CLAY FORMATION

Calcite shows a variety of textural forms such as replacement of PDFs in quartz and inclusion in zeolite veins that contain small amounts of high-T hydrothermal minerals, consistent with

crystallization in an impact-induced hydrothermal system at 146 Ma; however, the grains are too small to date directly. The calcite veins in the upper part of the drillcore postdate all other hydrothermal features and give ages of 66.46 ± 0.74 (114 m), 28.1 ± 1.1 (144.09), 13.95 ± 4.32 (143.02 m) and 16 ± 47 Ma (131.9 m). Values for MSWD before removing outliers range between 6.6 and 32, and after outlier removal, the MSWD values range between 1.6 and 2.1, which is slightly lower than values reported for LA-ICPMS of low U and Pb speleothems matrices (cave carbonates) (Woodhead and Petrus, 2019). According to the criteria of Roberts et al. (2020), the U-Pb ages suggest a predominately well-behaved closed-system at 66.46 ± 0.74 (114 m), and minor evidence of open system behaviour, resulting in ages at 28.1 ± 1.1 (144.09 m) and 13.95 ± 4.32 (143.2 m). The 66 Ma U-Pb age lies within the error of clay K-Ar ages of 57.4 ± 7.14 Ma (119 m) and 59.45 ± 7.74 Ma (216 m), but is younger than the oldest clay age of 105.8 ± 4.4 Ma (214.4 – 214.5 m), suggesting two possibilities: either the veins and clays are impact-related and their isotopic systems were reset subsequently to different extents; or the ages indicate younger events that occurred at 110, 66, 30 and 19 Ma. Sample depth for clay K-Ar analysis shows no effect on resultant ages, but finer clay grain sizes yielded younger smectite-illite ages (Figure 4.34). Uysal et al. (2006) indicated that the grain size-age relationship can be attributed to thermal events or fault movements, as they are responsible for the loss of radiogenic ^{40}Ar in fine-grained clays. The smaller particle size and lower crystallinity favour argon diffusion, indicating that an earlier generation of illite underwent alteration or partial resetting (Uysal et al., 2006). This relationship is consistent with the observation that < 0.2 µm fractions with 57.4 ± 7.14 Ma (119 m) and 59.45 ± 7.74 Ma (216 m) yield younger K-Ar ages. The K – Ar age versus grain size shows an inclined age spectrum, which is described to arise from the presence of multiple generations of illite due to the resetting of earlier illite inherited from older rocks by younger illite minerals (Uysal et al., 2020). Therefore, the smectite-illite with a K – Ar age of 110 Ma could have been reset. Thus, its true age could be older than 110 Ma and maybe even exhibit the impact age of 146 Ma.

5.4. TRACE ELEMENT COMPOSITIONS OF VEIN CALCITE

5.4.1. Genetic relationships between calcites

Morphology and distribution of calcite within the M4 drillcore suggest that distinct types of calcite formed in microfractures, shock deformation features, and in cavities in the matrices of target rocks and impactites. Sub-horizontal calcite veins occur only at the upper part of the drillcore. While the calcite in PDFs, microcracks in quartz grains and within the matrices is texturally tied to the retrograde alteration seen in impact hydrothermal systems, the vein-hosted calcite is studied to understand its source(s) of fluids.

The four analyzed samples (M4 V1-4) also show no trend in $\delta^{13}C_{PDB}$–$\delta^{18}O_{SMOW}$ diagram (Figure 4.26). The data points are widely scattered, however, there seems to be two generations of calcite veins in each sample. The older generation of calcite veins in M4 V2-4 is identified by heavy oxygen isotopes (21.45 to 27.39 ‰), and the younger generation of calcite veins in M4 V2-4 is identified by light oxygen isotopes (19.00 – 21.81 ‰). These values overlap from sample to sample (i.e., the older generation in sample M4 V3 slightly overlaps with the younger generation in M4 V2). Calcite veins analyzed by Quandt et al. (2018), which exhibit similar morphologies as calcite veins in the M4 drillcore, suggest that transition in microtextures result from slight changes in fluid chemistry (Quandt et al., 2018) and possibly from differing modes of fracturing (Bons, 2000; Quandt et al., 2019). No C-O isotopic analyses were obtained on M4 S1(2) and M4 GG2, but based on their different REE anomalies (Figure 4.29), they clearly fall under a different generation from M4 V1 and younger calcite veins of M4 V2. Therefore, the MIS have multiple generations of calcite veins. The difference in REE patterns also suggests no genetic link. Mixing of fluids is possible (see Figure 4.26), and potential fluid sources should be explored further.

The ^{13}C values (-4 to -21 ‰) of MIS vein calcites are consistent with a freshwater source enriched in dissolved organic carbon (Talm and Rust, 1997), indicating that calcite veins may have formed under equilibrium with naturally occurring waters such as meteoric water (depleted ^{13}C) and possibly mixed with fluids from the dissolution of marine carbonates or low T metamorphic fluids

(Figure 4.26). Therefore, hydrothermal and marine sources are considered in Sections 5.4.2 and 5.4.3.

5.4.2. Influence of hydrothermal fluids

The M4 calcite vein samples display LREE-enriched total concentrations, which are characteristics of hydrothermal sources originating from meteoric water that interacted with geological formations (Bau, 1991). The enrichment of LREEs is seen in carbonate-rich fluids or alkaline fluids where CO_3^{2-} and OH^- species form complexes with REEs (Debruyne et al., 2016). Normally, hydrothermal fluids contain strong ligands such as OH^-, F^-, CO_3^{2-}, SO_4^{2-} and PO_4^{3-} available to bond with REE^{3+}, but also the REEs favour ligands with intermediate bonds such as Cl^- (Debruyne et al., 2016). The amount of Cl^- incorporated in one of the calcite vein sample (M4 V2) analysed by EMPA is very minor (< 0.01 wt.%). Figure 5.1 displays a *CHA*rge-*Ra*dius-*C*ontrolled (*CHARAC*) field, which represents trace elements Y-Ho with similar charge and radius behaving chemically the same and retaining a constant chondritic ratio of 27.7 ± 2.7 (Bau, 1996;1997). The field ranges from 24 < Y/Ho < 34 (Bau, 1996), and elemental ratios within the *CHARAC* field are considered normal for trace element behaviour that are *CHA*rge and *Ra*dius *C*ontrolled. Igneous rocks show Y/Ho ratios close to the chondritic ratios (Bau, 1996) and so is sample M4 S1 (2) and the majority (62%) of sample M4 GG2 (Figure 5.1), indicating CHARAC behaviour of Y/Ho in these two vein calcites are influenced by silicate melts. Samples M4 S1 (2) and M4 GG2 show a positive Eu anomaly, indicating formation in the reducing environment (Figure 5.1). The positive Eu anomaly is attributed to $Eu^{2+,}$ which occurs in poor-oxygen hydrothermal solutions where T > 200 ℃ (Sverjensky, 1989; Bau et al., 2010). The Two monomineralic calcite vein samples, M4 S1(2) and M4 GG2 are the only two samples influenced by only hydrothermal fluids (Figure 5.2).

The M4 calcite vein samples elemental ratios of Y/Ho (29.4 to 50.9; Table 4.4) fall above a chondritic Y/Ho ratio of 28 and thus display positive Y anomalies (Bau et al., 1996). The majority of M4 V1a (75 %), M4 V1b (100 %), M4 V1c (86 %) and M4 V2 (88 %) may indicate mixing of hydrothermal sources with marine sources (Figure 4.26). M4 V1 falls slightly in the oxidation field in the Y/Ho versus Eu/Eu* diagram (Figure 5.1; Quandt et al., 2019). The M4 V1 also shows a strong negative Ce anomaly, which is an indicator for oxic fluids (Bau et al., 1996; 2010). The

variation of Ce/Ce* is controlled by the redox sensitivity of Ce (Bau et al., 1996). Under oxidizing environments, Ce^{3+} oxidises to Ce^{4+}, which can be fractionated from other REE by particle absorption into authigenic marine carbonates and facilitated by sorption of Ce^{4+} to Fe^{-} and Mn-oxides (Bau and Dulski, 1996; Bau and Koschinsky, 2009). Therefore, negative Ce can also be produced in marine carbonates undergoing chemical alteration under oxic conditions (Tostevin et al., 2016).

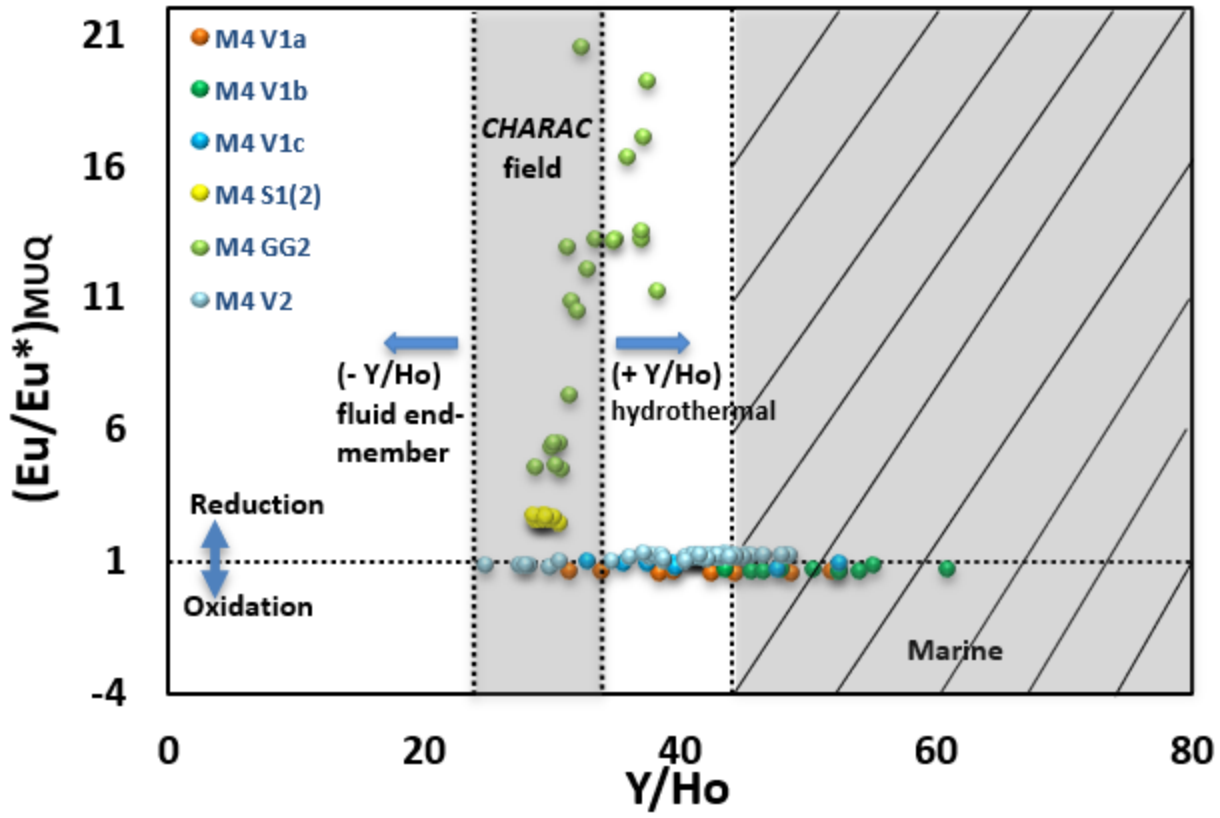


Figure 5.1. Y/Ho versus MUQ-normalised Eu anomalies (Eu/Eu) of calcite veins in the M4 drillcore. Hydrothermal and marine Y/Ho ratios refer to Bau and Dulski (1996) and Bau et al. (1996), respectively.*

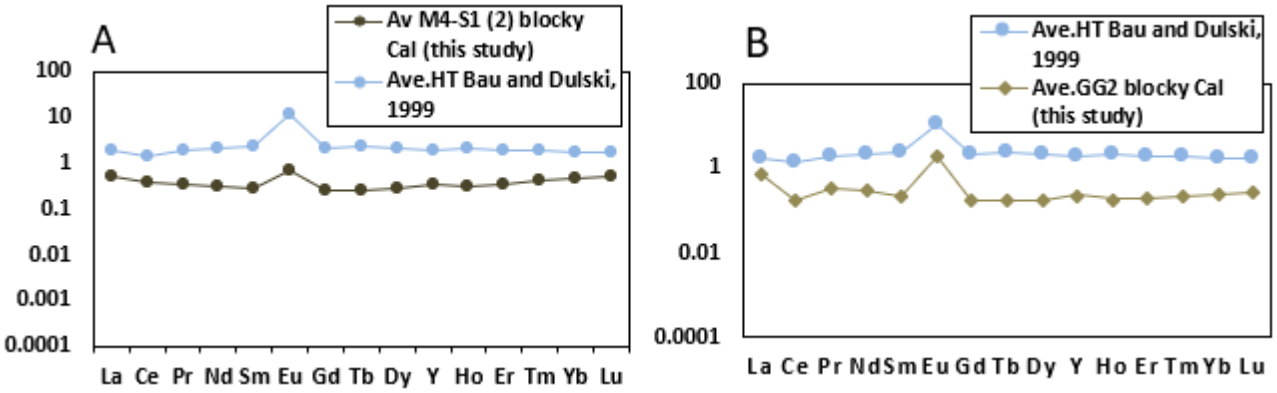


Figure 5.2. MUQ-normalised (mud sediments from Queensland) REE patterns of calcite veins in samples M4 S1(2) shown in A and M4 GG2 shown in B, matched with hydrothermal fluids (Bau and Dulski, 1999).

5.4.3. Influence of connate waters from marine carbonates

It has been noted that Y and Ho can be used to identify the origin and different fluid sources (Bolhar, 2004; Middleton et al., 2014). Marine carbonates have a Y/Ho of 44 – 74 (Bau et al., 1996). Only intra-sample M4 V1b with an average Y/Ho ratio of 50.9 lies within the marine carbonates range and shows the presence of Mg distribution (see Figure 5.3), a possible indicator for marine carbonates. Other intra-subsamples of M4 V2, M4 V1a and M4 V1c also have marine-like Y/Ho ratios, but the majority lies in hydrothermal field (Figure 5.1). Based on the $\delta^{18}O_{V\text{-}SMOW}$ - $\delta^{13}C_{V\text{-}PDB}$ diagram, M4 V1 and other calcite veins show a possible mixing between metamorphic fluids, marine carbonates and organic carbon from sedimentary carbonates (Figure 4.26). Marine trace element signatures may be incorporated into the calcite veins by leaching of REE by connate waters from marine carbonates; in the case of MIS, this would be either from rocks underlying or limestone and dolomite of the Campbell Rand Subgroup around the MIS. Marine carbonates are characterised by enrichment of HREE, positive La, Gd, and Y anomaly with negative Ce anomaly (Debruyne et al., 2016); geochemical signatures seen in samples of the M4 V1b do not resemble marine source (Figure 4.29B). But because the mixing of hydrothermal and marine fluids is proposed, then maybe HREE from the marine carbonate fluids were retained along the pathways.

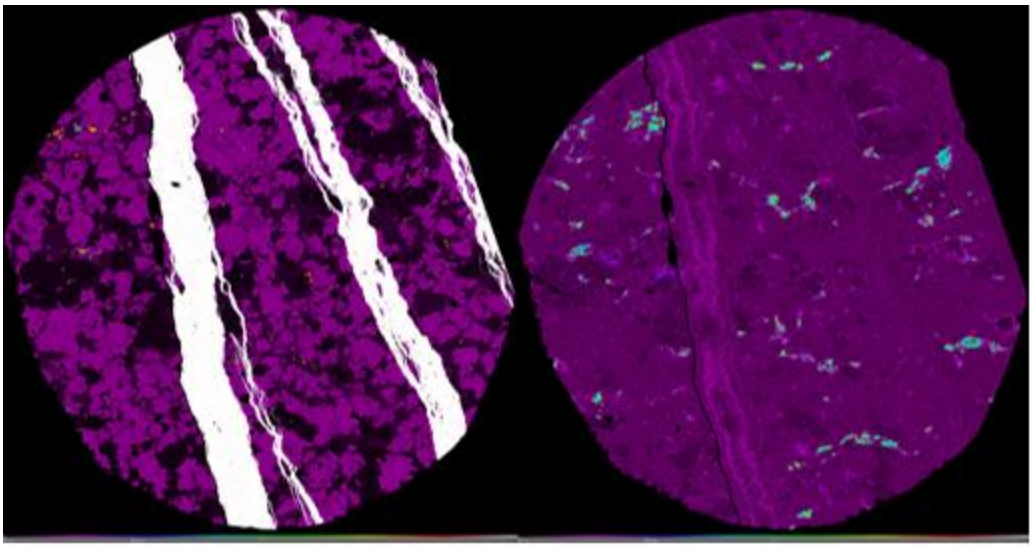


Figure 5.3. Elemental maps of calcite veins within a granodioritic gneiss from 114m showing Ca and Mg distribution.

M4 V1 elongated to blocky calcites match with carbonates from Uysal et al. (2011; Figure 5.4), which were interpreted to derive from tectonically-controlled carbonate vein growth, that was aided by episodic rupturing and subsequent sealing events (Figure 5.4). The Eu^{2+} as seen in M4 V1 calcite veins (Figure 4.29; Figure 5.4), does not indicate poor-oxygen hydrothermal solutions like in M4 S1 (2) and M4 GG2 (Figure 5.2), as these veins occurred under oxic conditions. Therefore, the Eu anomaly can also form under low-temperature (< 200°C) conditions during vein cementation, particularly when hydrothermal fluids interact with plagioclase-rich rocks (Sener et al., 2017).

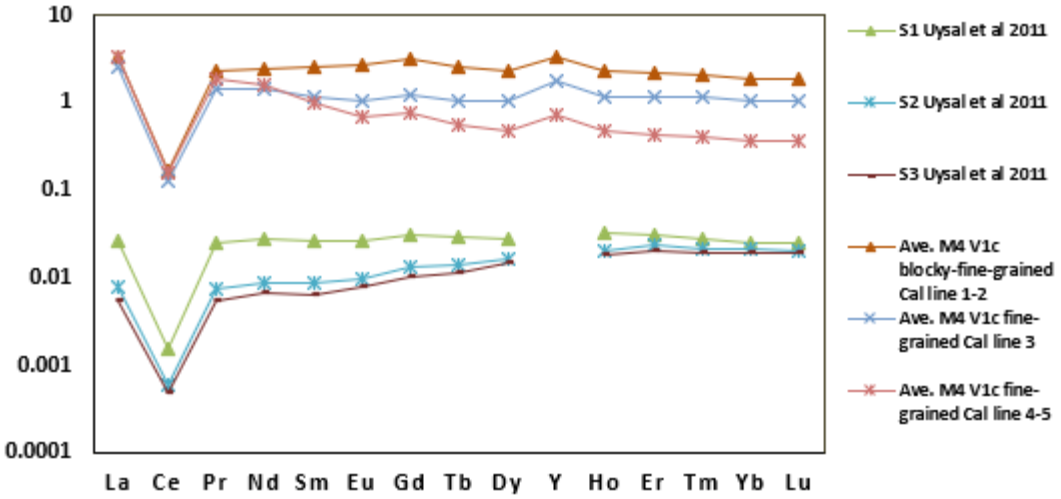


Figure 5.4. MUQ-normalised (mud sediments from Queensland) REE patterns of calcite veins in samples M4 V1C from calcite line 1 to line 5, matched with calcite veins from Uysal et al. (2011). S1-3 represents stage 1 of formation to stage 3.

If the connate water source from underlying rocks is considered, then M4 V1b might resemble dolomite due to its high Mg content (Figure 5.3). However, the distribution of Mg in M4 V1b is not seen in other calcite vein samples in the same vicinity. Therefore, high-Mg content might be derived locally. Y/Ho ratios as high as 30 might signify preferential sorption of REE, i.e., Ho relative to Y, into Fe and Mn oxyhydroxides along fluid pathways (Bau and Dulski, 1999; Debruyne et al., 2016). This phenomenon could be linked to petrographic evidence seen in M4 V1b illustrating calcite veins cutting through biotite rimmed by hydroxides (Figure 4.16H). Due to the lack of major element data for M4 V1b, and not enough evidence from other samples, M4 V1b is concluded to be calcite with Mg-content leached from the biotite along fluid pathways.

5.4.4. Temperature of calcite veins

As seen in microtextures, stable isotopic data, REEY and geochronology, the calcite veins are widely scattered and difficult to interlink. Therefore, temperatures are estimated for all possible fluid sources. Calcite veins in monomineralic blocky cement resembles that formed in hydrothermal fluids, as shown in Figure 5.2, which suggests temperatures above 200 ℃. The polymineralic calcite, i.e., calcite-zeolite and fibrous to elongate-blocky to fine-grained calcite veins formed under equilibrium with mixing of low T hydrothermal fluids and sedimentary

carbonate fluids (includes marine and non-marine settings). For polymineralic calcite veins, different fluid reservoirs would have to be assumed to predict the temperature of calcite veins. Obtaining the fluid reservoir can be done in two ways: 1) from known $\delta^{18}O$ values documented in existing literature and 2) by assuming the reservoir when the $\delta^{18}O$ of starting fluid is unknown and applying a range of fluid ^{18}O values.

Assuming that calcite formed under equilibrium with naturally occurring waters, then the expected temperature can be modelled from the Equation (O'Neill et al. 1969):

$$1000 \ln \alpha = 2.78 (10^6 T^{-2}) - 3.39 \quad (5.1)$$

T is in Kelvin and the fractionation factor (α) is determined from the literature, where α is

$$\frac{1000 + \delta^{18}O_{calcite}}{1000 + \delta^{18}O_{water}};$$

the $\delta^{18}O_{calcite}$ was measured in this study (19.00 and 27.39 ‰), but the $\delta^{18}O$ fluids are unknown or can be adapted from existing literature. The temperature at which the calcite forms is constrained by using possible fluid reservoirs.

5.4.4.1. Oxygen reservoir ranges and isotope temperature

The basement of the MIS comprises primarily Neoarchean granitoid gneisses. Metamorphic fluids from granitoids have a range of $\delta^{18}O$ values of 6 to 13 ‰ (Bindeman, 2021). Therefore, the metamorphic fluids leached from granitoids suggest that the T evolved from 125.5 to 140.7 ℃. The granitoids in some areas are overlain by the Transvaal-Griqualand West Supergroup, which contains tidal flat carbonates and shallow marine deposits. Assuming the underlying rocks and marine carbonate rocks surrounding the MIS contributed to the formation of calcite veins, the $\delta^{18}O$ values of these underlying rocks must be used as a source for marine source influence. Jonker and Abiye (2017) estimated these marine carbonate aquifers to have $\delta^{18}O$ values of -5.93 and -4.62 ‰ and using Equation 5.1, the temperature of formation is estimated to range between 8.5 and 41.1 ℃.

More recent work by R.L. Gibson (per comms., 2024) suggests that calcite veining may be present in the lower part of the Kalahari Group sediments in the borehole WF05 from the MIS, although this observation is not seen in the M4 drillcore due to core loss. If this is true, then it could mean that the calcite veining is related to meteoric waters associated with the formation of the Kalahari Basin. Meteoric water from freshwater has a ^{13}C-depleted carbon isotope value (Veizer and Hoefs, 1976; Talma and Rust, 1997; Hoefs, 2009), which agrees with ^{13}C values (-4 to -21 ‰) of MIS vein calcites. In addition, carbonates precipitating from freshwater form low-Mg calcite cement (James and Choquette, 1984; Hays and Grossman, 1991), a signature seen in the MIS calcite veins. Thus, $\delta^{13}C$ for the MIS M4 calcites is an indicator of a meteoric source. Therefore, the temperature of equilibration with meteoric waters can be estimated by using Equation 5.2 below from Hays and Grossman (1991).

$$T_{°C} = 15.7 - 4.36(\delta^{18}O_{cl} - \delta^{18}O_w) + 0.12(\delta^{18}O_{cl} - \delta^{18}O_w) \quad (5.2)$$

Values for $\delta^{18}O_{cl}$ are measured calcite values and values for $\delta^{18}O_w$ are derived from parental fluid source and T stands for temperature. In the equation, the $\delta^{18}O_w$ is given in SMOW and $\delta^{18}O_{cl}$ in PDB; therefore, the measured $\delta^{18}O_{cl}$ are converted from SMOW to PDB using the Equation 5.3 by Coplen et al., 1983.

$$\delta^{18}O_{PDB} = 0.97002\delta^{18}O_{SMOW} - 29.98 \quad (5.3)$$

Sources for meteoric fluids are groundwater, lakes, glaciers and rainwater. Groundwater is recharged by rainwater, rivers and lakes. Unfortunately, the groundwater aquifer in the Kalahari Basin has been difficult to constrain due to highly variable recharge rates (Abiye et al. 2021). However, the average $\delta^{18}O_w$ of groundwater in the Kalahari Basin ranges between -9.8 and -4 ‰, and the $\delta^{18}O_{cl}$ of the M4 calcite veins ranges between -11.55 and -3.41 ‰. Therefore, the M4 calcite veins are estimated to have formed at a low T of 13.2 to 23.1 ℃. No literature exists on isotopic composition of rainfall occurrences, surface and lakes or rivers and streams around the Morokweng Impact Structure for comparison.

5.5. COMPARISON WITH OTHER IMPACT STRUCTURES

5.5.1. Chicxulub impact structure

The Chicxulub impact crater, formed approximately 66 million years ago and measuring about 180 km in diameter, resides within the northern Yucatán Peninsula and the southern Gulf of Mexico basin (Simpson et al., 2020). This impact structure formed in a marine setting, while the Morokweng Impact Structure (MIS) is a terrestrial impact. Drilling of the M0077A drillcore has penetrated ~830 m deep into Chicxulub's peak ring, revealing structural characteristics and shock metamorphism (Simpson et al., 2020). Some similarities with the M4 drillcore of the Morokweng Impact Structure were observed by Gibson et al. (2019; 2024a), particularly parallels in lithology and shock metamorphism between the two impact structures, suggesting significant geological alteration processes at play within both impact structures.

Abramov and Kring (2007) and Simpson et al. (2015; 2020) analyzed the peak-ring setting of Chicxulub impact structure. Simpson et al. (2020) noted pervasive and intense alteration of glass-rich deposits in areas with high porosity and permeability, which are dominated by clay minerals. A spatial distribution of hydrothermal alteration involving alkali feldspar, zeolite, Fe-Mg smectites and carbonates was noted. The carbonates are dominated by calcite and occurred in the latter phase of hydrothermal mineralization at < 200 ℃. They are commonly associated with zeolite, a pattern seen in the MIS. The calcites at Chicxulub are characterised by high-Mg and high-Mn, whereas MIS calcites are characterised by low-Mn and low-Mg (analyzed calcites are not linked to the impact but hydrothermal calcites exist). Temperature models estimated maximum temperatures at 220℃ and suggested the cooling may persist up to 1.5 to 2.3 Myr for a 180 Km crater (Abramov and Kring, 2007). For comparison, the 35 km Manson impact structure is modelled to have taken up to 1 Myr to cool (McCarville and Crossey, 1996). Therefore, 70 km Morokweng impact structure can be inferred to cool between 1 to 1.5 Ma. The source of fluids for the Chicxulub impact structure is a mixture of impact melt and cold seawater (Osinski et al., 2020b; Simpson et al., 2020). The Morokweng Impact Structure, on the other hand, may have cooled by circulation of meteoric fluids, followed by later mixing of low-T alteration due to hydrothermal fluids with marine carbonate-rich fluids and groundwater influx.

5.5.2. Puchezh-Katunki structure

The Puchezh-Katunki structure formed at 195.9 ± 1.0 Ma (Holm-Alwmark et al. 2021). The crater diameter is the same as the Morokweng Impact Structure (~80 km) and both are terrestrial impact structures. The extensive and deep drilling data from Puchezh-Katunki allows full study of temperature versus depth. Evidence for hydrothermal alteration in the Puchezh-Katunki structure (Naumov, 2002; 2005) and numerical modelling (e.g. Abramov and Kring, 2007) suggest that the initial post-impact geothermal gradient was >100 °C vertically, with post-impact hydrothermal temperature distribution ranging between 50 and 350 °C.

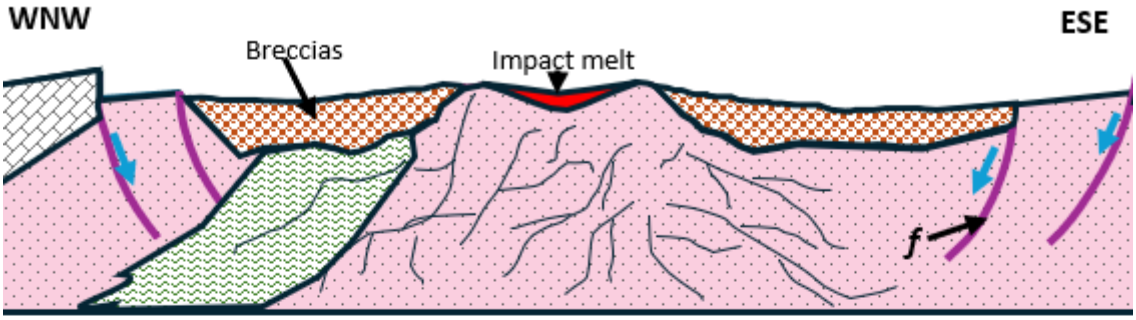
The Puchezh-Katunki structure exhibits the vertical zonation of post-impact hydrothermal alteration due to thermal gradients (Naumov, 2005) proposed for large-impact structures (Kirsimae and Osinski et al., 2013). The Na-zeolite is more abundant in the upper parts of the drillcore, then followed by Na-Ca zeolites in the middle parts and Ca-zeolite in the lower parts of the drillcore (Naumov, 2005). The M4 drillcore is dominated by Ca-heulandite and Ca-chabazite (± Na). Ca-chabazite often occurs with minor alteration of Ca-laumontite in vugs and vein margins (Masiu, 2025, unpublished data). The substitution of calcite by anhydrite downward can be observed in the M4 drillcore and is similar to what has been observed in the Puchezh-Katunki structure.

5.6. IMPLICATIONS FOR REGIONAL TECTONIC SETTING

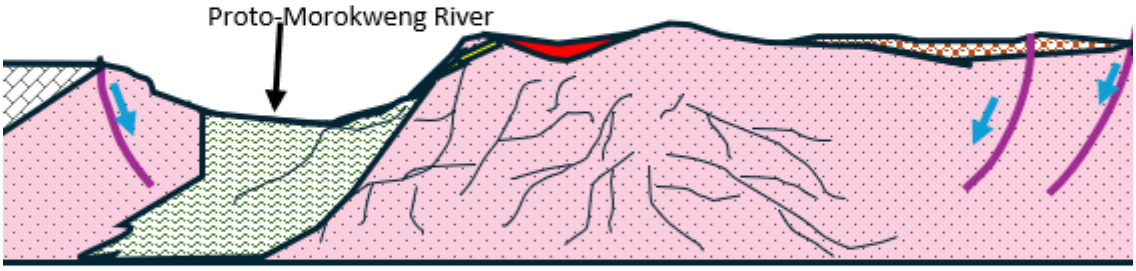
The region around the Morokweng Impact Structure is strongly affected by dykes (Anhaeusser et al., 2010), including one dyke that appears to postdate the impact (Westgate et al., 2021). The MIS was affected by tectonic events that led to erosion and uplift post-146 Ma. This includes Early Cretaceous rifting between 135 – 114 Ma (Jelsma et al., 2009; Westgate et al., 2021), which resulted in the uplift and erosion of the interior of southwestern Africa and uplift along the Etosha-Griqualand-Transvaal axis (Partridge et al., 2006). The uplifted areas resulted in a drainage system that continued to flow until the end of the Cretaceous (86-65 Ma; Partridge et al., 2006). These rivers flanked the neighbouring regions, including the Morokweng impact structure that was cut by the proto-Morokweng River (Karoo River) in the Mid-Late Cretaceous (Partridge, 1998; Haddon, 2005).

The Campanian-Maastrichtian rifting events reactivated faults at ±80 – 65 Ma extending down to Archaean basement rocks and Transvaal-Griqualand Supergroup rocks indicating widespread tectonic influences in the region (Partridge et al., 2006; Westgate et al., 2021). Thus, waters from the drainage systems eroded and infiltrated the rocks underlying the MIS. Although no age data for the Machavie dyke, it cuts the MIS and, thus, may have influenced the hydrothermal fluids within the structure. The reactivation of faults under extensional and compressional stress regimes continued until the Cenozoic Epoch (Westgate et al., 2021). This resulted in notable uplift of the Kalahari basin at 30 Ma (Partridge et al., 2006) and subsequent erosion and uplift at ~23 Ma. Vertebrate fossils contained in the reworked gravel sediments formed by an active major valley system of the Orange River and its distributaries suggest formation at 17 – 15 Ma (Partridge et al., 2006). The sub-catchment of the Orange River includes the Molopo River (233,200 Km^2), Vaal River (193 780 Km^2), Orange River itself (356,230 Km^2) and Fish River (108, 780 Km^2) (Zawada et al., 1996). The flooding of the Orange River may have influenced the sub-catchment closest to the MIS (i.e., Vaal River) to infiltrate the crater. This geological setting is consistent with the meteoric source that preceded deposition of the Kalahari Group sediments, influencing local hydrogeological conditions (Figure 5.5).

MIS evolution after the meteorite impact (≤ 145 Ma) : Formation of a complex structure, characterized by intense fracturing, enabling the infiltration of impactites through the fractures.



Post-impact calcite vein processes (≤ 66 Ma): Erosion by drainage system resulted in the penetration of fluids into the underlying lithologies, leading to the deposition and cementation of calcite veins.



Late-stage evolution (≤ 30 Ma): Continued erosion and uplift facilitated the formation of late calcite veins. Subsequently, the MIS was buried under the Kalahari Group sediments.

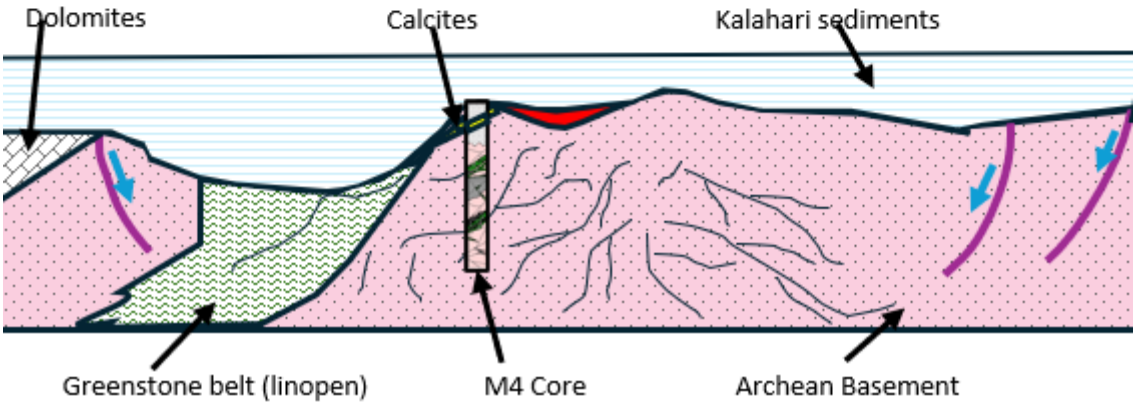


Figure 5.5. Schematic proposed exhumation-related events around the Morokweng impact structure region.

The timing of M4 calcite vein formation, namely at 66 Ma ± 0.72, coincides with reported episodes of extensional and compressional tectonic activity from the Cretaceous to the Mesozoic (Westgate et al., 2021). Specifically, reactivations occurred at 66 Ma (Partridge et al., 2006; Westgate et al., 2021). The formation of the veins in M4 V1 sample with 66 Ma year age, show similar formation events reported by Uysal et al. (2011). In monomineralic blocky calcite veins from samples M4 S1 (2) and M4 GG2 resemble a onefold crack and seal nature that indicates an opening caused by extensional forces seen in blocky calcites (Quandt et al., 2018; 2019). The 28.1 ± 1.1, and 13.95 ± 4.32 Ma, coincides with paleo-uplifts in the region. Therefore, their formation is attributed to cycles of uplift by tectonic processes and erosion events. These exhumation-related stress-release joints opened sub-horizontally in the granitoid rocks after the removal of overburden, which caused the release of stress in the underlying rocks.

5.7. RECOMMENDATIONS AND FUTURE WORK

This study outlines the geochronology and geochemistry of post-impact hydrothermal alteration within the MIS. Based on the age of impact-induced hydrothermal alteration, titanite grains could potentially be dated, although they may have been affected by alteration. Additionally, temperatures can also be inferred from chlorite and titanite thermobarometry. A fluid inclusion study on calcite cleavage planes is also recommended to achieve more accurate temperature reconstructions of calcite veins.

6. CONCLUSIONS

The Morokweng Impact Structure is cut by post-impact hydrothermal zeolite veins. These contain high-T minerals clinopyroxene, andradite, actinolite, titanite and low-T minerals magnetite/haematite, anhydrite, smectite and calcite; additionally, monomineralic anhydrite and calcite veins and calcite-zeolite veins are observed. Calcite veins occur as the last phase in different morphologies and are limited to the upper section of the drillcore. The microtextural differences between calcite veins range from fibrous/stretched to elongate-blocky to blocky calcite and fine-grained calcites and are attributed to the mode of fracturing.

Carbon and oxygen isotopic compositions indicate mixing among metamorphic fluids and marine carbonates. Thus, calcite veins were formed at temperatures > 200 ℃ in hydrothermal solutions and under low-T fluids < 140.7 ℃. These calcite veins typically exhibit low Mg content (except for one sample showing high Mg) and contain Mn and high Fe. Geochemical anomalies of rare earth elements (REE) such as Ce, Eu, La and Y vary from sample to sample, indicating changes in fluid chemistry.

Extensional stress regimes and erosional exhumation occurred during the late Cretaceous period at 86 – 65 Ma (Partridge et al., 2006; Westgate et al., 2021) and again during the Early Oligocene to Early Miocene period at 30, 23 and 17 – 15 Ma (Partridge et al., 2006). These periods broadly coincide with calcite U-Pb ages of 66.46 $\pm$ 0.74, 16 $\pm$ 47, 28.1 $\pm$ 1.1, and 13.95 $\pm$ 4.32 Ma. The older calcite vein coincides with smectite-illite clay ages of 57.4 ± 7.14 Ma (119 m) and 59.45 ± 7.74 Ma (216 m). Two other smectite-illite clay samples yield ages of 105.8 ± 4.4 Ma (214.4 – 214.5 m) and 68.9 ± 48.9 Ma (121.8 m). The K-Ar isotopic system of smectite-illite clays were reset. This study incorporated vein microtextures, stable isotopic compositions, trace element data and radiometric dating to unravel the history of post-impact alteration of calcite veins within the Morokweng impact structure.

7. REFERENCES

Abramov, O. and Kring, D. A. (2007). Numerical modelling of impact-induced hydrothermal activity at the Chicxulub crater. Meteoritics Planetary Science, 42, pp. 93–112.

Abiye, T., Verhagen, B., Freese, C., Harris, C., Orchard, C., van Wyk, E., Tredoux, G., Pickles, J., Kollongei, J., Xiao, L., Levin, M., Butler, M., Diamond, R., Grellier, S., Talma, S., Lorentz, S., Chaplot, V. and Xu, Y. (2013). The use of isotope hydrology characterise and assess resources in South(ern) Africa. Water Research Commission, TT 570/13

Aldahan, A. A. (1990). Alteration and mass transfer in cataclasites and mylonites in 6.6 km of granitic crust at the Siljan impact structure, central Sweden. Contributions to Mineralogy and Petrology, 105, pp. 662–676.

Andreoli, M.A.G., Ashwal, L.D., Hart, R.J. and Huizenga, J.M. (1999a). A Ni and PGE-enriched quartz norite impact melt complex in the Late Jurassic Morokweng impact structure, South Africa, in: Dressler, B.O., and Sharpton, V.L. Large Meteorite Impacts and Planetary Evolution II, Geological Society of America, Special Papers, 339, pp. 91-108.

Andreoli, M. A .G., Hart, R. J., Cooper, G. R. J., Stengel, I., Webb, S., Haddon, I., Skala, R. and Viola, G. (2007). The 144 Ma Morokweng impact crater, South Africa: geophysical and borehole evidence for a ~240 km structure. 10th SAGA Biennial Conference, ISBN: 978-0-620-38241.

Andreoli, M. A. G., Hart, R. J., Cooper, R. J. G. and Webb, S. (2008). The Morokweng impact crater, South Africa: A large complex, multiring structure with a ~ 130 km radius external ring and asymmetric radial sectors. Large Meteorite Impacts and Planetary Evolution IV, Abstract 3048.

Anhaeusser, C. R., Stettler, E., Gibson, R. L. and Cooper, G. R. J. (2010). A possible Mesoarchaean impact structure at Setlagole, North West Province, South Africa: Aeromagnetic and field evidence. South African Journal of Geology,113, pp. 413-436.

Barrat, J. A., Bayon, G. and Lalonde, S., (2023). Calculation of cerium and lanthanum anomalies in geological and environmental samples. Chemical Geology, 615, pp.121202.

Bau, M. (1991). Rare-earth element mobility during hydrothermal and metamorphic fluid-rock interaction and the significance of the oxidation state of europium. Chemical Geology, 93, pp. 219–230.

Bau, M. (1996). Controls on the fractionation of isovalent trace elements in magmatic and aqueous systems: evidence from Y/Ho, Zr/Hf, and lanthanide tetrad effect. Contrib. Mineral. Petrol. 123, pp. 323–333.

Bau, M. (1997). The lanthanide tetrad effect in highly evolved felsic igneous rocks – a reply to the comment by Y. Pan. Contrib. Mineral. Petrol. 128, pp. 409–412.

Bau, M. and Dulski, P. (1996). Comparative study of yttrium and rare-earth behaviors in fluorine-rich hydrothermal fluids. Contributions to Mineralogy and Petrology, 119, pp. 213–223.

Bau, M. and Dulski, P. (1999). Comparing Yttrium and Rare Earths in Hydrothermal Fluids from the Mid-Atlantic Ridge: Implications for Y and REE Behaviour during Near Vent Mixing and for the Y/Ho Ratio of Proterozoic Seawater. Chemical Geology, 155, pp. 77-90.

Bau, M. and Koschinsky, A. (2009). Oxidative scavenging of cerium on hydrous Fe oxide: evidence from the distribution of rare earth elements and yttrium between Fe oxides and Mn oxides in hydrogenetic ferromanganese crusts. Geochemical Journal, 43, pp. 37–47.

Bau, M. and Möller, P. (1992). Rare Earth Element Fractionation in Metamorphogenic Hydrothermal Calcite, Magnesite and Siderite*.

Bau, M., Balan, S., Schmidt, K. and Koschinsky, A. (2010). Rare earth elements in mussel shells of the Mytilidae family as tracers for hidden and fossil high-temperature hydrothermal systems. Earth Planet. Sci. Lett.299, 310–316.

Bau, M., Koschinsky, A., Dulski, P. and Hein, J. R. (1996). Comparison of the partitioning behaviours of yttrium, rare earth elements, and titanium between hydrogenetic marine

ferromanganese crusts and seawater. Geochimica et Cosmochimica Acta, 60(10), pp. 1709-1725.

Beccaluva, L., Bianchini, G., Natali, C. and Siena, F. (2020). Plume-related Paranà-Etendeka igneous province: An evolution from plateau to continental rifting and breakup. Lithos, 105484, pp. 362 – 363.

Bindeman, I.N. (2021) Triple Oxygen Isotopes in Evolving Continental Crust, Granites, and Clastic Sediments. Mineralogy and Geochemistry, 86, pp. 241-290.

Bolhar, R., Kamber, B. S., Moorbath, S., Fedo, C. M. and Whitehouse, M. J. (2004). Characterisation of early Archaean chemical sediments by trace element signatures. Earth and Planetary Science Letters, 222(1), pp. 43-60.

Bons, P. D. (2000). The formation of veins and their microstructures. In: Jessell, M.W., Urai, J.L. (Eds.), Stress, Strain and Structure, A Volume in Honour of W D Means. Journal of the Virtual Explorer (on-line).

Bons, P. D., Elburg, M. A. and Gomez-Rivas, E. (2012). A review of the formation of tectonic veins and their microstructures. Journal of Structural Geology, 43, pp. 33–62.

Botha, B. J. V., Thomas, M. A., Malherbe, S. J., Thomas, R. J. (1986). Aspects of the Tertiary and Quaternary geology of Gordonia, Northern Cape Province. Annals Geological Survey of South Africa, 20, pp. 41-44.

Broom-Fendley, S., Heaton, T., Wall, F. and Gunn, G. (2016). Tracing the fluid source of heavy REE mineralisation in carbonatites using a novel method of oxygen-isotope analysis in apatite: The example of Songwe Hill, Malawi. Chemical Geology, 440, pp. 275–287.

Cao, C., Liu, X.-M., Bataille, C. P., & Liu, C. (2020). What do Ce anomalies in marine carbonates really mean? A perspective from leaching experiments. Chemical Geology, 532, 119413.

Chen, C. and Sun, W. (2017). Tracing the origin of peak rings at Chicxulub. Solid Earth Sciences 2. pp. 63 – 64.

Cho, M., Maruyama, S. and Liou, J. G. (1987). An experimental investigation of heulandite-laumontite equilibrium at 1000 to 2000 bar P_{fluid}. Contributions to Mineralogy and Petrology, 97, pp. 43–50.

Collins, G. S., Melosh, H. J. and Osinski, G. R. (2012). The impact-cratering process. Elements, 8(1), pp. 25-30.

Coplen, B. T., Kendall, C. and Hopple, J. (1983). Comparison of stable isotope reference samples. Nature, 302, pp. 236-238.

Cornell, D. H., Minnaar, H., Frei, D. and Kristoffersen, M. (2018). Precise microbeam dating defines three Archaean granitoid suites at the southwestern margin of the Kaapvaal Craton. Precambrian Research, 304, pp. 21-38.

Corner, B., Reimold, W. U., Brandt, D. and Koeberl, C. (1997). Morokweng impact structure, Northwest Province, South Africa: Geophysical imaging and some preliminary shock petrographic studies. Earth and Planetary Science Letters, 146, pp. 351-364.

Cox, M. A., Erickson, T. M., Schmieder, M., Christoffersen, R., Ross, D. K., Cavosie, A. J., Bland, P. A., Kring, D. A. and IODP–ICDP Expedition 364 Scientists. (2020). High resolution microstructural and compositional analyses of shock deformed apatite from the peak ring of the Chicxulub impact crater. Meteoritics and Planetary Science, 55, pp. 1715-1733.

Crossey, L. J., Kudo, A. M. and McCarville, P. (1994). Post-impact hydrothermal systems: Manson impact structure, Manson, Iowa [abs]. In: Lunar and Planetary Sciences XXV, pp. 299–300.

Dalrymple, G. B. and Lanphere, M. A. (1969). Potassium-argon dating, W.H. Freeman, San Francisco, pp. 258.

de Beer, J.H. and Blume, J. (1985). Geophysical and hydrogeological investigations of the ground-water resources of western Hereroland, South West Africa/Namibia. Transactions Geological Society of South Africa, 88, pp. 483-493.

Dickin, P. A. (1997). Radiogenic Isotope Geology. Cambridge University Press, Cambridge, 2, pp. 490.

Duuring, P., Rowins, S. M., McKinley, B. S. M., Dickinson, J. M., Diakow, L. J., Kim, Y.-S. and Creaser, R. A. (2009). Magmatic and structural controls on porphyry-style Cu–Au–Mo mineralization at Kemess South, Toodoggone District of British Columbia, Canada. Mineralium Deposita, 44(4), pp. 435–462.

Dressler, B. (1990). Shock metamorphic features and their zoning and orientation in the Precambrian rocks of the Manicouagan structure, Quebec, Canada. Tectonophysics, 171, pp. 229–245.

Drost, K., Chew, D., Petrus, J. A., Scholze, F., Woodhead, J. D., Schneider, J. W. and Harper, D. A. (2018). An image mapping approach to U-Pb LA-ICP-MS carbonate dating and applications to direct dating of carbonate sedimentation. Geochemistry, Geophysics, Geosystems, 19(12), pp. 4631-4648.

Encarnacion, J., Fleming, T. F., Elliot, D. H. and Eales, H. V. (1996). Synchronous emplacement of Ferrar and Karoo dolerites and the early breakup of Gondwana. Geology 24: pp. 535 – 538.

Fakudze, B. B. (2020). Integrated physical property studies of the Morokweng Structure M4 core, Honours project. pp. 77.

Farver, R. J. (1994). Oxygen self-diffusion in calcite: Dependence on temperature and temperature and water fugacity. Earth and Planetary Science Letters, 121, pp. 575-587.

Ferrière, L. and Osinski, G. R. (2012). Shock Metamorphism, Impact Cratering: Processes and Products, pp 106-124.

French, B. M. (1998). Traces of Catastrophe: A Handbook of Shock-Metamorphic Effects in Terrestrial Meteorite Impact Structures. Lunar and Planetary Institute Contribution, 954, pp. 120.

French, B. M. and Koeberl, C. (2010). The convincing identification of terrestrial meteorite impact structures: What works, what doesn't, and why. Earth-Science Reviews, 98(1), pp. 123-170.

Gallegos, Z. E., Newsom, H. E., Crossey, L. J., Vaniman, D. T., Osinski, G. R. and Lee, P. (2015). Interpreting Impact-induced Hydrothermal geochemistry using Authigenic mineral assemblages. 46th Lunar and Planetary Science Conference: 2892.

Gat. J. R. (1996). Oxygen and hydrogen isotopes in the hydrologic cycle, Earth planetary, 24, pp. 225-262.

Gibson, R. L., Wela, S. S. and Andreoli, M. A. G., (2017). Origin of suevite by mechanical mixing of friction melt and cataclasites during peak ring formation in the Morokweng impact structure, South Africa. Abstract 1364, Lunar and Planetary Science Conference XLVIII.

Gibson, R. L., Wela, S. S. and Andreoli, M. A. G. (2019). Structural analysis of the M4 drill core, Morokweng impact structure (South Africa) – implications for peak ring formation processes. In: Large Meteorite Impacts and Planetary Evolution Conference VI. Abstract #5051.

Gibson, R. L., Wela, S. S., Bybee, G. M., Frei, D. and Andreoli, M. A. G. (2022). Granitoid gneisses of the Morokweng impact structure: Implications for Neoarchaean evolution of the western Kaapvaal craton. Lithos, pp. 426-427, 106793.

Gibson, R. L., Wela, S. S., Rae, A. S. P. and Andreoli, M. A. G. (2024a). Shock petrographic and numerical modeling constraints on the morphology and size of the Morokweng impact structure, South Africa. Meteoritics and Planetary Science, 59(12), pp. 3250-3281.

Gibson, R. L., Wela, S. S., Vonopartis, L. and Andreoli, M. A. G. (2024b). Melt breccias in parautochthonous basement rocks of the Morokweng impact structure, South Africa – evidence for a friction origin. Journal of African Earth Sciences, 214, 105239.

Grieve, R. A., Langenhorst, F. and Stöffler, D. (1996). Shock metamorphism of quartz in nature and experiment: II. Significance in geoscience. Meteoritics and Planetary Science, 31, pp. 6-35.

Goetz, F. H. A., Vane, G., Solomon, E. J. and Rock, N. B. (1985). Imaging spectrometry for Earth Remote Sensing. Science, 228(4704), pp. 1147-1153.

Guo, L., Hou, L., Liu, S. and Nie, F. (2018). Rare Earth Elements Geochemistry and C–O Isotope Characteristics of Hydrothermal Calcites: Implications for Fluid-Rock Reaction and Ore-Forming Processes in the Phapon Gold Deposit, NW Laos. Minerals, 8(10), pp. 438.

Haddon, I. G. (2004). The sub-Kalahari Geology and Tectonic Evolution of the Kalahari basin, Southern Africa. University of the Witwatersrand, Johannesburg, pp. 343 (PhD thesis).

Haddon, I. G. and McCarthy, T. S. (2005). The Mesozoic – Cenozoic interior sag basins of Central Africa: the Late-cretaceous – Cenozoic Kalahari and Okavango basins. Journal of African Earth Sciences, 43, pp. 316–333.

Hanson, E. K., Moore, J. M., Bordy, E. M., Marsh, J. S., Howarth, G. and Robey, J. V. A. (2009). Cretaceous erosion in central South Africa: Evidence from upper-crustal xenoliths in kimberlite diatremes. South African Journal of Geology, 112, pp. 125-140.

Hargitai, H., Reimold, W. U. and Bray, V. J. (2015). Impact structure, Encyclopedia of Planetary Landforms, 2, pp. 988 – 1023.

Hart, R. J., Andreoli, M. A. G., Tedious, M., Moser, D., Shawl, L. D., Edie, E. A., Webb, S. J. and Brandt, D. (1997). Late Jurassic age for the Morokweng impact structure, southern Africa, Earth Planetary Science Letters, 147, pp 25 – 35.

Hart, R. J., Cloete, M., McDonald, I., Carlson, R. W. and Andreoli, M. A. G. (2002). Siderophile-rich inclusions from the Morokweng impact melt sheet, South Africa: possible fragments of a chondritic meteorite. Earth and Planetary Science Letters, 198, pp. 49 - 62.

Hays, D. P. and Grossman, L. E. (1991). Oxygen isotopes in meteoric calcite cements as indicators of continental paleoclimate. Geology, 19 (5), pp. 441 – 444.

He, Z., Wang, X., Xiao, X., Wan, X., and Wei, Q. (2022). The Origin of Carbonate Components in Carbonate Hosted Pb-Zn Deposit in the Sichuan-Yunnan-Guizhou Pb-Zn Metallogenic Province and Southwest China: Take Lekai Pb-Zn Deposit as an Example. Minerals, 12, pp. 1615.

Henkel, H., Reimold, W. U., and Koeberl, C. (2002). Magnetic and gravity model of the Morokweng impact structure. Journal of Applied Geophysics, 49 (3), pp. 129-147.

Hill, C. A., Polyak, V. J., Asmerom, Y. and Provencio, P. P. (2016). Constraints on a Late Cretaceous uplift, denudation, and incision of the Grand Canyon region, southwestern Colorado Plateau, USA, from U-Pb dating of lacustrine limestone. Tectonics, 35, pp. 896–906.

Hickman-Lewis, K., Cavalazzi, B., Sorieul, S., Gautret, P., Foucher, F., Whitehouse, M. J. and Westall, F. (2020). Metallomics in deep time and the influence of ocean chemistry on the metabolic landscapes of Earth's earliest ecosystems. Scientific Reports, 10(1).

Hoefs, J. (2009). Stable isotope geochemistry, 6th edition, Springer-Verlag Berlin Heidelberg, ISBN: 978-3-540-70703-5.

Holm-Alwmark, S., Jourdan, F., Ferrière, L., Alwmark, C. And Koeberl, C. (2021). Resolving the age of the Puchezh-Katunki impact structure (Russia) against alteration and inherited $^{40}Ar^{*}$ – No link with extinctions. Geochimica et Cosmochimica Acta, 301, pp. 116 – 140.

James, P. N. and Choquette, W. P. (1984). Diagenesis 9. Limestones - The Meteoric Diagenetic Environment. Geoscience Canada, 11, 4, pp. 160 – 194.

Jelsma, H., Barnett, W., Richards, S. and Lister, G. (2009). Tectonic setting of kimberlites. Lithos, 112 (1), pp. 155 – 165.

Jonker, B. and Abiye, T. A. (2017). Groundwater potential in the Kalahari region of South Africa. South African Journal Geology, 120, pp. 385–402.

Kamber, B. S., Greig, A. and Collerson, K. D. (2005). A new estimate for the composition of weathered young upper continental crust from alluvial sediments, Queensland, Australia. Geochimica et Cosmochimica Acta, 69(4), pp. 1041-1058.

Kempe, U. and Götze, J. (2002). Cathodoluminescence (CL) behaviour and crystal chemistry of apatite from rare-metal deposits, Mineralogical magazine, 66(1), pp. 151 – 172.

Kirsimae, K. and Osinski, G. R. (2013). Impact-Induced Hydrothermal Activity. Impact Cratering: Processes and Products, First Edition, pp. 76-89.

Kenkmann, T., Collins., G. S., and Wunnemann, K. (2013). The Modification Stage of Crater Formation. Impact Cratering, pp. 60 – 75.

Kenkmann, T. and Artemieva, N. (2021). The terrestrial impact crater record: A statistical analysis of morphologies, structures, ages, lithologies, and more. Meteoritics & Planetary Science, 56(5), pp. 1024–1070.

Kenny, G. G., Harrigan, C. O., Schmitz, M. D., Crowley, J. L., Wall C. J., Andreoli, M. A. G., Gibson, R. L. and Maier W. D. (2021). Timescales of impact melt sheet crystallization and the precise age of the Morokweng impact structure, South Africa. Earth and Planetary Science Letters, 567, 117013.

Khumalo, B. K., Ashwal, D. L., Hayes, B., Iaccheri, M. L., Meintjes, P. G. and Webb, J. S. (2024). Neoarchean lavas of the Ventersdorp Large Igneous Province, South Africa: Sr-Nd-Hf isotopic and trace element evidence for a long-lived plume beneath a stationary African Continent. Earth-Science Reviews, 252, 104752.

Koeberl, C., Armstrong, R. A. and Reimold, W. U. (1997). Morokweng, South Africa: A large impact structure of Jurassic-Cretaceous boundary age. Geology, 25, pp. 731-734.

Koeberl, C. and Reimold, W. U. (2002) Geochemistry and petrography of impact breccias and target rocks from the 145 Ma Morokweng impact structure, South Africa. Geochimica et Cosmochimica Acta, 67, 10, pp. 1837–1862.

Koeberl, C. and Reimold, W. U. (2003). Post-impact hydrothermal activity in meteorite impact craters and potential opportunities for life. Astronomical Society of the Pacific, San Franscico, pp. 299-304.

Kovaleva, E., Huber, M.S., Fourie F. and Pittarello, L. (2018). Comparative study of pseudotachylite microstructures in felsic and mafic rocks from the Vredefort impact structure, South Africa. Implications for the experimental studies. South African Journal of Geology, 121.4, pp. 403-420.,

Kozdon, R., Ushikubo, T., Kita, N. T., Spicuzza, M. and Valley, J. W. (2009). Intratest oxygen isotope variability in the planktonic foraminifer N. pachyderma: Real vs. apparent vital effects by ion microprobe. Chemical Geology, 258, pp. 327-337.

Kring, D. A., Tikoo, S. M., Schmieder, M., Riller, U., Rebolledo-Vieyra, M., Simpson, S. L., Osinski, G. R., Gattacceca, J., Wittmann, A., Verhagen, C. M., Cockell, C. S., Coolen, M.

J. L., Longstaffe, F. J., Gulick, S. P. S., Morgan, J. V., Bralower, T. J., Chenot, E., Christeson, G. L., Claeys, P., Ferrière, L., Gebhardt, C., Goto, K., Green, S. L., Jones, H., Lofi, J., Lowery, C. M., Ocampo-Torres, R., Perez-Cruz, L., Pickersgill, A. E., Poelchau, M. H., Rae, A. S. P., Rasmussen, C., Sato, H., Smit, J., Tomioka, N., Urrutia-Fucugauchi, J., Whalen, M. T., Xiao, L. and Yamaguchi, K. E. (2020). Probing the hydrothermal system of the Chicxulub impact crater. Science. Advances, 6: eaaz3053.

Lawrence, M. G., Greig, A., Collerson, K. D. and Kamber, B. S. (2006). Rare Earth Element and Yttrium Variability in South East Queensland Waterways. Aquatic Geochemistry, 12(1), pp. 39–72.

Lee, C-T. A., Luffi, P., Chin, E. J., Bouchet, R., Dasgupta, R., Morton, D. M., Le Roux, V., Yin, Q-Z. and Jin, D. (2012). Copper systematics in arc magmas and implications for crust-mantle differentiation. Science, 336, pp. 64–68

Liu, J., Zheng, M., Cook, N. J., Long, X., Deng, J. and Zhai, Y. (2007). Geological and geochemical characteristics of the Sawaya'erdun gold deposit, southwestern Chinese Tianshan Ore Geol. Rev., 32 (1-2), pp. 125-156.

Linol, B., De Wit, M. J., Guillocheau, F., De Wit M. C. J., Anka, Z. and Colin, J. P. (2015). Formation and Collapse of the Kalahari Duricrust ['African Surface'] Across the Congo Basin, with Implications for Changes in Rates of Cenozoic Off-Shore Sedimentation Geology and Resource Potential of the Congo Basin, Regional Geology Reviews.

Maier, W. D., Andreoli, M. A. G., McDonald, I., Higgins, M. D., Boyce, A. J., Shukolyukov, A., Lugmair, G. W., Ashwal, L. D., Graser, P., Ripley, E. M. and Hart, R. J. (2006). Discovery of a 25-cm asteroid in the giant Morokweng impact crater, South Africa: Nature, 441, pp. 203–206.

Masiu, T. (2025). Petrographic and hyperspectral analysis of post-impact hydrothermal alteration in the M4 core from the Morokweng Impact Structure, South Africa. MSc dissertation (unpublished; MSc dissertation), University of Witwatersrand, South Africa.

McGregor, M., Walton, L.E., McFarlane R.M.C. and Spray, G.J. (2020). Multiphase U-Pb geochronology of sintered breccias from the Steen River impact structure, Canada: Mixed

target considerations for a Jurassic-Cretaceous boundary event. Geochimica et Cosmochimica Acta, 274, pp. 136-156.

Means, W. D. and Li, T. (2001). A laboratory simulation of fibrous veins: some first observations. Journal of Structural Geology 23, pp. 857 – 863.

Melosh, H. J. (1989). Impact cratering: A geologic process. New York: Oxford University Press. pp. 253.

McCarville, P. and Crossey, L. J. (1993). Post-impact hydrothermal alteration of the Mason impact stricture. In: Lunar and Planetary Sciences XXV, pp. 861–862

McDonald, I., Andreoli, M. A. G, Hart, R. J. and Tredoux, M. (2001). Platinum-group elements in the Morokweng impact structure South Africa: Evidence for the impact of a large ordinary chondrite projectile at the Jurassic-Cretaceous boundary. Geochimica et Cosmochimica Acta, 65, pp. 299-309.

Meteoritical Society. (2018). Earth Impact Database. Retrieved June 19, 2024, from http://www.passc.net/EarthImpactDatabase/New%20website_05-2018/Index.html

Middleton, A. W., Uysal, I. T. and Golding, S. D. (2015). Chemical and mineralogical characterisation of illite–smectite: Implications for episodic tectonism and associated fluid flow, central Australia. Geochimica et Cosmochimica Acta, 148, pp. 284–303.

Milos, R. (2012). Distribution and Origin of Clay Minerals during Hydrothermal Alteration of Ore Deposits. Chapter 5, pp. 81-100.

Moffett, J. W. (1990). Microbially mediated cerium oxidation in seawater. Nature 345, pp. 421–423.

Morgan, J. V., Gulick, S. P. S., Bralower, T., Chenot, E., Christeson, G., Claeys, Ph., Cockell, C., Collins, G. S., Coolen, M. J. L., Ferrière, L., Gebhardt, C., Goto, K., Jones, H., Kring, D. A., Le Ber, E., Lofi, J., Long, X., Lowery, C., Mellett, C., Ocampo-Torres, R., Osinski, G. R., Perez-Cruz, L., Pickersgill, A., Pölchau, M., Rae, A., Rasmussen, C., Rebolledo-Vieyra, M., Riller, U., Sato, H., Schmitt, D. R., Smit, J., Tikoo, S., Tomioka, N., Urrutia-Fucugauchi, J., Whalen, M., Wittmann, A., Yamaguchi, K. E. and Zylberman, W. (2016). The formation of peak rings in large impact craters. Science, 354, pp. 878–882.

Mügge, O. (1928). Über die Entstehung faseriger Minerale und ihrer Aggregationsformen. Neues Jahrbuch für Mineralogie, Geologie und Paläontologie, 58A, pp. 303-348.

Naumov, M. V. (1999). The hydrothermal-metasomatic mineral formation (in Russian). In: Deep Drilling in the Puchezh-Katunki Impact Structure (eds Masaitis VL, Pevzner LA), pp. 276–286. VSEGEI Press, St Petersburg.

Naumov, M. V. (2002). Impact-generated hydrothermal systems: Data from Popigai, Kara, and Puchezh-Katunki impact structures. In: Meteorite Impact Structures in Precambrian Shields (eds Plado J, Pesonen LJ), pp. 117 –171.

Naumov, M. V. (2005). Principal features of impact-generated hydrothermal circulation systems: mineralogical and geochemical evidence. Geofluids, 5(3), pp. 165-184.

Newhouse, W. H. (1969). Ore deposits as related to structural features. New York: Hafner Publishing Co. pp. 280.

Nuriel, P., Weinberger, R., Kylander-Clark, A. R. C., Hacker, B. R. and Craddock, J. P. (2017). The onset of the Dead Sea transform based on calcite age-strain analyses. *Geology*, 45(7), pp. 587-590.

O'neill, J. R., Clayton, R. N., Mayeda, T. K. (1969). Oxygen isotope fractionation in divalent metal carbonates, Journal of Chemical Physics, 52, pp. 5547-5558.

Osinski, G. R., Spray, J. G. and Lee, P. (2001). Impact-induced hydrothermal activity within the Haughton impact structure, arctic Canada: Generation of a transient, warm, wet oasis. Meteoritics and Planetary Science, 36, pp. 731–745.

Osinski, G. R. (2005). Hydrothermal activity associated with the Ries impact event, Germany. Geofluids, 5(3), pp. 202-220.

Osinski, G. R., Ferriere, L., Grieve, R. A. F. and Losiak, A. (2022). Impact Earth: A review of the terrestrial impact record. Earth-Science Reviews, 232(E01008):104112

Paisarnsombat, S. (2008). Impact-induced hydrothermal systems: The Manicouagan example. PhD. Thesis, pp. 369.

Pan, Y. and Fleet, E. M. (1989). Cr-rich calc-silicates from the Helmo area, Ontario, Canadian mineralogists, 27, pp. 565 – 577.

Partridge, T. C. (1998). Of diamonds, dinosaurs and diastrophism: 150 million years of landscape evolution in southern Africa. South African Journal of Geology, 101 (3), pp. 167-184.

Partridge, T. C., Botha, G. A. and Haddon, I. G. (2006). Cenozoic deposits of the interior. The Geology of South Africa, pp. 585 – 604.

Partridge, T. C. and Maud, R. R. (2000). Macro-Scale Geomorphic Evolution of Southern Africa. The Cenozoic of Southern Africa, Oxford Monographs on Geology and Geophysics, 40, pp. 3–18.

Paton, C., Hellstrom, J., Paul, B., Woodhead, J. and Hergt J. (2011). Iolite: Freeware for the visualisation and processing of mass spectrometric data, J. Anal. At. Spectrom., 26, pp. 2508–2518.

Pickersgill, A. E., Jaret, S. J., Pittarello, L., Fritz, J. and Harris, R. S. (2021). Shock effects in feldspars: an overview. In Large Meteorite Impacts and Planetary Evolution VI, Geological Society of America,550, pp. 507-535.

Poelchau, M. H. and Kenkmann, T. (2011). Feather features: A low-shock-pressure indicator in quartz. Journal of Geophysical Research: Solid Earth, 116(B2).

Quandt, D., Micheuz, P., Kurz, W. and Krenn, K. (2018). Microtextures and fluid inclusions from vein minerals hosted in the Pillow Lavas of the Troodos supra-subduction zone. Lithosphere, 10(4), pp. 566-578.

Quandt, D., Micheuz, P., Kurz, W., Kluge, T., Boch, R., Hippler, D. and Hauzenberger, C. A. (2019). Geochemistry of vein calcites hosted in the Troodos Pillow Lavas and their implications for the timing and physicochemical environment of fracturing, fluid circulation, and vein mineral growth. Geochemistry, Geophysics, Geosystems

Rammuki, P. T. (2019). Petrographic and Geochemical Characteristics of Archaean Basement Rocks in the M3 Drillcore, Morokweng Impact Structure, North West Province. Honours Project (unpublished), University of the Witwatersrand, pp. 55.

Rasbury, E. T. and J. M. Cole (2009), Directly dating geologic events: U-Pb dating of carbonates, Review Geophysics, 47, RG3001.

Reimold, W. U., Koeberl, C. and Bishop, J. (1994). Roter Kamm impact crater, Namibia: geochemistry of basement rocks and breccias. Geochimica et Cosmochimica Acta, 58, pp. 2689–2710.

Reimold, W. U., Armstrong, R. A. and Koeberl, C. (2002). A deep drillcore from the Morokweng impact structure, South Africa: petrography, geochemistry and constrains on the crater size. Earth and Planetary Science Letters, 201, pp. 221-232.

Renne, P. R., Ernesto, M., Pacca, I. G., Coe, R. S., Glen, J. M., Prevot, M. and Perrin, M. (1992). The age of Paraná flood volcanism, rifting of Gondwanaland, and the Jurassic-Cretaceous boundary. Science, 258, pp. 975–979.

Riller, U., Poelchau, M. H., Rae A. S. P., Schulte, F. M., Collins, G. S., Melosh, J., Grieve, R. A. F., Morgan, J. V., Gulick, S. P. S., Lofi, J., Diaw, A., Call, N. M. and Kring, D. A. (2018). The IODP-ICDP Expedition 364 Science Party, Rock fluidization during peak-ring formation of large impact structures. Nature, 562, pp. 511–518.

Ring, U. and Bolhar, R. (2020). Tilting, uplift, volcanism and disintegration of the South German block. Tectonophysics, 795, 228611.

Roberts, D. and Gee, D. G. (1985). An introduction to the structure of the Scandinavian Caledonides. The Caledonide Orogen – Scandinavia and Related Areas. Wiley, Chichester, pp. 55–68.

Roberts, N. M. W., Rasbury, E. T., Parrish, R. R., Smith, C. J., Horstwood, M. S. and Condon, D. J. (2017). A calcite reference material for LA-ICP-MS U-Pb geochronology. Geochemistry, Geophysics, Geosystems. 18, pp. 2807–2814.

Roberts, N. M., Drost, K., Horstwood, M. S., Condon, D. J., Chew, D., Drake, H., Milodowski, A. E., McLean, N. M., Smye, A. J., Walker, R. J. and Haslam, R. (2020). Laser ablation inductively coupled plasma mass spectrometry (LA-ICP-MS) U–Pb carbonate geochronology: strategies, progress, and limitations. Geochronology, 2(1), pp. 33-61.

Rudnick, R. L, and Gao, S. (2014). Composition of the continental crust. Treatise on geochemistry, 3, pp. 1–64.

Schmieder, M. and Kring, D. A. (2020). Earth's Impact Events Through Geologic Time: A List of Recommeded Ages for Terrestrial Impact Structures and Deposits. Astrobiology 20, pp. 91-141.

Şener, M. F., Şener, M. and Uysal. I. T. (2017). The evolution of the Cappadocia Geothermal Province, Anatolia (Turkey): geochemical and geochronological evidence, Hydrogeology Journal, 25, pp. 2323–2345

Shannon, R. D. (1976). Revised ionic radii and systematic studies of interatomic distances in halides and chalcogenides. Acta Crystallogr A32, pp. 751–767

Simpson, S. L. (2015). Geochemical and mineralogical studies of meteorite impact-generated hydrothermal systems on Earth and tracing sources of water: observations from the Rochechouart impact structure, France. University of Glasgow, pp. 223 (MSc dissertation).

Simpson, S. L., Osinski G. R., Longstaffe F.J., Schmieder, M. and Kring, D. A. (2020). Hydrothermal alteration associated with the Chicxulub impact crater upper peak-ring breccias. Earth and Planetary Science Letters 547 (116425).

Smit, P. J. (1977). Die Geohidrologie in die Opvanggebied van die Molopo rivier in die Noordelijke Kalahari, Bloemfontein. University of the Orange Free State, pp. 354 (PhD. Thesis).

Steiger, R. H. and Jäger, E. (1977). Subcommission on geochronology: convention on the use of decay constants in geochronology and cosmochronology, Earth Planetary Science Letters, 36, pp. 359–362,

Stöffler, D. and Langenhorst, F. (1994). Shock metamorphism of quartz in nature and experiment: I. Basic observation and theory. Meteoritics, 29, pp. 155-181.

Stöffler, D. and Grieve, R. A. F. (2007). Impactites, Chapter 2.11 in Fettes, D. and Desmons, J. (eds.) Metamorphic Rocks: A Classification and Glossary of Terms, Recommendations of the 256 International Union of Geological Sciences. Cambridge University Press, Cambridge, United Kingdom, pp. 82-92.

Sturchio, N. C., Antonio, M. R., Soderholm, L., Sutton, S. R. and Brannon, J. C. (1998). Tetravalent Uranium in Calcite. Science 281, pp. 971–973.

Sverjensky, D.A. (1989). Europium redox equilibria in aqueous solution. Earth Planetary Science Letters, 67, pp. 70–78.

Tan Q., Xia, Y., Xie., Z., Yan, J. and Wei, D. (2015). S, C, O, H, and Pb isotopic studies for the Shuiyindong Carlin-type gold deposit, Southwest Guizhou, China: constraints for ore genesis, China Journal Geochemistry, 34(4), pp. 525 – 539.

Talma, U. and Rust, S. A. (1997). Stable isotope characterization of calcrete, lake marl and stromatolites in the Etosha region, Namibia. African Journal, 1, pp. 75 – 80.

Teboul, P.-A., Durlet, C., Gaucher, E. C., Virgone, A., Girard, J.-P., Curie, J., and Camoin, G. F. (2016). Origins of elements building travertine and tufa: New perspectives provided by isotopic and geochemical tracers. Sedimentary Geology, 334, pp. 97–114.

Tera, F., & Wasserburg, G. J. (1972). U-Th-Pb systematics in three Apollo 14 basalts and the problem of initial Pb in lunar rocks. Earth and Planetary Science Letters, 14(3), pp. 281–304.

Thomas, D. S. G. and Shaw, P. A. (1991a). The Kalahari Environment. Cambridge University Press. pp. 284.

Tinker, J., De Wit, M. and Brown, R. (2008b). Linking source and sink: evaluating the balance between onshore erosion and off- shore sediment accumulation since Gondwana Break-up, South Africa. Tectonophysics, 455, pp. 94 – 103.

Tostevin, R., Shields, G. A., Tarbuck, G. M., He, T., Clarkson, M. O. and Wood, R. A. (2016). Effective use of cerium anomalies as a redox proxy in carbonate-dominated marine settings. Chemical Geology, 438, pp. 146–162

Turtle, E. P., Pierazzo, E. and O'Brien, P. D. (2003). Numerical modelling of impact heating and cooling of the Vredefort impact structure. Meteoritics & Planetary Science, 38 (2), pp. 293 – 303.

Uysal, I. T., Mutlu, H., Altunel, E., Karabacak, V. and Golding, S. D. (2006). Clay mineralogical and isotopic (K–Ar, δ18O, δD) constraints on the evolution of the North Anatolian Fault Zone, Turkey. Earth and Planetary Science Letters, 243, pp. 181–194.

Uysal, I. T., Golding, S. D, Bolhar, R., Zhao, J.-X., Feng, Y., Greig, A. and Baublys, K. (2011). CO2 degassing and trapping during hydrothermal cycles related to Gondwana rifting in eastern Australia, Geochim. Cosmochim. Ac., 75, pp. 5444–5466

Uysal, I. T., Piane, D. C., Todd, J. A. and Zwingmann, H. (2020). Precambrian faulting episodes and insights into the tectonothermal history of north Australia: microstructural evidence and K–Ar, 40Ar–39Ar, and Rb–Sr dating of syntectonic illite from the intracratonic Millungera Basin. Solid Earth, 11, pp 1653 – 1679.

Van Niekerk, H. S., Gutzmer, J., Beukes, N. J., Phillips, D. and Kiviets, G. B. (1999). A $^{40}Ar/^{39}Ar$ age of supergene K-Mn oxyhydroxides in a post-Gondwana soil profile on the Highveld of South Africa. South African Journal of Science, 95, pp. 450-454.

Veizer, J. and Hoefs, J. (1976). The nature of O^{18}/O^{16} and C^{13}/C^{12} secular trends in sedimentary carbonate rocks. Geochim. Cosmochim. Acta 40, pp. 1387-1395.

Veizer J., Hoefs J., Ridler, R. H., Jensen, L. S. and Lowe, D. R. (1989). Geochemistry of Precambrian carbonates: I. Archean hydrothermal systems. Geochimica et Cosmochimica Acta, 53, pp. 845-857.

Vermeesch, P. (2019). Exploratory analysis of Provenance data using R and the Provenance package. Minerals, 9(3), pp. 193.

Versh E., Kirsimäe K., Jõeleht A. and Plado J. (2003). Impact induced hydrothermal system at Kärdla crater: Development and Biological Consequences (abstract #4120). 3rd International Conference on Large Meteorite Impacts.

Walton, E. L., Sharp, T. G., Hu, J. and Tschauner, O. (2017). Investigating the response of biotite metamorphism: Examples from the Steen River impact structure, Canada. Meteoritics & Planetary Science, 53 (1), pp 75-92.

Wang, J., Chang, J., Chao, L., Han, Z., Wang, T. and Han, H. (2020). Significance of Calcite Trace Elements Contents and C-O Isotopic Compositions for Ore-Forming Fluids and Gold Prospecting in the Zhesang Carlin-Like Gold Deposit of Southeastern Yunnan, China. Minerals, 10, pp. 338.

Wela, S. S. (2017). A lithological, petrographic, and geochemical investigation of the M4 borehole core, Morokweng Impact Structure, South Africa. University of Witwatersrand, South Africa. pp. 273 (MSc dissertation).

Westgate, M., Manzi, M. S. D., Malehmir, A., Gibson, R. L., Andreoli M. A. G. and Bumby. A. (2021). A reappraisal of legacy reflection seismic data from the western margin of the Kaapvaal craton, South Africa, with implications for Mesozoic-Cenozoic regional tectonics. Tectonophysics, 813 (2289134).

Woodhead, J. Reisz, R., Fox, D., Drysdale, R., Hellstrom, J., Maas, R., Cheng, H. and Edwards, R. L. (2010). Speleothem climate records from deep time? Exploring the potential with an example from the Permian. Geological Society of America, 38 (5), pp. 455–458.

Woodhead, J. and Petrus, J. (2019). Exploring the advantages and limitations of in situ U–Pb carbonate geochronology using speleothems. Geochronology, 1, pp. 69 – 84.

Zawada, K. P., Hattingh, J. and van Bladeren, D. (1996). Paleoflood hydrological analysis of selected South Africa Rivers, Water Research Commission, 509 (1).

Zhang, W., Deng, X., Peng, L., Zhang, Y., Xu, D., Liu, H. and Lai, C. (2020). Rare earth elements and carbon-oxygen isotopes of calcite from the Tongjiachong Cu deposit, South China: Implications for fluid source and mineral precipitation. Ore Geology Reviews, 116, 103236.

Zhong, S. and Mucci, A. (1989). Calcite and aragonite precipitation from seawater solutions of various salinities: precipitation rates and overgrowth compositions. Chemical Geology, 78(3), pp. 283–299.

Zürcher, L. and Kring, D. A. (2004). Hydrothermal alteration in the core of the Yaxcopoil-1 borehole, Chicxulub impact structure, Mexico. Meteoritics and Planetary Science, 39, pp 1199-1221.

8. APPENDICES

APPENDIX 1: PETROGRAPHY

Appendix 1.1 Post-impact hydrothermal alteration around biotite

Table 1.1 and Figure 1.1-1.3 show a representation of alteration of biotite within monzonite sample M4 R8. Composition (in wt.% oxide) and single-point EDS analyses.

M4 R8	Pt1	Pt2	Pt3	Pt5	Pt6	Pt7	Pt8	Pt9	Pt10	Pt11
SiO_2	67.15	73.37	40.06	39.72	38.31	68.66	68.54	29.83	30.57	64.34
P_2O_5			15.4							
TiO_2			2.32		2.07			20.81	19.79	
Al_2O_3	20.31	17.87		19.54	16.12	18.77	19.86	2.58	2.44	20.31
FeO			5.53	16.19	20.79		3.13	2.73	1.05	1.32
MgO				17.37	13.92		1.64			
CaO	0.77		1.9			6.67	5.36	24.41	26.4	
Na_2O	11.78	8.76				1.18	1.47			8.39
K_2O				2.85	3.66	0.82			0.6	3.05
ZrO_2			33.27							
BaO			1.52					19.64	19.15	
SrO						1.83				
Co				0.76	0.61					
In				3.57	4.52					2.59

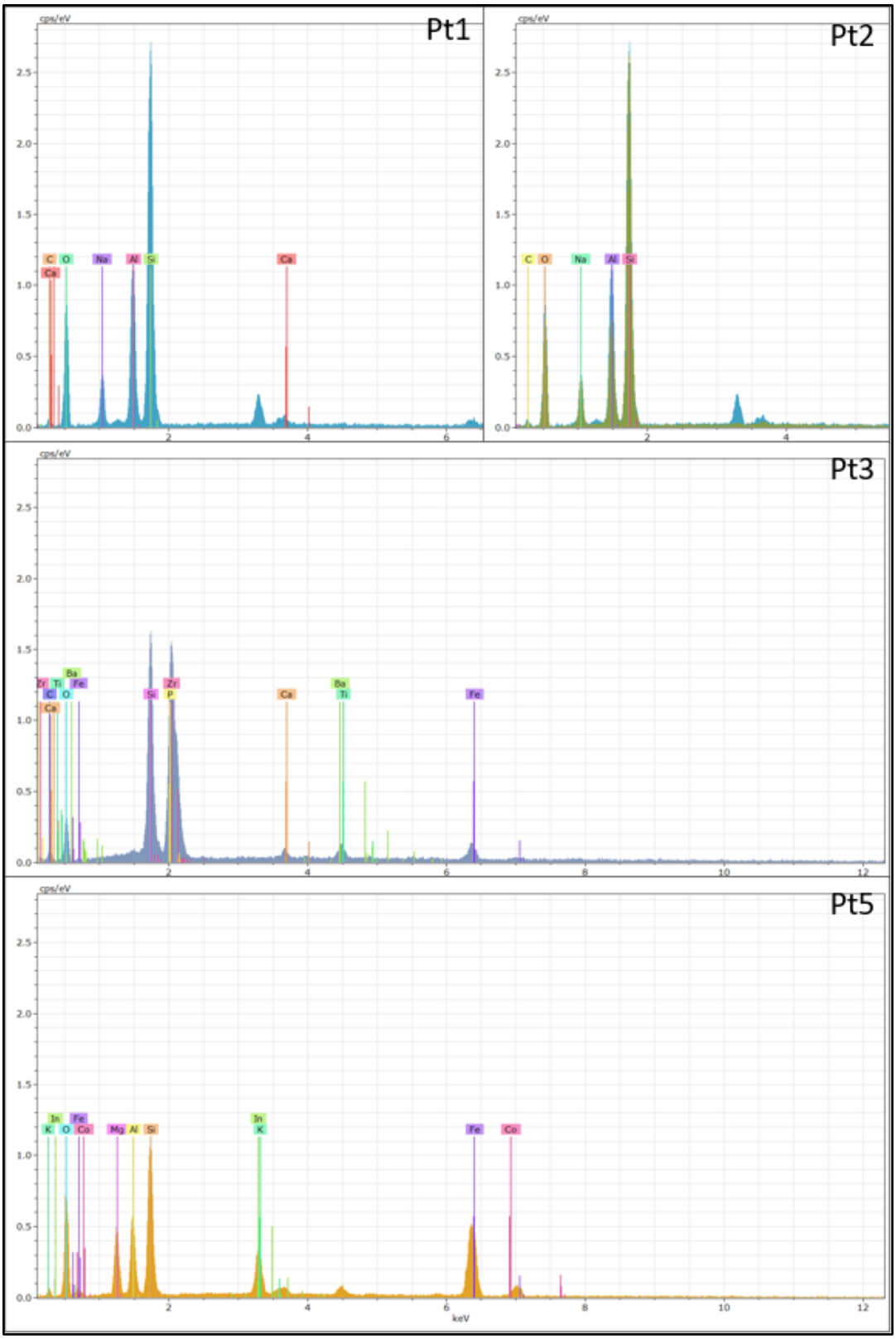


Figure 1.1. EDS spectra showing point 1 and 2 representing plagioclase, Pt3 representing zircon and Pt5 representing biotite.

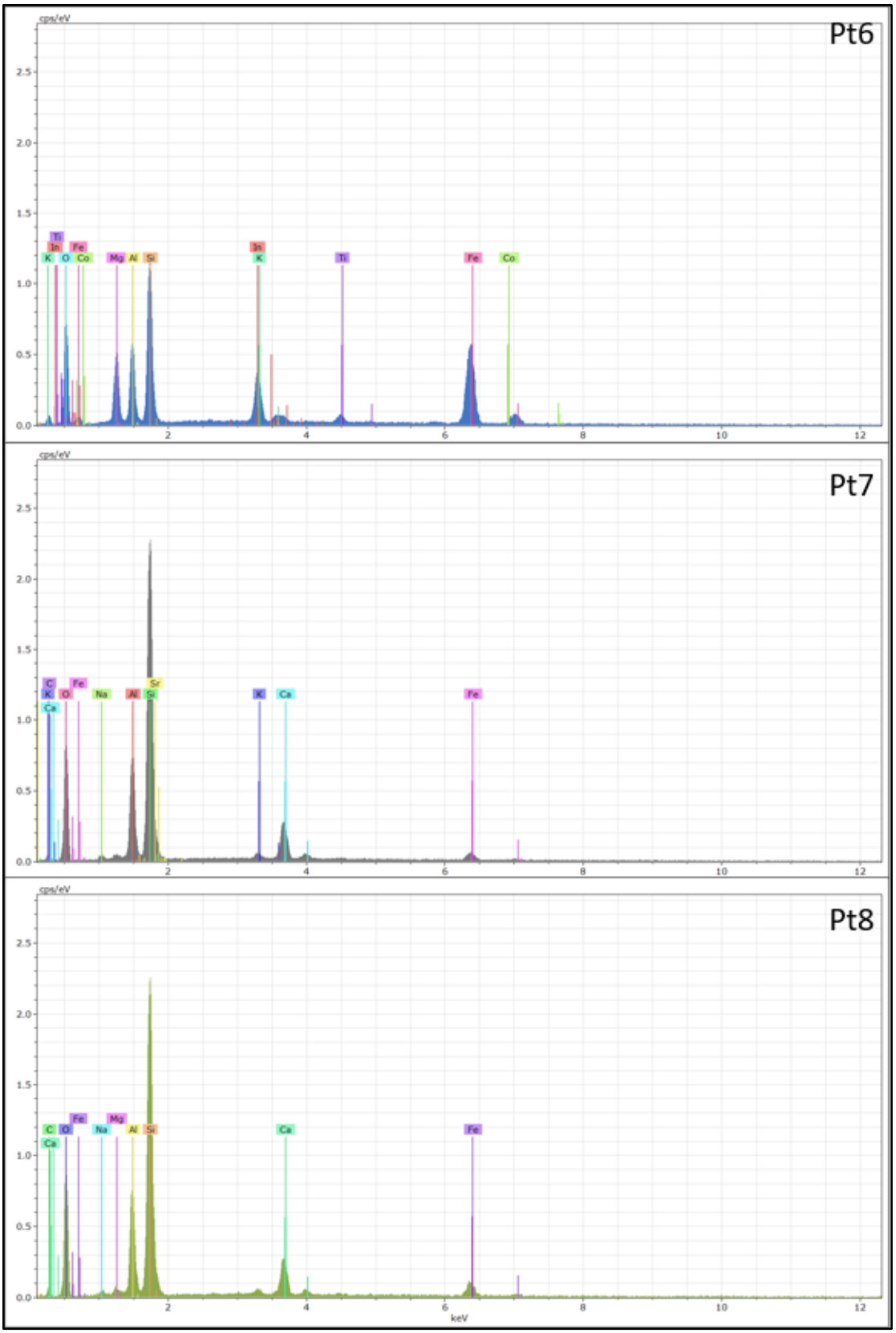


Figure 1.2. EDS spectra showing point 6 representing biotite, Pt7 and Pt8 representing Prehnite.

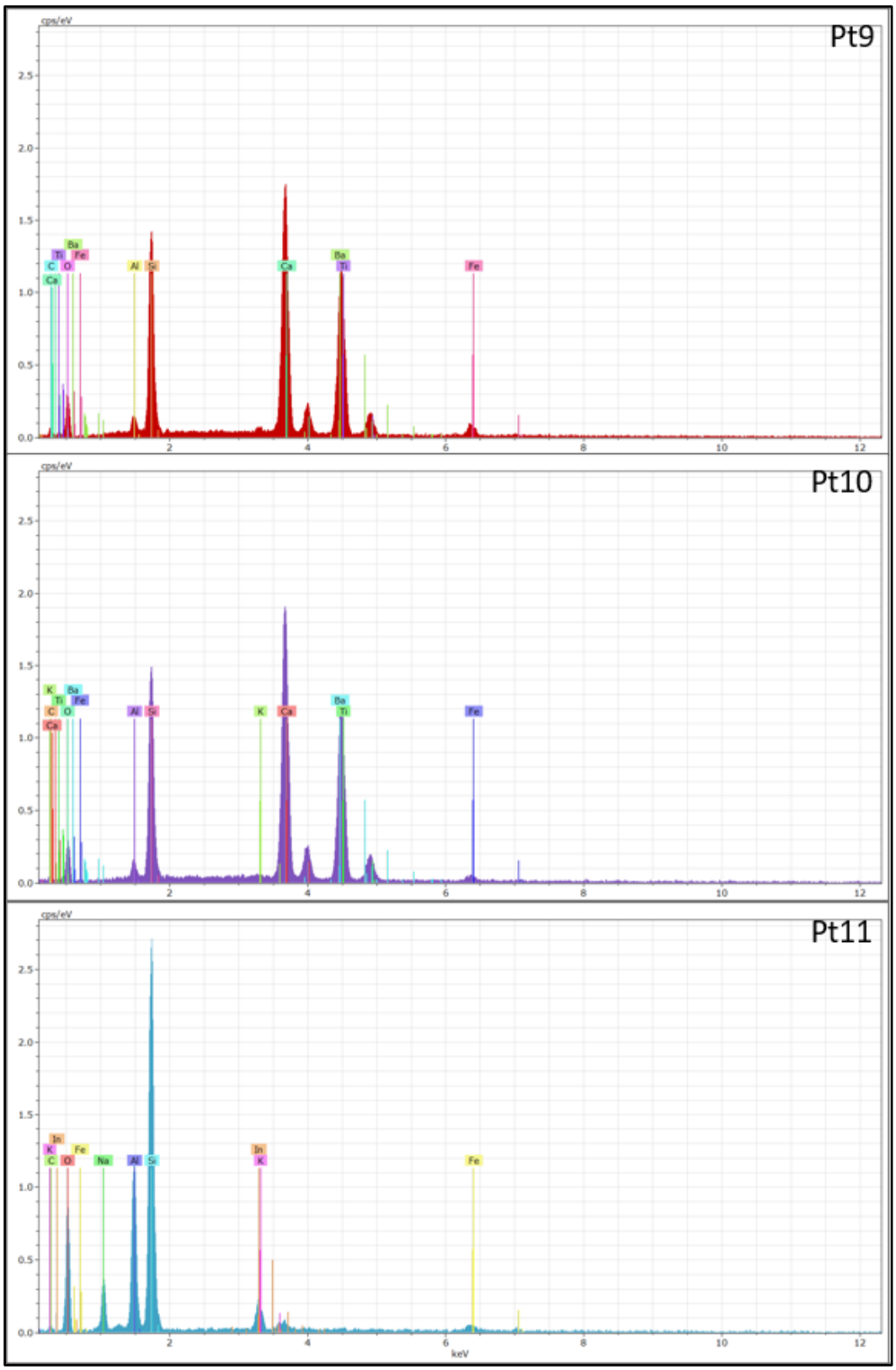


Figure 1.3. EDS spectra showing point 9 and 10 representing titanite and Pt11 representing alkali feldspar.

Appendix 1.2A Elemental map distribution of sample M4 R12

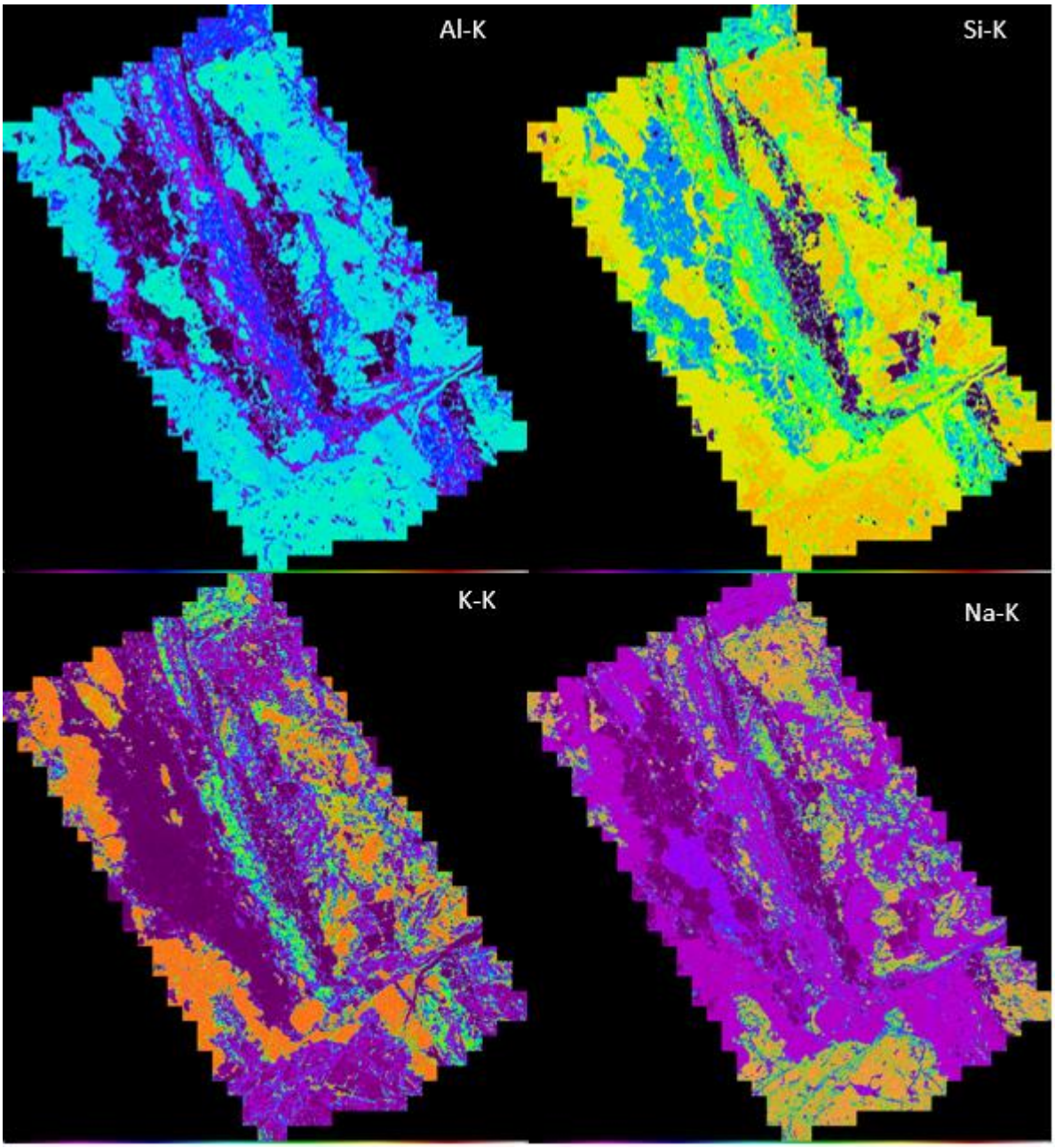


Figure 1.4. Elemental maps showing the distribution of Al, Si, K and Na. Each map is displaying relative intensity scale dark/black (element-deficient; left) and bright/white (element-rich). The fracture is more enriched in Si and K in the core and depleted around the rims. Na more depleted than Al.

Appendix 1.2B Elemental map distribution of sample M4 R12

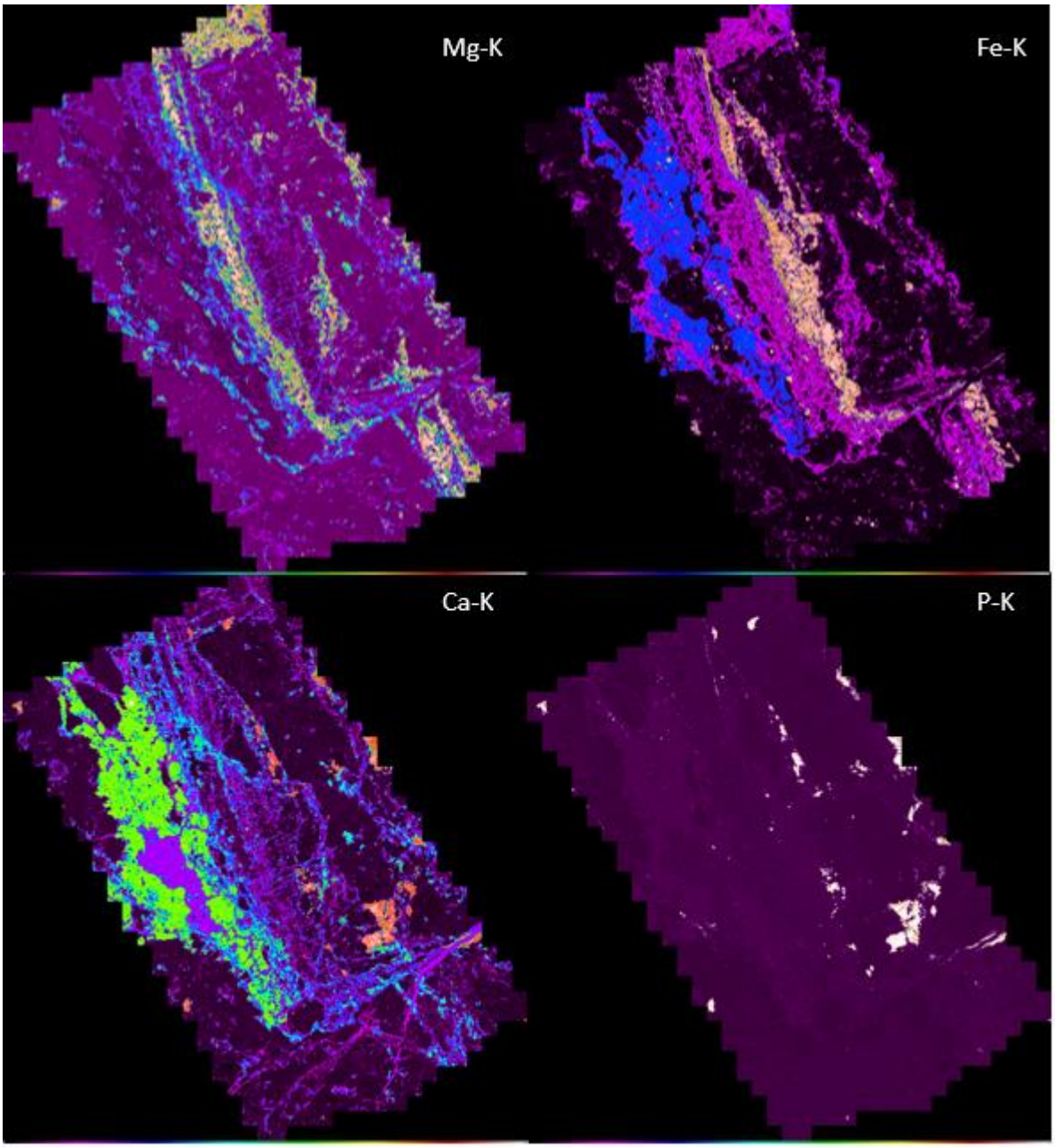


Figure 1.5. Elemental maps showing the distribution of Mg, Fe, Ca and P. Each map is displaying relative intensity scale dark/black (element-deficient; left) and bright/white (element-rich). The fracture is depleted in P and show Mg, Ca and Fe distribution from rim to core.

Appendix 1.3A Aired-dried XRD illite-smectite clays

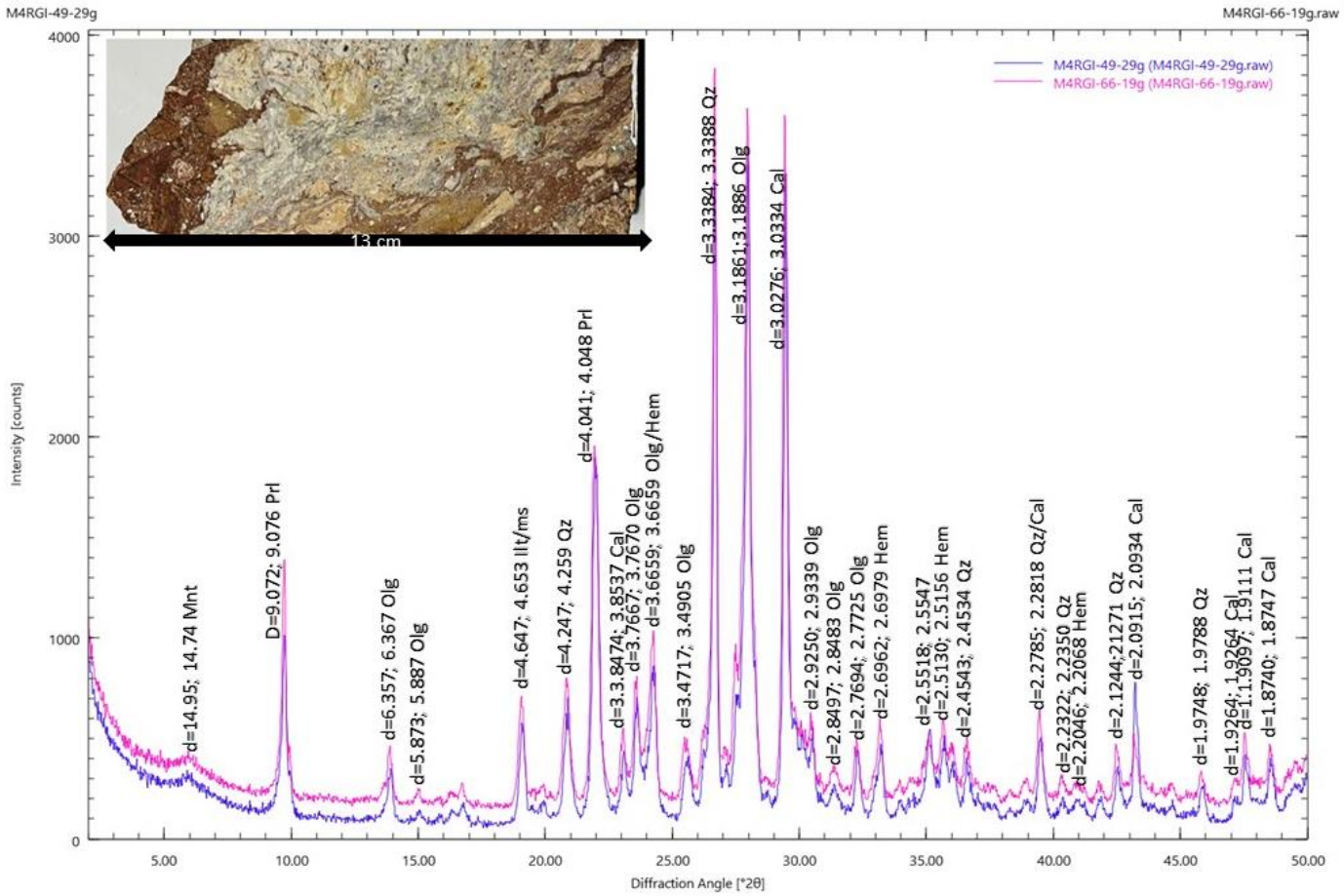


Figure 1.6. Aired-dried XRD spectra for sample M4 RG1 from 146 m showing major peaks of Mnt =Montmorillonite; Prl =pyrophyllite; Olg = oligoclase; Ilt = illite; Ms = muscovite; Qz = quartz; Cal = calcite; Hem = haematite. Pink spectra shows 19g of measured rock powder and blue spectra shows 29g of measured rock powder.

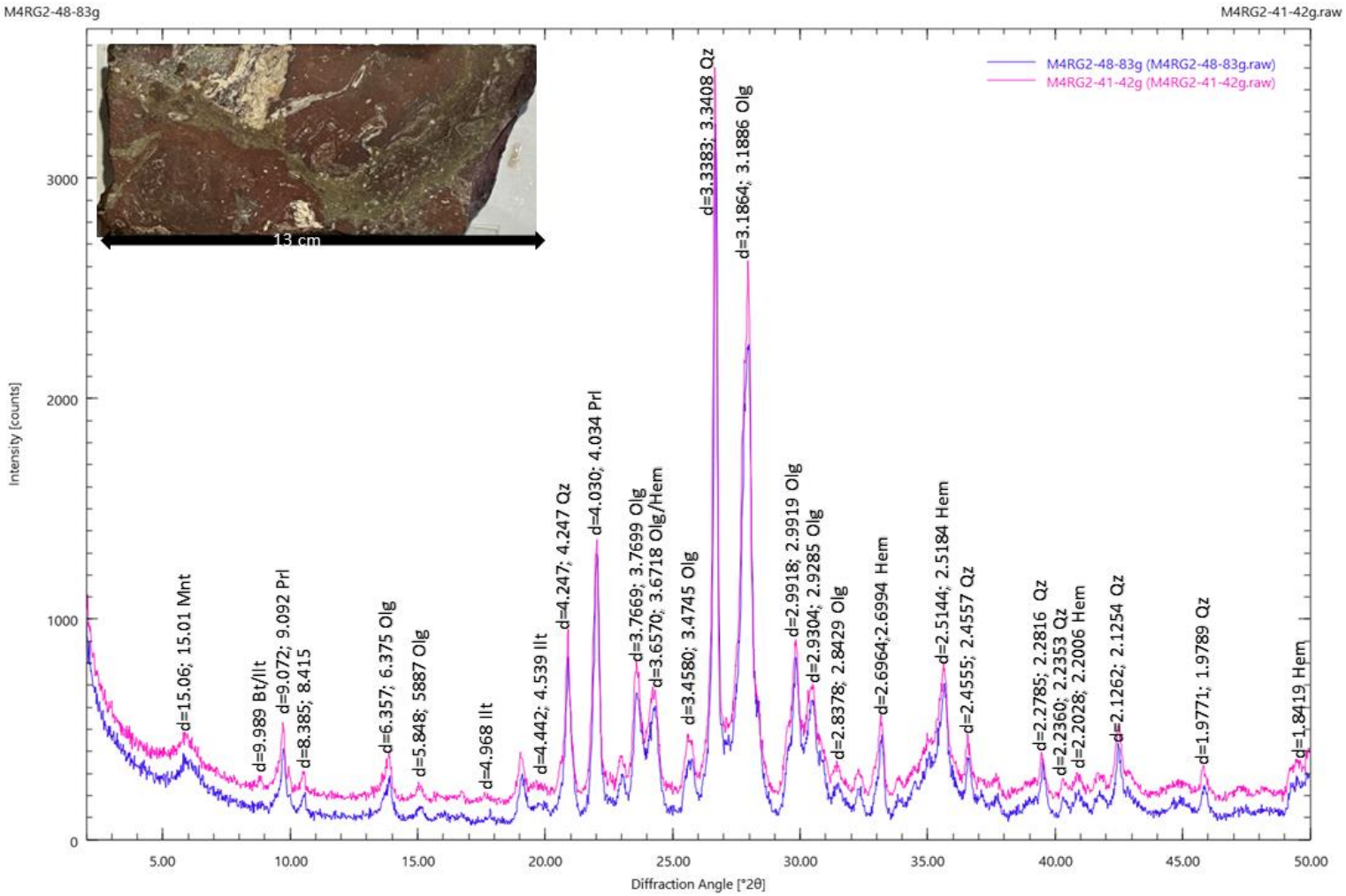


Figure 1.7. Aired-dried XRD spectra for sample M4 RG2 from 262 m showing major peaks of Mnt =Montmorillonite; Prl = pyrophyllite; Olg = oligoclase; Ilt = illite; Bt = biotite; Qz = quartz; Hem = haematite. Pink spectra shows 42g of measured rock powder and blue spectra shows 83g of measured rock powder.

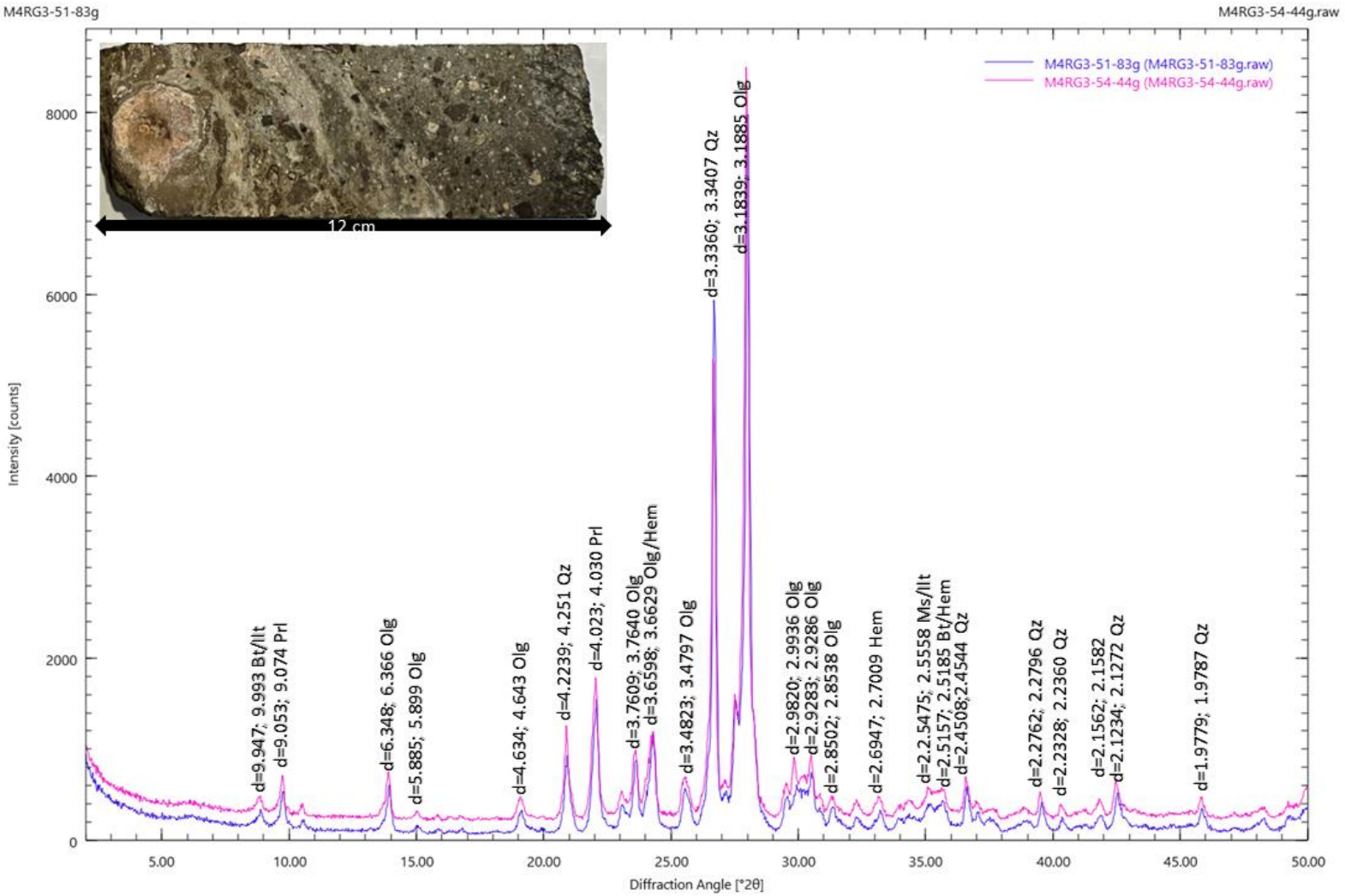


Figure 1.8. Aired-dried XRD spectra for sample M4 RG3 from 301 m showing major peaks of Prl = pyrophyllite; Olg = oligoclase; Ilt = illite; Bt = biotite; Qz = quartz; Hem = haematite. Pink spectra shows 44g of measured rock powder and blue spectra shows 83g of measured rock powder.

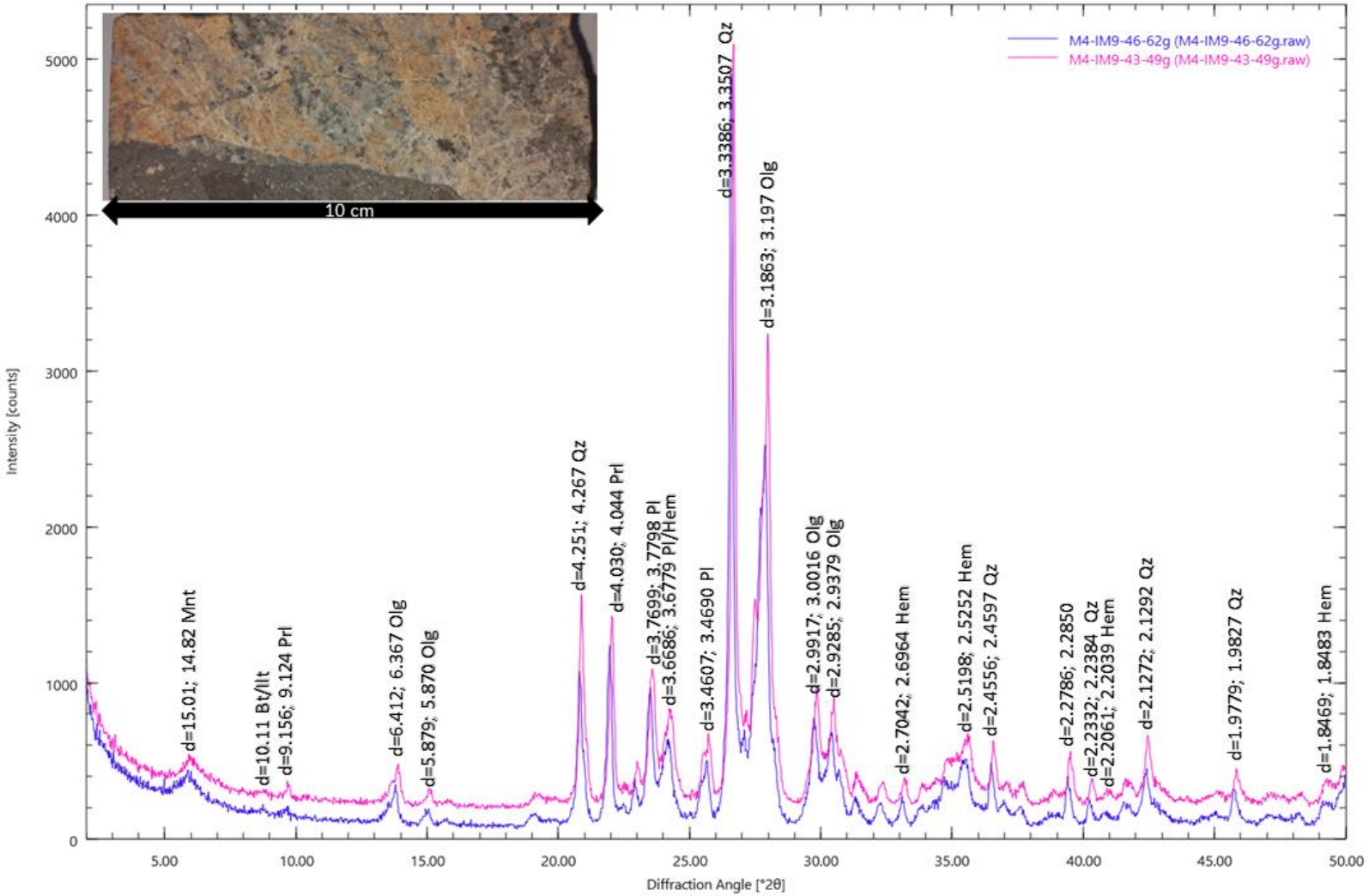


Figure 1.9. Aired-dried XRD spectra for sample M4 IM9 from 299 m showing major peaks of Mnt =Montmorillonite; Prl = pyrophyllite; Olg = oligoclase; Ilt = illite; Bt = biotite; Qz = quartz; Pl = plagioclase; Hem = haematite. Pink spectra shows 49g of measured rock powder and blue spectra shows 62g of measured rock powder.

Appendix 1.3B Glycolated

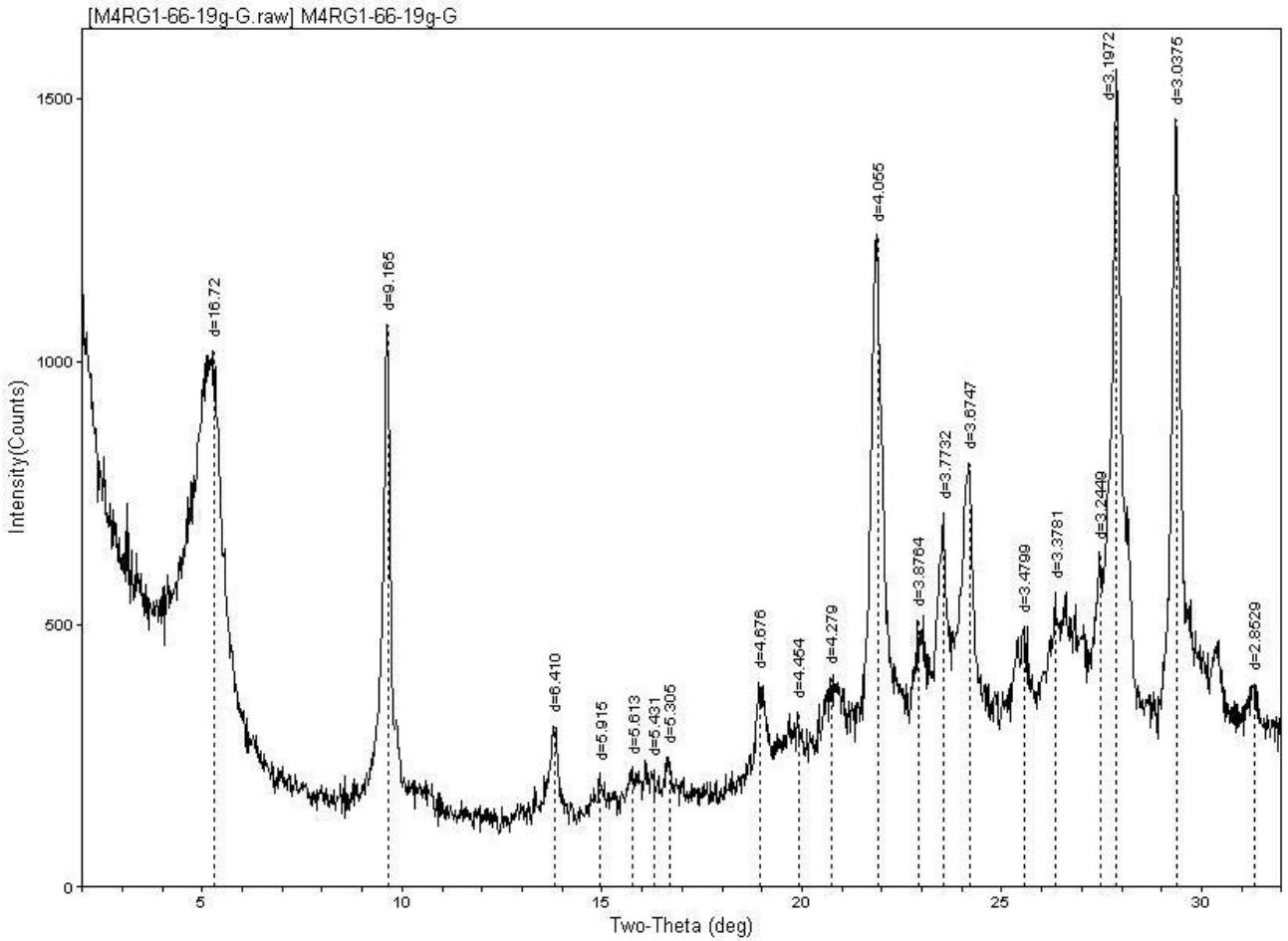


Figure 1.10. Glycolated XRD spectra for sample M4 RG1 from 146 m showing major peaks labelled in Figure 6. Spectra shows 19g of measured rock powder.

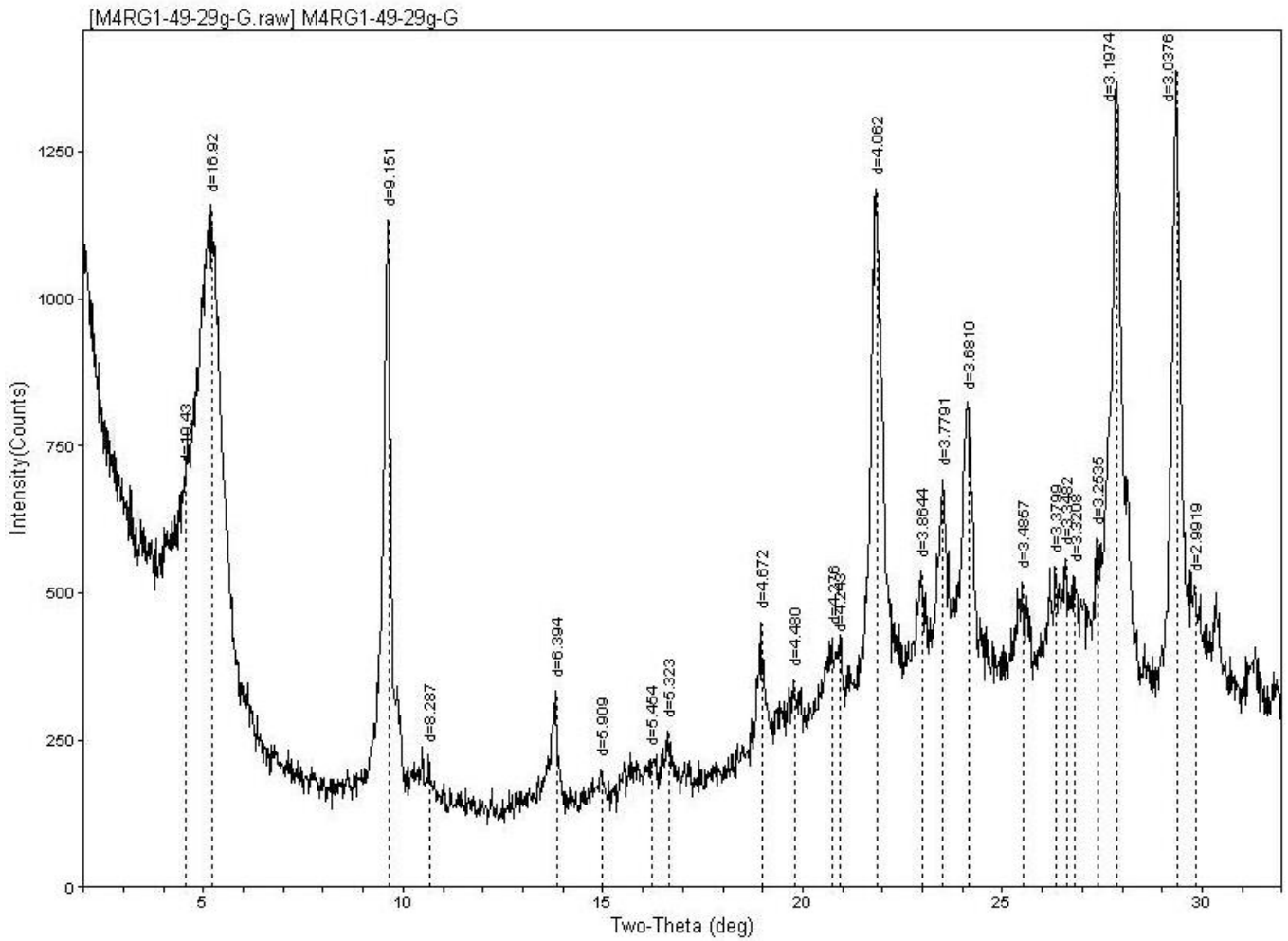


Figure 1.11. Glycolated XRD spectra for sample M4 RG1 from 146 m showing major peaks labelled in Figure 6. Spectra shows 29g of measured rock powder.

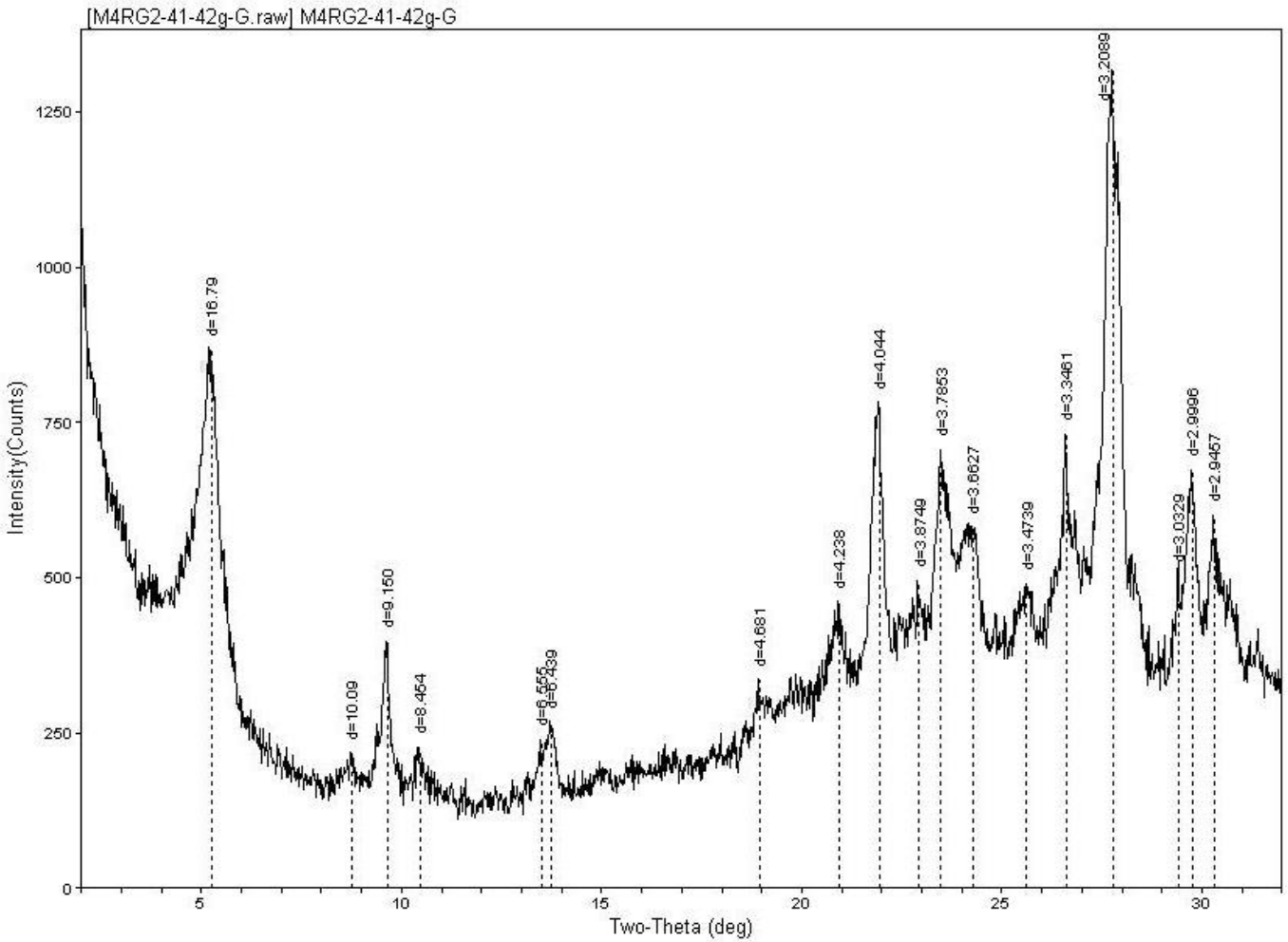


Figure 1.12. Glycolated XRD spectra for sample M4 RG2 from 262 m showing major peaks labelled in Figure 7. Spectra shows 42g of measured rock powder.

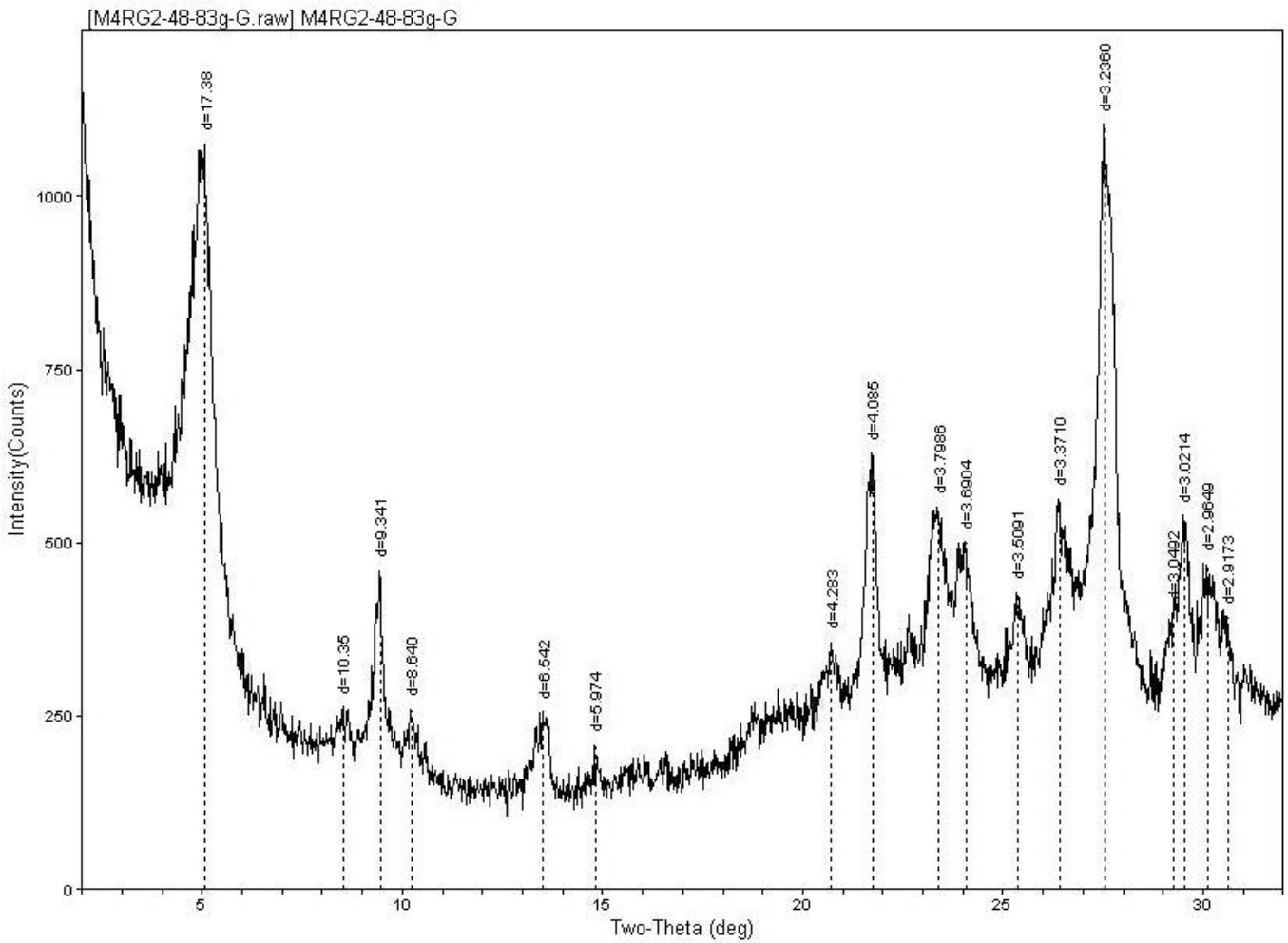


Figure 1.13. Glycolated XRD spectra for sample M4 RG2 from 262 m showing major peaks labelled in Figure 7. Spectra shows 83g of measured rock powder.

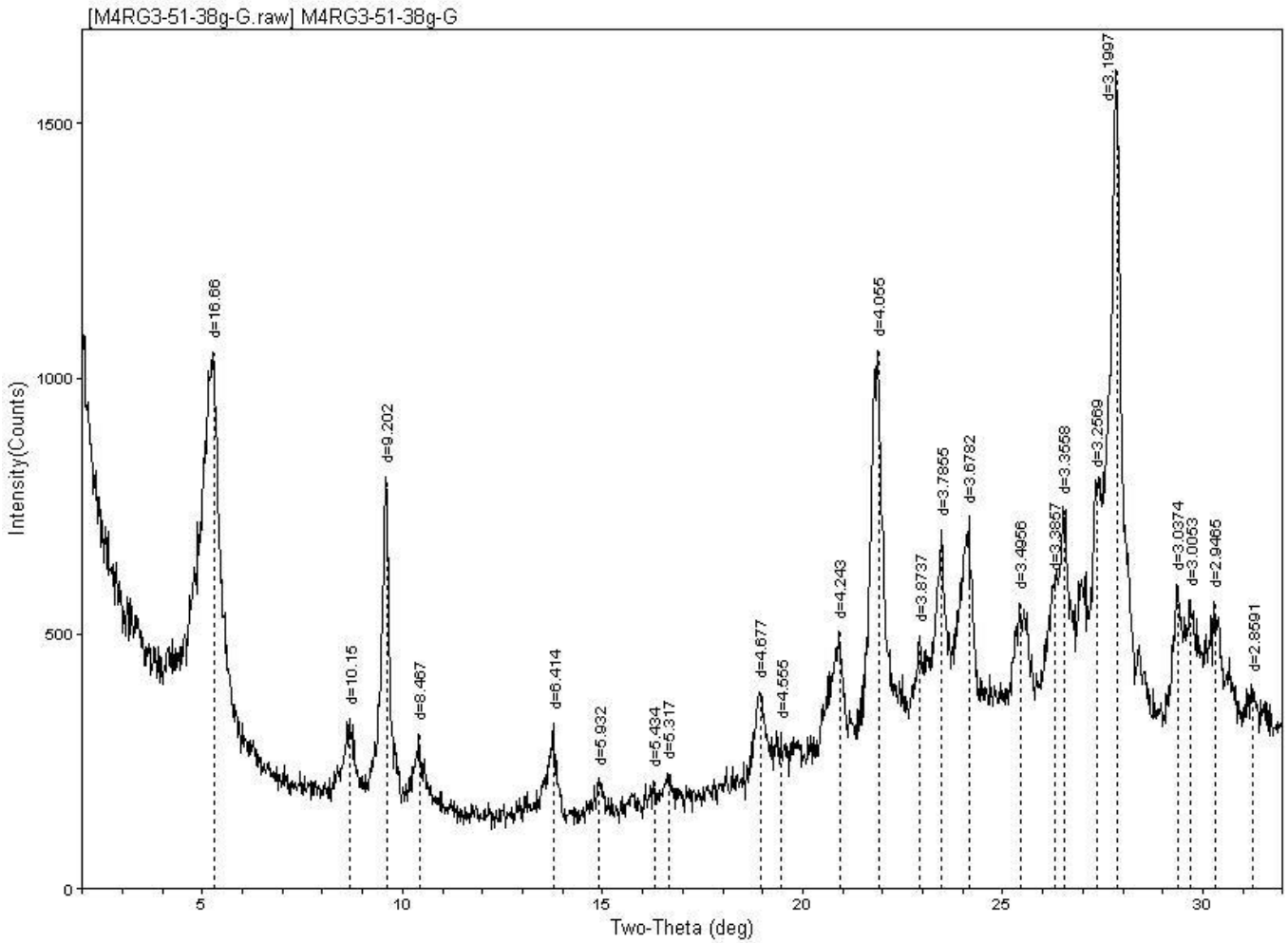


Figure 1.14. Glycolated XRD spectra for sample M4 RG3 from 301 m showing major peaks labelled in Figure 8. Spectra shows 38g of measured rock powder.

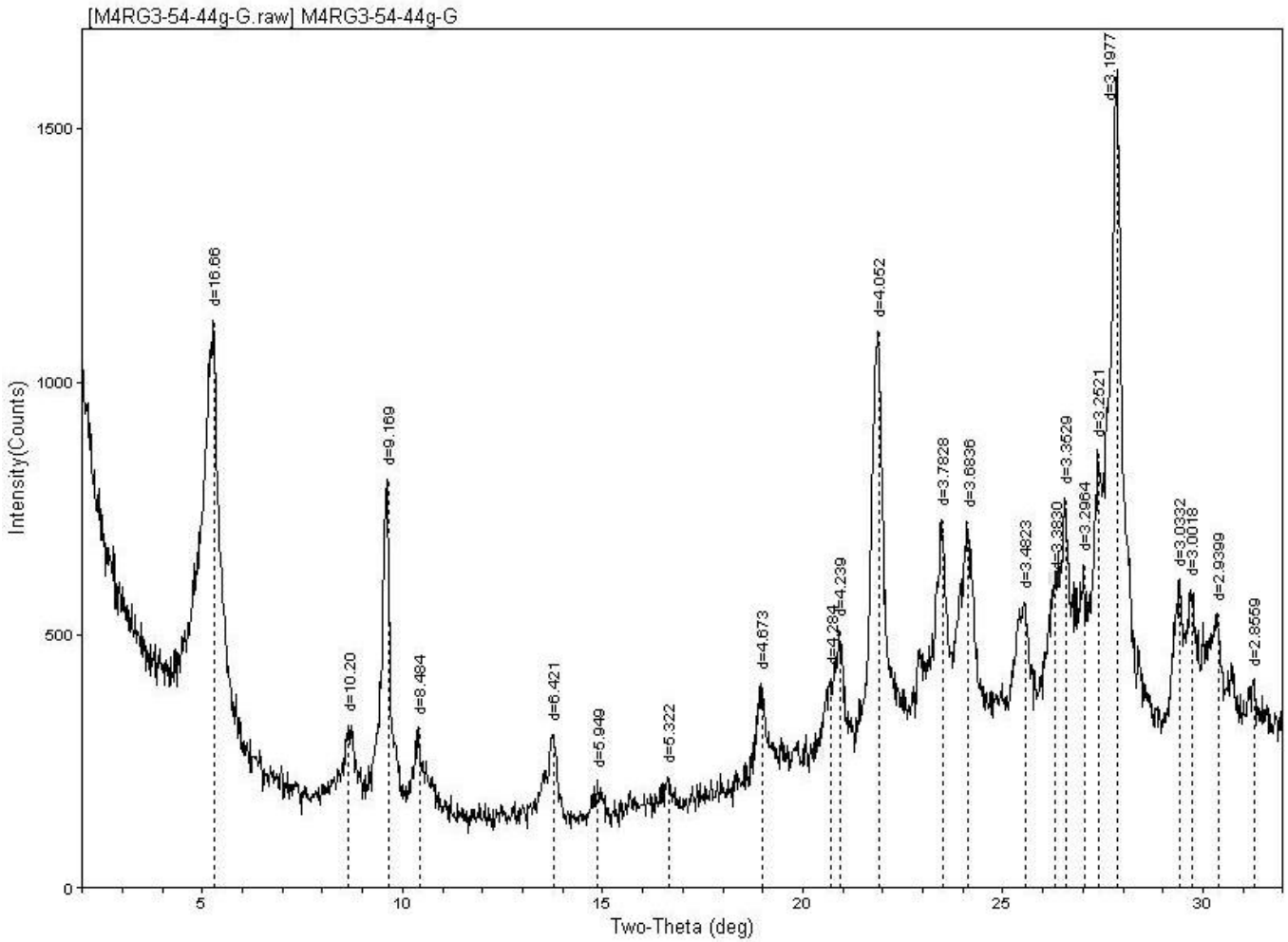


Figure 1.15. Glycolated XRD spectra for sample M4 RG3 from 301 m showing major peaks labelled in Figure 8. Spectra shows 44g of measured rock powder

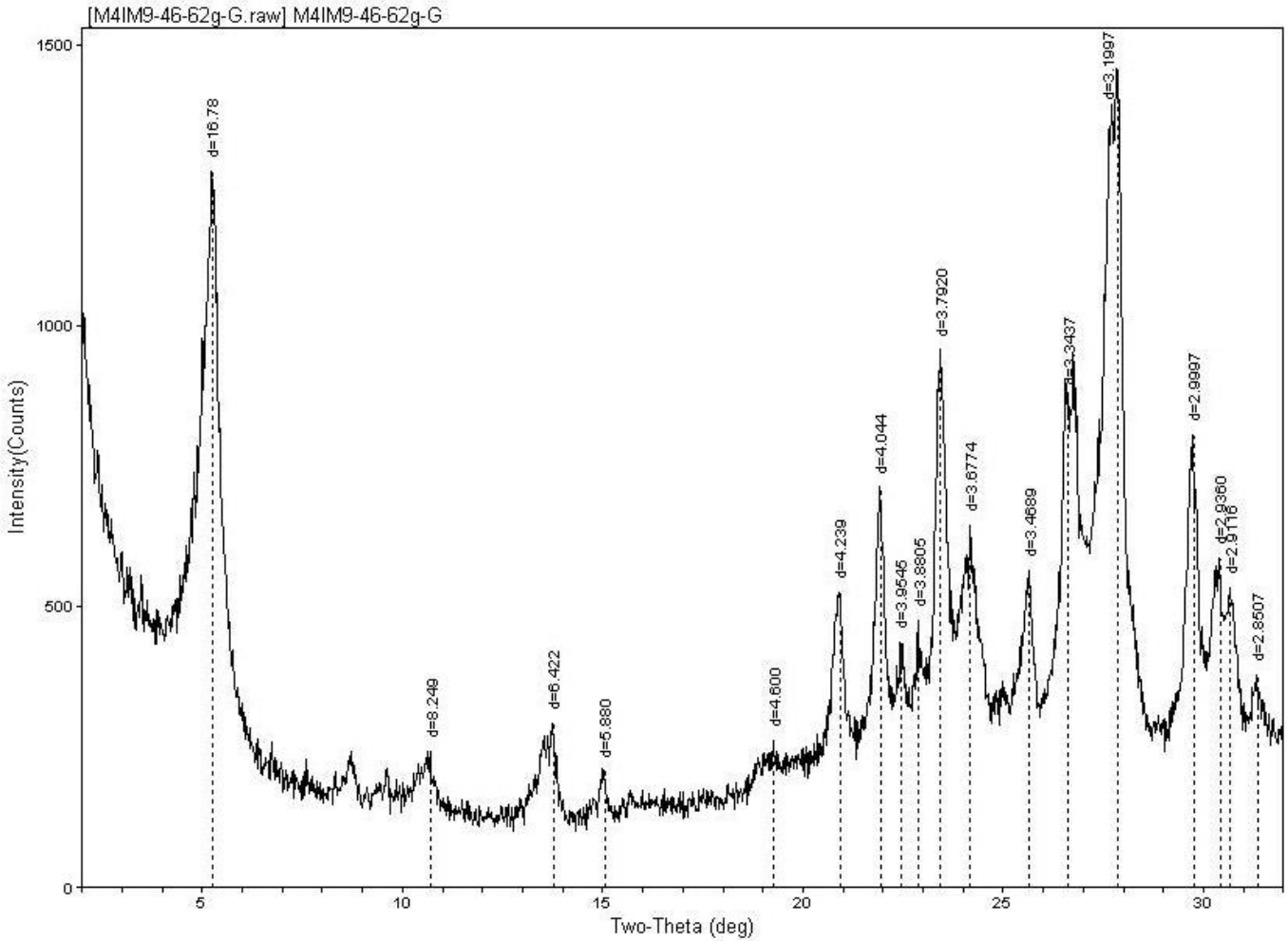


Figure 1.16. Glycolated XRD spectra for sample M4 IM9 from 299 m showing major peaks labelled in Figure 8. Spectra shows 62g of measured rock powder

Appendix 1.4 Zeolite veins with titanite-apatite grains

Table 1.2 EDS results from spot analysis of tiny crystals incorporated on the margins of zeolite vein from 262 m representing secondary titanite + apatite.

Spots analysis	Na_2O	MgO	Al_2O_3	SiO_2	P_2O_5	S	K_2O	CaO	MnO	FeO
Pt3A6.txt	1.70	1.24	6.12	19.62	21.13	0.55		34.20	1.65	3.13
Pt2A6.txt	1.59	0.91	9.43	27.64	21.82	0.57	1.01	27.96	1.05	2.23
Pt1A6.txt	2.70	2.44	7.41	23.38	21.93	0.64		28.03	1.47	3.91

APPENDIX 2: GEOCHEMISTRY

Appendix 2.1 Stable isotope data

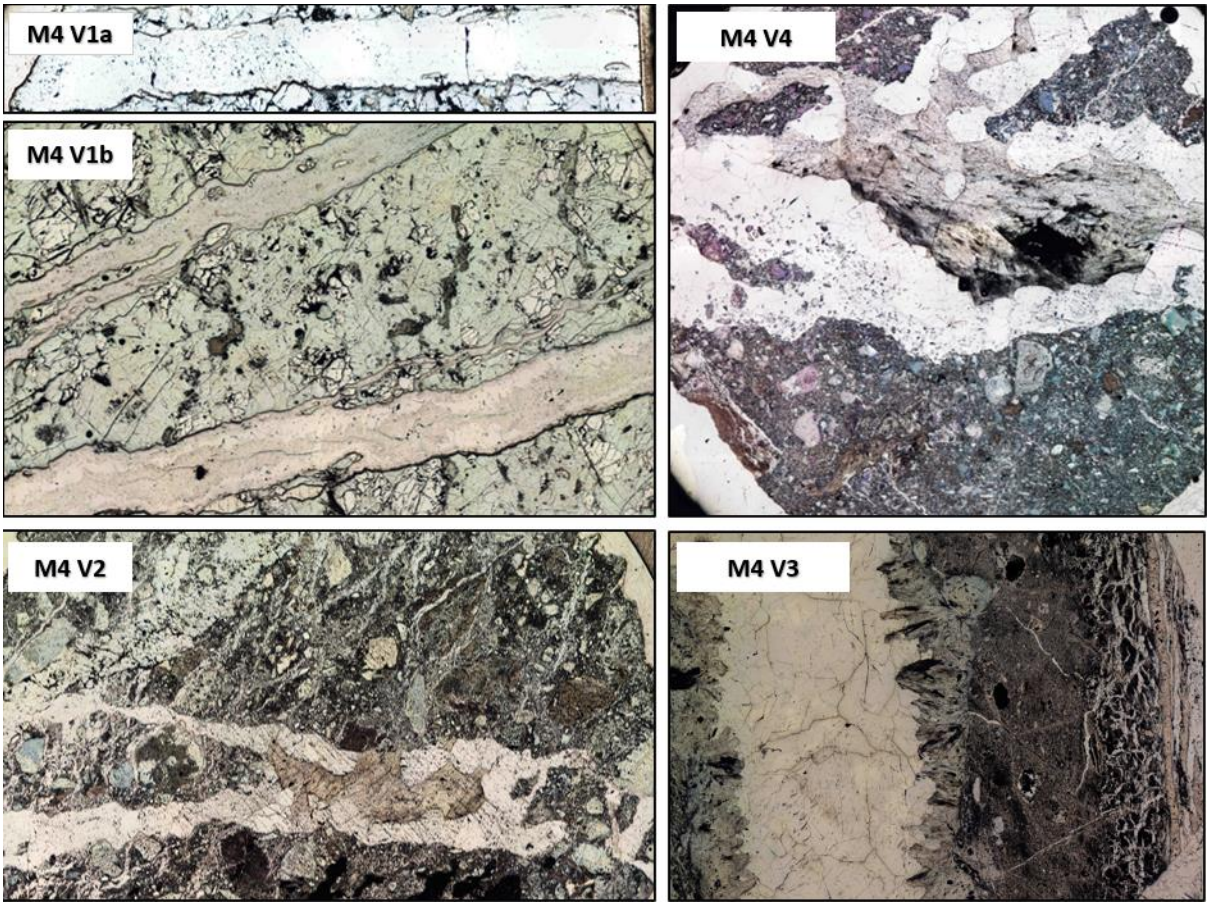


Figure 2.1: Cross-section of 25 mm thick mounts displaying the morphology of calcite veins analyzed for C-O isotope geochemistry. In M4 V1a and M4 V1b, two distinct tones are observed in the carbonates from rim to core: the lighter shade represents dolomite, while the darker shade represents calcite. In M4 V2, M4 V3, and M4 V4, the veins are a few millimeters thick, traversing a fine matrix of suevite rock. Blocky calcite veins are associated with zeolite in M4 V2 and M4 V4, and with plagioclase in M4 V3.

Table 2.1. Oxygen isotope composition of calcite veins

M4 V1b		**M4 V1a**		**M4 V2**		**M4 V3**		**M4 V4**	
Sub-sample	δ18O SMOW ‰	Sub-sample	δ18O SMOW ‰	Sub-sample	δ18O SMOW ‰	Sub-sample	δ18O SMOW ‰	Sub-sample	δ18O SMOW ‰
1	24,67	Top Rim 4	25,22	Younger 7	21,37	Younger 14	19,00	Younger 1	20,42
2	23,72	7	25,97	10	22,59	15	19,88	3	20,07
3	23,47	10	25,08	11	21,81	16	19,34	5	20,14

4	23,03	Core 2	23,41		12	21,08		17	19,86		6	21,99
5	24,81		5	23,50		14	20,62		18a	19,33		8	20,49
6	23,80		8	22,93		15	21,91		18b	19,68		9	19,90
7	23,84		11	22,99		16	21,78		19	20,28		10	20,62
8	24,79	Lower Rim 3		24,90	Older 1		26,47		20	20,03		11	20,64
9	23,92		6	25,44		2	26,34		21	19,56		12	20,68
10	22,86		9	25,61		3	26,64		22	20,86	Older 2		22,04
11	25,30					4	25,82	Older 4	6	21,45			22,42
13	24,35					5	23,74		7	21,28		13	24,71
14	24,66					6	25,39		8	22,32		14	22,53
15	24,88					8	25,47		9	21,35		15	21,80
16	26,18					9	25,04		10	23,31			
17	26,25					13	24,44		12	20,88			
18	27,39					17	26,65						
19	26,17												
20	24,72												
21	26,18												
22	26,89												

Table 2.2. Carbon and oxygen isotope compositions of calcite veins from the upper section of the M4 core.

M4 V1a calcite				M4 V1b calcite		
		δ18O	δ13C		δ18O	δ13C
Spots		(‰)VSMOW	(‰)VPDB	Spots	(‰)VSMOW	(‰)VPDB
Top Rim	7	25.97	-7.71	13	24.35	-4.37
Core	8	22.93	-9.24	15	24.88	-8.13
	11	22.99	-9.40	16	26.18	-6.98
Bottom Rim	9	25.61	-8.61	M4 V1c calcite		
				18	27.39	-7.16

M4 V2 Older calcite			M4 V4 Older calcite		
Spots	(‰)VSMOW	(‰)VPDB	Spots	(‰)VSMOW	(‰)VPDB
6	25.39	-11.80	13	24.71	-21.03
8	25.47	-14.33	15	21.80	-15.02
17	26.65	-10.60			
M4 V2 Younger calcite			M4 V4 Younger calcite		
7	21.37	-5.19	1	20.42	-5.11

11	21.81	-3.99	3	20.07	-5.68
14	20.62	-4.29	9	19.90	-4.69
			2	22.04	-7.03

M4 V3 Older calcite			M4 V3 Younger calcite		
	δ18O	δ13C		δ18O	δ13C
Spots	(‰)VSMOW	(‰)VPDB	Spots	(‰)VSMOW	(‰)VPDB
6	21.45	-16.16	14	19.00	-19.4544
8	22.32	-16.5846	18	19.68	-19.4062
10	23.31	-18.9589	20	20.03	-19.7958

Appendix 2.2: Trace element geochemical data for calcite veins

Table 2.3. Trace element concentrations in calcite veins from the M4 drillcore and standards used.

	Sc	Ti	Rb	Sr	Zr	Nb	Ba	Hf	Ta	Pb	Th
M4 V1_1	10.57	30.4	0.1560	1101	0.2470	0.1180	173	0.0041	0.0007	3.38	97.1
M4 V1_2	0.609	0.2530	Below LOD	173.0	0.0059	0.0023	Below LOD	Below LOD	0.00003	0.0054	0.0576
M4 V1_3	0.479	0.90	Below LOD	151.9	0.0108	0.0034	Below LOD	Below LOD	Below LOD	0.0198	0.0012
M4 V1_4	1.293	Below LOD	Below LOD	198.8	Below LOD	0.0015	Below LOD	0.0006	Below LOD	0.0130	0.0400
M4 V1_5	4.370	0.4010	Below LOD	106.4	0.0097	0.0020	Below LOD	Below LOD	0.00018	0.0153	1.0150
M4 V1_6	0.510	0.2850	Below LOD	399.0	0.0107	0.0019	0.0508	0.0008	Below LOD	0.0090	0.0258
M4 V1_7	0.582	0.4430	Below LOD	177.9	0.0117	0.0032	0.0300	Below LOD	Below LOD	0.0068	0.0134
M4 V1_8	0.726	0.2400	Below LOD	207.2	0.0078	0.0017	0.0400	Below LOD	0.00019	0.0085	0.0425
M4 V1_9	0.834	0.2930	Below LOD	177.8	0.0073	0.0013	0.0280	Below LOD	Below LOD	0.0114	0.0677
M4 V1_10	Below LOD	0.4940	Below LOD	285.6	0.6320	Below LOD	0.5720	Below LOD	Below LOD	Below LOD	Below LOD
M4 V1_11	0.084	0.1090	Below LOD	296.0	0.0231	0.0006	0.0399	Below LOD	Below LOD	Below LOD	0.0088
M4 V1_12	Below LOD	0.1710	Below LOD	205.9	0.0461	0.0016	0.0284	Below LOD	Below LOD	Below LOD	0.0001
M4 V1_13	0.106	0.0640	Below LOD	471.0	0.0123	Below LOD	0.0290	Below LOD	Below LOD	0.0057	Below LOD
M4 V1_14	Below LOD	0.2950	Below LOD	193.9	0.4230	0.0018	0.1720	0.0034	0.00006	0.0032	0.0530
M4 V1_15	0.104	0.1870	Below LOD	225.3	0.1269	0.0012	0.0630	Below LOD	Below LOD	Below LOD	0.0556
M4 V1_16	Below LOD	Below LOD	Below LOD	314.0	0.0122	0.0007	0.0290	Below LOD	Below LOD	0.0050	0.0011
M4 V1_17	0.269	0.158	Below LOD	309.0	0.0552	0.0015	0.0280	Below LOD	0.00008	0.0048	0.0044
M4 V1_18	Below LOD	0.157	Below LOD	537.0	0.0536	0.0021	Below LOD	0.0009	Below LOD	0.0074	0.0003
M4 V1_19	0.077	0.13	0.0292	489.0	0.0314	0.0022	0.0760	Below LOD	0.00026	0.0033	Below LOD
M4 V1_20	Below LOD	Below LOD	Below LOD	757.0	0.0110	0.0014	0.2420	Below LOD	Below LOD	0.0031	0.0023
M4 V1_21	0.044	Below LOD	Below LOD	181.9	0.0216	0.0007	0.0780	Below LOD	0.00005	Below LOD	Below LOD
M4 V1_22	0.908	0.67	0.0760	408.9	0.0215	0.0011	0.4640	0.0016	0.00018	0.0360	1.8100
M4 V1_23	1.664	4	0.4940	422.7	0.1970	0.0021	1.9900	0.0080	0.00026	0.2250	1.0050
M4 V1_24	0.415	Below LOD	Below LOD	324.8	0.0231	0.0009	0.4200	Below LOD	0.00012	0.0415	5.4300
M4 V1_25	0.240	0.19	0.0149	448.0	0.0155	0.0016	0.2140	Below LOD	0.00004	0.0328	0.0780

M4 V1_26	0.374	0.289	0.1870	279.9	0.0187	0.0008	0.7100	0.0007	0.00016	0.0528	0.3560
M4 V1_27	0.161	0.521	Below LOD	239.0	0.7620	0.0023	0.0910	0.0052	Below LOD	0.0202	0.3200
M4 V1_28	0.894	1.26	0.800	281.0	0.1960	0.0014	3.4700	0.0036	Below LOD	0.2980	0.3930

	Sc	Ti	Rb	Sr	Zr	Nb	Ba	Hf	Ta	Pb	Th
M4 GG2_1	9.4	644	164	257	492	1.85	1300	11.2	0.16	49.5	2.48
M4 GG2_2	1.7	120	28	192	78	0.32	220	2	0.02	10.1	0.48
M4 GG2_3	2.2	140	38	235	106	0.44	310	2.90	0.05	13.7	0.90
M4 GG2_4	2.2	140	38	281	106	0.41	300	2.50	0.04	12.3	0.83
M4 GG2_5	8.7	617	158	278	476	1.9	1280	10.8	0.16	47.5	2.45
M4 GG2_6	8.39	608	155	270	464	1.77	1260	10.6	0.15	44.9	2.47
M4 GG2_7	2	130	37	239	99	0.39	290	2.50	0.04	13.5	0.98
M4 GG2_8	9.55	686	177	268	519	1.98	1419	11.9	0.17	52.6	2.98
M4 GG2_9	10.6	775	201	270	599	2.3	1611	13.9	0.20	59.8	3.13
M4 GG2_10	8.81	641	167	279	499	1.87	1347	11.9	0.18	48.9	2.61
M4 GG2_11	10.0	729	188	270	568	2.09	1510	13.3	0.19	58.4	2.91
M4 GG2_12	2.30	120	32	266	87	0.36	240	2.10	0.04	10.2	1.18
M4 GG2_13	9.52	720	185	265	562	2.13	1488	13.0	0.18	52.9	2.95
M4 GG2_14	2.80	190	53	208	150	0.58	410	3.70	0.06	17.0	0.82
M4 GG2_15	3.80	220	60	245	170	0.65	450	4.10	0.06	17.0	0.98
M4 GG2_16	2.70	180	48	245	130	Below LOD	370	3.40	Below LOD	15.1	0.74
M4 GG2_17	2.90	170	47	212	133	0.52	360	3.20	0.05	13.9	0.73
M4 GG2_18	3.10	105	32	490	76	0.3	230	1.90	0.03	12.7	0.63
M4 GG2_19	3.60	210	58	229	160	0.64	440	4.20	0.06	17.0	0.94
M4 GG2_20	1.50	90	25	248	69	0.28	200	1.90	0.02	9.7	0.54
M4 GG2_21	7.20	370	95	450	260	1.05	710	6.70	0.10	29.0	1.54
M4 GG2_22	9.80	660	172	282	479	1.91	1340	11.3	0.18	44.5	2.55

	Sc	Ti	Rb	Sr	Zr	Nb	Ba	Hf	Ta	Pb	Th
M4 S1(2)_1	16.0	967	235	263	886	2.77	1604	20.8	0.24	53.6	3.95
M4 S1(2)_2	15.4	984	237	265	886	2.90	1622	21.1	0.24	52.4	3.87

M4 S1(2)_3	14.7	974	235	264	882	2.83	1620	21.3	0.25	52.8	3.93
M4 S1(2)_4	15.0	970	237	266	891	2.91	1646	21.5	0.25	53.3	3.95
M4 S1(2)_5	14.9	979	239	267	898	2.92	1641	21.2	0.25	52.0	3.84
M4 S1(2)_6	15.3	977	236	264	888	2.87	1636	21.2	0.24	52.8	3.99
M4 S1(2)_7	14.9	976	238	267	900	2.97	1645	21.4	0.25	52.3	3.89
M4 S1(2)_8	14.9	980	235	264	891	2.91	1631	21.5	0.25	53.3	3.97
M4 S1(2)_9	14.6	974	236	263	885	2.81	1613	21.4	0.24	53.0	3.96
M4 S1(2)_10	14.3	983	237	266	871	2.96	1634	21.4	0.26	53.5	3.97
M4 S1(2)_11	14.4	979	237	267	871	2.93	1631	20.9	0.25	53.1	3.87
M4 S1(2)_12	14.6	975	239	267	875	2.95	1644	21.2	0.25	53.9	4.01
M4 S1(2)_13	14.1	976	234	264	865	2.92	1639	21.6	0.26	54.4	3.99
M4 S1(2)_14	14.3	983	237	266	875	2.87	1640	21.8	0.26	52.5	4.06

	Sc	Ti	Rb	Sr	Zr	Nb	Ba	Hf	Ta	Pb	Th
NIST610_1	473	524	420	527	373	473	449	327	452	390	426
NIST610_2	473	524	420	528	379	476	453	335	462	396	435
NIST610_3	465	525	407	515	385	466	450	327	450	368	417
NIST610_4	468	523	409	516	416	467	447	329	452	374	418
NIST610_5	468	522	405	510	405	461	442	328	449	381	409
NIST610_6	469	525	406	513	403	464	447	339	455	379	415
NIST610_7	462	517	399	502	401	455	436	343	454	382	415
NIST610_8	492	524	422	529	438	478	458	359	475	382	429
NIST610_9	476	521	409	513	433	467	447	353	462	368	420
NIST610_10	475	521	397	509	423	462	443	347	451	336	410
G_NIST612_1	40.6	42.5	31.0	78.3	41.0	39.9	38.7	41.9	40	38.7	38.2
G_NIST612_2	41.0	44.6	31.5	79.0	32.9	39.9	39.5	31.8	38.4	38.6	37.6
G_NIST612_3	41.2	44.1	31.2	78.6	40.9	40.1	40.0	40.7	41.9	38.4	38.1
G_NIST612_4	40.9	43.6	31.6	78.4	35.0	39.6	39.3	32.8	39.1	38.7	37.6
G_NIST612_5	41.3	44.1	31.6	78.5	37.2	40.1	40.2	33.0	39.3	38.6	38.1
G_NIST612_6	40.8	44.1	31.6	78.0	37.0	39.9	39.9	32.7	38.9	38.5	37.1
G_NIST612_7	41	44.5	31.7	78.9	44.2	40.3	40.1	40.8	41.3	38.6	37.6

G_NIST612_8	40.8	44.2	31.7	79.3	36.4	40.4	40.3	33.4	39.1	38.6	37.2
G_NIST612_9	41.2	44.1	31.5	78.3	39.7	39.9	39.4	37.8	40.4	38.6	38.4
G_NIST612_10	40.9	44.0	31	77.6	38.1	39.8	39.3	36.2	40.2	38.6	38.1
G_NIST612_11	41.0	44.1	31.4	78.6	37.3	40.0	39.9	34.4	39.6	38.5	37.7
G_NIST612_12	41.1	44.8	31.7	78.6	38.1	40.3	40.2	35.2	40.8	38.8	38.5
G_NIST612_13	41.0	43.6	31.5	79.1	38.1	40.0	39.4	34.9	40.4	38.6	38.1
G_NIST612_14	40.9	44.1	31.4	78.3	38.0	39.6	39.4	34.8	40	38.5	37.6
G_NIST612_15	40.8	43.5	31.3	78.0	37.9	40.0	39.3	34.9	39.8	38.7	37.6
G_NIST612_16	41.3	44.0	31.7	79.1	38.4	40.4	40.2	35.2	39.6	38.5	37.3
G_NIST612_17	41.0	43.9	30.9	78.0	37.7	39.7	39.2	35.7	40.2	38.6	37.9

Table 2.4. Major elements and trace elements concentrations in calcite veins from M4 drillcore and standards used.

	Mg	Al	Si	Ti	V	Cr	Mn	Fe	Co	Ni	Rb	Sr	Pb	U
M4 V2_1	73.1	Below LOD	1480	Below LOD	1.2	3.87	2102	9.1	Below LOD	0.15	Below LOD	50.40	0.02	0.1520
M4 V2_2	49.1	Below LOD	1121	Below LOD	Below LOD	3.75	2532	Below LOD	Below LOD	Below LOD	Below LOD	26.99	Below LOD	0.0006
M4 V2_3	33.4	Below LOD	Below LOD	Below LOD	0.019	3.99	1604	Below LOD	Below LOD	Below LOD	Below LOD	20.14	Below LOD	0.0034
M4 V2_4	46.2	Below LOD	Below LOD	Below LOD	Below LOD	3.74	2201	Below LOD	Below LOD	Below LOD	Below LOD	25.95	Below LOD	0.0005
M4 V2_5	56.3	2.8	1555	Below LOD	0.009	3.72	3067	1.60	Below LOD	Below LOD	Below LOD	10.97	Below LOD	0.0014
M4 V2_6	39.9	Below LOD	1558	Below LOD	0.022	3.73	2336	0.80	Below LOD	Below LOD	Below LOD	17.04	0.009	0.0077
M4 V2_7	84	38	1570	2	0.135	4.28	1696	19.0	Below LOD	Below LOD	Below LOD	24.70	0.029	0.0052
M4 V2_8	50	Below LOD	1470	Below LOD	0.04	3.79	2026	3.70	Below LOD	Below LOD	Below LOD	18.48	Below LOD	0.0061
M4 V2_9	57	Below LOD	970	Below LOD	Below LOD	3.78	3370	0.85	Below LOD	Below LOD	Below LOD	19.40	Below LOD	0.0011
M4 V2_10	112	Below LOD	1310	Below LOD	0.018	4.03	2955	11.61	Below LOD	Below LOD	Below LOD	44.10	0.039	0.0029
M4 V2_11	190	Below LOD	2580	Below LOD	2	600	2144	Below LOD	Below LOD	Below LOD	8	27.47	0.037	0.0080
M4 V2_12	Below LOD	Below LOD	800	Below LOD	Below LOD	4.02	5870	Below LOD	Below LOD	Below LOD	Below LOD	11.10	0.0056	0.0006
M4 V2_13	54	Below LOD	1390	Below LOD	0.054	3.93	2492	Below LOD	Below LOD	Below LOD	Below LOD	28.67	0.0085	0.0630
M4 V2_14	63	Below LOD	1660	Below LOD	Below LOD	3.93	2452	6.7	Below LOD	Below LOD	Below LOD	11.73	0.025	0.0054
M4 V2_15	117	5.1	1480	Below LOD	Below LOD	4.09	3956	2.6	Below LOD	Below LOD	Below LOD	11.01	0.023	0.0020
M4 V2_16	33.4	4.7	1110	Below LOD	0.014	4.06	1446	0.9	Below LOD	Below LOD	Below LOD	27.80	Below LOD	0.0033
M4 V2_17	98	Below LOD	Below LOD	Below LOD	Below LOD	4.05	5330	1.29	Below LOD	Below LOD	Below LOD	10.64	0.0152	Below LOD

M4 V2_18	54	Below LOD	1550	Below LOD	Below LOD	4.14	2349	Below LOD	Below LOD	Below LOD	0.014	17.68	0.029	0.0110
M4 V2_19	160	600	1950	31	2.7	15	3410	500	Below LOD	2	13	70.00	0.81	0.3400
M4 V2_20	259700	21000	2115000	935	5.3	20.4	81	855	Below LOD	Below LOD	58.6	239.0	52.8	3.2120
M4 V2_21	450	470	5900	31	3.9	600	2160	900	Below LOD	1.2	12	41.60	0.83	0.1200
M4 V2_22	2910	197	29300	13.2	Below LOD	4.39	2033	17.5	Below LOD	Below LOD	0.78	33.80	0.68	0.0391
M4 V2_23	158000	8500	1270000	570	3.99	16.3	1280	680	Below LOD	Below LOD	37.3	146.0	36.4	2.0300
M4 V2_24	35	0.61	Below LOD	Below LOD	Below LOD	4.08	1079	Below LOD	Below LOD	Below LOD	Below LOD	27.19	Below LOD	0.0006
M4 V2_25	190	10.2	2640	0.53	0.026	4.05	2795	7.6	Below LOD	Below LOD	0.023	29.17	0.04	0.0720
M4 V2_26	71.5	Below LOD	1050	Below LOD	Below LOD	3.88	6510	0.77	Below LOD	Below LOD	Below LOD	13.62	Below LOD	0.0211
M4 V2_27	48.2	Below LOD	1520	Below LOD	Below LOD	3.97	3258	0.51	Below LOD	Below LOD	Below LOD	8.96	0.006	0.0034
M4 V2_28	40.7	Below LOD	1381	Below LOD	Below LOD	3.73	2736	0.62	Below LOD	Below LOD	Below LOD	11.99	Below LOD	0.0154
M4 V2_29	44.1	Below LOD	1350	18	Below LOD	3.83	2701	0.90	Below LOD	Below LOD	Below LOD	10.79	Below LOD	0.0020
M4 V2_30	115	2.78	1790	Below LOD	0.051	3.84	3539	10.7	Below LOD	Below LOD	Below LOD	60.40	0.051	0.0270
M4 V2_31	21.2	Below LOD	630	Below LOD	Below LOD	4.03	708	Below LOD	Below LOD	Below LOD	Below LOD	26.38	Below LOD	0.0004
M4 V2_32	Below LOD	Below LOD	Below LOD	Below LOD	Below LOD	4.27	1237	8	Below LOD	Below LOD	Below LOD	20.32	0.036	0.0100
M4 V2_33	44.7	11	1360	0.3	0.069	4.03	2147	26	Below LOD	Below LOD	0.027	21.90	0.51	0.0690
M4 V2_34	29.6	Below LOD	Below LOD	Below LOD	Below LOD	4.03	1294	Below LOD	Below LOD	Below LOD	Below LOD	17.47	Below LOD	0.0005
M4 V2_35	Below LOD	Below LOD	1590	Below LOD	Below LOD	3.99	2937	6.24	Below LOD	Below LOD	Below LOD	27.10	0.0189	0.0063
M4 V2_36	240	32	2400	8	2.5	1200	2600	43	Below LOD	Below LOD	0.033	18.19	0.57	0.0450
M4 V2_37	59.3	Below LOD	890	Below LOD	Below LOD	4.09	2860	Below LOD	Below LOD	Below LOD	Below LOD	31.00	0.0188	0.0010
M4 V2_38	115000	6230	930000	429	3	14.3	2210	470	Below LOD	3.9	26.7	136.8	27.2	1.4800
M4 V2_39	93000	290000	10600000	890	12.9	380	300	4200	Below LOD	Below LOD	46	970.0	53	3.3000
M4 V2_40	260100	14680	2167000	958	5.38	25.9	36	841	Below LOD	1.6	60.2	232.0	55.4	3.3300
M4 V2_41	53	0.9	Below LOD	Below LOD	Below LOD	4.03	3006	Below LOD	Below LOD	Below LOD	Below LOD	13.86	0.0043	Below LOD
M4 V2_42	59.9	Below LOD	Below LOD	Below LOD	Below LOD	3.99	3446	Below LOD	Below LOD	Below LOD	Below LOD	14.39	Below LOD	0.0003
M4 V2_43	61	4.6	1410	0.46	0.039	4.04	3999	7.9	Below LOD	Below LOD	Below LOD	11.44	0.023	0.0026
M4 V2_44	42000	2600	370000	173	Below LOD	12.1	1910	269	Below LOD	1.2	11.1	61.00	10.6	0.7100
M4 V2_45	237000	14270	2216000	970	6.3	48	48	1600	Below LOD	1.9	70	265.0	62	3.7700
M4 V2_46	66.8	30	1727	Below LOD	0.78	3.95	2258	44	Below LOD	Below LOD	0.07	48.35	0.0223	0.1450
M4 V2_47	610	151	5400	6.1	2.5	700	2396	101	Below LOD	0.247	14	46.30	1.7	1.6900
M4 V2_48	69.1	Below LOD	1520	Below LOD	2.1	1000	3540	Below LOD	Below LOD	Below LOD	2.4	8.69	0.017	0.0046

M4 V2_49	91.8	Below LOD	Below LOD	Below LOD	Below LOD	4.09	2932	Below LOD	Below LOD	Below LOD	Below LOD	58.70	0.0089	0.0053
M4 V2_50	126	Below LOD	1550	Below LOD	0.25	3.96	2830	8.39	Below LOD	0.143	Below LOD	76.90	0.0215	0.2490
M4 V2_51	1163	2870	18000	117	111	38.9	237	17700	1.62	4.4	0.31	85.60	5.36	1.6900
M4 V2_52	2400	4560	37000	47	17.2	13.3	63	2860	Below LOD	1.42	1.06	85.70	1.76	0.3360

	Mg	Al	Si	Ti	V	Cr	Mn	Fe	Co	Ni	Rb	Sr	Pb	U
NIST612_1	77	11500	337000	44	39	36	38	51	35	39	32	78	39	38
NIST612_2	76	11100	334500	44	39	36	38	51	35	39	32	79	39	38
NIST612_3	77	12200	336700	44	39	36	38	51	35	39	31	79	38	36
NIST612_4	77	11140	339200	44	39	36	38	51	35	39	32	78	39	36
NIST612_5	77	12200	336200	44	39	36	39	52	36	40	32	79	39	38
NIST612_6	77	11300	335000	44	39	35	37	50	34	39	31	78	39	37
NIST612_7	77	11100	336700	44	39	36	39	52	35	39	32	80	39	37
NIST612_8	75	11200	336200	44	39	36	38	50	35	38	31	78	39	36
NIST612_9	77	11100	336400	44	39	36	38	51	35	39	32	79	39	37
NIST612_10	77	11200	336900	44	39	36	38	52	35	39	31	78	39	38
NIST612_11	77	11100	336500	44	39	36	38	51	35	39	32	78	39	37
NIST612_12	76	11000	333900	44	39	36	38	51	35	39	31	78	39	37
NIST612_13	77	11300	334500	44	39	36	38	51	35	39	31	78	39	37
NIST612_14	78	11200	338200	44	39	36	38	51	35	39	31	78	39	37
NIST612_15	77	11100	334000	44	39	36	38	51	35	39	32	79	39	38
NIST612_16	77	11200	337900	44	39	36	38	51	35	39	31	78	39	38
NIST612_17	76	11100	334800	44	39	36	38	51	35	39	31	78	39	37
NIST614_1	41	11230	342600	3.3	Below LOD	2.5	1.7	14	Below LOD	1.3	Below LOD	47	2.4	0.9
NIST614_2	40	10010	338900	3.5	Below LOD	2.1	1.7	14	Below LOD	1.2	Below LOD	48	2.3	0.8
NIST614_3	39	9520	339500	3.8	1.0	2.7	2.0	14	Below LOD	1.0	0.8	48	2.6	0.9
NIST614_4	39	9490	339300	3.3	1.0	2.7	2.0	14	Below LOD	0.9	0.9	49	2.5	0.9
NIST614_5	39	9642	343600	3.3	1.0	2.4	2.1	14	Below LOD	0.9	0.9	48	2.4	0.9
NIST614_6	39	9520	335800	3.2	Below LOD	2.5	2.0	15	Below LOD	1.1	0.9	48	2.6	0.9
NIST614_7	40	9683	341500	3.7	Below LOD	2.5	2.0	15	Below LOD	1.7	0.9	48	2.5	0.9

Appendix 2.3 Rare earth elements and yttrium for calcite veins

Table 2.5. Results of REEY in calcite veins from M4 drillcore and standards used.

	Y	La	Ce	Pr	Nd	Sm	Eu	Gd	Tb	Dy	Ho	Er	Tm	Yb	Lu
M4 V1_1	82.1	55.6	114	12.3	50.9	12.0	2.86	13.0	1.92	11.7	2.40	6.26	0.98	6.48	1.017
M4 V1_2	4.14	229	0.75	26.2	81.0	6.73	0.64	2.86	0.19	0.66	0.10	0.18	0.02	0.10	0.017
M4 V1_3	4.12	45	0.27	7.04	26.6	2.72	0.31	1.63	0.12	0.46	0.08	0.16	0.02	0.09	0.016
M4 V1_4	5.15	198	0.50	37.2	122	12.0	1.14	4.52	0.33	1.11	0.15	0.27	0.03	0.16	0.026
M4 V1_5	14.1	640	18.3	142	503	50.2	4.74	18.6	1.13	3.43	0.45	0.76	0.08	0.35	0.054
M4 V1_6	6.15	371	0.97	36.7	113	8.73	0.83	3.77	0.23	0.81	0.13	0.26	0.03	0.14	0.022
M4 V1_7	3.92	379	1.45	37.5	109	7.67	0.71	3.12	0.18	0.60	0.09	0.17	0.02	0.09	0.016
M4 V1_8	3.94	643	3.46	67.2	192	13.2	1.14	4.52	0.25	0.75	0.10	0.19	0.02	0.10	0.017
M4 V1_9	5.27	306	4.44	37.7	118	10.8	1.07	4.66	0.29	0.96	0.13	0.24	0.03	0.13	0.021
M4 V1_10	42.4	1.73	0.19	0.34	2.11	0.80	0.27	1.91	0.33	2.74	0.77	2.48	0.40	2.55	0.412
M4 V1_11	1.07	6.1	0.06	1.22	4.71	0.56	0.07	0.34	0.03	0.12	0.02	0.05	0.01	0.03	0.006
M4 V1_12	0.66	12	0.06	2.01	7.60	0.64	0.06	0.31	0.02	0.07	0.01	0.03	0.00	0.02	0.005
M4 V1_13	1.09	21.5	0.09	3.92	14.6	1.19	0.13	0.55	0.04	0.14	0.02	0.05	0.01	0.03	0.006
M4 V1_14	18.0	1	0.14	0.21	1.05	0.30	0.08	0.47	0.08	0.67	0.21	0.76	0.13	0.91	0.157
M4 V1_15	3.85	34.4	0.29	5.58	19.6	1.57	0.18	0.78	0.07	0.34	0.08	0.21	0.03	0.19	0.031
M4 V1_16	0.81	9.74	0.04	1.61	5.98	0.53	0.07	0.29	0.02	0.11	0.02	0.04	0.01	0.03	0.005
M4 V1_17	3.40	26.9	0.31	4.34	15.5	1.68	0.21	1.05	0.09	0.39	0.07	0.16	0.02	0.11	0.019
M4 V1_18	3.99	11.7	0.09	1.58	6.27	0.85	0.13	0.70	0.06	0.31	0.07	0.16	0.02	0.11	0.021
M4 V1_19	0.44	4.69	0.02	0.64	2.14	0.21	0.02	0.13	0.01	0.05	0.01	0.02	0.00	0.01	0.004
M4 V1_20	3.45	4.10	0.07	0.66	2.39	0.36	0.07	0.37	0.04	0.27	0.06	0.16	0.02	0.11	0.016
M4 V1_21	0.40	1.19	0.02	0.25	1.05	0.16	0.02	0.11	0.01	0.04	0.01	0.02	0.00	0.01	0.002
M4 V1_22	138	156	8.02	28.7	113	26.0	6.08	27.7	3.51	19.3	3.89	9.87	1.44	8.60	1.242
M4 V1_23	86.2	148	15.8	21.9	82.1	13.8	2.83	12.9	1.72	10.4	2.30	6.23	0.94	5.60	0.835
M4 V1_24	42.3	59.7	22.1	10.4	44.5	9.99	2.42	10.7	1.27	6.65	1.29	3.18	0.46	2.70	0.390
M4 V1_25	5.05	58.2	0.28	7.93	27.3	3.02	0.36	1.70	0.14	0.61	0.11	0.25	0.03	0.17	0.027
M4 V1_26	128	108	5.02	18.2	77.5	17.0	4.24	20.3	2.63	15.2	3.25	8.47	1.21	7.11	1.056

M4 V1_27	25.7	16.2	2.02	2.47	10.1	1.87	0.44	2.31	0.31	2.05	0.49	1.42	0.22	1.30	0.207
M4 V1_28	40.4	154	21.8	23.1	79.7	10.7	1.75	8.12	0.93	5.05	1.02	2.60	0.37	2.17	0.327

	Y	La	Ce	Pr	Nd	Sm	Eu	Gd	Tb	Dy	Ho	Er	Tm	Yb	Lu
M4 GG2_1	8.41	13.5	17.2	2.18	7.52	1.33	1.28	1.07	0.18	1.36	0.27	0.78	0.14	1.04	0.17
M4 GG2_2	4.05	21.2	5.5	1.94	6.24	0.83	3.29	0.62	0.08	0.49	0.11	0.27	0.05	0.32	0.05
M4 GG2_3	4.61	20.2	6.9	2.13	6.99	0.98	2.82	0.82	0.10	0.62	0.14	0.38	0.06	0.43	0.08
M4 GG2_4	2.80	10.1	7.1	1.17	3.90	0.51	1.17	0.40	0.06	0.40	0.09	0.26	0.05	0.30	0.06
M4 GG2_5	9.20	43	18.8	4.22	13.6	1.83	4.10	1.47	0.21	1.40	0.29	0.94	0.15	0.97	0.18
M4 GG2_6	11.1	36.6	21.1	4.47	14.9	2.31	6.20	1.75	0.25	1.59	0.36	0.97	0.17	1.14	0.21
M4 GG2_7	3.70	13.9	7.7	1.60	5.09	0.73	1.90	0.49	0.08	0.46	0.10	0.31	0.05	0.35	0.07
M4 GG2_8	9.52	18	18.8	2.70	9.56	1.61	1.90	1.34	0.21	1.47	0.31	0.98	0.15	1.09	0.19
M4 GG2_9	9.8	17.4	21.0	2.82	10.3	1.62	1.64	1.42	0.25	1.39	0.34	1.12	0.17	1.16	0.20
M4 GG2_10	10.3	22.3	18.1	3.12	11.0	1.77	2.78	1.46	0.24	1.52	0.33	0.97	0.17	1.16	0.19
M4 GG2_11	10.2	22.1	20.1	3.21	11.3	1.89	2.19	1.60	0.24	1.41	0.34	1.03	0.18	1.13	0.21
M4 GG2_12	5.65	27.4	11.1	2.97	9.56	1.27	4.48	0.94	0.12	0.74	0.15	0.40	0.07	0.46	0.09
M4 GG2_13	9.88	19.6	19.8	2.89	10.4	1.86	2.12	1.40	0.21	1.51	0.33	0.95	0.16	1.12	0.20
M4 GG2_14	4.40	16.2	6.3	1.74	5.79	0.85	2.20	0.69	0.10	0.58	0.13	0.39	0.07	0.45	0.08
M4 GG2_15	8.37	50	7.7	4.94	16.4	2.16	5.90	1.62	0.21	1.14	0.24	0.63	0.10	0.71	0.12
M4 GG2_16	4.70	17.3	5.1	2.03	7.05	1.04	2.54	0.82	Below LOD	0.62	Below LOD	0.37	Below LOD	0.41	0.07
M4 GG2_17	6.20	28.9	6.0	2.91	9.67	1.36	4.01	1.14	0.14	0.81	0.17	0.48	0.08	0.53	0.09
M4 GG2_18	4.59	28.7	5.5	3.11	9.76	1.28	5.34	0.93	0.12	0.64	0.14	0.39	0.06	0.53	0.09
M4 GG2_19	5.67	25.1	7.8	2.54	8.80	1.18	3.46	1.04	0.13	0.75	0.16	0.48	0.07	0.56	0.11
M4 GG2_20	3.16	9.5	4.6	1.11	3.85	0.52	1.78	0.40	0.07	0.40	0.09	0.26	0.04	0.30	0.05
M4 GG2_21	11.6	50	11.5	5.23	17.4	2.51	6.00	2.00	0.27	1.56	0.30	0.86	0.13	0.94	0.16
M4 GG2_22	8.30	15.2	17.3	2.35	7.94	1.52	1.42	1.09	0.20	1.19	0.27	0.83	0.14	0.95	0.16

	Y	La	Ce	Pr	Nd	Sm	Eu	Gd	Tb	Dy	Ho	Er	Tm	Yb	Lu
M4 S1(2)_1	11.1	15.6	26.7	2.86	10.0	1.68	1.03	1.51	0.24	1.59	0.38	1.14	0.20	1.38	0.26
M4 S1(2)_2	11.2	15.6	26.9	2.87	9.9	1.89	1.01	1.60	0.24	1.57	0.37	1.16	0.20	1.42	0.24

M4 S1(2)_3	11.2	15.6	26.9	2.90	10.2	1.82	1.04	1.58	0.24	1.63	0.39	1.15	0.20	1.46	0.25
M4 S1(2)_4	11.4	15.9	27.2	2.94	10.3	1.88	1.03	1.52	0.23	1.64	0.39	1.18	0.20	1.45	0.27
M4 S1(2)_5	11.4	15.8	27.1	2.92	10.3	1.76	1.04	1.59	0.24	1.63	0.38	1.21	0.20	1.37	0.25
M4 S1(2)_6	11.4	15.9	27.1	2.90	9.9	1.76	1.04	1.45	0.25	1.67	0.39	1.20	0.20	1.45	0.25
M4 S1(2)_7	11.3	15.9	27.4	2.99	10.2	1.85	1.05	1.44	0.26	1.66	0.39	1.14	0.20	1.39	0.25
M4 S1(2)_8	11.3	15.7	27.0	2.90	10.1	1.81	1.06	1.57	0.24	1.65	0.38	1.16	0.21	1.45	0.24
M4 S1(2)_9	11.2	15.5	26.7	2.87	10.1	1.82	1.02	1.53	0.23	1.64	0.38	1.19	0.21	1.45	0.26
M4 S1(2)_10	11.4	15.6	27.1	2.92	10.2	1.82	1.03	1.55	0.25	1.70	0.38	1.17	0.20	1.39	0.26
M4 S1(2)_11	11.4	15.6	26.9	2.92	10.0	1.79	1.05	1.49	0.24	1.67	0.38	1.21	0.21	1.39	0.25
M4 S1(2)_12	11.4	15.9	27.2	2.97	10.4	1.94	1.06	1.47	0.24	1.65	0.39	1.21	0.21	1.45	0.25
M4 S1(2)_13	11.3	15.8	27.1	2.89	10.3	1.77	1.06	1.53	0.25	1.60	0.40	1.20	0.21	1.42	0.26
M4 S1(2)_14	11.4	15.9	27.3	2.94	10.1	1.83	1.04	1.48	0.26	1.62	0.39	1.22	0.22	1.38	0.26

	Y	La	Ce	Pr	Nd	Sm	Eu	Gd	Tb	Dy	Ho	Er	Tm	Yb	Lu
NIST610_1	441	449	471	444	419	438	395	401	380	374	416	402	415	393	412
NIST610_2	443	454	477	452	425	444	403	406	388	382	426	411	424	402	420
NIST610_3	434	444	466	444	415	435	396	399	381	375	415	401	412	391	406
NIST610_4	435	442	463	442	412	432	398	398	385	379	416	400	412	391	405
NIST610_5	433	434	453	434	403	423	392	389	379	372	408	392	403	385	397
NIST610_6	436	439	460	441	412	433	403	397	390	384	418	401	414	396	405
NIST610_7	427	430	452	431	406	426	399	392	389	384	416	399	412	394	403
NIST610_8	453	451	474	451	427	445	418	406	406	399	431	412	427	409	417
NIST610_9	441	441	465	440	418	435	411	397	401	394	421	402	416	402	404
NIST610_10	438	434	457	432	410	429	406	391	395	387	412	393	406	394	393
G_NIST612_1	38.3	35.6	38.7	36.5	35.9	38.1	36.3	36.1	37.8	37.5	38.3	37.5	38.4	39.6	37.1
G_NIST612_2	37.5	35.6	38.6	36.8	35.6	37.8	33.5	36.4	33.9	34.2	37.0	37.4	36.9	38.0	36.3
G_NIST612_3	38.6	36.1	39.4	38.0	36.6	38.7	37.5	37.3	39.3	38.9	39.4	38.6	39.2	40.7	37.3
G_NIST612_4	37.3	35.5	38.3	37.0	35.3	37.7	34.2	36.3	34.5	35.2	37.5	38.1	37.8	39.2	36.9
G_NIST612_5	37.7	36.1	38.8	37.5	35.9	38.1	33.8	36.8	34.5	34.8	37.6	38.2	37.9	38.8	37.4
G_NIST612_6	37.4	35.7	38.5	37.6	35.6	38.0	33.7	36.6	34.2	34.6	37.2	37.7	37.2	38.4	36.3
G_NIST612_7	38.7	36.1	38.9	37.9	36.4	38.2	37.9	36.9	39.3	38.9	39.0	37.8	38.5	40.2	36.7

G_NIST612_8	37.9	36.0	38.9	37.5	35.9	38.2	34.5	36.8	35.1	35.2	37.7	37.8	37.7	38.8	37.0
G_NIST612_9	38.5	35.8	38.6	37.0	36.0	38.0	37.3	36.7	38.6	38.3	39.1	38.2	38.9	40.4	37.5
G_NIST612_10	38.1	35.5	38.4	37.0	35.7	37.8	36.1	36.2	37.4	37.3	38.5	38.0	38.6	39.8	37.1
G_NIST612_11	37.8	35.8	38.7	37.2	35.9	38.2	34.4	36.8	35.4	35.7	37.7	38.0	37.7	38.9	36.8
G_NIST612_12	38.1	36.0	39.0	37.8	36.2	38.4	34.8	37.2	36.0	36.3	38.4	38.7	38.5	39.7	37.5
G_NIST612_13	37.7	35.7	38.5	37.0	35.7	37.9	34.5	36.6	35.5	35.7	37.9	38.0	38.0	39.3	37.2
G_NIST612_14	37.6	35.5	38.4	37.2	35.7	38.0	34.5	36.8	35.7	35.8	37.9	37.9	37.7	39.0	36.5
G_NIST612_15	37.9	35.7	38.7	37.4	36.0	38.1	34.8	36.7	35.9	35.8	37.9	37.8	37.9	39.1	36.6
G_NIST612_16	38.5	36.2	39.2	37.5	36.3	38.4	35.1	36.6	36.2	36.1	37.9	37.8	37.8	39.1	36.6
G_NIST612_17	38.0	35.5	38.5	36.7	35.6	37.9	35.2	36.4	36.6	36.5	38.2	38.2	38.1	39.5	37.0

	Y	La	Ce	Pr	Nd	Sm	Eu	Gd	Tb	Dy	Ho	Er	Tm	Yb	Lu
M4 V2_1	11.0	22.2	43.5	5.72	25.6	4.18	0.97	3.22	0.32	1.68	0.29	0.64	0.08	0.46	0.06
M4 V2_2	7.06	4.98	9.62	1.56	7.24	1.37	0.37	1.32	0.15	0.89	0.17	0.43	0.06	0.34	0.05
M4 V2_3	2.92	1.62	4.08	0.69	3.22	0.59	0.17	0.54	0.06	0.37	0.07	0.19	0.02	0.16	0.02
M4 V2_4	2.76	1.20	2.32	0.39	1.70	0.34	0.10	0.31	0.04	0.28	0.06	0.18	0.03	0.18	0.03
M4 V2_5	20.5	5.28	12.7	2.36	12.9	3.00	0.90	3.44	0.43	2.54	0.50	1.24	0.15	0.79	0.11
M4 V2_6	17.8	8.31	16.2	2.61	13.5	2.95	0.87	3.16	0.36	2.04	0.39	0.92	0.11	0.53	0.07
M4 V2_7	3.01	1.99	4.81	0.80	3.66	0.65	0.17	0.57	0.07	0.36	0.07	0.18	0.02	0.17	0.02
M4 V2_8	15.1	10.3	19.6	2.89	14.5	2.97	0.87	3.14	0.33	1.79	0.35	0.82	0.09	0.46	0.06
M4 V2_9	2.65	0.86	2.10	0.35	1.72	0.33	0.09	0.32	0.05	0.28	0.06	0.17	0.03	0.17	0.03
M4 V2_10	10.2	5.28	15.0	2.20	11.4	2.59	0.72	2.42	0.26	1.31	0.23	0.53	0.06	0.30	0.04
M4 V2_11	13.0	10.8	19.4	2.73	13.3	2.40	0.69	2.41	0.26	1.45	0.29	0.68	0.08	0.42	0.06
M4 V2_12	2.67	0.86	2.06	0.34	1.68	0.33	0.11	0.40	0.05	0.32	0.07	0.19	0.03	0.19	0.03
M4 V2_13	12.6	9.33	14.2	2.09	10.1	1.90	0.57	2.14	0.24	1.41	0.28	0.71	0.08	0.44	0.07
M4 V2_14	19.6	13.1	19.2	2.99	14.3	2.87	0.87	3.29	0.39	2.29	0.46	1.12	0.13	0.68	0.09
M4 V2_15	3.13	1.10	2.81	0.50	2.44	0.50	0.15	0.51	0.07	0.37	0.08	0.21	0.03	0.21	0.03
M4 V2_16	2.27	0.81	1.90	0.29	1.38	0.25	0.08	0.27	0.04	0.23	0.05	0.17	0.02	0.18	0.03
M4 V2_17	2.55	1.04	2.31	0.38	1.68	0.27	0.08	0.30	0.04	0.27	0.06	0.18	0.03	0.19	0.03
M4 V2_18	15.2	7.43	12.5	1.87	9.10	1.88	0.58	2.22	0.29	1.78	0.36	0.92	0.11	0.61	0.09
M4 V2_19	11.8	33.9	65.1	7.20	30.1	4.01	0.94	2.70	0.28	1.43	0.24	0.58	0.07	0.41	0.05

M4 V2_20	11.5	22.2	43.2	4.66	17.7	3.09	0.51	2.26	0.32	2.11	0.41	1.23	0.20	1.51	0.21
M4 V2_21	17.3	56.4	114	13.3	54.6	7.80	1.54	5.36	0.52	2.53	0.45	1.01	0.13	0.71	0.10
M4 V2_22	8.36	5.46	10.4	1.62	7.64	1.39	0.41	1.46	0.17	1.0	0.20	0.51	0.07	0.43	0.06
M4 V2_23	15.7	17.1	34.1	4.10	17.1	3.28	0.72	2.83	0.36	2.21	0.45	1.24	0.17	1.10	0.18
M4 V2_24	1.49	0.66	1.51	0.22	1.00	0.18	0.05	0.18	0.02	0.16	0.03	0.10	0.01	0.11	0.02
M4 V2_25	14.9	14.9	36.8	4.90	24.0	4.56	1.22	3.94	0.39	2.0	0.36	0.82	0.09	0.51	0.07
M4 V2_26	6.15	1.51	3.81	0.71	3.83	0.88	0.26	0.97	0.12	0.73	0.15	0.37	0.05	0.25	0.04
M4 V2_27	26.6	6.83	14.8	2.73	14.8	3.51	1.10	4.22	0.52	3.12	0.62	1.53	0.18	0.93	0.12
M4 V2_28	17.9	8.49	14.1	2.36	12.0	2.53	0.78	2.93	0.36	2.14	0.42	1.06	0.13	0.67	0.09
M4 V2_29	13.4	8.88	13.1	1.91	8.91	1.78	0.54	2.10	0.26	1.61	0.33	0.87	0.11	0.62	0.08
M4 V2_30	10.5	11.9	26.4	3.28	15.5	2.78	0.71	2.41	0.25	1.35	0.24	0.58	0.07	0.40	0.05
M4 V2_31	0.90	0.40	0.96	0.14	0.62	0.12	0.03	0.10	0.01	0.09	0.02	0.06	0.01	0.06	0.01
M4 V2_32	1.50	0.74	1.88	0.30	1.39	0.26	0.07	0.24	0.03	0.17	0.03	0.09	0.01	0.08	0.01
M4 V2_33	8.28	4.50	12.2	2.0	9.90	2.50	0.70	2.40	0.23	1.21	0.21	0.47	0.05	0.24	0.03
M4 V2_34	1.60	0.63	1.49	0.22	1.06	0.19	0.05	0.19	0.03	0.16	0.04	0.11	0.02	0.12	0.02
M4 V2_35	15.2	11.8	27.1	3.83	19.3	3.85	1.07	3.67	0.38	2.03	0.36	0.84	0.09	0.51	0.06
M4 V2_36	3.56	1.94	3.89	0.57	2.65	0.53	0.15	0.55	0.07	0.44	0.09	0.23	0.03	0.24	0.03
M4 V2_37	8.04	9.06	10.8	1.59	6.81	1.22	0.36	1.31	0.17	0.98	0.20	0.51	0.06	0.38	0.05
M4 V2_38	6.31	10.8	22.1	2.27	8.60	1.60	0.25	1.22	0.18	1.05	0.21	0.67	0.10	0.69	0.11
M4 V2_39	7.70	15.6	32.0	3.30	12.0	2.30	0.43	2.10	0.29	1.80	0.31	1.04	0.16	0.58	0.21
M4 V2_40	11.8	23.2	44.6	4.86	18.8	3.11	0.52	2.38	0.33	2.14	0.43	1.24	0.22	1.34	0.21
M4 V2_41	3.09	1.36	2.96	0.47	2.20	0.44	0.12	0.45	0.06	0.36	0.07	0.22	0.03	0.20	0.03
M4 V2_42	2.26	0.88	2.10	0.35	1.69	0.31	0.09	0.30	0.04	0.25	0.05	0.16	0.02	0.16	0.03
M4 V2_43	11.8	2.67	6.32	1.23	6.88	1.65	0.51	1.96	0.24	1.41	0.27	0.69	0.07	0.41	0.05
M4 V2_44	12.6	11.6	21.3	2.84	12.4	2.39	0.61	2.24	0.28	1.62	0.35	0.92	0.13	0.72	0.12
M4 V2_45	13.4	26.4	51	5.60	21.4	4.00	0.66	2.59	0.40	2.37	0.48	1.49	0.23	1.64	0.24
M4 V2_46	12.4	28.0	56	6.66	29.4	4.49	1.01	3.49	0.35	1.79	0.32	0.74	0.09	0.51	0.07
M4 V2_47	21.8	67.1	140	15.7	66.5	9.65	1.95	6.67	0.64	3.19	0.54	1.28	0.16	0.91	0.12
M4 V2_48	24.3	4.70	11.8	2.45	14.2	3.90	1.27	4.56	0.59	3.45	0.65	1.64	0.19	1.01	0.13
M4 V2_49	2.96	1.08	2.43	0.42	1.94	0.40	0.11	0.39	0.05	0.31	0.06	0.19	0.03	0.20	0.03
M4 V2_50	9.73	35.2	79	7.16	29.4	3.87	0.84	2.65	0.26	1.31	0.23	0.55	0.07	0.41	0.06

M4 V2_51	21.4	67.0	28	9.10	33.0	5.20	1.10	4.50	0.60	3.60	0.70	1.98	0.29	1.90	0.28
M4 V2_52	6.81	38.8	2.06	4.83	15.7	1.60	0.40	1.17	0.13	0.77	0.16	0.52	0.09	0.68	0.11

	Y	La	Ce	Pr	Nd	Sm	Eu	Gd	Tb	Dy	Ho	Er	Tm	Yb	Lu
NIST612_1	38.0	35.9	38.9	37.3	36.2	38.6	35.4	36.8	36.2	36.1	37.8	37.9	38.3	39.3	36.9
NIST612_2	38.3	35.9	38.7	37.1	36.1	38.2	35.3	37.0	36.3	36.2	38.1	38.0	38.3	39.3	36.9
NIST612_3	38.1	35.6	38.4	37.0	35.3	37.5	34.6	36.3	35.7	35.8	38.0	38.0	38.4	39.7	37.1
NIST612_4	38.1	36.0	39.1	37.3	35.9	38.4	35.2	36.9	36.4	36.2	38.5	38.2	38.3	39.1	36.5
NIST612_5	38.1	35.7	38.6	37.2	35.7	38.0	34.7	36.3	35.6	35.8	37.9	38.0	37.4	38.6	36.8
NIST612_6	37.9	35.8	38.6	37.2	35.8	38.1	34.9	36.5	35.6	35.7	37.7	38.0	37.8	38.9	36.9
NIST612_7	38.5	36.2	39.1	37.2	36.0	37.9	34.5	36.2	35.7	35.7	38.1	38.0	38.0	39.3	37.1
NIST612_8	37.5	35.8	38.5	37.2	36.0	38.3	35.2	37.2	36.6	36.4	38.3	38.2	38.4	39.3	36.5
NIST612_9	38.0	35.8	38.8	37.2	35.9	38.1	34.8	36.4	35.6	35.6	37.7	37.6	37.8	39.1	36.8
NIST612_10	38.0	35.9	39.1	37.2	36.3	38.3	35.2	36.9	36.1	36.1	38.0	38.1	37.8	39.5	37.0
NIST612_11	38.2	35.8	38.7	37.2	35.8	37.9	34.6	36.4	35.7	35.9	38.0	37.9	37.4	39.0	37.0
NIST612_12	38.1	35.8	38.6	37.2	35.9	38.3	35.1	36.9	36.0	36.1	38.1	38.0	37.6	38.8	36.8
NIST612_13	38.1	35.9	38.6	37.4	35.8	38.0	34.7	36.5	35.9	36.0	38.0	38.1	38.2	39.4	37.3
NIST612_14	37.8	35.7	38.4	37.0	35.3	37.6	34.5	36.3	35.8	35.9	37.9	37.9	37.5	38.9	36.7
NIST612_15	38.4	36.0	39.0	37.3	36.1	38.7	35.5	37.4	36.7	36.6	38.5	38.3	38.3	39.8	37.2
NIST612_16	38.0	35.8	38.8	37.2	36.1	38.2	34.9	36.7	35.9	35.9	37.8	37.8	37.7	39.4	36.7
NIST612_17	37.7	35.8	38.6	37.2	36.0	38.7	35.3	37.4	36.4	36.0	38.1	38.0	38.1	39.5	36.9
NIST614_1	0.79	0.73	0.82	0.77	0.77	0.78	0.78	0.76	0.76	0.82	0.79	0.80	0.78	0.81	0.77
NIST614_2	0.80	0.75	0.83	0.78	0.79	0.81	0.81	0.81	0.77	0.80	0.78	0.80	0.78	0.79	0.76
NIST614_3	0.83	0.74	0.83	0.78	0.81	0.82	0.80	0.77	0.76	0.79	0.81	0.80	0.79	0.82	0.77
NIST614_4	0.83	0.75	0.83	0.77	0.77	0.86	0.81	0.79	0.76	0.81	0.81	0.77	0.79	0.80	0.77
NIST614_5	0.83	0.74	0.82	0.77	0.78	0.83	0.81	0.80	0.77	0.80	0.80	0.79	0.78	0.81	0.77
NIST614_6	0.82	0.74	0.83	0.78	0.80	0.84	0.81	0.80	0.77	0.79	0.80	0.80	0.80	0.83	0.77
NIST614_7	0.84	0.74	0.81	0.76	0.80	0.83	0.79	0.78	0.76	0.81	0.79	0.78	0.78	0.76	0.77

APPENDIX 3: GEOCHRONOLOGY

Appendix 3.1. U-Pb ages of calcite veins.

Table 3.1. Fist set of Uranium and Lead isotopic compositions analyzed and the standards DB, RIO and RS used.

DB					RIO					RS				
07/35	Error	06/38	Error	rho	07/35	Error	06/38	Error	rho	07/35	Error	06/38	Error	rho
2.1	0.22	0.0327	0.0025	0.997	0.082	0.008	0.0087	0.0001	0.199	0.81	0.07	0.053	0.001	0.092
1.4	0.03	0.0243	0.0003	0.669	0.125	0.046	0.0095	0.0005	0.989	1.11	0.12	0.057	0.002	0.482
3.0	0.11	0.0399	0.0011	0.929	0.071	0.005	0.0090	0.0002	0.159	0.93	0.08	0.054	0.002	0.068
2.1	0.07	0.0307	0.0007	0.909	0.079	0.006	0.0089	0.0002	0.034	0.76	0.08	0.053	0.001	-0.077
1.5	0.04	0.0244	0.0005	0.879	0.065	0.005	0.0093	0.0002	-0.073	1.09	0.09	0.060	0.002	0.153
1.4	0.04	0.0249	0.0004	0.846	0.188	0.014	0.0096	0.0002	0.655	1.26	0.13	0.055	0.002	0.700
1.8	0.04	0.0271	0.0004	0.851	0.067	0.004	0.0089	0.0001	-0.038	0.53	0.06	0.051	0.001	-0.026
1.0	0.02	0.0193	0.0002	0.703	0.068	0.004	0.0085	0.0001	0.046	0.69	0.06	0.049	0.001	0.004

M4 S1(2)					M4 GG2					M4 V1				
07/35	Error	06/38	Error	rho	07/35	Error	06/38	Error	rho	07/35	Error	06/38	Error	rho
0.108	0.016	0.005	0.000	0.182	166	11	1.35	0.10	0.941	3.10	0.19	0.0337	0.0016	0.219
1.140	0.097	0.016	0.001	0.345	227	15	1.83	0.14	0.974	2.27	0.15	0.0282	0.0016	0.230
0.667	0.043	0.010	0.001	0.323	172	8	1.38	0.07	0.948	1.86	0.09	0.0257	0.0010	0.080
0.990	0.130	0.014	0.001	0.004	120	11	0.94	0.09	0.887	2.46	0.17	0.0302	0.0018	0.107
0.510	0.150	0.008	0.001	0.071	174	6	1.43	0.06	0.893	1.10	0.08	0.0194	0.0010	0.146
0.207	0.016	0.005	0.000	-0.015	189	9	1.33	0.07	0.562	1.06	0.07	0.0192	0.0007	0.153
0.383	0.036	0.006	0.000	0.154	138	8	1.15	0.08	0.851	0.97	0.08	0.0178	0.0008	-0.036
0.284	0.037	0.005	0.000	0.091	59	1	0.47	0.01	0.002	2.89	0.14	0.0399	0.0016	0.004
0.884	0.043	0.010	0.000	0.086	208	10	1.64	0.08	0.918	1.95	0.11	0.0276	0.0012	0.090
0.930	0.130	0.011	0.001	0.265	249	5	1.96	0.04	0.748	2.21	0.14	0.0277	0.0014	0.031

0.294	0.032	0.007	0.000	-0.019	73	2	0.56	0.01	0.607	0.78	0.04	0.0166	0.0005	0.040
0.354	0.033	0.009	0.000	-0.018	56	1	0.45	0.01	0.314	0.23	0.02	0.0120	0.0004	-0.109
6.190	0.530	0.087	0.005	0.380	86	3	0.68	0.03	0.887	0.67	0.08	0.0161	0.0011	0.035
6.840	0.480	0.090	0.005	0.122	95	2	0.73	0.02	0.509	0.83	0.09	0.0168	0.0013	-0.029
44.55	0.920	0.421	0.009	0.568	49	1	0.39	0.01	0.788	1.01	0.06	0.0194	0.0007	0.123
23.60	1.600	0.220	0.013	0.302	50	1	0.39	0.01	0.399	1.46	0.11	0.0227	0.0010	0.156
46.20	3.800	0.509	0.043	0.937	73	2	0.56	0.02	0.803	1.32	0.13	0.0211	0.0013	0.515
111.8	3.900	1.014	0.035	0.958	66	3	0.53	0.02	0.969	0.50	0.03	0.0146	0.0003	-0.014
1.264	0.093	0.023	0.001	0.427	52	2	0.43	0.02	0.924	0.52	0.03	0.0145	0.0005	-0.051
3.830	0.440	0.043	0.003	0.173	30	1	0.24	0.01	0.259	0.73	0.06	0.0159	0.0008	-0.107
1.240	0.170	0.019	0.002	0.177	128	3	1.04	0.02	0.396	0.53	0.04	0.0148	0.0007	0.066
4.540	0.420	0.050	0.005	0.499	119	3	1.02	0.03	0.761	0.46	0.03	0.0142	0.0004	-0.069
1.900	0.190	0.022	0.002	0.116	42	1	0.34	0.01	0.461	0.11	0.01	0.0106	0.0001	0.072
0.620	0.120	0.010	0.001	0.035	44	2	0.35	0.02	0.718	0.25	0.02	0.0129	0.0003	0.187
0.190	0.100	0.005	0.001	0.161	67	2	0.53	0.02	0.825	0.50	0.07	0.0256	0.0015	0.208
1.280	0.150	0.014	0.001	-0.004	70	2	0.55	0.01	0.820	0.11	0.01	0.0107	0.0002	-0.003
0.461	0.074	0.009	0.001	0.220	101	3	0.79	0.04	0.667	0.13	0.01	0.0111	0.0002	0.099
0.176	0.024	0.005	0.000	0.206	93	2	0.74	0.03	0.632	1.35	0.19	0.0266	0.0022	0.389
0.670	0.110	0.022	0.002	0.151	64	3	0.54	0.02	0.473	0.16	0.01	0.0130	0.0003	0.112
4.480	0.260	0.052	0.003	0.374	26	4	0.21	0.02	0.925	0.12	0.01	0.0107	0.0001	0.024
0.540	0.080	0.011	0.001	0.006	87	2	0.69	0.02	0.749	0.49	0.04	0.0172	0.0008	0.093
0.143	0.037	0.006	0.001	0.307	49	1	0.40	0.01	0.383	1.24	0.15	0.0253	0.0020	-0.117
0.049	0.017	0.005	0.000	0.039	90	5	0.69	0.04	0.808	0.13	0.01	0.0107	0.0001	0.080
0.052	0.006	0.003	0.000	0.143	125	3	1.00	0.02	0.804	0.64	0.09	0.0217	0.0012	0.086
0.228	0.031	0.006	0.000	0.090	63	2	0.51	0.01	0.759	0.24	0.02	0.0137	0.0004	0.125
0.574	0.068	0.015	0.001	0.370	58	3	0.45	0.02	0.840	1.35	0.06	0.0188	0.0006	0.235
0.261	0.069	0.007	0.001	-0.037	77	2	0.59	0.02	0.758	1.44	0.06	0.0209	0.0006	0.069
0.216	0.048	0.006	0.001	-0.026	177	5	1.41	0.04	0.805	4.13	0.17	0.0432	0.0018	0.284
2.140	0.190	0.022	0.002	0.326	389	6	2.72	0.04	0.495	0.80	0.04	0.0134	0.0004	0.188
40.84	0.750	0.365	0.006	0.816	77	3	0.59	0.03	0.135	8.56	0.32	0.0710	0.0018	0.447
60	3.300	0.557	0.025	0.310	347	12	2.50	0.08	0.575	4.08	0.16	0.0370	0.0011	0.302

5.540	0.400	0.047	0.003	0.932	33	1	0.26	0.01	0.668	8.60	0.22	0.0763	0.0023	0.124
0.810	0.140	0.011	0.001	0.011	295	7	2.05	0.06	0.437	4.81	0.32	0.0442	0.0025	0.362
2.880	0.190	0.029	0.002	0.561	89	3	0.67	0.02	0.861	1.63	0.08	0.0228	0.0007	0.111
0.850	0.140	0.012	0.002	0.335	44	2	0.34	0.01	0.925	4.14	0.19	0.0430	0.0016	0.522
146	10.000	1.274	0.077	0.844	43	11	0.33	0.09	0.952	2.05	0.14	0.0262	0.0012	0.297
9.8	1.200	0.086	0.008	0.570	52	1	0.39	0.01	0.507	1.25	0.08	0.0195	0.0007	-0.076
7.790	0.190	0.076	0.001	0.550	73	1	0.57	0.01	0.666	1.72	0.15	0.0243	0.0015	0.340
1.153	0.059	0.016	0.001	0.758	101	2	0.75	0.01	0.642					
71.3	1.100	0.587	0.008	0.610	82	3	0.69	0.02	0.562					
37.20	2.500	0.329	0.017	0.949	86	3	0.65	0.02	0.727					
0.820	0.110	0.010	0.001	0.035										
0.195	0.026	0.004	0.000	0.166										
0.447	0.068	0.007	0.001	0.914										
2.670	0.240	0.025	0.002	0.939										
1.060	0.200	0.012	0.002	0.202										
33.6	1.100	0.292	0.010	0.822										
2.630	0.230	0.027	0.002	-0.059										
3.840	0.220	0.038	0.002	0.434										
1.820	0.300	0.020	0.002	0.240										
0.471	0.079	0.009	0.001	0.048										
1.067	0.066	0.014	0.001	0.102										
0.389	0.085	0.008	0.001	0.002										
5.330	0.280	0.054	0.003	0.259										

Table 3.2. Uranium-lead isotopic compositions for sample M4 V2 and the standards used (DB and RIO)

M4 V2					DB				
07/35	Error	06/38	Error	rho	07/35	Error	06/38	Error	rho
64	17	0.52	0.13	0.950	0.802	0.013	0.0174	0.00017	0.54114
21	10	0.19	0.08	0.176	0.808	0.013	0.01768	0.00018	0.50811
161	18	1.28	0.14	0.834	0.818	0.02	0.01725	0.00019	0.65711
164	14	1.55	0.17	0.634	0.688	0.01	0.01636	0.00014	0.62674
151	15	1.22	0.10	0.880	0.743	0.0085	0.0167	0.00011	0.42383
15	3	0.16	0.04	0.275	0.794	0.01	0.01714	0.00012	0.47239
182	23	1.51	0.20	0.929	0.8238	0.0098	0.01751	0.00014	0.58905
225	28	2.05	0.25	0.862	0.7845	0.0089	0.01735	0.00014	0.56172
169	13	1.38	0.12	0.560					
277	24	2.08	0.22	0.689	RIO				
194	28	1.58	0.20	0.738	0.0604	0.0074	0.00867	0.00015	0.14779
3	1	0.02	0.00	-0.049	0.0567	0.005	0.00881	0.00013	0.18001
192	26	1.55	0.21	0.973	0.0593	0.0061	0.00867	0.00013	-0.04551
308	12	2.80	0.12	0.699	0.0465	0.0061	0.00857	0.00014	0.059121
56	3	0.50	0.04	0.270	0.1129	0.0099	0.00915	0.00016	0.40765
133	13	1.25	0.15	0.587	0.0513	0.0055	0.00854	0.00013	0.024941
128	9	1.16	0.09	0.753	0.0496	0.0049	0.00857	0.00013	-0.03798
404	54	3.09	0.41	0.807					
447	9	4.23	0.09	0.784					
130	30	1.23	0.31	0.674					
169	43	1.47	0.36	0.943					
176	65	1.10	0.33	0.963					
219	55	1.82	0.44	0.877					
147	28	1.24	0.31	0.814					
161	16	1.28	0.12	0.565					
77	6	0.71	0.06	0.658					
145	12	1.29	0.13	0.641					

46	4	0.37	0.04	0.399
47	8	0.42	0.08	0.111
192	26	1.69	0.25	0.957
147	13	1.32	0.16	0.863
535	5	4.66	0.04	0.812
9	1	0.08	0.00	0.171
2	0	0.02	0.00	0.333
3	1	0.04	0.01	0.082
70	15	0.54	0.12	0.600
2	0	0.02	0.00	-0.001